



THESIS

Cardiff School of Medicine

THESIS PRESENTED TO CARDIFF UNIVERSITY FOR THE DEGREE OF
DOCTOR OF PHILOSOPHY

by

Evgeniia Lobanova

**LINKING AMYLOID, INFLAMMATION AND LIPIDS
TO ALZHEIMER'S DISEASE USING STATE-OF-THE-
ART IMAGING TECHNIQUES**

Supervisors: Prof. Kathy Triantafilou
Dr. Martha Triantafilou

Cardiff 2019

Contents

List of abbreviations	5
List of figures	9
Abstract.....	20
Acknowledgements	23
Chapter 1. Introduction.....	24
Chapter 2. Literature Review.....	26
2.1. Major contributors to Alzheimer’s disease pathogenesis.....	26
2.1.1. Amyloid- β plaques in Alzheimer’s disease.....	26
2.1.2. Lipid-amyloid interplay in Alzheimer’s disease	28
2.1.3. Inflammation in Alzheimer’s disease.....	30
2.2. State-of-the-art imaging techniques in the study of Alzheimer’s disease brains	37
2.3. Multivariate unmixing analysis for micro-spectroscopy images.....	40
Chapter 3. Theoretical framework.....	43
3.1. Formulation of hyperspectral image unmixing problem	43
3.1.1. Forward scattering problem	43
3.1.2. Inverse scattering problem	43
3.2. Singular Value Decomposition with Automatic Divisive Correlation (SVD-ADC) for noise filtering	44
3.2.1. Formulation of SVD-ADC	44
3.2.2. Validation of SVD-ADC.....	47
3.3. Bottom Gaussian Fitting (BGF) for background subtraction	49
3.3.1. Formulation of BGF	50
3.3.2. Validation of BGF.....	52
3.4. Efficient Quantitative Unsupervised/Partially Supervised Non-negative Matrix Factorization (Q-US/PS-NMF)	53
3.4.1. Formulation of Q-US/PS-NMF.....	53
3.4.2. Validation of Q-US/PS-NMF.....	56
3.5. Findings	56
Chapter 4. Methodology	59

Chapter 5. Chemical imaging of formalin-fixed-paraffin-embedded brain sections by point-scan Raman micro-spectroscopy	62
5.1. Introduction	62
5.2. Method.....	64
5.2.1. Human tissue samples and tissue preparation	64
5.2.2. Point-scan Raman micro-spectroscopy instrumentation	66
5.2.3. Hyperspectral Image Unmixing analysis	67
5.3. Results and discussion	68
5.3.1. Chemical composition of hippocampal A β plaques: key chemical components	73
5.3.2. Spatial distributions of key chemical components in hippocampal A β plaques	78
5.3.3. Chemical composition of cortical A β plaques: key chemical components.....	88
5.3.4. Spatial distributions of key chemical components in cortical A β plaques.....	90
5.4. Findings	100
Chapter 6. Three-dimensional chemical imaging of thick frozen brain sections by line-scan Raman micro-spectroscopy.....	101
6.1. Introduction	101
6.2. Method.....	102
6.2.1. Human tissue samples and tissue preparation	102
6.2.2. Line-scan Raman micro-spectroscopy instrumentation	103
6.2.3. Hyperspectral Image Unmixing analysis	103
6.3. Results	105
6.3.1. Chemical composition of frozen human brain tissues in Alzheimer’s disease: key chemical components	108
6.3.2. Spatial distributions of key chemical components in frozen human Alzheimer’s disease brains	112
6.4. Findings	118
Chapter 7. Correlative fluorescence imaging of amyloid- β with ASC speck and microglia in human Alzheimer’s disease brains: inflammatory response to amyloid- β aggregation.....	121
7.1. Introduction	121
7.2. Method.....	122
7.2.1. Human tissue samples	122
7.2.2. Immunohistochemistry.....	122
7.2.3. Laser-scanning confocal fluorescence microscopy instrumentation.....	123

7.2.4. Analysis	123
7.3. Results	126
7.4. Findings	133
Chapter 8. Correlative fluorescence imaging of amyloid- β with ASC speck and complement component 9 in human Alzheimer's disease brains: inflammatory response to amyloid- β aggregation	134
8.1. Introduction	134
8.2. Method.....	135
8.2.1. Human tissue samples	135
8.2.2. Immunohistochemistry	135
8.2.3. Laser-scanning confocal fluorescence microscopy instrumentation.....	136
8.2.4. Analysis.....	137
8.3. Results	139
8.4. Findings	152
Chapter 9. Discussion and conclusions	153
9.1. Raman micro-spectroscopy as a label-free tool for correlative 2D and 3D chemical imaging of A β plaques with both neuroinflammatory and lipidomic biomarkers of altered metabolism in AD human brains.....	153
9.2. Revealing novel brain imaging biomarkers for AD diagnosis	155
9.3. Revealing pro-inflammatory microglia phenotype as a signature of human AD brains affected by A β amyloidosis	156
9.4. Pro-phagocytic effect of MAC pores on clearance of small A β plaques vs. pro-inflammatory potential of MAC pores on ASC speck-induced spreading of A β pathology in human AD brains: hypothetic cycle of AD pathogenesis	158
9.5. Concluding remarks on the link between A β amyloidosis and neuroinflammation	160
Supplementary material.....	191
References	192
Publication list	214

List of abbreviations

AA = arachidonic acid

AD = Alzheimer's disease

A β = amyloid- β

ACAT = acyl-coenzyme A:cholesterol acyltransferase,

AICD = APP intracellular domain

ANLS = Alternating Non-negativity-constrained Least Squares

APOE = apolipoprotein E

APP = A β precursor protein

ASC = apoptosis-associated speck-like protein containing a caspase recruitment domain

AsLS = Asymmetric Least Squares

BACE = β -secretase

BGF = Bottom Gaussian Fitting

BSA = bovine serum albumin

CARD = caspase recruitment domain

CARS = Coherent anti-Stokes Raman scattering

CLAC = collagen-like amyloidogenic component

CE = cholesterol esters

CNS = central nervous system

CHL = cholesterol

COX = cyclooxygenase

CR1 = complement component (3b/4b) receptor 1

CRS = Coherent Raman scattering

C9 = Complement component 9

C99 = membrane-bound C-terminal fragment

DAMPs = damage-associated molecular patterns

DIC = Differential interference contrast

DS = Down syndrome

EAE = experimental autoimmune encephalomyelitis

FA = fatty acid

FAD = familial AD

FC-NNLS = fast combinatorial non-negativity-constrained least squares

FDG-PET = fluorodeoxyglucose PET

FM = Fluorescence Microscopy

GA = Glatiramer Acetate

Gly = glycine

GM1 = monosialotetrahexosylganglioside

GA β = GM1-ganglioside-bound A β

GWAS = genome-wide associated studies

HCA = Hierarchical Cluster Analysis

HNE = 4-hydroxy-2-trans-nonenal

Hyp = hydroxyproline

LC-MS = liquid chromatography-MS

LPS = lipopolysaccharide

IDE = insulin-degrading enzyme

IFN- γ = interferon- γ

IL-1 β = interleukin-1 β

iPS = induced pluripotent stem

MAC = membrane attack complex

MALDI = Matrix-Assisted Laser Desorption Ionization

MASP-1 = mannose-associated serine protease 1

MB = Mannose-binding

MCR = Multivariate Curve Resolution

MMP-9 = matrix metalloproteinase 9

MNF = Maximum Noise Fraction

MBL = Mannose-binding lectin

MRC = Medical Research Council

MRI = Magnetic Resonance Imaging

MS = Mass spectrometry

NEP = neprilysin

Nep = neutral endopeptidase

NLRP3 = nucleotide-binding oligomerization domain (NOD)-like receptor protein 3

NLS = Negative least squares

NMDA = N-methyl-D-aspartate

NMF = Negative Matrix Factorization

NO = nitric oxide

NRF = Noise removal factor

NSAID = non-steroidal anti-inflammatory drugs

OBB = Oxford Brain Bank

PBS = phosphate buffered saline

PCA = Principal Component Analysis

PET = Positron-Emission Tomography

PC = phosphatidylcholine

PPAR γ = peroxisome proliferator-activated receptor γ

Pro = proline

PRPs = pattern recognition receptors

PSEN = presenilin

PYD = pyrin domain

RHS = right hand-side

Q-HIU = quantitative hyperspectral image unmixing

Q-US/PS-NMF = quantitative unsupervised/partially supervised non-negative matrix factorization

ROS = reactive oxygen species

SEM = standard error of mean

SIMS = Secondary-Ion Mass Spectrometry

SNP = single-nucleotide polymorphisms

SNR = signal-to-noise ratio

SRS = Stimulated Raman scattering

STX-3 = syntaxin-3

SVD-ADC = Singular Value Decomposition with Automatic Divisive Correlation

CSF = cerebrospinal fluid

STD = standard deviation

TGF- β = transforming growth factor- β

TNF- α = tumor necrosis factor- α

TWOBC = Thomas Willis Oxford Brain Collection

Tyr = tyrosine

VCA = Vertex Component Analysis

YM1 = chitinase-like protein-1

List of figures

Fig. 2.1: Acute (A) versus chronic (B) activation of microglia in the course of neuroinflammatory diseases including AD. Treatment allowing to stimulate the conversion of a pro-inflammatory M1 microglia phenotype into anti-inflammatory state and inhibit neuroinflammation using a selection of therapeutic agents, such as glatiramer acetate (GA), bexarotene, and peroxisome proliferator-activated receptor γ (PPAR γ) agonists (C). EAE = experimental autoimmune encephalomyelitis, MS = multiple sclerosis. Reproduced from (Cherry *et al.* 2014) under the terms of the Creative Commons Attribution License 4.0 (CC BY 4.0) in line with the BioMed Central Ltd license agreement.....32

Fig. 2.2: An overview of the three complement activation pathways. Mannose-binding lectin = MBL, mannose-associated serine protease 1, 2 = MASP-1, 2. Reproduced with permission from (Walport 2001), Copyright Massachusetts Medical Society.35

Fig. 2.3: A hypothetical temporal model reporting 5 AD biomarkers. Reproduced from (Selkoe and Hardy 2016) under the terms of the CC BY 4.0 license.37

Fig. 3.1: Comparison of the SVD-ADC (A, blue line) method with MNF + S-G filtering (A, magenta line) using the Raman data of biochemical standard mixtures with white Gaussian noise (C, blue line), showing the efficiency of the SVD-ADC to reduce noise from the Raman data by 98% and resulting in denoised Raman spectra (C, red dashed line) to be almost identical to the reference one (C, grey line). The autocorrelation coefficients map of singular vectors received from SVD-ADC analysis of the given Raman data is shown in panel B. The green dashed diagonal line represents a decision line of a 50% cut-off for mean autocorrelation coefficients, that separates the coefficients above the line (circled cross signs – meaningful components) from those below it (cross signs – noise).....48

Fig. 3.2: A schematic illustration showing a principle of BGF method used for background subtraction from Raman signal.....51

Fig. 3.3: Comparison of the BGF method with AsLS using the Raman data with known background (black dashed lines), showing the accurateness of the BGF to produce the true baseline (red lines) that subtract both low (B) and high (C) background. AsLS baselines are shown by green.52

Fig. 3.4: Dependence of the factorisation error $\delta E(C_{11}, C_{12}, C_{13}, \dots, S_{11}, S_{12}, \dots)$ on the element C_{12} for fixed other elements.55

Fig. 3.5. Flowchart listing 3 main steps of the Q-HIU data analysis.58

Fig. 4.1: Schematic energy diagrams representing spontaneous Raman scattering and fluorescence.	59
Fig. 4.2: A typical Raman micro-spectroscopy setup. Reproduced from (Wu <i>et al.</i> 2011) with permission of PNAS.	61
Fig. 5.1. Large-scale DIC image of the hippocampus of sample Ah1 (A). The region of interest outlined by square (dashed line) measured by Raman micro-spectroscopy and post-proved to contain A β plaque (B). The chemical decomposition of this Raman image into individual chemical components with spatially-resolved Raman concentration and spectral profiles using the Q-HIU data analysis (C).	69
Fig. 5.2: Schematic of a hyperspectral Raman cube (A). The arrows with letters B and C mark two pixels, Raman spectra of which are shown on the panels B and C, respectively. The input Raman spectrum (blue line) before the SVD-ADC and the corresponding noise-filtered Raman spectrum (black line) after this procedure (B-C). The results of background subtraction using the bottom Gaussian fitting is shown by the green line: the bottom Gaussian fit (red dashed line) is subtracted from the noise-filtered Raman spectrum, giving background-free Raman spectrum. Spatio-spectral autocorrelation coefficients map of singular vectors resulted from SVD-ADC (D). The dotted diagonal line represents a decision line of $R_{th} = 50\%$ cut-off for mean autocorrelation coefficients R_i , separating the coefficients above the line (circled cross signs – meaningful components) from those below it (cross signs – noise). The spatial distribution and corresponding spectra of two singular vectors with the mean autocorrelation coefficients with values $\cong 75\%$ and $\cong 25\%$ as indicated on the panel D (E-F). On both panels, 38 Raman images are labelled according to the sample source and represents cortical regions.	71
Fig. 5.3: Raman spectra of the chemical components (blue solid lines) colocalizing with hippocampal A β plaques, obtained from the simultaneous Q-US/PS-NMF analysis of 30 hippocampal A β plaques (5 AD patients) together with 10 control Raman maps (2 elderly humans without AD). C4 (A) has spectral characteristics resembling collagen XXV (see text). C9 (B) is a mixture of aggregated A β_{1-42} peptides and saturated lipids with cholesteryl derivatives. C10 (C) is a mixture of fibrin and arachidic acid. C16 (D) is attributed to carotenoids. C17 (E) is attributed to iron oxide. The chemical attribution of components C9, C10, C16 and C17 is based on the comparison with analytical standard Raman spectra of pure chemical species. Fits are shown by the red dotted lines and found using NLS algorithm. Corresponding R^2 are also indicated. The fit in (B) is a superposition of the Raman spectrum of synthetic A β_{1-42} fibrils (magenta line) and cholesteryl palmitate (green line); the contributions are separately shown in the inset for the fingerprint region. The fit in (C) is a superposition of fibrin (magenta line) and arachidic acid	

(green line); the contributions are shown in the inset. The red line in (D) is the Raman spectrum of β -carotene. The red line in (E) is the Raman spectrum of Fe_3O_475

Fig. 5.4: Spatial distributions of the Raman concentration and the corresponding component spectra of $\mathbb{C}4$ for the measured AD hippocampal brain regions together with controls (labelled according to the sample source as Ah1,..., Ah5, and Ch1, Ch2, respectively) on colour scales as indicated, retrieved from the simultaneous Q-US/PS-NMF unmixing analysis of 30 hippocampal A β plaques (5 AD patients) together with 10 control Raman maps (2 elderly humans without AD).79

Fig. 5.5: Spatial distributions of the Raman concentration and the corresponding component spectra of $\mathbb{C}9$ for the measured AD hippocampal brain regions together with controls (labelled according to the sample source as Ah1,..., Ah5, and Ch1, Ch2, respectively) on colour scales as indicated, retrieved from the simultaneous Q-US/PS-NMF unmixing analysis of 30 hippocampal A β plaques (5 AD patients) together with 10 control Raman maps (2 elderly humans without AD).80

Fig. 5.6: Spatial distributions of the Raman concentration and the corresponding component spectra of $\mathbb{C}10$ for the measured AD hippocampal brain regions together with controls (labelled according to the sample source as Ah1,..., Ah5, and Ch1, Ch2, respectively) on colour scales as indicated, retrieved from the simultaneous Q-US/PS-NMF unmixing analysis of 30 hippocampal A β plaques (5 AD patients) together with 10 control Raman maps (2 elderly humans without AD).81

Fig. 5.7: Spatial distributions of the Raman concentration and the corresponding component spectra of $\mathbb{C}16$ for the measured AD hippocampal brain regions together with controls (labelled according to the sample source as Ah1,..., Ah5, and Ch1, Ch2, respectively) on colour scales as indicated, retrieved from the simultaneous Q-US/PS-NMF unmixing analysis of 30 hippocampal A β plaques (5 AD patients) together with 10 control Raman maps (2 elderly humans without AD).82

Fig. 5.8: Spatial distributions of the Raman concentration and the corresponding component spectra of $\mathbb{C}17$ for the measured AD hippocampal brain regions together with controls (labelled according to the sample source as Ah1,..., Ah5, and Ch1, Ch2, respectively) on colour scales as indicated, retrieved from the simultaneous Q-US/PS-NMF unmixing analysis of 30 hippocampal A β plaques (5 AD patients) together with 10 control Raman maps (2 elderly humans without AD).83

Fig. 5.9: Images of hippocampal A β plaques with different morphologies and non-demented control regions shown in jet colour scale: the fibrillar (A), cored neuritic (B), core-only (C) and diffuse neuritic (D) plaques referring to AD samples, labelled as Ah1_001, Ah2_001, Ah3_001,

Ah4_001, respectively, and two control regions (E,F), corresponding to non-demented elderly individuals marked as Ch1_001, Ch2_001. Rows 1-2: the regions of Raman measurements, indicated by white square and visualized by DIC microscopy of the unlabelled samples (A2-F2) and by fluorescence microscopy of the plaque areas (A1-D1) after staining with Th-S. Row 3: pseudo-colour images for the A β plaques and control regions using C4 (collagen XXV) as blue, C9 (a mixture of fibrillar A β ₁₋₄₂ and saturated cholesteryl esters) as green, and C10 (a mixture of fibrin and arachidic acid) as red, scaled to saturate at 25% of maximum colour channel. Rows 4-8: spatial concentration profiles of the selected components, on colour scales as indicated. The Raman concentrations in panel D4, D5 is rescaled by a factor of two for visibility. The corresponding component spectra are indicated as white lines in the first column (see also Fig. 5.3). Scale bars: 10 μ m.85

Fig. 5.10: A scatter plot of the sample mean concentrations is given for 30 hippocampal A β plaques (5 AD patients) and 10 control (2 elderly humans without AD) Raman images versus component number (C4, C9, C10, C16, and C17). The mean and standard deviation of each cohort are indicated by the error bars. The significance in pairwise difference in the concentration levels between AD and control groups was determined by two-sample two-tailed *t*-test with unequal variances. **p* < 0.05, ****p* < 0.001, *****p* < 0.0001, ******p* < 0.00001. Here, AD = Alzheimer's disease; C = control.86

Fig. 5.11: A scatter plot of the sample median concentrations is given for 30 hippocampal A β plaques (5 AD patients) and 10 control (2 elderly humans without AD) Raman images versus component number (C4, C9, C10, C16, and C17). The median of each cohort is indicated by the plus sign. The significance in pairwise difference in the concentration levels between AD and control groups was determined by the Wilcoxon rank sum test. ****p* < 0.001, *****p* < 0.0001, ******p* < 0.00001. Here, AD = Alzheimer's disease; C = control.87

Fig. 5.12: Colocalization histograms of concentration (%) for C9 - C10 (upper row) and for C9 - C4 (lower row) for each diseased (5 AD patients) and control (2 individuals) hippocampal samples, which refer to AD and non-demented elderly individuals, labelled as Ah1 (A), Ah2 (B), Ah3 (C), Ah4 (D), Ah5 (E) and Ch1 (F), Ch2 (G). Statistics on these samples was determined by the analysis of 10 (from Ah1), 9 (from Ah2), 5 (from Ah3), 1 (from Ah4), 5 (from Ah5) plaques, and 6 (Ch1), 4 (Ch2) control regions with a typical size of each Raman image of about 50 \times 50 μ m². The Pearson's correlation coefficients *R* for each case subject are shown.88

Fig. 5.13: Raman spectra of the chemical components (blue solid lines) colocalizing with cortical A β plaques, obtained from the simultaneous Q-US/PS-NMF analysis of 31 cortical A β plaques (6 AD patients) together with 7 control Raman maps (2 elderly humans without AD). C4 (A) is a mixture of A β ₁₋₄₂ fibrils and saturated lipids with cholesteryl derivatives. C7 (B) is assigned to

calcium phosphate crystals. C11 (C) is a mixture of fibrin and arachidic acid. C16 (D) is attributed to carotenoids. C20 (E) is attributed to iron oxide. The chemical attribution of components C4, C7, C11, C16 and C20 is based on the comparison with analytical standard Raman spectra of pure chemical species. Fits are shown by the red dotted lines and found using NLS algorithm. Corresponding R^2 are also indicated. The fit in (A) is a superposition of the Raman spectrum of synthetic A β ₁₋₄₂ fibrils (magenta line) and cholesteryl palmitate (green line); the contributions are separately shown in the inset for the fingerprint region. The red line in (B) is the Raman spectrum of calcium phosphate. The fit in (C) is a superposition of fibrin (magenta line) and arachidic acid (green line); the contributions are shown in the inset. The red line in (D) is the Raman spectrum of β -carotene. The red line in (E) is the Raman spectrum of Fe₃O₄.89

Fig. 5.14: Spatial distributions of the Raman concentration and the corresponding component spectra C4 for the measured AD cortical brain regions together with controls (labelled according to the sample source as Ac1,...,Ac6, and Cc1, Cc2, respectively) on colour scales as indicated, retrieved from the simultaneous Q-US/PS-NMF unmixing analysis of 31 cortical A β plaques (6 AD patients) together with 7 control Raman maps (2 elderly humans without AD).91

Fig. 5.15: Spatial distributions of the Raman concentration and the corresponding component spectra C7 for the measured AD cortical brain regions together with controls (labelled according to the sample source as Ac1,...,Ac6, and Cc1, Cc2, respectively) on colour scales as indicated, retrieved from the simultaneous Q-US/PS-NMF unmixing analysis of 31 cortical A β plaques (6 AD patients) together with 7 control Raman maps (2 elderly humans without AD).92

Fig. 5.16: Spatial distributions of the Raman concentration and the corresponding component spectra C11 for the measured AD cortical brain regions together with controls (labelled according to the sample source as Ac1,...,Ac6, and Cc1, Cc2, respectively) on colour scales as indicated, retrieved from the simultaneous Q-US/PS-NMF unmixing analysis of 31 cortical A β plaques (6 AD patients) together with 7 control Raman maps (2 elderly humans without AD).93

Fig. 5.17: Spatial distributions of the Raman concentration and the corresponding component spectra C16 for the measured AD cortical brain regions together with controls (labelled according to the sample source as Ac1,...,Ac6, and Cc1, Cc2, respectively) on colour scales as indicated, retrieved from the simultaneous Q-US/PS-NMF unmixing analysis of 31 cortical A β plaques (6 AD patients) together with 7 control Raman maps (2 elderly humans without AD).94

Fig. 5.18: Spatial distributions of the Raman concentration and the corresponding component spectra C20 for the measured AD cortical brain regions together with controls (labelled according to the sample source as Ac1,...,Ac6, and Cc1, Cc2, respectively) on colour scales as indicated, retrieved from the simultaneous Q-US/PS-NMF unmixing analysis of 31 cortical A β plaques (6 AD patients) together with 7 control Raman maps (2 elderly humans without AD).95

Fig. 5.19: Images of cortical A β plaques with different morphologies and non-demented control regions shown in jet colour scale: the neuritic (A, B), core-only (C) and cored neuritic (D) plaques referring to AD samples, labelled as Ac1_001, Ac2_001, Ac2_002, Ac3_001, respectively, and two control regions (E,F), corresponding to non-demented elderly individuals marked as Cc1_001, Cc2_001. Rows 1-2: the regions of Raman measurements, indicated by white square and visualized by DIC microscopy of the unlabelled samples (A2-F2) and by fluorescence microscopy of the plaque areas (A1-F1) after staining with Th-S. Row 3: pseudo-colour images for the A β plaques and control regions using C4 (a mixture of fibrillar A β ₁₋₄₂ and saturated cholesteryl esters) as blue, C20 (iron oxide) as green, and C11 (a mixture of fibrin and arachidic acid) as red, scaled to saturate at 25% of maximum colour channel. Rows 4-8: spatial concentration profiles of the selected components, on colour scales as indicated. The corresponding component spectra are indicated as white lines in the first column (see also Fig. 5.3). Scale bars: 10 μ m.96

Fig. 5.20: A scatter plot of the sample mean concentrations is given for 31 cortical A β plaques (6 AD patients) and 7 control (2 elderly humans without AD) Raman images versus component number (C4, C7, C11, C16, and C20). The mean and standard deviation of each cohort are indicated by the error bars. The significance in pairwise difference in the concentration levels between AD and control groups was determined by two-sample two-tailed *t*-test with unequal variances. **p* < 0.05, ***p* < 0.01, *****p* < 0.00001. Here, AD = Alzheimer's disease; C = control.97

Fig. 5.21: A scatter plot of the sample median concentrations is given for 31 cortical A β plaques (6 AD patients) and 7 control (2 elderly humans without AD) Raman images versus component number (C4, C7, C11, C16, and C20). The median of each cohort is indicated by the plus sign. The significance in pairwise difference in the concentration levels between AD and control groups was determined by the Wilcoxon rank sum test. **p* < 0.05, ***p* < 0.01. Here, AD = Alzheimer's disease; C = control.98

Fig. 5.22: Colocalization histograms of concentration (%) for C20 - C16 for each diseased (6 AD patients) and control (2 individuals) samples in the cortex, which refer to AD and non-demented individuals, labelled as Ac1 (A), Ac2 (B), Ac3 (C), Ac4 (D), Ac5 (E), Ac6 (F) and Cc1 (G), Cc2 (H). Statistics on these samples was determined by the analysis of 3 (from Ac1), 13 (from Ac2), 7 (from Ac3), 2 (from Ac4), 3 (from Ac5), 3 (from Ac6) plaques, and 4 (Cc1), 3 (Cc2) control regions with a typical size of each Raman image of about 50 \times 50 μ m². The Pearson's correlation coefficients *R* for each case subject are shown.99

Fig. 6.1: Schematic of a hyperspectral Raman cube (A). The arrows with letters B and C mark two pixels, Raman spectra of which are shown on the panels B and C, respectively. The input Raman spectrum (blue line) before the SVD-ADC and the corresponding noise-filtered Raman spectrum (black line) after this procedure (B-C). The results of background subtraction using the bottom

Gaussian fitting is shown by the green line: the bottom Gaussian fit (red dashed line) is subtracted from the noise-filtered Raman spectrum, giving background-free Raman spectrum. Spatio-spectral autocorrelation coefficients map of singular vectors resulted from SVD-ADC (D). The dotted diagonal line represents a decision line of $R_{th} = 50\%$ cut-off for mean autocorrelation coefficients R_i , separating the coefficients above the line (circled cross signs – meaningful components) from those below it (cross signs – noise). The spatial distribution and corresponding spectra of two singular vectors with the mean autocorrelation coefficients with values $\cong 80\%$ and $\cong 28\%$ as indicated on the panel D (E-F). On both panels, Raman images are labelled according to the sample source and represents hippocampal regions.106

Fig. 6.2: Raman spectra of the chemical components (blue solid lines) colocalizing with hippocampal A β plaques, obtained from the Q-US/PS-NMF analysis of AD human brain tissues together with non-demented controls. C1 (A) has spectral characteristics resembling phosphatidylcholine. C2 (B) resembles actin. C6 (C) is attributed to a mixture of fibrin and saturated lipids with cholesteryl derivatives. C9 (E) can be represented as a mixture of aggregated A β peptide and *trans* lipids such as a *trans* isomer of arachidonic acid. The chemical attribution of components C1, C2, C6 and C9 is based on the comparison with analytical standard Raman spectra of pure chemical species. Fits are shown by the red dotted lines and found using NLS algorithm. Corresponding R^2 are also indicated. The fit in (A) is the Raman spectrum of phosphatidylcholine. The fit in (B) is the Raman spectrum of actin. The fit in (C) is a superposition of fibrin (magenta line) and cholesteryl palmitate (green line); the contributions are shown in the separate figure D. The fit in (E) is a superposition of the Raman spectrum of synthetic A β_{1-42} fibrils (magenta line) and arachidonic acid (green line); the contributions are separately shown in the figure F for the fingerprint region.....110

Fig. 6.3: 3D spatial distributions of the Raman concentration and the corresponding component spectra of C1 from the measured AD hippocampal brain regions and non-demented controls labelled according to the sample source as AD1, AD2, AD3, and C1 on colour scales as indicated, retrieved from the simultaneous Q-US/PS-NMF unmixing analysis of 3D Raman images of the human AD tissues affected by A β pathology together with non-demented control regions. 3D distribution is shown by a sequential representation of each image plane of a representative *z*-stack as AD1_01z1, AD1_01z2, AD1_01z3;...; C1_01z01-z10. A typical step between neighbour planes was 3 μm , except for the AD1_01z1-z3 stack, where a 5 μm step was used. In all panels, a typical image size is $127 \times 127 \mu\text{m}^2$, except for the AD1_02z1-z7 images of a $127 \times 98 \mu\text{m}^2$ in size.113

Fig. 6.4: 3D spatial distributions of the Raman concentration and the corresponding component spectra of C2 from the measured AD hippocampal brain regions and non-demented controls

labelled according to the sample source as AD1, AD2, AD3, and C1 on colour scales as indicated, retrieved from the simultaneous Q-US/PS-NMF unmixing analysis of 3D Raman images of the human AD tissues affected by A β pathology together with non-demented control regions. 3D distribution is shown by a sequential representation of each image plane of a representative z-stack as AD1_01z1, AD1_01z2, AD1_01z3;...; C1_01z01-z10. A typical step between neighbour planes was 3 μm , except for the AD1_01z1-z3 stack, where a 5 μm step was used. In all panels, a typical image size is 127 \times 127 μm^2 , except for the AD1_02z1-z7 images of a 127 \times 98 μm^2 in size.

.....114

Fig. 6.5: 3D spatial distributions of the Raman concentration and the corresponding component spectra of C6 from the measured AD hippocampal brain regions and non-demented controls labelled according to the sample source as AD1, AD2, AD3, and C1 on colour scales as indicated, retrieved from the simultaneous Q-US/PS-NMF unmixing analysis of 3D Raman images of the human AD tissues affected by A β pathology together with non-demented control regions. 3D distribution is shown by a sequential representation of each image plane of a representative z-stack as AD1_01z1, AD1_01z2, AD1_01z3;...; C1_01z01-z10. A typical step between neighbour planes was 3 μm , except for the AD1_01z1-z3 stack, where a 5 μm step was used. In all panels, a typical image size is 127 \times 127 μm^2 , except for the AD1_02z1-z7 images of a 127 \times 98 μm^2 in size.

.....115

Fig. 6.6: 3D spatial distributions of the Raman concentration and the corresponding component spectra of C9 from the measured AD hippocampal brain regions and non-demented controls labelled according to the sample source as AD1, AD2, AD3, and C1 on colour scales as indicated, retrieved from the simultaneous Q-US/PS-NMF unmixing analysis of 3D Raman images of the human AD tissues affected by A β pathology together with non-demented control regions. 3D distribution is shown by a sequential representation of each image plane of a representative z-stack as AD1_01z1, AD1_01z2, AD1_01z3;...; C1_01z01-z10. A typical step between neighbour planes was 3 μm , except for the AD1_01z1-z3 stack, where a 5 μm step was used. In all panels, a typical image size is 127 \times 127 μm^2 , except for the AD1_02z1-z7 images of a 127 \times 98 μm^2 in size.

.....116

Fig. 6.7: Unmixed label-free Raman image of the plaque composition (B) in human AD brains: the core enriched with A β fibrils and oxidized *trans* polyunsaturated lipids such as AA (green) and the surrounding halo composed of lipoproteins with high CEs content (red). Combined fluorescence images of A β -stained (green) plaques co-labelled for GSDMD (red) and microglia (blue) (A) as well as ASC specks (red) (C), showing the localization of ASC specks and pore-forming GSDMD (indicated by white square) to the microglial membranes all correlated to the sites of the CE-rich plaque halo in the representative Raman image (B), indicating pyroptotic

cell death of highly inflammatory immune response around the plaque. In panel B, Ox- <i>trans</i> -AA = oxidized trans isomer of arachidonic acid.....	118
Fig. 7.1: Individual and merged channels fluorescence images of the thresholded A β , microglia and ASC speck fluorescence intensities for one cortical (A) and one hippocampal (B) plaques. In all panels, the white circles of smaller and larger radius indicate the area of plaque core and halo, respectively, selected for the quantification.	124
Fig. 7.2: Individual and merged channels fluorescence images of activated microglia (Iba1, blue) and ASC specks (AL177, red) around A β plaque (6E10, green) in the frontal lobe brain region of a patient with AD. Colocalization of anti-A β /ASC specks within Iba1-positive microglia supports the hypothesis of inflammasome activation in response to A β aggregation. Scale bars, 10 μ m.	126
Fig. 7.3: Representative fluorescence image of co-deposition of A β with ASC speck-positive microglia in the hippocampal brain region of a patient with AD. The zoom of the outlined image area is shown on the right and indicates the inflammasome activation within microglia in close proximity to the A β plaque resulting in the distinct ASC speck formations. Scale bars, 20 μ m.	127
Fig. 7.4: Individual and merged channels fluorescence images of ASC specks (AL177, red) integrated into the A β cores and microglia (Iba1, blue) around in the frontal lobe (A) and hippocampal (B, C) brain regions of two patients with AD. Scale bars, 10 μ m in all panels.....	128
Fig. 7.5: (A-C) Quantification of relative microglia, ASC speck and A β -positive volumes within the plaque core, halo and whole plaque for cortical versus hippocampal plaques of AD human brains. Data are represented as histogram distributions (top panels) and mean \pm SEM (bottom panels). The examination of each antibody reactivity for hippocampal plaque (AD) versus non-demented control (non-AD) regions is also given, confirming a statistically significant increase of microglia, ASC and A β immunoreactivity in plaque regions.	130
Fig. 7.6: Quantification of cortical and hippocampal plaques revealing a high degree of the A β -microglia (A) and A β -ASC speck (B) colocalization in the plaque core, halo and whole plaque, except hippocampal core with a statistically non-significant microglial A β coverage. Data are represented as mean \pm SEM.	131
Fig. 7.7: (A-B) Quantification of the A β -ASC speck-microglia immunolabelled fluorescence images revealing a significant shift of the microglial activation to the pro-inflammatory state in the cortical plaque cores compared to the hippocampal ones. Data are represented as mean \pm SEM.	132
Fig. 8.1: Individual and merged channels fluorescence images of the thresholded A β , C9 and ASC speck fluorescence intensities for one cortical (A) and one hippocampal (B) plaques. In all panels,	

the white circles of smaller and larger radius indicate the area of plaque core and halo, respectively, selected for the quantification.....	137
Fig. 8.2: Individual and merged channels fluorescence images of the MAC pores (C9, blue) integrated into the A β core (Th-S, green) and ASC specks (AL177, red) around in the hippocampal brain region of AD patient. Scale bars, 10 μ m.	140
Fig. 8.3: Individual and merged channels fluorescence images showing the ring-shaped deposits of MAC pores (C9, blue) within the A β core (Th-S, green) and ASC specks (AL177, red) around in the hippocampal brain region of AD patient. Scale bars, 10 μ m.	141
Fig. 8.4: Individual and merged channels fluorescence images revealing the presence of MAC pores (C9, blue) within the A β core (Th-S, green) with ASC specks (AL177, red) around in the hippocampal brain region of AD patient. Scale bars, 10 μ m.	142
Fig. 8.5: Activation of the NLRP3 inflammasome and ASC speck assembly are triggered in response to sublytic MAC deposition in AD human brains. Figure shows the colocalization of the MAC (C-9, blue) and ASC specks (AL177, red) to the membranes of apoptotic cells activated within the core of the A β plaque (Th-S, green) in the hippocampal brain region of AD patient 5. Scale bars, 10 μ m.	143
Fig. 8.6: Individual and merged channels fluorescence images showing the co-accumulation of MAC pores (C5b-9, blue) and ASC specks (AL177, red) throughout the cortical A β plaque (Th-S, green) in the frontal lobe brain region of AD patient 4. Scale bars, 10 μ m.	144
Fig. 8.7: Individual and merged channels fluorescence images showing the significant accumulations of MAC pores (C9, blue) and ASC specks (AL177, red) in the cortical A β plaque (Th-S, green) of the hippocampal brain region of AD patient 2. Scale bars, 10 μ m.	145
Fig. 8.8: (A-C) Quantification of relative C9, ASC speck and A β -positive volumes within the plaque core, halo and whole plaque for cortical versus hippocampal plaques of AD human brains. Data are represented as histogram distributions (top panels) and mean \pm SEM (bottom panels). The examination of each antibody reactivity for hippocampal plaque (AD) versus non-demented control (non-AD) regions is also given, confirming a statistically significant increase of C9, ASC and A β immunoreactivity in plaque regions and the specificity of the used antibodies.	146
Fig. 8.9: (A-B) Quantification of cortical and hippocampal plaques revealing a high degree of the A β -C9 colocalization in the plaque core, halo and whole plaque that indicate the significance of the pore-forming C9 accumulation within the core and halo of the A β plaques. Data are represented as mean \pm SEM. The histogram distributions of the correlation value for C9-A β complex ($RC9 + A\beta$) are also included (A, top panel). For the hippocampal region, a comparison of $RC9 + A\beta$ between plaques and normal control regions coming from non-AD patients is given.....	147

Fig. 8.10: Quantification of cortical and hippocampal plaques revealing a colocalization of ASC specks with A β (A) and C9 (B) in the plaque core, halo and whole plaque, except the cortical plaque core. (C) Quantification indicating the significance of the neuroprotective MAC effect on A β plaque shrinkage compared to the neurotoxic effect of ASC on A β plaque growth exclusively in the cortical plaque core. Data are represented as mean \pm SEM.148

Fig. 8.11: Quantification of the C9-ASC-A β -stained cortical plaques revealing an inverse correlation of C9 with A β levels and therefore indicating the pore-forming C9 as a potential driver of A β phagocytosis able to lower A β concentration in AD brains: fluorescence images of the C9-positive plaques (A,C,E) and corresponding dependence of A β from C9 levels within the area of their colocalization at the sites of the plaque core (B,D,F). The representative Pearson's correlation coefficients R are also indicated on top. Scale bars in all panels, 10 μ m.149

Fig. 8.12: Quantification of plaque diameter in two brain regions showing a striking difference in the size of cortical plaques compared to hippocampal ones. A resulting p -value is given.150

Fig. 8.13: (A-D) Quantification of C9 correlation with the size of plaque core (A,B) and whole plaque diameter (C,D) in the frontal lobe and the hippocampal brain regions revealing a reduced pore-forming C9 coverage of cortical plaques with larger core diameter. (E-H) Quantification of ASC speck correlation with the size of plaque showing a decreased ASC speck coverage of larger plaques in the hippocampus (H). Pearson's correlation coefficients R are also given.151

Abstract

Accumulation of amyloid- β ($A\beta$) peptide in plaques, aberrant lipid metabolism, and neuroinflammation are considered by many of utmost biological importance for Alzheimer's disease (AD) progression. Despite this significance, the link among these three aspects is still under study. To that end, there is a great need for the research which investigates in detail the relationship among aggregated proteins, lipids and neuroinflammatory components of AD human brains.

My thesis utilizes cutting edge label-free optical technique, Raman micro-spectroscopy, combined with an efficient quantitative biomedical image unmixing analysis, to investigate in detail the spatio-chemical composition and correlation of $A\beta$ plaques with both neuroinflammatory biomarkers and lipids in post-mortem AD human brains. Two types of post-mortem human brain samples from AD patients together with non-demented elderly controls were investigated using point- and line-scan Raman micro-spectroscopy modalities: 5 μm thick formalin-fixed-paraffin-embedded and 20-50 μm thick frozen brain sections.

For the formalin-fixed samples studied by point-scan Raman micro-spectroscopy, the analysis reveals significant structural and functional changes in lipid and protein (including $A\beta$ fibrils of cross- β sheet structure and tau filaments) chemical composition as well as increased concentrations of oxidative stress and inflammatory biomarkers strongly co-localizing in $A\beta$ plaques of diseased tissues compared to controls. In particular, $A\beta$ plaques are found to consist of the micro-scale accumulations of chemical components attributed to cholesteryl esters with saturated long-chain fatty acids (FAs), $A\beta$ fibrils, fibrin/arachidic acid, collagen-like amyloidogenic component (CLAC), β -carotene, magnetite, and calcium phosphate, which altogether reflect the persistent presence of neuroinflammation in AD brains. The oxidation status of lipids is supported by the presence of *trans* double bonds in the Raman spectrum of the identified component, forming during lipid peroxidation. Furthermore, the presence of arachidic acid indicates the conversion of arachidonic acids to eicosanoids occurring in the process of oxidative damage. Importantly, I also demonstrated that the statistical parameters of identifying biomolecules differentiate AD brains from non-demented ones, implying their potential to be used in the diagnosis of AD. Therefore, my PhD thesis presents a new tool for the biomolecular characterization and correlative imaging of the AD brain tissues, providing a better understanding of the relationship between $A\beta$ plaques and their lipid and inflammatory microenvironment. These findings could open the prospect for new anti-inflammatory and antioxidant drug strategies.

For the frozen tissues without fixative artefacts, 3D line-scan Raman micro-spectroscopy allowed to distinguish intracellular and extracellular volumetric accumulations of pathogenic A β species assembled into the cross- β structured fibrils as retrieved from the label-free AD brain samples. The analysis reveals two types of lipid aggregates spatially colocalizing with the A β plaques. In particular, the A β plaque core and neuronal cell bodies are found to contain the significant accumulations of polyunsaturated lipids, spectrally assigned to an oxidized form of a *trans* isomer of arachidonic acid, that are co-aggregated with the A β protein in one chemical component. The high content of the oxidised polyunsaturated *trans* lipids within the A β deposits is indicated by an enhanced Raman band of *trans* lipids at 1668 cm⁻¹, appearing during lipid peroxidation of the cellular membranes by free radicals, combined with an absent Raman band of *cis* lipids near 1656 cm⁻¹. The oxidation modification of the A β -associated polyunsaturated acid is also suggested by the missing band around 3004 cm⁻¹, which is a diagnostic band of unsaturated FAs. The significant accumulations of the oxidatively-modified arachidonic acid with the pathogenic A β fibrils might indicate unresolved neuroinflammation and oxidative damage implicated in human AD brains in response to chronic A β accumulation. The halo surrounding the A β core is revealed to consist of lipoproteins with a high cholesteryl ester content found colocalizing with the activated microglial processes and spatially correlated with the pro-inflammatory components of the immune system including a pore-forming gasdermin D protein, reflecting the cell pyroptosis. The analysis also discovered the ellipsoid-shaped cloud accumulated around the A β -positive neurons and consisting of an actin protein, possibly representing the lytic material of the dead neuronal cells underwent the cell pyroptosis. Altogether, Raman micro-spectroscopy has proven to distinguish the spatially resolved chemically specific lipid and protein accumulations, characteristic of oxidative damage and neuroinflammation, colocalizing to A β -affected brain regions in label-free human AD brains, thereby providing a useful imaging tool for the identification of the molecular signs of AD tissue pathology.

My thesis utilizes high-resolution confocal fluorescence microscopy to characterise inflammation coupled to A β aggregation in human AD brains, that can underline the causes of AD and deliver new treatment strategies. Formalin-fixed-paraffin-embedded post-mortem brain tissues were recruited from human individuals affected by AD. Brain tissues were assessed in the hippocampus and frontal lobe by co-immunostaining for spatial correlation and distribution of specific neuroinflammatory protein components with microglia and A β plaques. These are the nucleotide-binding oligomerization domain (NOD)-like receptor protein 3 (NLRP3)-derived apoptosis-associated speck-like protein containing a caspase recruitment domain (ASC), and complement cytolytic pathway activation protein component 9 of a membrane attack complex (MAC).

Quantitative analysis reveals the accumulations of numerous ASC specks, indicative of the NLRP3 inflammasome activation, and the MAC pores both colocalizing to the A β core and halo, thereby indicating the MAC as a possible driver of the pro-inflammatory immune response in AD brains. My data support the hypothesis that MAC at the sites of A β accumulation induces the activation of the inflammasomes, immunological pattern recognition receptors (PRRs), that results in the secretion of the ASC specks and maturation of the pro-inflammatory cytokines into the extracellular space through the MAC-induced permeable membranes of the A β -affected cells, both contributing to A β pathology spreading. Importantly, the quantification of A β plaques shows that the MAC pores incorporated into the A β core can contribute to shrinkage of the A β plaque area through phagocytosis, observed to be a more profound effect for newly formed deposits of a smaller diameter. The quantification of microglial processes in the A β plaque regions reveal the significance of the disease-associated microglia phenotype activation, characterising by presence of numerous ASC specks within their soma. This microglia phenotype might represent a sustained pro-inflammatory population of microglia evolved due to continuous A β aggregation in AD human brains.

Acknowledgements

I express my deepest gratitude and warmest acknowledgments to my supervisors Prof. Kathy Triantafilou and Dr. Martha Triantafilou for their generous support, invaluable discussions and enormous help for my PhD project and to me. They have greatly contributed to my thesis by their advices, comments and guidance and I am very much grateful to Kathy and Martha for the unique opportunity to work with them on the project on precious human AD brain tissue. Kathy and Martha always helped me to find a solution of both scientific and everyday problems and have been a constant source of encouragement during my studies. It was a great pleasure and honour for me to work in their lab. Special thanks to Dr. Iestyn Pope, Dr. Michael Kukharsky, and Jack Hales for working together. They kindly helped me to resolve my scientific questions and support me with experiment training and guidance in the beginning of my PhD studies. I also express my sincere thanks to Dr. Iestyn Pope for his help with the fabrication of the sample holders, Prof. Wolfgang Langbein and Prof. Paola Borri for provision with optical setup facilities and fruitful discussions, and Dr. Hakan Keles for his expert opinion on my thesis, which was very helpful to me.

I wish to express my most sincere gratitude and appreciation to donors, their families and all staff from the Thomas Willis Oxford Brain Collection (TWOBC) and the Medical Research Council (MRC) Brain Bank Network for the opportunity to work with human AD brain tissues. My warmest and deepest thanks go to my husband, talented scientist and my favourite colleague Dr. Sergey Lobanov for fruitful discussions, huge support and flawless guidance on my project and lot of other aspects. I am always inspired by your strong scientific skills and talent, and I wish you big exciting results in science.

Finally, I also wish to thank my family and my friends who are always supportive to me.

Chapter 1. Introduction

Alzheimer's disease (AD) is an age-related neurodegenerative disorder, characterized by the extracellular accumulation of amyloid- β (A β) peptide in the senile plaques and the intracellular deposits of the microtubule-associated protein tau in the neurofibrillary tangles. According to the World Alzheimer Report 2019, over 50 million people worldwide live with AD in 2019 (Alzheimer's Disease International 2019). Patients show a gradual onset and progression of memory loss and other cognitive deficits. Although most patients are diagnosed at 65 years or later, scientists believe that AD pathology begins two or even three decades before the disease onset with the clinical symptoms pronounce (Jack *et al.* 2013), therefore implying that AD is a progressive disease of the middle age population. Alongside obesity and diabetes, AD is a modern disorder with a consistently increasing number of patients. For instance, AD is estimated to affect about 152 million people globally by 2050 (Alzheimer's Disease International 2019). Despite being considered as a 21st century epidemic, there is still no cure for AD and the etiology of the disease remains obscure.

The study of the spatio-chemical composition and correlation of A β plaques with both neuroinflammatory biomarkers and lipids in post-mortem AD human brains is of great importance to understanding the underlying causes and progression of AD. There is an increasing body of evidence that aggregation of A β , aberrant lipid metabolism and neuroinflammation are involved in AD pathology. Therefore, research elucidating the link among these three aspects can open the prospect for new drug strategies to be potentially tested and successfully utilised in Alzheimer's disease treatment. Furthermore, the study reporting correlative chemical imaging of A β plaques and their bioenvironment in AD human brains with high spatial resolution and chemical specificity in a non-destructive manner is very demanding due to the need of development of new reliable methods and biomarkers to perform such studies.

According to the literature, a range of spectroscopic and imaging techniques have been applied to the study of AD human brains. These include but are not limited to Fluorescence Microscopy (FM), Mass spectrometry (MS), Liquid Chromatography-MS (LC-MS), Positron-Emission Tomography (PET), Magnetic Resonance Imaging (MRI), etc. Alternatively, a promising method to study the biochemical composition of tissues is vibrational optical micro-spectroscopy. The basic principle of these methods is originated from excitation and further detection of the intrinsic vibrations of chemical bonds in molecules using laser light, and therefore the unique ability of these techniques to provide a non-invasive label-free chemically specific imaging of biomedical samples make them very attractive for many biological applications. Therefore, the study

presenting a direct application of high-resolution label-free vibrational micro-spectroscopy to biochemical characterization of human AD brain tissues is very demanding. This biomedical study can reveal specific imaging biomarkers of the altered AD metabolism associated with the A β plaque pathology, which is directly relevant for the disease diagnosis. In combination with high-resolution fluorescence microscopy, such studies can link amyloid aggregation and defective microglia-mediated A β clearance to specific inflammatory pathways, which might point to new drug strategies for possible AD treatment and prevention.

In the course of the Literature Review (**Chapter 1**), I will report the current knowledge on major contributors to AD pathogenesis (**Section 2.1**). Specifically, I will discuss in detail why and how A β plaques (**Section 2.1.1**), aberrant lipid metabolism (**Section 2.1.2**) and inflammatory/immunological processes (**Section 2.1.3**) might be involved in AD initiation and progression. In **Section 2.2**, I will cover cutting edge imaging techniques in the study of brain tissue. In **Section 2.3**, I will discuss existing multivariate hyperspectral unmixing methods applied to biomedical image analysis.

Chapter 2. Literature Review

2.1. Major contributors to Alzheimer's disease pathogenesis

A number of hypotheses such as amyloid cascade, lipid dysregulation and inflammation have been proposed for the AD pathogenesis, suggesting that AD is a multifactorial complex disorder. A β plaques, aberrant lipid metabolism and neuroinflammation can be considered as the three major contributors to AD.

2.1.1. Amyloid- β plaques in Alzheimer's disease

It is widely accepted that the extracellular accumulation of A β in senile plaques is a principal event in the pathogenesis of AD (Selkoe 2001a) and there are many lines of evidence supporting a dominant role of A β dyshomeostasis in the initiation of AD (Selkoe and Hardy 2016). Genetic studies in early-onset familial forms of AD, which account for 5-10% of all AD cases, suggest that the mutations in A β precursor protein (*APP*), presenilin 1 (*PSEN1*) and *PSEN2* genes, which encode the proteins that generate A β by proteolytic processing, lead to the overproduction of A β peptides and their subsequent self-aggregation into advanced phase transition stages ranging from monomers to misfolded monomers, dimers, oligomers, protofibrils, fibrils and ultimately to A β plaques (Bertram *et al.* 2010). In sporadic late-onset AD, which represents 90-95% of the total AD cases, it is thought that the dysregulations of A β clearance pathways may cause persistent A β aggregation, leading to neuronal dysfunction (Mawuenyega *et al.* 2010). Importantly, the initial model of AD, which helped to support amyloid hypothesis, was Down syndrome (DS), caused by trisomy of chromosome 21. Since the *APP* gene is encoded on chromosome 21 and it is overexpressed in DS brains, DS is considered to be a unique model for study AD pathology (Iwatsubo *et al.* 1995). The link between the overproduction of *APP* and A β accumulation has been widely studied and the results show that DS brains develop A β -associated pathology manifesting by progressive accumulation of the A β plaques starting in the teenage years (Lemere *et al.* 1996). Furthermore, human AD cellular model using cortical neurons differentiated from induced pluripotent stem (iPS) cells and embryonic stem cells of DS patients indicates that these generated neurons secrete high-level of A β peptides, shown to form A β aggregates, and cause increased tau phosphorylation (Shi *et al.* 2012).

Fundamentally, A β peptides of different lengths are generated from the sequential *APP* cleavages by β -secretase (BACE) and γ -secretase (Selkoe 2001b). Initially, β -secretase cuts *APP* to produce soluble *APP* (β -*APPs*) and a membrane-bound C-terminal fragment (C99). Then, cleavage by γ -

secretase of C99 generates A β and the APP intracellular domain (AICD) counterparts. The resulting products of such C99 processing are amyloidogenic peptides: A β ₁₋₄₀ and A β ₁₋₄₂. However, it had not been clear until 2009 what are the intermediate steps of C99 processing. At that time, it was elucidated that C99 is firstly cut at the membrane–cytoplasm boundary, generating two long A β ₁₋₄₈ and A β ₁₋₄₉ intermediates, which are in turn processed by the sequential release of tripeptides, finally resulting in the generation of A β ₁₋₄₂ and A β ₁₋₄₀, respectively (Takami *et al.* 2009). The longer A β ₁₋₄₂ fragments tend to be more hydrophobic and more prone to aggregation into toxic A β oligomers (Haass and Selkoe 2007), which were found to be the major chemical component of neuritic plaques (Jarrett *et al.* 1993). Recently, it has been shown *in vitro* and *in vivo* that mild increases in temperature significantly affect the γ -secretase processing function resulting in a release of longer A β _{1-n} ($n \geq 42$) peptides, which might be potentially more toxic (Szaruga *et al.* 2017). It was also suggested that the disturbance of the γ -secretase stability (e.g.: by increased temperature or mutations in *PSEN*), might increase the risk of sporadic forms of AD, similarly to the familial AD, where the mutations in *PSEN* and *APP* induce the abnormal APP processing and further release of long A β peptides. Additional evidence demonstrates that the inhibition of γ -secretase activity leads to the undetectable levels of pathogenic A β production by iPS-cell cortical neurons derived from DS patients, thereby indicating the possible use of stem-cell therapy in AD treatment (Shi *et al.* 2012).

Prevailing evidence suggests that soluble A β oligomers are more pathogenic compared to inert insoluble A β aggregates. These toxic A β oligomers can easily flow into synapses and disrupt the connections between neurons (Shankar *et al.* 2008). A β oligomer-induced toxicity is mediated by interactions with neuron receptors and lipid membranes (Kayed *et al.* 2003). It has been shown that injection with soluble A β oligomers into wild-type mouse leads to impairment of synaptic plasticity via overstimulation of extrasynaptic N-methyl-D-aspartate receptor (NMDA) death signalling (Li *et al.* 2011). Similarly, pathogenic A β dimers isolated from human AD brain are demonstrated to induce AD pathology in rodent hippocampus by decreasing dendritic spine density, inhibiting long-term potentiation, and enhancing long-term synaptic depression (Shankar *et al.* 2008).

Amyloid hypothesis is also supported by clinical evidence. Specifically, the studies in humans demonstrate that abnormal levels of cerebrospinal fluid (CSF) A β ₁₋₄₂ marker and amyloid-positive PET scans precede other AD symptoms by many years and even decades (Selkoe and Hardy 2016). Importantly, ongoing immunotherapeutic trials using monoclonal A β antibodies such as solanezumab, crenezumab, and aducanumab have already showed positive affect on slowing cognitive decline in mild AD patients (Cummings *et al.* 2018). Altogether, prevailing evidence

widely accepts that an imbalance between production and clearance of toxic A β peptides occurs very early in disease and can be considered as an initiating factor for AD. Therefore, targeting A β dyshomeostasis represents a therapeutic strategy with already promising results (Kumar *et al.* 2015).

2.1.2. Lipid-amyloid interplay in Alzheimer's disease

There is a growing body of research evidence that the dysregulation of lipid pathways is implicated in several neurodegenerative disorders, including AD. In his early studies in 1910, Alois Alzheimer noted the higher occurrence of “adipose inclusions” in the brain of AD patients suggesting aberrant lipid metabolism is involved in the course of AD (Di Paolo and Kim 2011). Only recently this link between lipid metabolism and AD has been strengthened with the discovery indicating that the apolipoprotein E (*APOE*) gene has the strongest known genetic risk factor for the development of late-onset AD (Corder *et al.* 1993). *APOE* encodes a ~34kDa protein that regulates cholesterol metabolism in the brain and triglyceride metabolism throughout the body. It binds A β and modulates its aggregation and clearance, suggesting a link between these hallmarks of AD.

It has been shown that the aggregation of A β is mediated by the interaction with different classes of lipids, including cholesterol (Sparks *et al.* 1994; Refolo *et al.* 2000; Paolo and Kim 2011), ganglioside (Yanagisawa *et al.* 1995; L. P. Choo-Smith *et al.* 1997; Matsuzaki and Horikiri 1999), phospholipids (McLaurin and Chakrabartty 1997; Lee *et al.* 2002) and fatty acids (FAs) (Prasad *et al.* 1998), leading to a cascade of pathological events including neuroinflammation and oxidative stress. One of the possible mechanisms elucidating the toxicity of A β -lipid interaction can be the formation of amyloid peptide ion channels in the neuronal membranes, leading to the disruption of intracellular calcium homeostasis (Kayed *et al.* 2009). It has been shown that the interaction of A β peptides with lipid bilayer membranes results in the formation of amyloid cation-specific ion channels or pores through which Ca²⁺ can pass into the cytosol. Specifically, A β -induced channel formation is demonstrated to increase the intracellular calcium concentration (Kawahara *et al.* 2000). It has been also suggested that A β incorporated into the lipid membranes can modify their structure and subsequently undergo aggregation in these membranes (Kawahara *et al.* 2000). Interestingly, the membrane fluidity quantified by the ratio of cholesterol to phospholipids influences the ability of antibiotic peptides to form ion channels (Warnock *et al.* 1993). Other studies hypothesised that the specific oligomer of pore-like morphology named annular protofibril can induce the ion dysregulation of membranes (Kayed *et al.* 2009) and the formation of toxic A β channels during A β oligomer internalization into the lipid

membranes requires the interaction with other A β species (Jang *et al.* 2013). More importantly, the relationship between A β -induced Ca²⁺ influx and neurotoxicity has been suggested by the finding showing that the voltage-sensitive Ca²⁺ channel blocker, nimodipine, attenuates the A β -mediated cell death (Weiss *et al.* 1994). Collectively, after A β channels are formed in the membranes of neuron cells, the disruption of ion homeostasis (including calcium) triggers a cascade of pathological processes, such as oxidative stress (Yatin *et al.* 1998) and tau phosphorylation (Takashima *et al.* 1993), which are able to boost neurodegeneration.

It has been suggested that the excessive production of free radicals results from the damage of cell membranes by A β (Butterfield *et al.* 1994). These free radicals such as reactive oxygen species (ROS) as well as redox metal ions can be considered as a reservoir of neurotoxicity in AD brains, which catalyse a continuous oxidation of lipid membranes (Markesbery 1997). A self-amplified reaction of lipid peroxidation releases very reactive products, which favour to interact with other biomolecules and generate new neurotoxic species responsible for neurodegeneration (Esterbauer *et al.* 1991; Butterfield *et al.* 2011). As an evidence, it has been shown that 4-hydroxy-2-trans-nonanal (HNE), the product of lipid peroxidation, can covalently modify the histidine side chains of A β , leading to increased aggregation of this peptide (Liu *et al.* 2008). In addition, neprilysin (NEP), a major protease that cleaves A β *in vivo*, has also been reported to be HNE modified in AD brains (Wang *et al.* 2003). On the other hand, there is a line of evidence that lipids themselves have detergent properties, promoting the disintegration of amyloid fibrils into toxic protofibrils and oligomers (Widenbrant *et al.* 2006; Martins *et al.* 2008). These free oligomers can bind to synaptic contacts (Deshpande *et al.* 2006), where they disrupt lipid membrane homeostasis (Milanesi *et al.* 2012). Altogether, these findings suggest that the amyloid-lipid interaction induce the overproduction of neurotoxic species through the pathogenic formation of amyloid ion pores in the neuronal membranes (linked to severe Ca²⁺ dyshomeostasis) as well as stimulate the continuous generation of free A β oligomers, both contributing to AD neurodegeneration.

An increasing body of evidence indicates that clustered gangliosides that reside in neuronal raft microdomains promote A β oligomer assembly into toxic membrane-associated fibrils (Matsuzaki *et al.* 2010) and the following mechanism has been suggested. A β binds to ganglioside-containing liposomes (Choo-Smith and Surewicz 1997), where it undergoes structural changes from α -helix to β -sheet conformation (McLaurin *et al.* 1998) possibly through interaction with liposomal lipid bilayers, which ultimately lead to the generation of A β fibrils (L.-P. Choo-Smith *et al.* 1997). It is important to note that A β binding to gangliosides is suggested to occur in presynaptic ganglioside-clustered raft membranes (Kakio *et al.* 2002), particularly rich in cholesterol (Kakio *et al.* 2001).

Furthermore, it has been indicated that the interaction of A β oligomers and gangliosides in neuronal lipid raft-like membranes results in the formation of the monosialotetrahexosylganglioside (GM1)-ganglioside-bound A β (GA β) complex, which accelerates A β assembly, induced by the conformation changes, into membrane β -sheet-rich fibrils, acting as a seed for further A β aggregation (Matsuzaki *et al.* 2010). Specifically, the immunostaining against GA β complexes reveals the presence of GA β -containing lysosomes in the AD brains accompanied by molecular characterization of GA β showing that both GA β and A β at the ends of growing fibrils exhibit a specific conformation which is required for A β polymerization (Hayashi 2004).

2.1.3. Inflammation in Alzheimer's disease

An increasing body of evidence suggests that inflammation is the central event in the initiation and progression of AD. Recently, association of inflammation and AD has been strongly supported by genome-wide association studies (GWAS), which identified *CR1* and *TREM2* genes encoding a complement component (3b/4b) receptor 1 and a triggering receptor expressed on microglia to be the risk genes for the development of sporadic late-onset forms of AD (Harold *et al.* 2009; Lambert *et al.* 2009; Guerreiro *et al.* 2013; Karch and Goate 2015). For instance, it has been suggested that the dysregulation of the TREM2 protein expression affected through the variants in the *TREM2* gene can cause functional defects in microglial response to A β aggregation as well as promote a pro-inflammatory cascade in AD brains (Guerreiro *et al.* 2013). Furthermore, the association studies of the relationship between *CR1* single-nucleotide polymorphisms (SNPs) genotypes and increased A β CSF levels indicated a positive correlation of these two, and therefore providing an additional evidence of the complement component (3b/4b) receptor 1 (CR1) implication in A β metabolism (Brouwers *et al.* 2012).

The inflammation hypothesis of AD is also supported by the epidemiological and preclinical evidences which indicate that anti-inflammatory drug therapy might be beneficial for the treatment of AD (Aisen 2002). Such studies suggest inhibiting inflammatory response using non-steroidal anti-inflammatory drugs (NSAIDs) in order to reduce AD pathology (Lim *et al.* 2000; Sung *et al.* 2004; McKee *et al.* 2008). In turn, the anti-inflammatory effect of NSAIDs can be explained through their association with inhibition of cyclooxygenase (COX) expression. Note, COX is the enzyme that converts arachidonic acid into prostaglandins and thromboxane known as the proinflammatory mediators. This enzyme has two isoforms: COX-1 and COX-2 (Aisen 2002). Given that COX might be considered as a promising therapeutic target for AD. Indeed, a preclinical study in triple transgenic AD (3 \times Tg-AD) mouse model demonstrates that the COX-1

selective inhibitor SC-560 protects the aged AD mice from inflammation, neuropathology and development of cognitive decline (Choi *et al.* 2013). However, several clinical studies in AD patients with mild to severe AD stage have shown no beneficial effect of NSAIDs, which specifically inhibit COX-2, on the protection from AD pathology (Aisen *et al.* 2000; Sainati *et al.* 2000).

During the course of disease, deposition of A β in the brain of AD patients constantly activate the brain-resident immune cells such as microglia and astrocytes (Rubio-Perez and Morillas-Ruiz 2012). Upon activation, microglia and astrocytes can initiate a pro-inflammatory cascade, resulting in the release of potentially cytotoxic molecules, such as cytokines (interleukin-1 β (IL-1 β), IL-6 and tumor necrosis factor- α (TNF- α)), complement factors (C1q, C3, C4, and C9), nitric oxide (NO), reactive oxygen species (ROS), etc., which may ultimately cause neurodegeneration (Meraz-Rios *et al.* 2013). Although the glial immune cells are abundantly found near A β plaques of AD brains, the conclusive role of microglia and astrocytes in the A β plaque development and neurodegeneration is still unknown (Condello *et al.* 2015; Chun *et al.* 2018; Merlo *et al.* 2018). Furthermore, the activation of glial cells in response to A β aggregation leads to a series of immunological events, involving the activation of various receptor signalling pathways and complement cascade, which an ultimate role in AD has not yet been elucidated.

In the following section, I will highlight the current knowledge and evidence from the literature on microglia as a cellular mediator as well as the NLRP3 inflammasome and complement component proteins as the molecular mediators of neuroinflammation in AD.

Microglia activation in AD

Microglia, resident phagocytes of the central nervous system (CNS), constantly survey the brain via their branching projections to defend, maintain and repair potential tissue damage. Microglia also play a crucial role in the brain development. As the primary innate immune cells of the brain, microglia can phagocytose dying cells, cellular debris, toxic protein aggregates including A β (Simard *et al.* 2006) as well as damaged and unnecessary neurons and synapses known as the synaptic pruning (Neumann *et al.* 2009; Schafer *et al.* 2012). By secreting various functional molecules (e.g.: cytokines and chemokines) and free radicals, microglia communicate with neighbouring immune cells and stimulate their activation. It is strongly suggested that abnormal A β aggregation in the brain causes microglia to move to the pathological area (Meyer-Luehmann *et al.* 2008) and secrete pro-inflammatory immune molecules including cytokines and chemokines after activation (Halle *et al.* 2008), that can further recruit neighbour immune cells as well as phagocytes from blood (Simard *et al.* 2006).

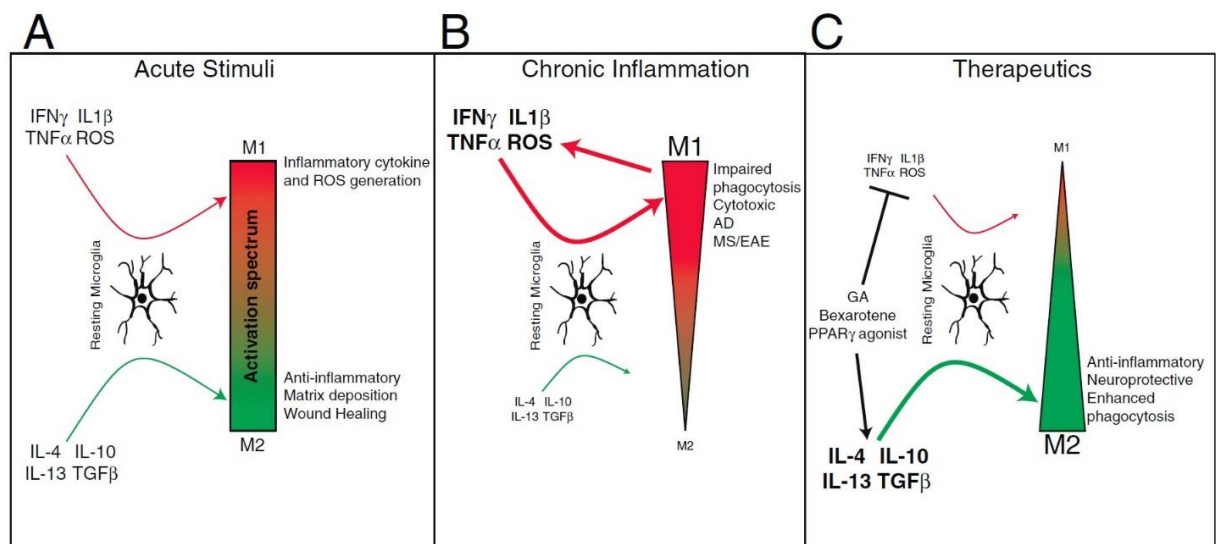


Fig. 2.1: Acute (A) versus chronic (B) activation of microglia in the course of neuroinflammatory diseases including AD. Treatment allowing to stimulate the conversion of a pro-inflammatory M1 microglia phenotype into anti-inflammatory state and inhibit neuroinflammation using a selection of therapeutic agents, such as glatiramer acetate (GA), bexarotene, and peroxisome proliferator-activated receptor γ (PPAR γ) agonists (C). EAE = experimental autoimmune encephalomyelitis, MS = multiple sclerosis. Reproduced from (Cherry *et al.* 2014) under the terms of the [Creative Commons Attribution License 4.0 \(CC BY 4.0\)](https://creativecommons.org/licenses/by/4.0/) in line with the BioMed Central Ltd license agreement.

On the other hand, there is a growing body of evidence that the subpopulation of microglia associated with the neurodegenerative disease progression has a unique phenotype, which is significantly different from the primary one, which is initially activated in response to $A\beta$ aggregation in early AD stage (Sarlus and Heneka 2017). Furthermore, it has been hypothesised that the middle/late-stage disease subtype of microglia can promote AD pathology, therefore indicating the possible microglia impairment in response to chronic $A\beta$ aggregation, leading to the failure of microglia to clear $A\beta$ (Wang *et al.* 2015; Sarlus and Heneka 2017). This suggested hypothesis can be explained as follows. Fundamentally, there are two polar states of microglia corresponding to the M1 and M2 phenotypes. The M1 phenotype is believed to provide pro-inflammatory impaired phagocytosis, associated with brain tissue damage and chronic inflammation. During this state, microglia secrete pro-inflammatory cytokines ($IL-1\beta$, $IL-6$, $IL-12$, $IL-17$, $IL-18$, $IL-23$), $TNF-\alpha$, interferon- γ ($IFN-\gamma$), ROS and chemokines (Subramaniam and Federoff 2017). In contrast, the M2 phenotype is thought to ensure anti-inflammatory neuroprotective phagocytosis promoting brain tissue healing (Cherry *et al.* 2014). The M2 microglia produce $IL-4$, $IL-13$ and $IL-10$ cytokines, transforming growth factor- β ($TGF-\beta$) (Subramaniam and Federoff 2017). According to (Cherry *et al.* 2014), in the course of prolonged/chronic inflammation, abundant levels of inflammatory cytokines skew the microglial polarization towards the M1 state. This skewed population of M1 microglia in turn generate new inflammatory cytokines, thereby promoting a conserved loop of continuous inflammation and propagation of the M1 state. To switch to the phagocytosis-promoting M2 phenotype of microglia,

bexarotene (retinoid X receptor agonist) has been used in the therapy of familial AD (FAD) mice, resulting in the significant reduction of A β plaque-affected brain areas and impressive recovery of cognitive function (see also Fig. 2.1) (Cramer *et al.* 2013).

It is important to note that the M1 phenotype of microglia prevail with age, i.e.: aged brains are more prone to activate the pro-inflammatory M1 microglia, thereby having the increased risk of pathology and neurodegeneration. This hypothesis is supported by studies in old non-demented mice having downregulation of receptors associated with A β engulfment (scavenger receptor A) and the A β degradation enzymes (neutral endopeptidase (Nep), insulin-degrading enzyme (IDE), and matrix metalloproteinase 9 (MMP-9) (Hickman *et al.* 2008). Furthermore, *in vitro* studies show that lipopolysaccharide (LPS)-induced M1 microglia lose the ability to phagocytose A β (Koenigsknecht-Talboo 2005). Furthermore, treatment with pro-inflammatory cytokines, such as IFN- γ and TNF α stimulating M1 microglia phenotype, results in the decreased A β uptake by M1 microglia and inefficient degradation of internalised A β (Yamamoto *et al.* 2008), therefore implying the limited ability of M1 microglia to clear A β . In contrast, the M2 population of microglia which has been stimulated by cytokines IL-4 and IL-10 show efficient phagocytic function and robust degradation of A β (Koenigsknecht-Talboo 2005; Balce *et al.* 2011). Furthermore, *in vivo* studies in an AD mouse model indicate that the 6-month-old mice already exhibiting A β aggregation has a clear presence of chitinase-like protein-1 (YM1)-positive microglia (marker of M2 phenotype) in the CNS. Whereas, by the advanced stage of disease (18 months) there was a decrease in YM1 mRNA levels together with a significant upregulation in pro-inflammatory factors, indicating a switch from M2 to M1 phenotype (Jimenez *et al.* 2008).

NLRP3 inflammasome activation in AD

As presented in the previous section, a conserved pattern of continuous A β aggregation causes the chronic activation of the innate immune system and impairment in phagocytic function of microglia (Heneka *et al.* 2015). Additional supporting evidence indicates that the increased expression of IL-1 β impairs microglial function to clear A β , leading to the further accumulation of A β in the AD brain (Heneka *et al.* 2010). Similarly, cells of individuals with severe AD are observed to contain increased amounts of pro-inflammatory cytokines and activated inflammasomes (Condello *et al.* 2015). One more data report the elevated pro-inflammatory cytokine IL-1 β levels in response to A β aggregation (Lucin and Wyss-Coray 2009). The link between IL-1 β and the inflammasome activation in response to toxic A β can be explained as follows. IL-1 β is generated from a chemically inactive precursor pro-IL-1 β and requires caspase-1-dependent processing for activation. Caspase-1 activation in turn is regulated by cytosolic

multiprotein complexes called inflammasomes, which can sense not only the microbial pathogen (Lamkanfi and Dixit 2012) but also misfolded proteins including A β (Halle *et al.* 2008) and pathological crystals (Latz 2010). Specifically, NLRP3 inflammasome can detect the pathological amyloid as a danger signal (Halle *et al.* 2008). This observation is consistent with the experimental studies indicating that aged APP/PS1 transgenic mice with NLRP3 or caspase-1 knock-out genes have reduced microglia-mediated IL-1 β production and A β pathology accompanied by improved cognitive function (Heneka *et al.* 2013). Additional evidence of the NLRP3 implication in AD pathology is supported by *in vitro* studies showing that soluble oligomeric A β cause the increased processing of mature-IL-1 β from pro-IL-1 β through ROS-induced activation of NLRP3 in microglia (Parajuli *et al.* 2013).

Recently, the discovery in an AD mouse model has elucidated the link between A β pathology and ASC specks (Venegas *et al.* 2017). In this study (Venegas *et al.* 2017), extracellular ASC species were indicated to spread A β toxicity by seeding A β oligomer assembly and the following mechanism has been suggested: ASC specks secreted by microglia rapidly bind to A β , where they seed A β nucleation. This hypothesis has been investigated in the same study (Venegas *et al.* 2017) by a series of experiments showing that intra-hippocampal injections of ASC specks lead to propagation of A β pathology in the FAD mice, whereas the FAD mice deficient in ASC expression is shown to be protected from this pathology. Also, it has been proven that anti-ASC antibody treatment stops the increase of A β pathology. Fundamentally, once activated, NLRP3 induce the polymerization of the adaptor apoptosis-associated speck-like protein containing a caspase (CARD)-recruitment domain (ASC) into large helical filaments via self-interactions of the pyrin domains (PYDs) of ASC. Then, ASC fibrils trigger the activation of caspase-1 via CARD interactions followed by proteolytic self-cleavage and further assembly of ASC fibrils into a micrometre-sized perinuclear complex called ASC speck (Venegas *et al.* 2017). By accumulation in the extracellular space, ASC specks show prion-like (prionoid) functions to recruit new ASC and caspase-1 in cells ingested ASC specks, thereby propagating inflammation (Franklin *et al.* 2014).

Complement component activation in AD

The complement system is an important innate and adaptive immune response effector. This system made of a number of proteins and proteases that are activated in cascade can be considered to play a crucial role in AD (Meraz-Rios *et al.* 2013). Generally, the activation of complement system (see Fig. 2.2 for details) involves the recruitment of the C1q molecule (classical pathway), mannose-binding lectin (mannose-binding (MB) lectin pathway) or C3 multifunctional protein (alternative pathway), which are responsible for defence to infections/various danger

signals, clearance of apoptotic cells, and elimination of supernumerary synapses (synaptic pruning) (Mawuenyega *et al.* 2010).

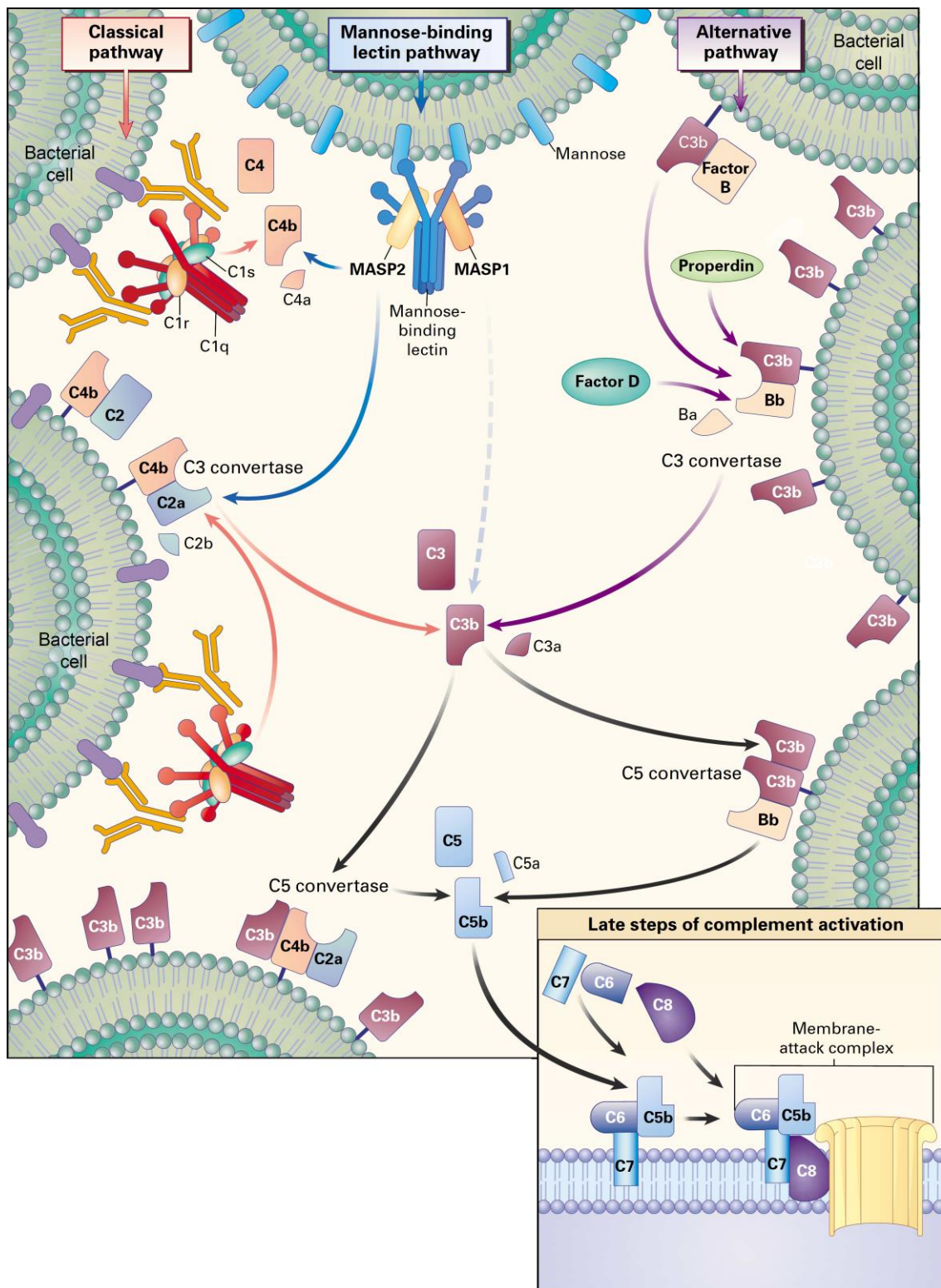


Fig. 2.2: An overview of the three complement activation pathways. Mannose-binding lectin = MBL, mannose-associated serine protease 1, 2 = MASP-1, 2. Reproduced with permission from (Walport 2001), Copyright Massachusetts Medical Society.

These three complement pathways converge at the formation of a C3 convertase, which cleaves a C3 protein into two fragments C3a and C3b. The activated C3b molecules can be sensed by

phagocytes through their surface CR1. Upon activation, the opsonin C3b labels the surface of pathogen, which is recognised by complement receptors of phagocytes resulting in their activation to the place of pathogen. Importantly, all pathways of complement activation involve the enzymatic cleavage of the C5 protein into the anaphylatoxin C5a and opsonin C5b followed by activation of the membrane attack complex (MAC). MAC consists of the complement proteins C5b, C6, C7, C8 binding to the outer surface of the target cell membrane, and numerous units of complement component 9 (C9) protein, which interact with each other to form a ring in the membrane. This ring structure creates a pore in the target cell membrane, which leads to their disrupted homeostasis and ultimately to the cell lysis (Bhakdi and Trandum-Jensen 1991). As a non-lethal cell effect, the MAC deposits can stimulate the pro-inflammatory cellular cascade by promoting the IL-1 β production through NLRP3 activation pathway (Laudisi *et al.* 2013; Triantafilou *et al.* 2013). The mechanism of this non-lethal MAC toxicity has been suggested by the finding showing that once the MAC pore is formed in the cell, there is an increased influx of Ca²⁺ ions into the cytosol followed by Ca²⁺ accumulations in the mitochondrial matrix (Morgan *et al.* 1986; Triantafilou *et al.* 2013). These intracellular Ca²⁺ deposits are in turn shown to induce the NLRP3 assembly, leading to caspase 1 activation and IL-1 β secretion (Triantafilou *et al.* 2013).

There is a line of evidence that a dysregulation of the classical complement pathway is implicated in the course of AD. The initial studies on complement activation in AD brains revealed that senile plaques, tangles and dystrophic neurites are immunopositive for the C1q, C3b, C4d, indicative of the classical complement cytolytic pathway activation, but immune-negative for the Bb fragment of Factor B and properdin, which are markers of the alternative pathway (McGeer *et al.* 1989; Rogers *et al.* 1992). Also, the C5b-9 representing the MAC, indicative of the full-blown complement activation, has been shown to stain only the dystrophic neurites of senile plaques as well as tangles (Rogers *et al.* 1992). More importantly, it has been speculated that A β peptide can self-activate the classical component cascade in an antibody-independent fashion (Rogers *et al.* 1992), and therefore under the AD conditions characterised by the abundance of A β species can be considered as a reservoir of the chronic neurotoxicity for the AD brain tissue. Consistent with this hypothesis, *in vitro* studies showed that C1q can recognize fibrillar and aggregated forms of A β ₁₋₄₂ and A β ₁₋₄₀, but not the monomeric forms. Since the C1q receptor is expressed in microglia, there is a hope that the increased expression of this molecule in AD brains might modulate the A β phagocytosis (Meraz-Rios *et al.* 2013). Specifically, some studies in cell cultures and mouse models indicate the ability of C1q to block the interaction of A β with microglia possibly by the scavenger receptor ligands polyinosinic acid and maleylated-bovine serum albumin (BSA), and therefore inhibiting the phagocytosis of A β by microglia (Webster *et al.* 2000). Additionally,

microglia also produce C3 molecules. The study on an AD APP transgenic mice deficient for C3 component revealed the beneficial role of C3 in the enhanced A β clearance and the ability to shift the pro-inflammatory M1 microglial response to M2 phenotype (Maier *et al.* 2008).

2.2. State-of-the-art imaging techniques in the study of Alzheimer's disease brains

According to a hypothetical temporal model indicating 5 AD biomarkers (Jack *et al.* 2013), amyloid PET imaging of living human brains is the earliest clinical marker for AD diagnosis, classifying the deposition of A β in amyloid plaques as a first detectable event in AD pathogenesis (see Fig. 2.3 for details).

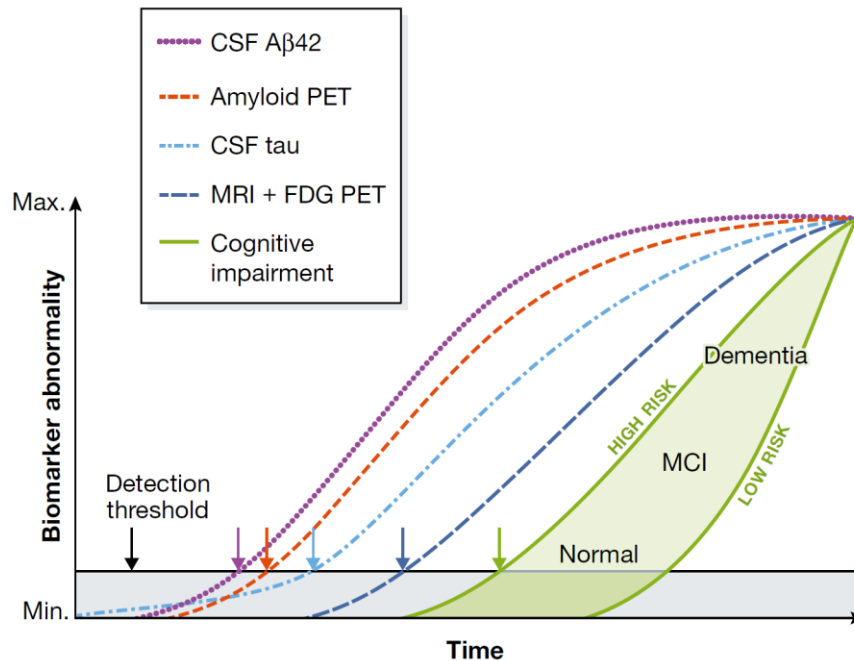


Fig. 2.3: A hypothetical temporal model reporting 5 AD biomarkers. Reproduced from (Selkoe and Hardy 2016) under the terms of the [CC BY 4.0 license](https://creativecommons.org/licenses/by/4.0/).

This *in vivo* imaging technique measures the uptake of amyloid PET tracers in brains, which are associated with fibrillar A β accumulations (Fleisher *et al.* 2011; Sojkova *et al.* 2011). The mechanism of the PET tracer (or radioactive isotope) usage to probe fibrillar A β burden in living brains can be explained as follows. Practically, two most common radionuclides with short half-life time which is widely used in PET are fluorine-18 [^{18}F] (~110 min) and carbon-11 [^{11}C] (~20 min). ^{18}F is an unstable radioactive isotope that decays to a stable oxygen-18 [^{18}O] isotope, resulting in production of numerous positrons:



Similarly, ^{11}C decays to a stable boron-11 [^{11}B] isotope:



These radioactive isotopes are used as a neuroimaging PET tracer designed to bind fibrillar amyloid in human brains, known as amyloid probe. In amyloid PET imaging, the amyloid probe is injected into the human body followed by brain incorporation, where the radioactive agent binds brain amyloid and undergoes transition to a stable form, resulting in positron e^+ emission. Then, the collision of the emitted positrons with electrons generates the bursts of γ -radiation, that are detected by PET scan. This principle is used for 3D PET image reconstruction, which retrieves amyloid concentration profiles in the brain. Although amyloid PET scan is a non-invasive technique that quantifies fibrillar amyloid burden in AD brains, it is a relatively expensive to perform: each PET scan costs \$1000-1200 US dollars.

In the model of 5 dynamic AD biomarkers (Jack *et al.* 2013), A β biomarkers measured by amyloid PET imaging are indicated as upstream, which permit the detection of the first pathological processes in AD human brains (see also Fig. 2.3 for details). Neurodegenerative biomarkers in turn are denoted as downstream, which can identify the signs of abnormal neuronal hypometabolism, triggered by progressive A β pathology and occurring roughly 10 years before the expected symptom onset (Bateman *et al.* 2012) (see Fig. 2.3 for details). Specifically, hypometabolism on [^{18}F] fluorodeoxyglucose PET (FDG-PET) are used as a measure of neurodegeneration (Jagust *et al.* 2010). FDG PET neuroimaging postulates that high radioactivity is associated with brain activity. This is achieved by measuring the uptake of radioactively labelled glucose or oxygen by brain cells with FDG. Since neurodegenerative processes lead to reduced metabolism of glucose and oxygen in AD brains, FDG-PET can be used to differentiate AD from other types of dementia.

Of other imaging tools available to detect pathological changes in AD brains, fluorescence microscopy identified the elevated accumulations of cholesterol in cores of mature A β plaques (Mori *et al.* 2001). However, this technique involves labelling the biomolecules of interest, and therefore is limited to study the chemical species, for which antibody is available. Furthermore, fluorescence microscopy does not allow to investigate the total chemical composition of the sample. Importantly, tagging can disturb the chemical structure of fragile lipids-amyloid co-arrangements. Among spectroscopy techniques, Mass Spectrometry (MS) provides chemical information on a broad range of biomolecular constituents, but requires sample ionization, involving chemical extraction of lipids from tissue sample. For instance, Liquid Chromatography-MS (LC-MS) revealed an increased level of diacylglycerol (+80%), glucosylceramide (+43%) and galactosylceramide (+33%), as well as decreased phosphatidylethanolamine (-25%) in the prefrontal cortex of AD human brains compared to controls. Furthermore, the entorhinal cortex of

AD individuals showed the elevated accumulations of lysobisphosphatidic acid (+82%), sphingomyelin (+20%), ganglioside GM3 (ceramide-N-tetose-N-acetylneuraminic acid) (+64%), and cholesterol esters (CEs) (+72%) in the form of CE-16:1, CE-16:0, and CE-18:1, associated with lipid droplets (Chan *et al.* 2012). In relation to MS-based imaging techniques, Matrix-Assisted Laser Desorption Ionization (MALDI) and Secondary-Ion Mass Spectrometry (SIMS) have been applied to *ex vivo* imaging of lipid, proteins and metals in brains (Grasso 2011; Braidy *et al.* 2014). Note, MALDI is limited by low spatial resolution of about 30-50 μm , whereas SIMS allows to achieve sub-micron resolution. However, both techniques are sample destructive, involving the partial degradation of a sample, and therefore cannot be applied to living brains. By detecting the intrinsic vibrations of chemical bonds in molecules, vibrational micro-spectroscopy techniques such as infrared absorption (Liao *et al.* 2013; Benseny-Cases *et al.* 2014) and Raman scattering microscopy (Diem 2015; Krafft *et al.* 2016) are non-invasive label-free chemically specific imaging approaches. However, infrared microscopy has limited spatial resolution due to the long wavelength of the infrared light. In contrast, Raman micro-spectroscopy can achieve sub-micron spatial resolution by applying light source of the visible range. Notably, a non-linear version of Raman micro-spectroscopy, coherent Raman scattering (CRS) microscopy shows additional enhancement in 3D spatial resolution due the multiphoton nonlinearity as well as faster acquisition speed compared to spontaneous Raman, and has been recently applied to examination of post-mortem brain tissues (Freudiger *et al.* 2008; Kiskis *et al.* 2015; Lee *et al.* 2015). Specifically, coherent anti-Stokes Raman scattering (CARS) micro-spectroscopy has been recently utilized to investigate lipid-amyloid co-arrangements in AD human brains (Kiskis *et al.* 2015). However, the spectral profiles measured by CARS do not resemble Raman spectra due to the interference between the vibrationally resonant and non-resonant parts of the third-order CARS susceptibilities, thus complicating their interpretation. Furthermore, the results on the chemical composition of brain tissues using CRS microscopy has been reported only in the CH-stretch vibrational region ($2700\text{-}3100\text{ cm}^{-1}$), which contain more overlaid vibrational bands compared to the fingerprint region complicating their assignment and interpretation. In relation to confocal Raman micro-spectroscopy, several studies have recently reported the chemical profiles of AD brains (Michael *et al.* 2014; Michael *et al.* 2017), revealing the sensitivity of confocal Raman to detect the pathogenic β -sheet chemical structure of amyloid fibrils and tau tangles both implicated in AD. Although these studies showed the spatial distribution of β -sheet structured protein of A β plaques by integrating Raman intensity of the amide-I peak in the range ($1649, 1698\text{ cm}^{-1}$), such Raman imaging does not represent an individual chemical substance such as fibrillar amyloid. Altogether, Raman micro-spectroscopy is a useful technique complementary to the conventional

approaches for molecular characterization and chemical imaging of pathogenic proteins and lipids in AD brain tissues without any labelling and high spatial resolution.

2.3. Multivariate unmixing analysis for micro-spectroscopy images

Over the past few decades, the progress in multivariate image analysis methods allowed to efficiently quantify the biochemical information from spectroscopic images. Specifically, spontaneous Raman micro-spectroscopy data have been processed using multivariate image reconstruction methods (Miljkovic *et al.* 2010; Krafft *et al.* 2017), such as Principal Component Analysis (PCA), Hierarchical Cluster Analysis (HCA), and K-Means cluster Analysis (KMA) (Zhang *et al.* 2005; Filik and Stone 2008; Krafft *et al.* 2016; Czamara *et al.* 2017; Michael *et al.* 2017), aiming to separate the data into convoluted spatially resolved spectra that represents molecular vibrations from multiple species. However, the resulting images represent variance rather than the Raman intensities of individual biochemical compounds in the sample composition, making these methods less quantitative.

Raman data have also been analysed using Vertex Component Analysis (VCA) (Hedegaard *et al.* 2011) and Multivariate Curve Resolution (MCR) (Andrew and Hancewicz 1998; Zhang *et al.* 2005; Piqueras *et al.* 2011; Vajna *et al.* 2012), which is also known as Non-negative Matrix Factorization (NMF) (Albuquerque and Poppi 2015). Compared to VCA requiring the presence of pixels with pure biochemical compounds, MCR/NMF does not imply this constraint, therefore providing broader chemical and biomedical applications.

In relation to CRS micro-spectroscopy (Camp and Cicerone 2015; Cheng and Xie 2015), CARS and Stimulated Raman scattering (SRS) images have been analysed by PCA (Lin *et al.* 2011), cluster analysis based on spectral phasor approach (Fu and Xie 2014), MCR (Zhang *et al.* 2013) and NMF (Di Napoli *et al.* 2016) both based on the Alternating Non-negativity-constrained Least Squares algorithm (ANLS). In contrast to PCA and HCA, MCR/NMF are more quantitative techniques, allowing to retrieve molecular fingerprints of physically meaningful chemical components in the sample composition. To note, CARS intensity spectra do not resemble in line-shape Raman-like vibrational bands but rather contain maxima and minima of intensity due to the interference between the vibrationally resonant and non-resonant part of the third-order CARS susceptibilities (Diem 2015). Therefore, CARS data analysis requires appropriate computational methods (Liu *et al.* 2009) to extract the Raman line-shape spectra *prior* to application of multivariate hyperspectral unmixing approaches as documented above.

It is important to note that the widely used MCR-ANLS method (Jaumot *et al.* 2015) utilizes computationally inefficient realization of the non-negative least squares (NLS) algorithm, which performance can be orders of magnitude slower compared to the NMF method based on fast combinatorial non-negativity-constrained least squares (FC-NNLS) (Van Benthem and Keenan 2004; Kim and Park 2007). This is because the conventional formulation of NLS algorithm (Lawson and Hanson 1995) is intended to work with a non-negative right hand-side (RHS) vector. Therefore, the multiple-RHS problem should be split into several (equal to the number of RHS vectors) independent sub-problems. In practice, by alternative dividing of the hyperspectral data matrix into either columns representing wavenumbers or rows corresponding to pixels, one can apply the standard NLS algorithm to the divided data matrix resulting in the quantified chemical information in the hyperspectral image. While this approach is straightforward, it tends to be computationally inefficient, because it can result in redundant calculations, which is particularly important for large-scale data analysis. For example, careful analysis of a typical Raman data-set ($\approx 50 \times 50 \times 10^3$ matrix) using popular MCR-ANLS software (Jaumot *et al.* 2015) and involving investigation of its dependence on the number of components leads to processing time of several days as performed on a standard PC. This becomes even worse for large-scale data analysis of multi-set Raman images ($\approx 10^3 \times 10^3 \times 10^3$ matrix) resulting in extremely long computational times of years. Thus, the development of fast multivariate image unmixing methods, which shorten processing times of large-scale data analysis to hours without compromising the accuracy, is highly demanding.

Aims of the PhD thesis:

Consistent with a large body of evidence outlined in the literature review, the long-standing model for A β -related AD pathogenesis requires further consideration and investigation, which explore specific innate immunity and lipid pathways that might be activated in response to chronic A β aggregation and play a role in spreading AD pathology. Furthermore, the development of novel brain imaging biomarkers with illness-state dependence are highly desirable for the AD diagnosis. To identify specific inflammatory components of the innate immune system and lipid types involved in A β amyloidosis, I will study human brain slices from AD patients, together with a 'control' cohort of elderly humans without AD using Raman micro-spectroscopy and high-resolution fluorescence microscopy. Therefore, the general aim of my PhD thesis is the biomolecular characterization and chemical imaging of the AD tissues and non-demented controls, with a focus on imaging of A β plaques and their pathological biochemical microenvironment. According to this aim, the following research challenges can be outlined:

1. Label-free Raman micro-spectroscopy imaging of fixed paraffin-embedded brain slices from AD patients together with non-demented controls to show statistically significant changes in chemical composition of the diseased brain tissues compared to controls. Along with abundant A β deposits, I hypothesise the chemical composition of AD brains will be characterised by increased accumulations of specific types of lipids as well as biomarkers associated with neuroinflammation co-localising with A β plaques (**Chapter 5**).
2. 3D Raman micro-spectroscopy imaging of unfixed frozen brain slices from AD patients together with non-demented controls to identify and demonstrate 3D distribution of key chemical components of diseased brains compared to controls as well as strengthen the findings received in the previous chapter (**Chapter 6**).
3. Correlative fluorescence imaging of specific immunolabelled pathogenic proteins (ASC specks and A β_{1-42}) and Iba-1-labelled microglia in fixed paraffin-embedded brain slices from AD patients to link amyloid aggregation and defective microglia-mediated A β clearance to specific inflammatory pathways (**Chapter 7**).
4. Correlative fluorescence imaging of specific immunolabelled inflammatory markers (ASC specks and MAC) and A β_{1-42} in fixed paraffin-embedded brain slices from AD patients to better understand the mechanism how activated complement components can affect amyloid clearance (**Chapter 8**).

Chapter 3. Theoretical framework

3.1. Formulation of hyperspectral image unmixing problem

3.1.1. Forward scattering problem

To introduce the hyperspectral image unmixing analysis, I will start with the presentation of forward scattering problem in this section, that can be formulated as the following research question. Given the specimens consist of a mixture of N pure chemical components with known individual Raman scattering cross-section spectra¹ $S_i(\nu), i = 1, 2, \dots, N$ and known spatial distributions of concentration $C_i(\mathbf{r})$, find a Raman intensity matrix $I(\mathbf{r}; \nu)$ from $S_i(\nu)$ and $C_i(\mathbf{r})$. Here, ν represents a Raman shift and $\mathbf{r} = (x, y; r)$ is a radius vector indicating the image pixel with coordinates (x, y) in the r^{th} Raman image.

Mathematically, this Raman intensity matrix $I(\mathbf{r}; \nu)$ can be represented as a superposition of the spatial distributions of concentration multiplied by corresponding pure spectra of the chemical constituents of the specimens:

$$I(\mathbf{r}; \nu) = \sum_{i=1}^N C_i(\mathbf{r})S_i(\nu). \quad (3.1)$$

This equation gives the solution of the forward scattering problem, which can be calculated using basic approaches of linear algebra.

3.1.2. Inverse scattering problem

For a broad range of biomedical applications, it is necessary to identify the composition of samples without prior knowledge of their chemical content. Mathematically, this represents the inverse scattering problem, that can be formulated as follows. Given a Raman intensity matrix $I(\mathbf{r}; \nu)$, decompose it into N separate chemical components having individual Raman spectra $S_i(\nu)$ and spatial concentration $C_i(\mathbf{r})$ profiles. Additionally, if one or several Raman spectra $S_i(\nu)$ and/or concentration profiles $C_i(\mathbf{r})$ are *a priori* known, this problem reduces to finding the rest of the spectral and concentration profiles of samples' constituents.

In typical point-scan Raman experiment, hyperspectral image is collected by raster scanning the sample through the focal point of the laser beam, and therefore the Raman dataset consists of the discrete coordinates x, y and wavenumbers ν : $x = \{x_i: i = 1, 2, \dots, N_x(r)\}$, $y = \{y_i: i =$

¹ In the following, I will omit “scattering cross-section” for brevity

$1, 2, \dots, N_y(r)\}$, $v = \{v_i: i = 1, 2, \dots, N_s\}$. Here, $N_x(r)$ and $N_y(r)$ are a number of pixel points in the r^{th} Raman image along x - and y -axes, respectively, and N_s is a number of spectral points in this image. Also, a set of radius vectors $\mathbf{r} = \{\mathbf{r}_i: i = 1, 2, \dots, N_p\}$, where $N_p = \sum_{r=1}^{N_r} N_x(\mathbf{r})N_y(\mathbf{r})$ is a total number of pixel points and N_r is a total number of hyperspectral images, can be created.

This notation leads to the representation of the Raman intensity $I(\mathbf{r}; v)$, spatial concentrations $C_i(\mathbf{r})$ and spectra $S_i(v)$ as matrices $I_{ij} = I(\mathbf{r}_i; v_j)$, $C_{ij} = C_i(\mathbf{r}_j)$, $S_{ij} = S_i(v_j)$, and expression Eq. (3.1) into the matrix form

$$\mathbf{I} = \mathbf{C}^T \mathbf{S}, \quad (3.2)$$

where the superscript T means matrix transpose.

From here on, I will use both matrix and explicit forms of the Raman intensity, concentration, and spectra.

Importantly, the inverse scattering problem aims to find unknown chemical composition from the Raman images using unsupervised hyperspectral image unmixing techniques, and therefore the problem of unknown image information retrieval is limited by the inability to detect the true concentrations of analytes. However, such image analysis allows to determine the concentrations of analytes up to a constant factor, which can be measured in Raman experiment for each individual analyte. In particular, once the Raman spectrum $S_i^0(v)$ of pure chemical substance (identified as a component from the hyperspectral image unmixing analysis) with the known chemical concentration c_i is measured, one could retrieve the chemical concentration of the analyte by multiplying its concentration profile $C_i(\mathbf{r})$ by a calibration factor $c_i \int S_i(v) dv / \int S_i^0(v) dv$. Therefore, in the course of my thesis, I will use the term ‘‘Raman concentration’’ instead of ‘‘chemical concentration’’, because calibration factors were unknown for my Raman datasets.

3.2. Singular Value Decomposition with Automatic Divisive Correlation (SVD-ADC) for noise filtering

3.2.1. Formulation of SVD-ADC

As documented in the literature, a standard formulation of Singular Value Decomposition (SVD) method (Golub and Van Loan 2013) applied to hyperspectral Raman images has been used to separate signal from noise by discarding small singular values and their corresponding singular vectors (scores and loadings) from further analysis (Uzunbajakava *et al.* 2003). Mathematically,

SVD algorithm in application to hyperspectral Raman intensity matrix \mathbf{I} projects the data into a new spatio-spectral orthonormal basis consisting of scores $C_i(\mathbf{r})$ and loadings $S_i(\mathbf{v})$

$$I(\mathbf{r}; \mathbf{v}) = \sum_{i \in N} C_i(\mathbf{r}) \lambda_i S_i(\mathbf{v}), \quad (3.3)$$

which is sorted by their descending singular values λ_i .

Here, $N = \{1, 2, \dots, \text{rank}(\mathbf{I})\}$ and $C_i(\mathbf{r}) \cdot C_j(\mathbf{r}) = S_i(\mathbf{v}) \cdot S_j(\mathbf{v}) = \delta_{ij}$, where the dots indicate Euclidean scalar products. For this, I use the notation of Euclidean scalar product for two vectors $S_i(\mathbf{v})$ and $S_j(\mathbf{v})$ (or $C_i(\mathbf{r})$ and $C_j(\mathbf{r})$) as follows:

$$S_i(\mathbf{v}) \cdot S_j(\mathbf{v}) = \sum_{k=1}^{N_s} S_i(\mathbf{v}_k) S_j(\mathbf{v}_k) \quad (3.4)$$

$$C_i(\mathbf{r}) \cdot C_j(\mathbf{r}) = \sum_{k=1}^{N_p} C_i(\mathbf{r}_k) C_j(\mathbf{r}_k) \quad (3.5)$$

In a matrix form, Eqs. (3.4)-(3.5) can be rewritten as follows:

$$S_i(\mathbf{v}) \cdot S_j(\mathbf{v}) = \sum_{k=1}^{N_s} S_{ik} S_{jk}, \quad (3.6)$$

$$C_i(\mathbf{r}) \cdot C_j(\mathbf{r}) = \sum_{k=1}^{N_p} C_{ik} C_{jk}. \quad (3.7)$$

It is suggested that chemically meaningful components have significantly higher singular values than noisy ones (Uzunbajakava *et al.* 2003).

However, sometimes, the meaningful chemical information is in the components with the smallest concentration, implying that selection of the optimum number of components is the main disadvantage of SVD. Such meaningful components might be colocalized in a small area of the image and therefore might correspond to small singular values that potentially will be filtered out during SVD leading to compromised results. It is therefore important that singular vectors (scores and loadings) with small singular values containing meaningful chemical information will be retained after SVD. As shown in (Lobanova and Lobanov 2019), such meaningful components appear to exhibit high values of autocorrelation function for small pixel shifts indicating that autocorrelation function provides more accurate sorting of the chemical information in the image. Altogether, selection of the optimum number of components in the SVD procedure should be considered very carefully.

As discussed in (Lobanova and Lobanov 2019), in case a chemical component is localised in a few pixels but exhibits distinct Raman spectral profile, which is equivalent to having a high value of spectral autocorrelation function, SVD might treat it as a singular component with small singular value and, therefore, this component will potentially be discarded from the further analysis. Therefore, autocorrelation function appears to be more reliable for assessing singular components than singular values.

To overcome this limitation of conventional SVD, recently SVD in a new formulation, called SVD with Automatic Divisive Correlation (SVD-ADC), has been proposed (Lobanova and Lobanov 2019). This method implements an additional step once SVD is performed, i.e.: for individual loadings $S_i(\nu)$ and scores $C_i(\mathbf{r})$ spectral R_i^S and spatial R_i^C autocorrelation coefficients at one pixel shift are calculated

$$R_i^S = R[S_i(\nu), S_i^\delta(\nu)], \quad (3.8)$$

$$R_i^C = \max_{\delta} R[C_i(\mathbf{r}), C_i^\delta(\mathbf{r})], \quad (3.9)$$

where $R[\dots]$ denotes correlation coefficient, which can be represented according to the following equations:

$$R[S_i, S_i^\delta] = \frac{|\sum_k (S_{ik} - \bar{S}_i) (S_{ik}^\delta - \bar{S}_i^\delta)|}{\sqrt{\sum_k (S_{ik} - \bar{S}_i)^2} \sqrt{\sum_k (S_{ik}^\delta - \bar{S}_i^\delta)^2}}, \quad (3.10)$$

$$R[C_i, C_i^\delta] = \frac{|\sum_k (C_{ik} - \bar{C}_i) (C_{ik}^\delta - \bar{C}_i^\delta)|}{\sqrt{\sum_k (C_{ik} - \bar{C}_i)^2} \sqrt{\sum_k (C_{ik}^\delta - \bar{C}_i^\delta)^2}}, \quad (3.11)$$

where $S_i^\delta(\nu)$ are loadings with “one” spectral point shift, i.e. $S_i^\delta(\nu_k) = S_i(\nu_{k+\delta})$, and $C_i^\delta(\mathbf{r})$ – scores with one image pixel shift along x - [$\delta = (\delta_x, 0)$] or y -axis [$\delta = (0, \delta_y)$], i.e. $C_i^{(\delta_x, \delta_y)}(\mathbf{r}_k) = C_i(\mathbf{r}_k + (\delta_x, \delta_y))$.

Therefore, SVD-ADC is intended to automatically sort the meaningful components from noise-dominated ones (e.g.: shot noise, read noise, residual noise after cosmic ray removal, etc.). For this, by mapping spatial autocorrelation coefficients R_i^C against spectral ones R_i^S for individual scores/loadings, one discard the singular components corresponding to mean autocorrelation coefficient $R_i = (R_i^C + R_i^S)/2$ lower than $R_{\text{thr}} = 50\%$. Then, by replacing the set N in Eq. (3.3) by the new set $N_{\text{thr}} = \{i: R_i > R_{\text{thr}}\}$ and performing the required summation, the Raman intensity matrix with reduced noise is found.

3.2.2. Validation of SVD-ADC

In (Lobanova and Lobanov 2019), it has been verified that SVD-ADC with the 50% cut-off efficiently differentiates the meaningful components from the noise-dominated ones on one simulated and two biochemical Raman datasets:

Dataset 1: a superposition of Gaussian functions resembling Raman-like signal superimposed by a background;

Dataset 2: Raman spectra of known mixtures of 8 pure chemical compounds (sphingomyelin, β -carotene, collagen, cholesteryl palmitate, elastin, iron transferrin, cholesterol, and iron (III) oxide) with simulated random spatial distribution of concentration superimposed by white Gaussian noise;

Dataset 3: large-scale Raman hyperspectral images of human atherosclerotic aortic tissues and corresponding non-atherosclerotic controls, consisting of both high and low concentrated biochemical compounds.

For **Dataset 2**, white Gaussian noise \mathbf{I}^n was added to the intensity matrix composed of the chemical mixture of pure Raman spectra \mathbf{I}^{mR} . Then, SVD-ADC filtering procedure with *no input* parameters was applied to the resulting matrix $\mathbf{I} = \mathbf{I}^{mR} + \mathbf{I}^n$. The results of this verification confirm that SVD-ADC allowed to significantly remove noise from the Raman data and resulted in the denoised \mathbf{I}^R matrix with reduced noise by two orders of magnitude ($\text{NRF} \approx 0.01$) as evident by Fig. 3.1A. Here, signal-to-noise ratio (SNR) and noise removal factor (NRF) were defined as follows:

$$\text{SNR} = \frac{\|\mathbf{I}^{mR}\|_F^2}{\|\mathbf{I}^n\|_F^2} \quad (3.12)$$

$$\text{NRF} = \frac{\|\mathbf{I}^R - \mathbf{I}^{mR}\|_F^2}{\|\mathbf{I}^n\|_F^2} \quad (3.13)$$

The efficiency of SVD-ADC is also demonstrated in Fig. 3.1B by the distribution of spatio-spectral autocorrelation coefficients for singular vectors retrieved from SVD-ADC for $\text{SNR} = 10$. This autocorrelation map validates localization of singular vectors representing noise (cross signs) around the origin of coordinates in contrast to highly correlated singular vectors assigned to meaningful components (circled cross signs) located at the upper-right corner. Thus, the meaningful components are filtered from noise-dominated ones by the dashed diagonal line representing $R_{\text{thr}} = 50\%$.

Furthermore, the accuracy of SVD-ADC is confirmed by Fig. 3.1C, showing that the denoised Raman spectrum \mathbf{I}^R (red dashed line) is almost indistinguishable from the reference one \mathbf{I}^{mR} (grey

line), even when the noise in the input Raman spectrum (blue line) is comparable with the Raman signal.

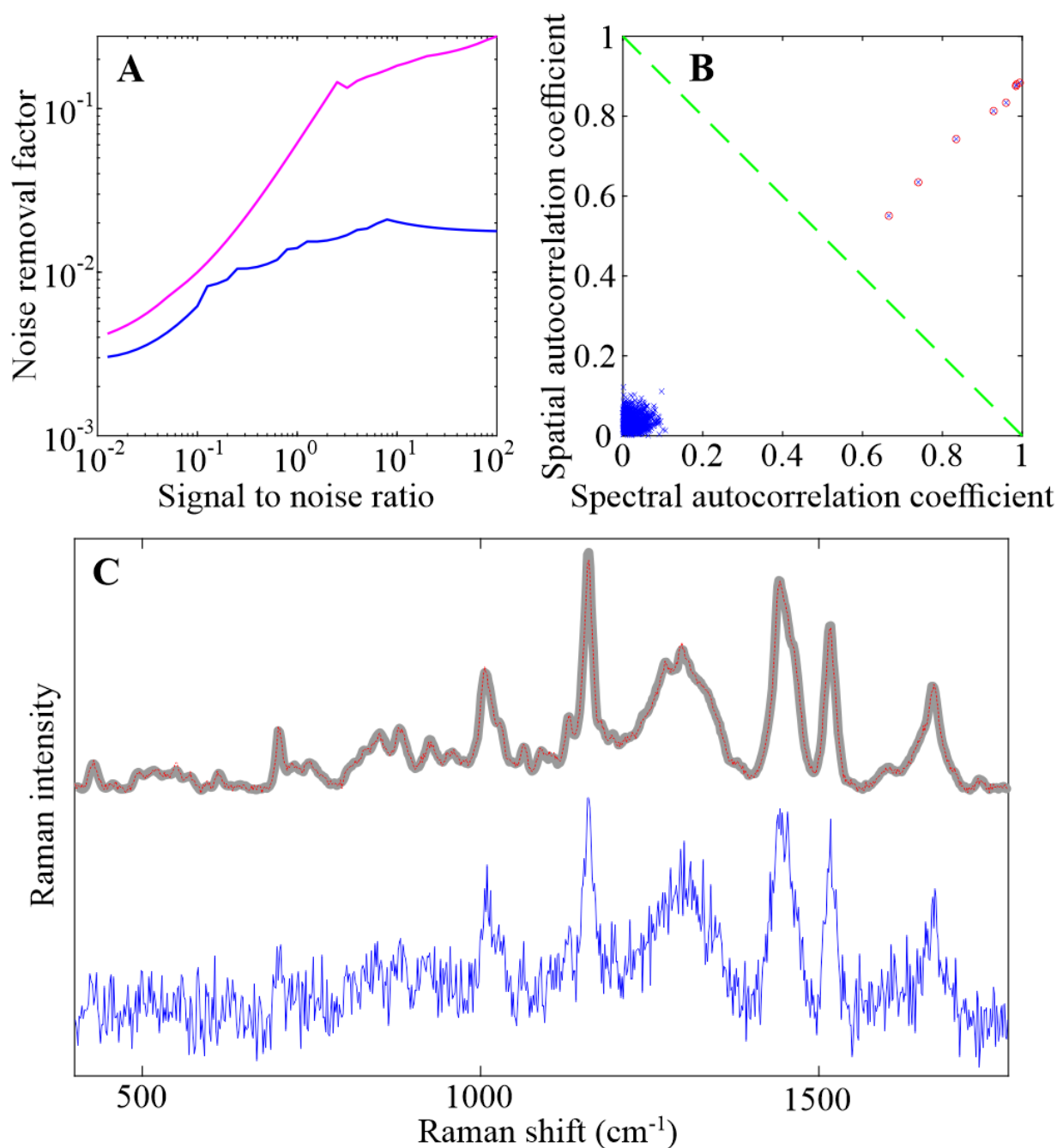


Fig. 3.1: Comparison of the SVD-ADC (A, blue line) method with MNF + S-G filtering (A, magenta line) using the Raman data of biochemical standard mixtures with white Gaussian noise (C, blue line), showing the efficiency of the SVD-ADC to reduce noise from the Raman data by 98% and resulting in denoised Raman spectra (C, red dashed line) to be almost identical to the reference one (C, grey line). The autocorrelation coefficients map of singular vectors received from SVD-ADC analysis of the given Raman data is shown in panel B. The green dashed diagonal line represents a decision line of a 50% cut-off for mean autocorrelation coefficients, that separates the coefficients above the line (circled cross signs – meaningful components) from those below it (cross signs – noise).

Furthermore, SVD-ADC was compared with Maximum Noise Fraction (MNF) method (Green *et al.* 1988) combined with Savitzky-Golay (S-G) filtering (Savitzky and Golay 1964) as shown in (Lobanova and Lobanov 2019). In particular, **Dataset 2** was processed using MNF and then N eigenimages ordered according to decreasing Signal-to-Noise Ratio (SNR) (or reducing image

quality) were used. The rest eigenimages were denoised using S-G filtering with two smoothing parameters: polynomial order and frame length. For this, optimization over these 3 parameters for each SNR, which minimizes denoising error, was performed. Finally, the application of inverse MNF to reduced noise eigenimages gives the resulting denoised data. As shown in Fig. 3.1A, both methods provide comparable NRF for noise-dominated data with SNR from the range (0.01, 1). However, when SNR is higher than 10, MNF allowed to reduce noise by just 80% (NRF = 20%), in contrast to SVD-ADC allowing to receive 98% of noise removal (NRF = 2%).

Importantly, the selection of optimal parameters for MNF and S-G filtering is *only* achievable when the true solution is known. In contrast, SVD-ADC method provides autonomous reduction of noise from the hyperspectral Raman data with *no input* parameters.

Altogether, the SVD-ADC approach, proposed in (Lobanova and Lobanov 2019), utilises autocorrelation coefficients of spatial and spectral singular vectors for noise filtering and allows to autonomously remove noise from Raman data with *no input* parameters.

3.3. Bottom Gaussian Fitting (BGF) for background subtraction

Raman spectra from tissue samples embedded on a standard glass slide typically exhibit an intense broad background associated with the fluorescence and amorphous scattering contributions from glass substrate and sample itself. Therefore, baseline correction algorithms via polynomial functions of different orders (Hirokawa 1980; Baek *et al.* 2009) and Asymmetric Least Squares (AsLS) method (Eilers 2003; Eilers 2004) are widely applied to hyperspectral image analysis for background correction (Peng *et al.* 2010; Piqueras *et al.* 2011; Albuquerque and Poppi 2015; Felten *et al.* 2015).

However, polynomial baseline removal methods in application to hyperspectral Raman images might be limited by low reproducibility of the results and a large number of factors, which significantly affect accuracy (Jirasek *et al.* 2004). In contrast, AsLS is considered to be a relatively accurate and automated method for background correction of hyperspectral Raman data (Felten *et al.* 2015).

It is important to note that the AsLS method involves the optimization over the smoothing λ and asymmetric p parameters, which can result in a fluorescent background being higher than measured Raman intensity, ultimately leading to negative non-physical Raman signal.

3.3.1. Formulation of BGF

In order to overcome the limitations of the AsLS method, a new algorithm, Bottom Gaussian Fitting (BGF), has been recently proposed and provides autonomous and accurate subtraction of a complex curved background from Raman micro-spectroscopy data (Lobanova and Lobanov 2019).

Compared to AsLS, BGF uses *only* one intuitive parameter, which has units of Raman wavenumbers (cm^{-1}) and indicates minimum width of broad background features.

The principles of this mathematical approach are proposed in (Lobanova and Lobanov 2019) and explained in the following.

The principle of this method is to perform background removal procedure independently for each image pixel i . Therefore, I will present a brief theory of BGF using only the second index in the Raman intensity matrix \mathbf{I}_{ij} labelling wavenumber, i.e. \mathbf{I}_j .

The Raman intensity \mathbf{I} can be split into two non-negative parts

$$\mathbf{I} = \mathbf{I}^{\text{R}} + \mathbf{I}^{\text{B}}, \quad (3.16)$$

where \mathbf{I}^{R} represents Raman signal and \mathbf{I}^{B} is a fluorescent background.

The method aims to find \mathbf{I}^{B} as a quasi-superposition of Gaussian functions with standard deviations (STD) larger than σ – *the only one parameter* that will be used for background subtraction.

By fixing some Raman shift ν_j , one could find maximum possible background intensity at this point I_j^{B} . Fig. 3.2 illustrates the principle of this search for the case of one narrow Raman peak ($\text{STD} < \sigma$) superimposed by a broad fluorescent background ($\text{STD} > \sigma$) both modelled as a Gaussian function. The figure contains a series of Gaussian functions (green, red, and magenta lines) with varying amplitude A and expectation value μ but fixed STD σ . Comparing values of these lines at the point ν_j , one finds that magenta Gaussian function has maxim value at this point. However, this line cannot be used as a background because it crosses the Raman intensity \mathbf{I} and, therefore, do not fit it from the bottom. The green line does not cross the Raman intensity \mathbf{I} , but its value is not maximum at the point ν_j . Only the red solid line tangents the Raman spectrum \mathbf{I} (fits from the bottom) and appears to quantify the representative Raman intensity \mathbf{I}^{R} at the point ν_j .

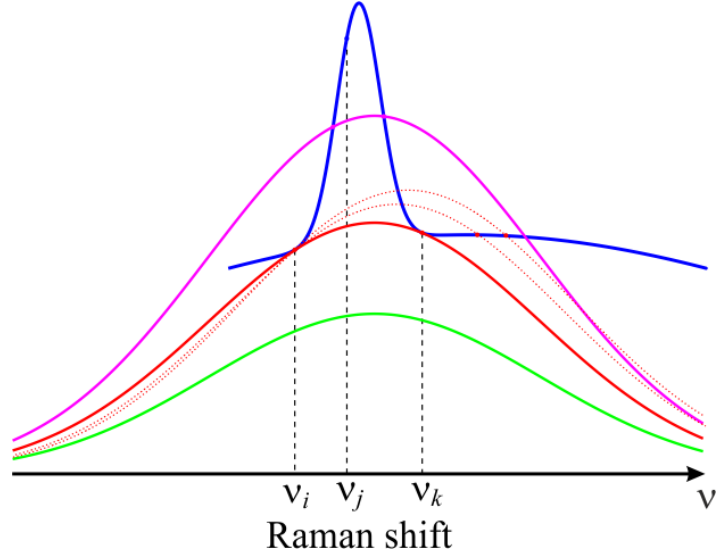


Fig. 3.2: A schematic illustration showing a principle of BGF method used for background subtraction from Raman signal.

Mathematically, since the background intensity \mathbf{I}^B tangents the Raman intensity \mathbf{I} , it should be determined as a Gaussian function $G_\sigma(\nu_j; \nu_i, I_i, \nu_k, I_k)$ of STD σ , which goes through left- (ν_i, I_i) and right-sided (ν_k, I_k) points of the Raman intensity \mathbf{I} corresponding to the considered Raman shift ν_j .

Furthermore, the tangent background fit \mathbf{I}^B (red solid line) has minimum Raman intensity value at the point ν_j compared to the red dotted and magenta lines.

Therefore, the bottom Gaussian fit can be defined as

$$I_j^B = \min_{i \leq j \leq k} G_\sigma(\nu_j; \nu_i, I_i, \nu_k, I_k), \quad (3.17)$$

where the Gaussian function

$$G_\sigma(\nu_j; \nu_i, I_i, \nu_k, I_k) = A e^{-\frac{(\nu_j - \mu)^2}{2\sigma^2}} \quad (3.18)$$

has amplitude A and expected value μ , which are implicitly defined as follows:

$$A e^{-\frac{(\nu_i - \mu)^2}{2\sigma^2}} = I_i, \quad A e^{-\frac{(\nu_k - \mu)^2}{2\sigma^2}} = I_k. \quad (3.19)$$

Repeating the procedure in Eq. (3.17) for all Raman shifts ν_j , one can retrieve a quasi-smooth curve \mathbf{I}^B fitting the Raman signal \mathbf{I} from the bottom, so that the residual of these two curves ($\mathbf{I}^R = \mathbf{I} - \mathbf{I}^B$) contains only sharp resonances representing Raman bands.

Optionally, after the background-free Raman-like signal \mathbf{I}^R is found using BGF, the spatially-resolved spectral auto-correlation coefficients for this matrix at one spectral point shift can be calculated. By discarding the spatial points, which have correlation values lower than 50%, from

the further analysis, one can achieve the partial elimination of spatial points, which are strongly distorted by noise due to dominated background, which might be orders of magnitude larger than the Raman signal.

3.3.2. Validation of BGF

In order to validate the accuracy of BGF, it was compared with AsLS algorithm (Eilers 2003; Eilers 2004) using Raman spectra \mathbf{I}^{mR} of biochemical mixtures with Gaussian background (**Dataset 2**) (Lobanova and Lobanov 2019).

For this, the dependence of background removal relative error

$$E = \frac{\max_{ij} \|I_{ij}^{\text{R}} - I_{ij}^{\text{mR}}\|}{\max_{ij} \|I_{ij}^{\text{mR}}\|} \quad (3.20)$$

on the corresponding parameters of BGF (σ , red line with crosses) and AsLS (λ and fixed $p = 10^{-3}$, green line with pluses) has been investigated. The results show that BGF allows to achieve relative error of 7%, whereas AsLS provides 64% relative error (see Fig. 3.3A). Note, \mathbf{I}^{R} is a background-subtracted Raman signal found from BGF or AsLS.

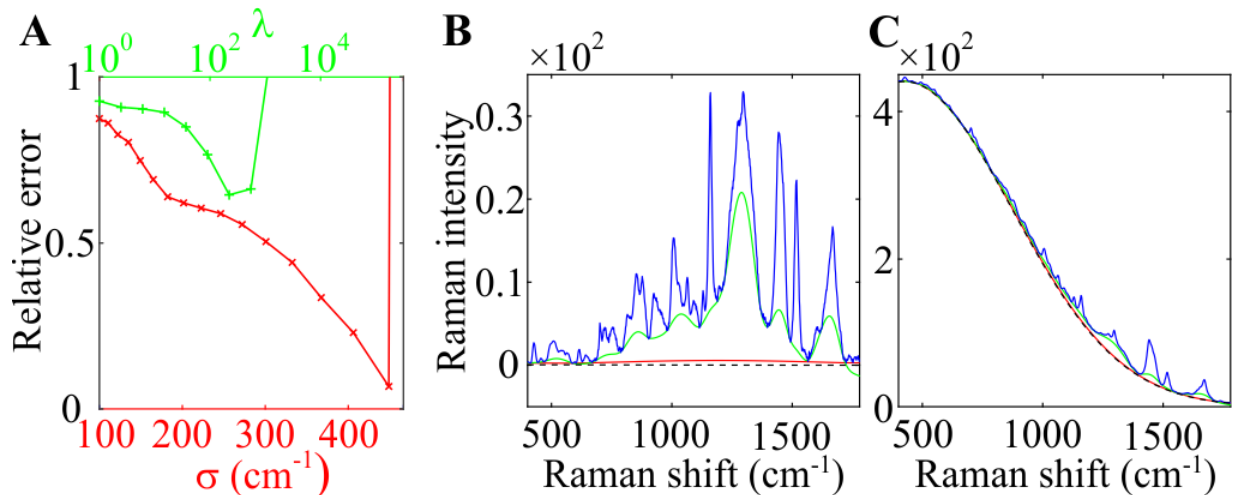


Fig. 3.3: Comparison of the BGF method with AsLS using the Raman data with known background (black dashed lines), showing the accurateness of the BGF to produce the true baseline (red lines) that subtract both low (B) and high (C) background. AsLS baselines are shown by green.

Application of BGF to Raman spectra (blue lines) for two spatial pixels with low (B) and high (C) true background (black dashed lines) reveals that BGF performs equally accurate for low and high background (red lines), in contrast to AsLS, which might produce the baseline (green lines), significantly overfitting the original Raman signal and having non-physical negative values (see Fig. 3.3B-C). Note, Fig. 3.3B-C are demonstrated for the following optimal parameters found from Fig. 3A: $\sigma = 449 \text{ cm}^{-1}$ (BGF) and $\lambda = 223, p = 10^{-3}$ (AsLS).

Also, the BGF method has been verified on large-scale Raman micro-spectroscopy images from human tissues in atherosclerosis and simulated Raman data as described in (Lobanova and Lobanov 2019).

3.4. Efficient Quantitative Unsupervised/Partially Supervised Non-negative Matrix Factorization (Q-US/PS-NMF)

3.4.1. Formulation of Q-US/PS-NMF

Applied to hyperspectral image analysis, NMF method (Paatero and Tapper 1994; Paatero 1997; Lee and Seung 1999; Lee and Seung 2001) is an unsupervised chemometric approach, allowing to factorise the spatially-resolved Raman intensity matrix \mathbf{I} into a superposition Eq. (3.2) of non-negative spatial concentration \mathbf{C} multiplied by corresponding non-negative spectra \mathbf{S} of individual biochemical components of the samples' composition. The aim of NMF is to find matrices \mathbf{C} and \mathbf{S} , which are unknown prior to factorization analysis.

In (Lobanova and Lobanov 2019), NMF has been generalised to work as a partially supervised method, called Efficient Quantitative Unsupervised/Partially Supervised Non-negative Matrix Factorization (Q-US/PS-NMF). This development is beneficial for various biomedical applications, e.g. fixation of the spectrum of paraffin-wax compound during supervised NMF in the Raman intensity matrix measured on paraffin-embedded samples. This option allows to remove the contribution of paraffin-wax residues from the spectra of chemical components of actual samples' composition.

Mathematically, the problem can be formulated as follows. Assuming N_k biochemical substances with Raman spectra $S_i(\nu), i = 1, \dots, N_k$ are known and I am aiming to find the rest $N_u = N - N_k$ spectra $S_i(\nu), i = N_k + 1, \dots, N$ together with the corresponding concentration profiles for both known and unknown components $C_i(\mathbf{r}), i = 1, 2, \dots, N$.

Let us denote known and unknown parts of the spectral matrix \mathbf{S} as \mathbf{S}_k and \mathbf{S}_u , respectively. Corresponding parts of the concentration matrix \mathbf{C} can be also written as \mathbf{C}_k and \mathbf{C}_u . Therefore, one can construct the following matrices

$$\mathbf{C} = \begin{pmatrix} \mathbf{C}_k \\ \mathbf{C}_u \end{pmatrix}, \mathbf{S} = \begin{pmatrix} \mathbf{S}_k \\ \mathbf{S}_u \end{pmatrix}, \quad (3.14)$$

Mathematically, these matrices should satisfy Eq. (3.2). But, practically, the experimentally measured Raman intensity matrix \mathbf{I} can be decomposed with a residue \mathbf{E} , known as a factorization error as follows

$$\mathbf{I} - \mathbf{C}^T \mathbf{S} = \mathbf{E}. \quad (3.15)$$

The solution of this equation must minimise Frobenius norm of the residue $\|\mathbf{E}\|_F$. In other words, the problem is reduced to finding two matrices \mathbf{C} and \mathbf{S} which minimize the following function

$$E(\mathbf{C}, \mathbf{S}) = \frac{1}{2} \|\mathbf{I} - \mathbf{C}^T \mathbf{S}\|_F^2 \quad (3.16)$$

subject to $C_{ij} \geq 0, S_{ij} \geq 0$.

Since Eq. (3.16) has minimum at the point (\mathbf{C}, \mathbf{S}) , any deviation from this point must increase Frobenius norm of the residue, i.e. $E(\mathbf{C}+\delta\mathbf{C}, \mathbf{S}+\delta\mathbf{S}) \geq E(\mathbf{C}, \mathbf{S})$ for any $\delta\mathbf{C}$ and $\delta\mathbf{S}$ subject to $C_{ij} + \delta C_{ij} \geq 0$ and $S_{ij} + \delta S_{ij} \geq 0$. This means that variation of the factorization error $\delta E \equiv E(\mathbf{C}+\delta\mathbf{C}, \mathbf{S}+\delta\mathbf{S}) - E(\mathbf{C}, \mathbf{S})$ at the point (\mathbf{C}, \mathbf{S}) must be non-negative

$$\delta E = \sum_{i=1}^N \sum_{j=1}^{N_p} \frac{\partial E}{\partial C_{ij}} \delta C_{ij} + \sum_{i=N_k+1}^N \sum_{j=1}^{N_s} \frac{\partial E}{\partial S_{ij}} \delta S_{ij} \geq 0. \quad (3.17)$$

Furthermore, each term in Eq. (3.17) must be equal or greater than zero since variations δC_{ij} and δS_{ij} are arbitrary.

In order to find a solution of Eq. (3.17), one can fix all elements in the matrices \mathbf{C} and \mathbf{S} except one element (for example, C_{12}) and explore the dependence of the factorization error $E(\mathbf{C}, \mathbf{S})$ on this element (C_{12}). Fig. 3.4 shows the graph of this function which is parabola. Two possible cases are considered in Fig. 3.4. Specifically, blue parabola has a minimum at positive C_{12} in which its derivative is zero, i.e. $\partial E / \partial C_{12} = 0$. Therefore, in order to satisfy Eq. (3.17), $\partial E / \partial C_{ij}$ must be zero for positive C_{ij} . The green parabola has a minimum at negative C_{12} , which is not permitted due to the non-negativity condition. Therefore, the constrained minimum must be translated to the nearest non-negative point, which is zero. Thus, $\partial E / \partial C_{ij}$ must be non-negative for $C_{ij} = 0$ in order to satisfy Eq. (3.17).

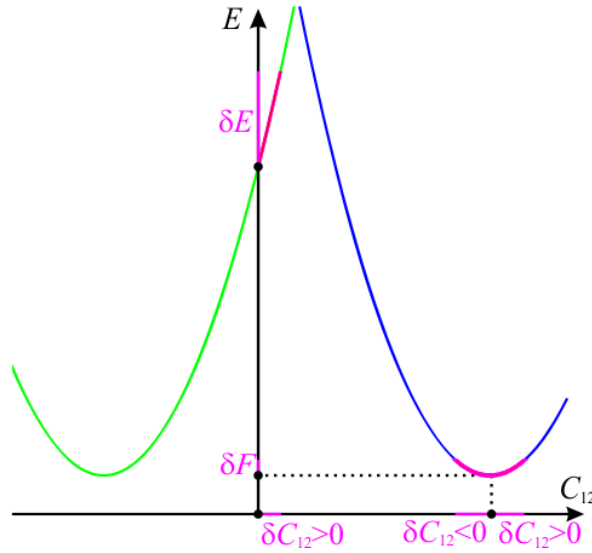


Fig. 3.4: Dependence of the factorisation error $\delta E(C_{11}, C_{12}, C_{13}, \dots, S_{11}, S_{12}, \dots)$ on the element C_{12} for fixed other elements.

These non-negativity requirements are known as the Karush-Kuhn-Tucker conditions (Lawson and Hanson 1995)

$$\frac{\partial E}{\partial C_{ij}} = 0 \text{ if } C_{ij} > 0, \quad \frac{\partial E}{\partial C_{ij}} \geq 0 \text{ if } C_{ij} = 0, \quad (3.18)$$

$$\frac{\partial E}{\partial S_{ij}} = 0 \text{ if } S_{ij} > 0, \quad \frac{\partial E}{\partial S_{ij}} \geq 0 \text{ if } S_{ij} = 0. \quad (3.19)$$

Note, Eq. (3.19) must be fulfilled only for unknown spectra, i.e. $i > N_k$.

By differentiating Eq. (3.16), one can find partial derivatives required for solving Eqs. (3.18)-(3.19)

$$\frac{\partial E}{\partial \mathbf{C}} = \mathbf{S}\mathbf{S}^T\mathbf{C} - \mathbf{S}\mathbf{I}^T, \quad (3.20)$$

$$\frac{\partial E}{\partial \mathbf{S}_u} = \mathbf{C}_u\mathbf{C}_u^T\mathbf{S}_u - \mathbf{C}_u\mathbf{I} + \mathbf{C}_u\mathbf{C}_k^T\mathbf{S}_k, \quad (3.21)$$

Note, Eqs. (3.18)-(3.21) represent a system of non-linear equations and inequalities, which can be solved in an iterative manner. For this, one should fix one matrix (\mathbf{C} or \mathbf{S}_u) and find another one (\mathbf{S}_u or \mathbf{C} , respectively) via NLS method (Lawson and Hanson 1995). This procedure can be done independently for each wavenumber if \mathbf{C} is fixed or pixel if \mathbf{S}_u is fixed. However, this procedure is not computationally efficient. Therefore, another method was developed (Van Benthem and Keenan 2004; Kim and Park 2007; Lobanova and Lobanov 2019) allowing to achieve fast computational performance. The principle of this approach is based on the operation with the whole matrices instead of vectors.

In order to quantitatively compare spatial Raman concentrations between samples, the normalisation conditions are required. As shown in (Lobanova and Lobanov 2019), the Q-US/PS-

NMF method fulfils the following normalisation conditions. First, spectrum for each resolved component is normalised so that

$$\int dvS_1(v) = \int dvS_2(v) = \dots = \int dvS_N(v). \quad (3.22)$$

Second, total mean concentration is normalized to be unity

$$\frac{1}{N_p} \sum_{j=1}^{N_p} \sum_{i=1}^N C_i(\mathbf{r}_j) = 1. \quad (3.23)$$

3.4.2. Validation of Q-US/PS-NMF

To validate the accuracy of Q-US/PS-NMF, it was compared with the MCR-ALS (Jaumot *et al.* 2015) and VCA (Nascimento and Dias 2005) methods using 8 pure Raman spectra of biochemical mixtures (**Dataset 2**, $32 \times 32 \times 804$ data matrix) and large-scale Raman micro-spectroscopy images from human tissues in atherosclerosis (**Dataset 3**, $\approx 6 \times 10^2 \times 10^3 \times 10^3$ multi-image data matrix) as shown in (Lobanova and Lobanov 2019).

For **Dataset 2**, it has been found that VCA was not able to find the original chemical components, providing the relative factorization error of 70%. In contrast, Q-US/PS-NMF allowed to achieve relative factorization error of 2.6%, 0.7%, and 0.5% for 1, 5, and 10 minutes of standard PC running times, respectively, and showed about 20 times more accurate results received for the same computational time compared to MCR-ALS (Lobanova and Lobanov 2019).

For **Dataset 3**, it has been shown that Q-US/PS-NMF allowed to retrieve the composition of atherosclerotic tissues and non-atherosclerotic controls into a number of individual biochemical components with mean Raman concentration down to 1% as deduced from the analysis with 11 components, providing 5% factorization error compared to 11% for VCA. Furthermore, compared to VCA, it has been demonstrated that Q-US/PS-NMF was able to detect additional chemical components, such as cholesterol and oxidatively-modified linoleic acid, which are well-established and important bio-markers of atherosclerosis (Lobanova and Lobanov 2019).

3.5. Findings

Collectively, three novel chemometric methods combined in the quantitative hyperspectral image unmixing Q-HIU methodology which is intended for the efficient quantitative analysis and decomposition of Raman micro-spectroscopy images were proposed in (Lobanova and Lobanov 2019). The methods were compared and verified with existing state-of-the-art approaches:

- SVD-ADC was compared with MNF method combined with S-G filtering;
- BGF was compared with AsLS method;
- Q-US/PS-NMF was compared with VCA and MCR-ALS algorithm.

These verifications with existing methods outlined above showed that the Q-HIU approach provides significantly more accurate results and efficient quantification with several orders of magnitude shorter computational time as testified on both simulated and real experimental Raman data (**Dataset 1, 2 and 3**). Furthermore, Q-HIU was validated to identify and quantify the unknown biochemical composition of analytes from the hyperspectral Raman data. Therefore, the Q-HIU is a new unprecedented chemometric methodology, which is well-suited for the biomolecular characterization and quantitative imaging of individual biochemical components in chemical and biomedical samples of various complexity.

In the course of my study chapters presenting the results on chemical composition of AD brain tissues and corresponding non-demented controls (**Chapter 5** and **Chapter 6**), I will utilise the Q-HIU chemometric methodology for the simultaneous multi-set analysis of my hyperspectral Raman micro-spectroscopy images as discussed in this chapter and summarised in an overview flowchart of Fig. 3.5. In brief, I will analyse my biomedical Raman data in three steps as follows (see an overview flowchart of Q-HIU analysis in Fig. 3.5):

- 1) Application of SVD-ADC, which autonomously filters spatially and spectrally uncorrelated noise from the Raman data;
- 2) Application of BGF for a robust subtraction of fluorescent background from the data;
- 3) Application of an efficient Q-US/PS-NMF via the FC-NNLS algorithm. I will use a partially supervised-NMF modality for my Raman data performed on paraffin-embedded brain samples (**Chapter 5**), where I will fix the known Raman spectrum of paraffin/wax compound in the factorizing Raman intensity matrix, which was measured on one of the brain samples. In **Chapter 6**, I will utilize an unsupervised-NMF for my Raman data acquired from frozen brain samples.

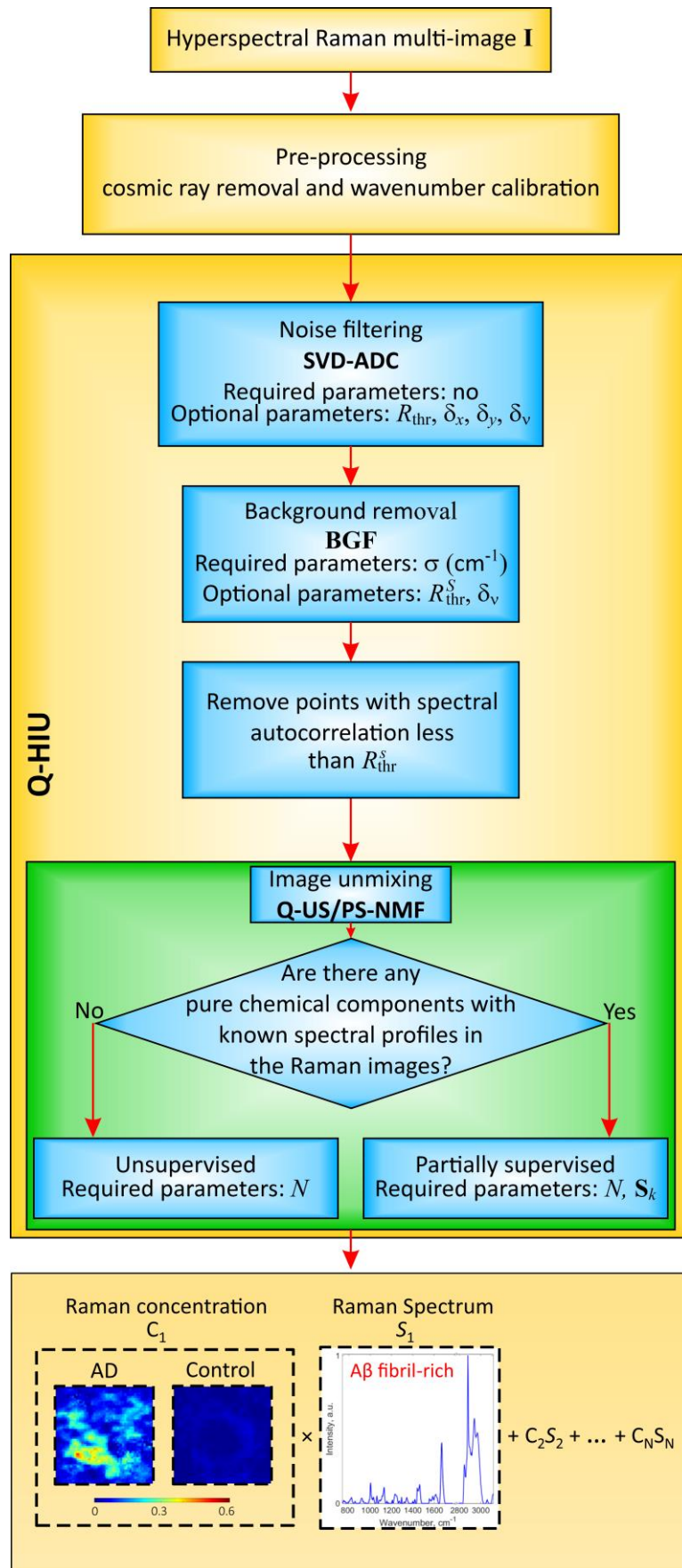


Fig. 3.5. Flowchart listing 3 main steps of the Q-HIU data analysis.

Chapter 4. Methodology

Confocal Raman micro-spectroscopy is a widely used analytical approach providing a chemically specific imaging of biomedical samples in non-invasive and label-free manner (Movasaghi *et al.* 2007; Krafft *et al.* 2016).

Raman effect also known as inelastic scattering phenomena is originated from the interaction of laser light of a frequency in visible range with the molecules in a sample (Diem 2015). Such interaction with the laser light illuminated onto the sample induces the vibrations of chemical bonds in the molecules of the sample, leading to back scattering of the incident light with the shifted energy. On a quantum level, the incident laser light excites the molecules in the sample to a virtual state, from where they undergo a transition back to the corresponding vibrational states of specific molecular bonds with low energy, thus releasing the scattered photon of a red shifted energy (see Fig. 4.1). Here, the vibrational frequency of chemical bonds in the molecules is equal to the energy difference between incident laser and Raman scattered light. A series of molecular vibrational frequencies each corresponding to the unique chemical bonds of the sample compounds form a Raman spectrum.

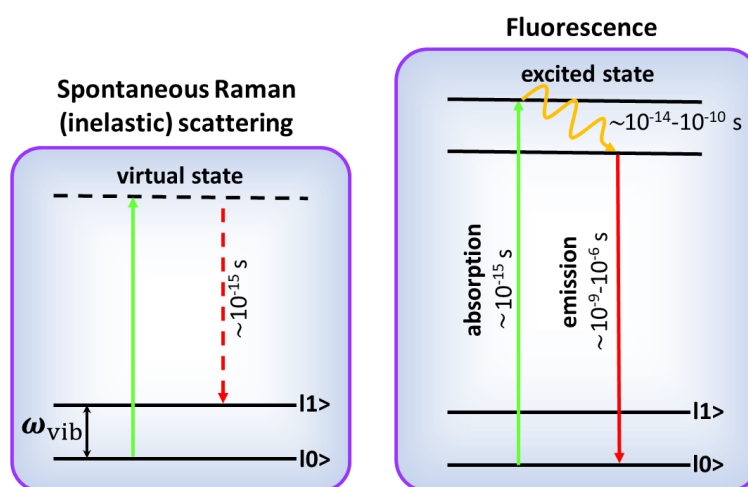


Fig. 4.1: Schematic energy diagrams representing spontaneous Raman scattering and fluorescence.

However, the Raman effect is weak, resulting in only one in 10^8 of the incident photons being inelastically scattered (Butler *et al.* 2016). Nevertheless, these photons contain information about the vibrations of molecules and therefore the chemical structure of the sample constituents. Applied to the detection of pathogenic aggregated proteins implicated in a range of neurodegenerative diseases, it has been reported that amyloid fibrils exhibit a unique chemical structure enriched in β -sheet conformations compared to unaggregated native amyloid protein with α -helix structure (Kurouski *et al.* 2015; Ji *et al.* 2018). Generally, a typical Raman spectrum of the protein in the fingerprint region has dominant contributions from three vibrational modes,

originating from the polypeptide backbone (amide bands) and from aromatic/non-aromatic side chains of amino acid residue. The most diagnostic bands used to reveal protein backbone conformations are the amide I vibration (1640–1680 cm^{-1}), which can be predominantly assigned to C=O stretching and a minor portion to out-of-phase C–N stretching; the amide II vibration ($\sim 1550 \text{ cm}^{-1}$), attributed to the coupled out-of-phase C–N stretching and N–H bending vibrations; and the amide III (1200–1340 cm^{-1}), also associated with the C–N stretching and N–H bending motions (Rygula *et al.* 2013). Of these vibrational bands, the amide I band is well established to probe the changes in the protein secondary structure including A β peptide (Wang *et al.* 2013; Ji *et al.* 2018). It has been revealed that the polypeptide backbone conformation of protein determines the position of the amide I band: a β -sheet conformation corresponds to the amide I band in the vibrational range 1667–1672 cm^{-1} , whereas α -helix structure is located in the 1655–1662 cm^{-1} range. Applied to detection of A β aggregation using SRS microscopy, A β fibrils with predominantly the β -sheet structure have a 10 cm^{-1} higher Raman shift frequency of the Amide I band compared to a native A β peptide in the α -helix conformation (Ji *et al.* 2018). Interestingly, there is a line of evidence that parallel and antiparallel β -sheet conformation of A β fibrils can be distinguished by Raman micro-spectroscopy (Schweitzer-Stenner *et al.* 2006; Kurouski *et al.* 2010; Schweitzer-Stenner 2012). It was suggested that anti-parallel β -sheet proteins have weaker peptide hydrogen bonding compared to those having parallel β -sheet structures, leading to a higher Raman shift of the amide I band for anti-parallel β -sheet proteins (Kurouski *et al.* 2015). However, comparison of the amide I band in the anisotropic Raman spectra for anti-parallel and parallel β -sheets revealed that the number of strands affect the position of the amide I peak, thus complicated their assignment (Kurouski *et al.* 2015). Specifically, a reduction in the number of strands from 12 to 1 induces a pronounced red-shift of the amide I band for the parallel β -sheets and only a slight peak shift for the anti-parallel β -sheets (Measey and Schweitzer-Stenner 2011). Therefore, the detection of parallel and anti-parallel β -sheet structure in A β fibrils based on the amide I Raman band is not possible.

Instrumentally, confocal Raman spectrometers that are based on either upright or inverted microscopes are commonly utilised for collection of Raman spectra of biological tissues. A laser source of visible wavelength is widely used for generating light and sample illumination. In point-scan Raman experiment, the Raman spectra also known as the multi-spectral hypercube is acquired by raster scanning the sample through the focal point of the laser beam. This multi-spectral hypercube consists of thousands discrete pixel points, each of which has individual Raman spectrum typically in a whole 50-4000 cm^{-1} spectral range with a high 5 cm^{-1} resolution. Schematic diagram of a conventional Raman setup can be found in Fig. 4.2.

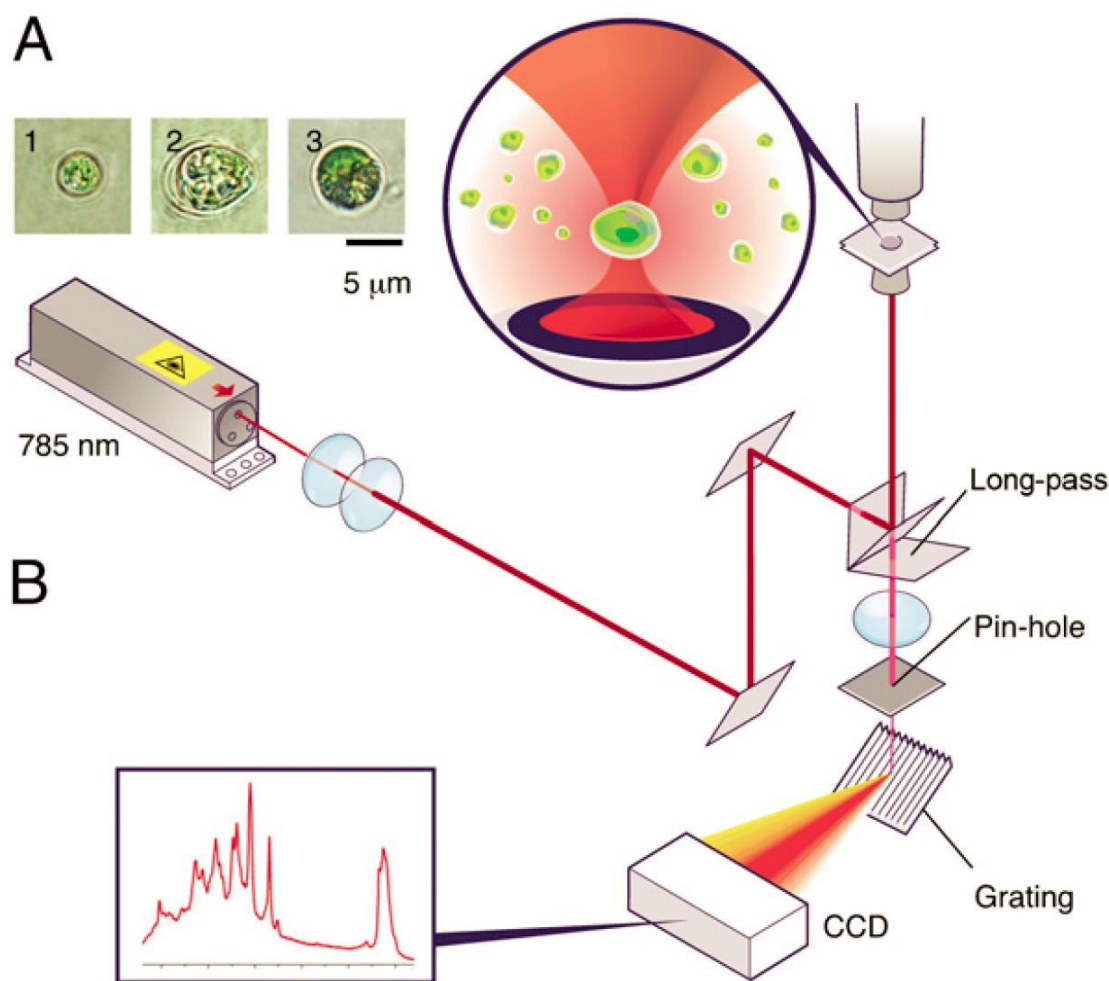


Fig. 4.2: A typical Raman micro-spectroscopy setup. Reproduced from (Wu *et al.* 2011) with permission of PNAS. Fluorescence microscopy is the essential tool for numerous biomedical applications, including *post-mortem* histological examination of different types of tissues. Fluorescence microscopy is based on the absorption and subsequent emission of light by fluorophores, chemical dyes or auto-fluorescent biochemical compounds. For this, the target biomolecule in a sample is attached with specific fluorophore conjugated antibody, which provides a fluorescent probe used for detection of the concentration of this fluorophore-bound target biomolecule. As can be explained by quantum theory, when the energy of the incident photon illuminating the fluorescently-labelled sample is equal to the energy of an electronic transition of the used fluorophore, the fluorophore molecule undergoes this transition occurring from the ground vibrational level of its electronic ground state to higher electronic and vibrational levels of the excited state. Then, this molecule rapidly relaxes to the lowest vibrational level of the excited state, from where it transits back to the electronic ground state, known as fluorescent emission of red-shifted photons (see Fig. 4.1). Compared to Raman effect, fluorescence has longer time scales ranging from nano- to micro-seconds in duration versus femtoseconds for Raman. To note, when fluorescent emission lasts longer than micro-seconds after the radiation light has been switched off, this effect can be attributed to phosphorescence.

Chapter 5. Chemical imaging of formalin-fixed-paraffin-embedded brain sections by point-scan Raman micro-spectroscopy

5.1. Introduction

Development of novel quantitative imaging biomarkers are of great interest for diagnosis and monitoring of AD (Jack *et al.* 2013). Complimentary to clinical imaging techniques such as PET and MRI, Raman micro-spectroscopy serves as a promising method for identification of new molecular markers of AD brains with quantitative chemical specificity, high spatial resolution, non-destructively and without the use of dyes or labels (Ryzhikova *et al.* 2014). In combination with advanced multivariate image analysis methods, Raman micro-spectroscopy shows a great potential for detection of early chemical changes of altered brain metabolism, so that AD brains could be differentiated from non-demented controls. Despite the significance of this research, a handful of Raman micro-spectroscopy studies in AD brain have been reported in the literature. Among them, the work presenting images of lipid-amyloid co-arrangements in AD human brains using a nonlinear version of Raman micro-spectroscopy, CARS, has been recently shown (Kiskis *et al.* 2015). However, in this study the spectral profiles of lipid deposits associated with the A β plaques have been extracted only in the CH-stretch vibrational region (2700-3100 cm⁻¹), which is more congested due to overlap of the characteristic vibrational bands compared to the fingerprint, complicating the chemical interpretation of spectra. This research paper also suggested the mechanism for A β pathology spreading according which lipid vesicles continuously interact with the A β plaque by pulling out the oligomer fragments from its halo. Next, there could be two possible scenarios for these released oligomers. One possibility is that they can flow into synapses, disrupting the connections between neurons. Another possibility could be that the released oligomers build up, thereby seeding a new A β plaque assembly. Altogether, this hypothesis indicates lipids as a possible driver of A β pathology. In relation to confocal Raman micro-spectroscopy, several studies have recently reported the chemical profiles of abnormal protein aggregates in AD brains (Michael *et al.* 2014; Michael *et al.* 2017), proving the sensitivity of confocal Raman to visualise the pathogenic β -sheet chemical structure of A β plaques and tau tangles. This research study based on the idea that the Raman spectrum of misfolded A β in the plaque composition exhibits the strongly amplified amide I band due to a high content of β -sheet structures (1667–1672 cm⁻¹) (Ji *et al.* 2018). An unfortunate corollary of this approach is that such

Raman imaging does not distinguish a unique molecular fingerprint of fibrillar A β from other proteins in the β -sheet conformation. To overcome this limitation, hyperspectral image unmixing analysis that retrieve the whole individual spectral profiles of chemical components in the sample should be utilised (Piqueras *et al.* 2011).

Comparison of spontaneous Raman and CARS micro-spectroscopy

Spatially resolved spectra received from spontaneous Raman and CARS micro-spectroscopies contain chemical and structural information about functional, endogenous biomolecules of cells and tissues (Krafft *et al.* 2016). However, CARS intensity spectra are complex in line-shape due to the interference between the vibrationally resonant and non-resonant part of the third-order CARS susceptibilities complicating their interpretation (Diem 2015). Therefore, CARS micro-spectroscopy requires appropriate transformation methods for extraction of the imaginary part of the CARS susceptibility, similar to the spontaneous Raman spectra and linear in concentration of analytes (Liu *et al.* 2009). CARS imaging also suffers from low signal-to-noise ratio in the fingerprint region (700-1800 cm^{-1}), that contains vibrational bands characteristic for the pathogenic conformation state of A β protein, making it important for investigation. As a consequence, all previous CARS micro-spectroscopy studies in brain tissue have been reported only in the CH-stretch region (2700-3100 cm^{-1}) (Kiskis *et al.* 2015; Lee *et al.* 2015), which is less chemically specific. Despite these limitations, CARS benefits from high signal intensities, due to the constructive interference of Raman scattered photons from coherently driven identical chemical bonds in the molecules within the focal volume. It also exhibits high intrinsic 3D spatial resolution because of the multiphoton nonlinearity and has inherent immunity from sample autofluorescence. It is therefore a fast-high-resolution micro-spectroscopy technique invaluable for biomedical imaging of living cells and *ex vivo* tissues. Of note, in biological samples with high autofluorescence such as aged brain tissue containing high concentrations of yellow-brown lipofuscin pigment from old neurons, the normally weak two-photon fluorescence might transform to a significant blue-shifted (relative to the excitation wavelengths) signal which is superimposed on the CARS spectra.

Spontaneous Raman spectra in turn consist of a series of vibrational bands representing unique molecular fingerprints of chemicals, making them easier to interpret. Furthermore, spontaneous Raman spectroscopy has a cheaper experimental set-up in terms of lasers and optics compared to the complex and expensive CARS optical system. It is important to note that a faster acquisition speed of Raman imaging could be achieved using a line-scan Raman modality by projecting the laser beam into a line rather than a point. With this set-up, the sample is scanned line by line rather

than pixel by pixel leading to a short image acquisition time of just several minutes. Better optical sectioning in turn could be gained using confocal microscopes.

The aim of this chapter is to probe spatially resolved chemical composition of A β plaques and their microenvironment using spontaneous Raman micro-spectroscopy in unstained AD human brain samples with a particular focus on correlative imaging of individual chemical components of amyloid plaques. The use of confocal Raman micro-spectroscopy over CARS is chosen to be optimal for the study of AD brain tissue due to the biological importance of both the fingerprint and CH-stretch vibrational regions that contain chemical information about pathological protein and lipid signatures of abnormal brain function. Sub-micron spatial resolution achieved with confocal Raman is well-suited for visualization of plaques which are typically 50 μm in size. Application of hyperspectral image unmixing analysis to acquired multi-set Raman images of AD brain tissues will be a useful toolbox for comprehensive visualization of three hallmarks of AD together: inflammation, A β , and lipids, that could shed the light on the significance of their association with the progression of AD.

5.2. Method

5.2.1. Human tissue samples and tissue preparation

Human brain tissue was sourced from the Thomas Willis Oxford Brain Collection (TWOBC), which is part of the Medical Research Council (MRC) Brain Bank Network, with the ethical approval of the Research Tissue Bank provided by the Oxford Brain Bank (OBB) Access Committee. A total of 5 hippocampal and 6 cerebral cortex diseased samples were recruited from the hippocampus of five AD subjects and the frontal lobe of other six individuals, who at the time of death were affected by AD. As a control cohort, 2 hippocampal and 2 cerebral cortex control samples were collected from the corresponding brain regions of non-demented elderly subjects, which were not diagnosed with AD based on histological examination (see Table 5.1). The AD brain group received the neuropathologic diagnosis based on standard criteria for AD. Brain sections were fixed with formalin, paraffin embedded, sectioned into 5 μm thick slices and mounted on standard glass slides. For Raman micro-spectroscopy measurements, formalin-fixed-paraffin-embedded brain samples were prepared according to the following protocol:

1. Formalin fixed brain tissue (5 μm thick) slides were deparaffinized using a standard dewaxing protocol consisting of three consecutive steps: 1) heating at 60-70 $^{\circ}\text{C}$ in a pre-heated oven for 1h; 2) removing the paraffin in xylene (two cycles for 20 minutes each);

- 3) rehydrating in a sequence of 100%, 90% and 70% ethanol for 5 minutes each, followed by three times washing in distilled water for 5 minutes each.
2. Brain slices were covered with 1X phosphate buffered saline (PBS) and a standard glass coverslip was attached on top followed by nail varnish sealing applied around the edges of the coverslip.
3. After Raman measurements, the samples were reopened and stained with Thioflavin S (Th-S) dye, which is a well-established indicator of A β plaque regions (Kelenyi 1967). For Th-S staining, brain slides were incubated in 1x PBS/1 % (m/v) Th-S solution for 10 minutes, followed by differentiation cycles with 80%, 95% ethanol for 2 minutes each and subsequent three times washing in PBS for 5 minutes each.

Table 5.1: Clinical characteristics of study participants. M = male; F = female, Control = non-demented control; AD = Alzheimer's disease.

Case Number	Age in years	Gender	Neuropathological diagnosis	The degree of Alzheimer's disease pathology (Hyman <i>et al.</i> 2013)	Brain region
Ah1	92	F	AD	Severe	Hippocampus
Ah2	87	F	AD	Severe	Hippocampus
Ah3	73	M	AD	Moderate	Hippocampus
Ah4	70	M	AD	Mild/Moderate	Hippocampus
Ah5	85	F	AD	Moderate	Hippocampus
Ac1	75	M	AD	Moderate	Frontal Lobe
Ac2	82	F	AD	Severe	Frontal Lobe
Ac3	85	F	AD	Severe	Frontal Lobe
Ac4	80	M	AD	Moderate	Frontal Lobe
Ac5	76	M	AD	Moderate	Frontal Lobe
Ac6	77	M	AD	Moderate	Frontal Lobe
Ch1	59	M	Control	Normal	Hippocampus
Ch2	61	F	Control	Normal	Hippocampus
Cc1	64	M	Control	Normal	Frontal Lobe
Cc2	60	F	Control	Normal	Frontal Lobe

In the course of this study chapter, I refer to AD and non-demented control (C) samples, each of which represents an individual, as Ah1, ..., Ah5 and Ch1, Ch2, respectively, examined in the hippocampus; and as Ac1, ..., Ac6, and Cc1, Cc2, examined in the frontal lobe of the cerebral cortex. A total of 61 A β plaques were investigated: 30 in the five hippocampal brain samples and 31 in the six cerebral cortex samples from the 11 AD individuals. Specifically, there were: 10, 9, 5, 1, and 5 plaques in the Ah1, Ah2, Ah3, Ah4, and Ah5 hippocampal samples, respectively; and 3, 13, 7, 2, 3, and 3 plaques in the Ac1, Ac2, Ac3, Ac4, Ac5, and Ac6 cortical samples.

5.2.2. Point-scan Raman micro-spectroscopy instrumentation

Raman imaging was carried out using a home-built multimodal laser-scanning microscope based on an inverted Nikon Ti-U stand, coupled to a Horiba Jobin-Yvon iHR 550 imaging spectrometer (300 grooves/mm grating) and an Andor CCD Newton DU-971N-BV detector (1600 × 400 pixels, 16 μm pixel size). A laser source (Laser Quantum GEM 532 nm, 2W) was used for excitation. The 532 nm laser excitation was filtered by a Semrock LL01-532 clean-up filter and coupled into the microscope by a dichroic mirror (Semrock LPD01-532RS). Raman scattering was collected in epi-direction, filtered with a long pass filter (Semrock BLP01-532R), and dispersed by the imaging spectrometer. The spectral resolution of the system was 4.9 cm⁻¹ with 30 μm width of the spectrometer entrance slit, and the detector length enabled to cover a spectral range (330, 4050) cm⁻¹. Raman images (about 50×50 μm²) for all brain samples were collected by raster-scanning the laser beam over a region of interest with a step size of 1 μm resulting in 50×50×1600 points hyperspectral Raman image (see an illustration of the hyperspectral Raman data cube in Fig. 5.2A) with a 1 second exposure time per Raman spectrum. Most Raman images were taken with a nominal laser power of 50 mW at the sample. Note that during data processing each image was normalized according to its laser energy which is (the laser power) × (the exposure time), making the Raman intensities comparable between samples. All images were collected using a 20× 0.75 NA dry objective (Nikon MRD00205) and a 1× tube lens. Confocal Raman imaging was provided by a horizontal slit (Thorlabs VA100), and the vertical input slit of the spectrometer. The estimated spatial resolution was 0.5 μm in-plane and 1 μm axially.

Prior to Raman measurements, an overview image for each sample across 10.4 × 6 mm², made of 24 × 18 tiles with 0.43 × 0.33 mm² tile size, was acquired using differential interference contrast (DIC) (see Fig. 5.1A for an example of such DIC image). In the DIC, a de-Senarmont compensator provided a phase offset of 20 degrees and a 0.72 NA dry condenser (Nikon MEL56100) with a DIC module (Nikon MEH52400) was used for illumination, combined with a matched DIC slider (Nikon MBH76220) in the objective, giving a shear of about 0.24 μm. A Hamamatsu ORCA 285 camera (1344 × 1024 pixels of 6.45 μm size) at 100 ms frame exposure time was used for detection at lowest gain (4.45 photoelectrons/count).

For fluorescence imaging of the Th-S stained brain samples, wide-field epi-fluorescence was performed using the same microscope stand, a Prior Lumen 200 (standard) 200W fluorescence illuminator light source, and a filter set consisting of a single band exciter (Semrock FF01-370/36) transmitting 352-388 nm, a single band dichroic (Semrock FF409-Di03) at 409 nm, and a single band emitter (Semrock FF02-447/60) transmitting 417-477 nm. Each image was collected with 200 ms exposure time and 10% lamp power.

5.2.3. Hyperspectral Image Unmixing analysis

Hyperspectral Raman data were analysed using a Quantitative Hyperspectral Image Unmixing (Q-HIU) method, consisting of the following main steps (see Chapter 3 for details). Firstly, the data were noise-filtered using Singular Value Decomposition with Automatic Divisive Correlation (SVD-ADC), enabling to remove components which are identified as noise using Pearson's auto-correlation coefficients for spatial and spectral singular vectors at one-pixel shift. Components with a mean Pearson's auto-correlation coefficient less than 50% were assigned to noise and therefore filtered out. Secondly, broad features in the Raman spectra, which represent fluorescent background, were subtracted using Bottom Gaussian Fitting (BGF) with a standard deviation (STD) of 900 cm^{-1} . Spatial points, for which the spectrally integrated background dominates (see Fig. A-22 and Fig. A-44 of Appendix A), were excluded from the analysis using the spatially-resolved Pearson's auto-correlation coefficients for background-corrected Raman intensity at one spectral pixel shift. The spatial points with the Pearson's coefficients less than 50% were attributed to noise-dominated and discarded. Finally, the efficient quantitative unsupervised/partially supervised non-negative matrix factorization (Q-US/PS-NMF) method via a fast combinatorial alternating non-negativity-constrained least squares algorithm was applied to the noise-filtered background-subtracted data. This algorithm (Lobanova and Lobanov 2019) factorizes the spectrally and spatially resolved data into a linear superposition of direct products of non-negative spatial concentration maps (matrix **C**) and corresponding non-negative spectra (matrix **S**), representing biochemical components of the samples' composition. For the reproducibility of the analysis, 20 repetitions with 20 000 iterations each were used during Q-US/PS-NMF. Each repetition converged to a local minimum of the factorization error. The final factorization expansion was selected as a pair of matrices (**C** and **S**) with minimum factorization error over 20 repetitions. In the factorizations to be presented in this chapter, the relative factorization error was about 2%. In order to compare the Raman concentrations of different chemical species between samples, the component spectra were normalized to have equal integrals, having a value chosen to result in a sum of the spatial concentrations with a mean of one.

In order to eliminate the contribution of wax residues to the spectral basis, the spectrum of the paraffin-wax compound, measured on one of the paraffin-embedded samples, was used as a fixed spectral component in the Q-US/PS-NMF. The Raman spectrum of wax is also shown in Appendix A (Fig. A-11 and Fig. A-32), together with the results of hyperspectral image unmixing analysis of hippocampal and cortical brain tissues.

To quantify the correlation of chemical components, received from the factorization analysis of Raman data, the Pearson's correlation coefficient R was calculated for spatial pixel concentrations

of each pair of individual components within each sample, representing a case subject. A significant correlation is considered with a p -value of <0.05 . The pairwise difference in mean and median concentrations of each component (C1...C5) between AD and non-demented populations of the hippocampal or cortical brain regions was tested by the two-sample two-tailed t -test for unequal variances (for mean concentration) and the Wilcoxon rank sum test (for median concentration), respectively. A p -value of <0.05 was considered statistically significant.

5.3. Results and discussion

Label-free confocal Raman micro-spectroscopy was used to investigate the biochemical composition of A β plaques and their bioenvironment in human AD brain tissues from the hippocampus and frontal lobe. The Q-HIU data analysis was performed simultaneously on all data of a given type of brain region (i.e. hippocampus or cortex), providing a direct comparison of spatial concentration profiles of chemical components in diseased and control samples. The idea of decomposition of a typical Raman image with A β plaque into individual chemical components with spatially-resolved Raman concentration and spectral profiles using Q-HIU analysis is shown in Fig. 5.1C.

To identify A β plaques, the brain samples were stained with Th-S (the well-established dye for identifying amyloid fibrils (Kelenyi, 1967)). To avoid the potential impact of the labelling artefacts and fluorescence background, the staining was performed *after* Raman imaging. To find potential areas containing plaques on label-free AD samples, I utilized large-scale DIC images (see example of this image in Fig. 5.1A). DIC contrast helped to identify potential A β plaques regions, which were used for the area selection for Raman measurements of label-free AD samples (see Fig. 5.1B). To validate that these regions are plaque-positive, I performed fluorescence microscopy of the measured areas on the same samples stained with the Th-S dye *after* Raman imaging on the label-free samples.

Intermediate steps of the Q-HIU data analysis on 38 Raman micro-spectroscopy images of cortical brain tissues in AD together with non-demented controls are shown in Fig. 5.2. Specifically, Fig. 5.2D shows the autocorrelation coefficients map for singular vectors received from the SVD-ADC analysis of 38 Raman images, labelled according to the sample source. The dotted diagonal line represents a decision line of a 50% cut-off for mean autocorrelation coefficients, that separates the coefficients above the line (circled cross signs – meaningful components) from those below it (cross signs – noise) as shown in Fig. 5.2D. Note that read-noise and shot noise are localized around zero, whereas physically meaningful components show high mean autocorrelation. For this

data, SVD-ADC with a 50% cut-off of mean autocorrelation coefficients has defined an approximating matrix, consisting of 36 singular components. To verify this number, I consider the spatial distribution and corresponding spectra for two singular vectors with the autocorrelation coefficients 25% lower and higher of 50% value (Fig. 5.2E-F). For a pair of discarded singular vectors, corresponding to 45% mean autocorrelation, spatial maps do not show any recognised pattern, and spectrum resembles noise, whereas for a pair of meaningful singular vectors with 75% mean autocorrelation, spatial maps show some colocalized features, and spectrum exhibits several clear Raman bands. To show the accuracy of SVD-ADC, I give the results of this method for two points from a typical cortical sample with high (B) and low (C) fluorescent background in Fig. 5.2B-C. As can be seen in the insets of Fig. 5.2B-C, SVD-ADC method allows to significantly reduce the noise from the image.

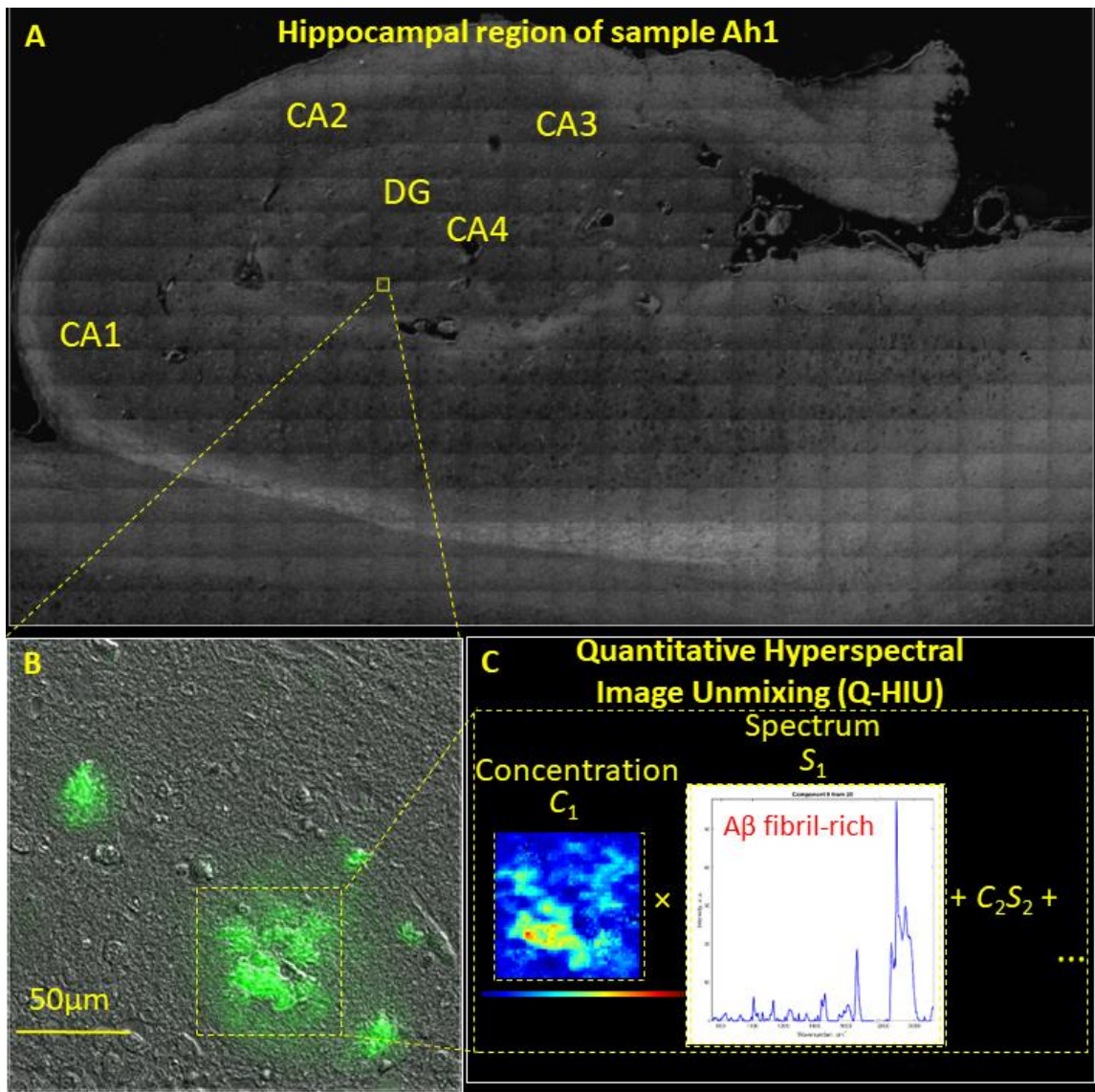


Fig. 5.1. Large-scale DIC image of the hippocampus of sample Ah1 (A). The region of interest outlined by square (dashed line) measured by Raman micro-spectroscopy and post-proved to contain $A\beta$ plaque (B). The chemical decomposition of this Raman image into individual chemical components with spatially-resolved Raman concentration and spectral profiles using the Q-HIU data analysis (C).

Also, Fig. 5.2B, C shows an example of BGF algorithm applied to the same Raman image, received from the SVD-ADC. The Raman spectra at two spatial pixels with high (B) and low (C) fluorescent background before (blue line) and after (green line) background removal with the representative bottom Gaussian fit (red line) are demonstrated in Fig. 5.2B-C. Similarly, as can be seen in the insets of Fig. 5.2B,C, the BGF algorithm allows to accurately subtract a fluorescent background from this image, even when a fluorescent background is about two orders of magnitude larger than the Raman signal (Fig. 5.2B).

The final step of the Q-HIU data analysis is Q-US/PS-NMF. Applied to separate factorization analysis of the Raman images of a given type of brain region (i.e. hippocampus or cortex), I identified that all Raman images are well represented using 20 separate components. When selecting 19 components, the Q-US/PS-NMF algorithm was checked to show a higher factorization error, whereas for 21 components the Raman spectrum of an additional component appeared to be less meaningful spectrally representing the split protein component from the previous analysis with 20 components. For both analyses, the chemical components, which attribution has been identified, are summarised in Table 5.2.

In the hippocampal brain regions, five of the 20 components were found to spatially colocalize with A β plaques, and exhibited spectra resembling those of known chemical species, which I will discuss in the course of this study chapter. In the cortical brain regions, four of these hippocampal components were reproduced, and furthermore a new component (C7) colocalizing with plaques was observed. The other 15 components were found not to significantly colocalize with A β plaques. Their attribution is given as follows. Two components in both analyses were found to be correlated with the Raman spectra of chemical constituents of glass substrate, and one component was found consistent with the Raman spectrum of water using an ID expert tool of Bio-Rad's KnowItAll Vibrational Spectroscopy software with Raman Spectral Libraries, where the degree of similarity between each component spectrum and corresponding reference spectrum is given by a correlation coefficient (R^2) (in %). Note, to avoid contamination with meaningful chemical components, wax component was fixed prior to the Q-US/PS-NMF analysis. Its Raman spectrum was measured on one of the paraffin-embedded sample and verified to be consistent with the Raman spectrum of wax (C11 in the hippocampus and C10 in the frontal lobe, $R^2 = 99\%$ for both analyses). Their Raman spectra and corresponding concentration profiles in the brain samples as retrieved from two separate Q-US/PS-NMF analyses with 20 components on Raman images from a given type of brain region (i.e. hippocampus or cortex) are given in Appendix A. In the course of the next sections, I will focus on the description and attribution of the chemical components, which are found to significantly colocalize with A β plaques. For the hippocampal brain regions, I

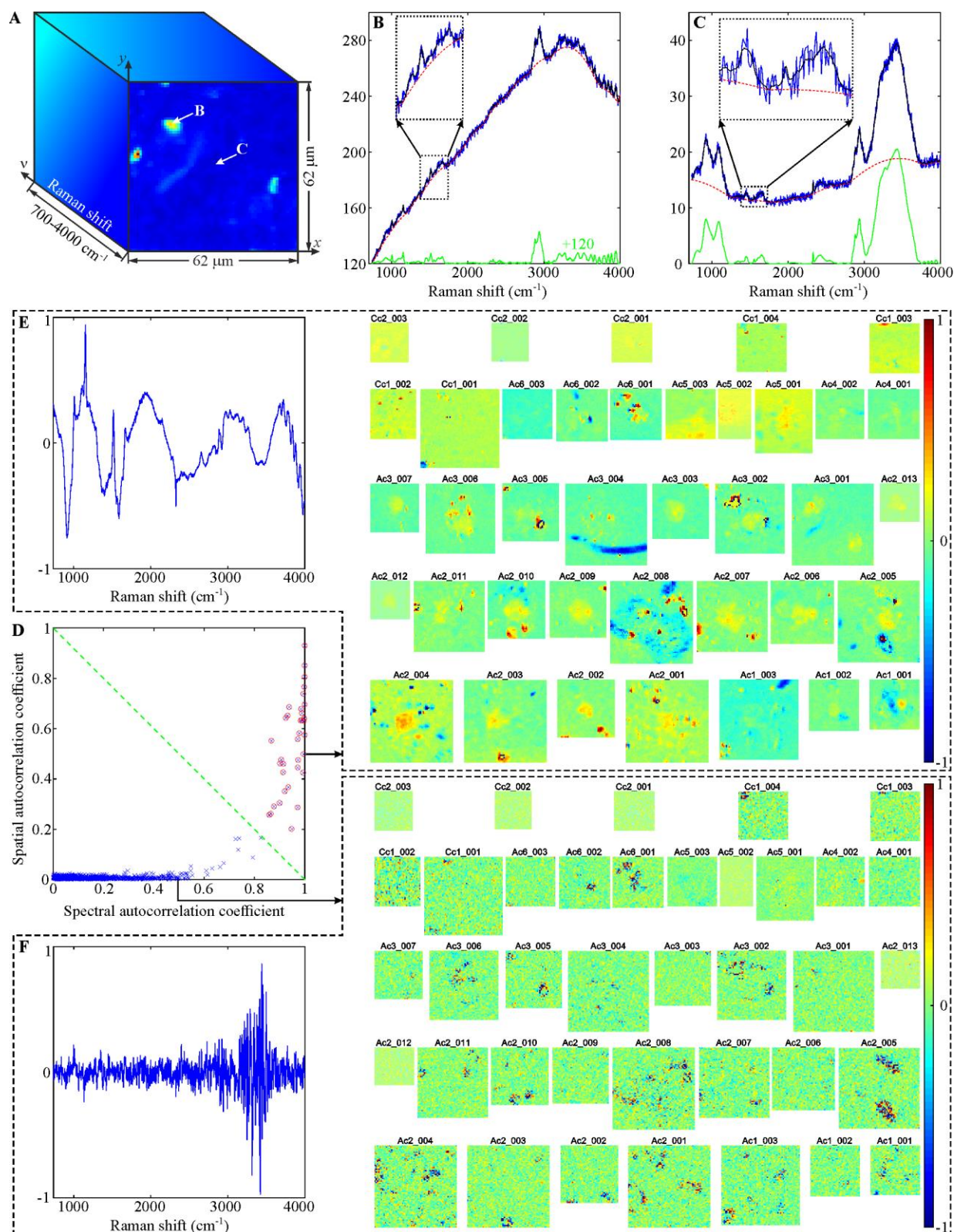


Fig. 5.2: Schematic of a hyperspectral Raman cube (A). The arrows with letters B and C mark two pixels, Raman spectra of which are shown on the panels B and C, respectively. The input Raman spectrum (blue line) before the SVD-ADC and the corresponding noise-filtered Raman spectrum (black line) after this procedure (B-C). The results of background subtraction using the bottom Gaussian fitting is shown by the green line: the bottom Gaussian fit (red dashed line) is subtracted from the noise-filtered Raman spectrum, giving background-free Raman spectrum. Spatio-spectral autocorrelation coefficients map of singular vectors resulted from SVD-ADC (D). The dotted diagonal line represents a decision line of $R_{th} = 50\%$ cut-off for mean autocorrelation coefficients R_i , separating the coefficients above the line (circled cross signs – meaningful components) from those below it (cross signs – noise). The spatial distribution and corresponding spectra of two singular vectors with the mean autocorrelation coefficients with values

$\cong 75\%$ and $\cong 25\%$ as indicated on the panel D (E-F). On both panels, 38 Raman images are labelled according to the sample source and represents cortical regions.

will examine in detail C4, C9, C10, C16, C17. Similarly, for the cortical brain regions, I will discuss C4, C7, C11, C16, C20. Note, in the following, I will sort these components by decreasing mean Raman concentration.

Table 5.2. Chemical component attribution retrieved from two separate Q-US/PS-NMF analyses with 20 components on Raman images from a given type of brain region (i.e. hippocampus or cortex).

Chemical component attribution	R^2 for component number C# retrieved from the Q-US/PS-NMF analysis with 20 components	
	Hippocampus	Frontal lobe
glass	98% (C1)	98% (C2)
BaO (glass)	98% (C2)	92% (C1)
collagen	(C4)	not found
water	85% (C6)	77% (C9)
A β ₁₋₄₂ fibrils + cholesteryl palmitate	84% - fingerprint (C9)	78% - fingerprint (C4)
fibrin + arachidic acid	90% (C10)	90% (C11)
β -carotene	82% (C16)	86% (C16), (C13)
Fe ₃ O ₄	93% (C17)	89% (C20)
calcium phosphate	not found	93% (C7)
wax	99% (C11)	99% (C10)
SiO ₂	89% (C19)	not found

5.3.1. Chemical composition of hippocampal A β plaques: key chemical components

Fig. 5.3 shows the Raman spectra of the 5 chemical components colocalized with A β plaques, as found from the Q-US/PS-NMF data analysis on 30 unstained hippocampal A β plaques (from 5 AD patients) together with 10 control Raman maps (from 2 elderly humans without AD) in the fingerprint (736-1780 cm⁻¹) and CH-stretch (2793-3122 cm⁻¹) regions. The ranges below 736 cm⁻¹ and above 3200 cm⁻¹ are dominated by fluorescence and Raman scattering from the glass slide/cover slip and Raman scattering from water, respectively, and therefore were excluded from the Q-US/PS-NMF analysis to avoid their interference with the chemical components, which are relevant for my study. For identification of chemical components' assignments, I used Bio-Rad's KnowItAll Vibrational Spectroscopy software with the Raman Spectral Libraries as a guide. Once I found the chemical assignment with this software, I compared the Raman spectra of the identified standards with the representative component spectra retrieved from my analysis using NLS algorithm as shown in Fig. 5.3. These comparisons revealed that 4 components can be spectrally assigned to a mixture of fibrillar A β ₁₋₄₂ and saturated lipids with cholesteryl derivatives such as cholesteryl palmitate at a ratio of about 4:1 (C9, $R^2 = 84\%$, Fig. 5.3B); a mixture of fibrin and arachidic acid at a ratio of about 4:1 (C10, $R^2 = 90\%$, Fig. 5.3C); β -carotene (C16, $R^2 = 82\%$, Fig. 5.3D); Fe₃O₄ (C17, $R^2 = 93\%$, Fig. 5.3E).

In the following, I will discuss the characteristic Raman bands of the identified chemical components C4, C9, C10, C16 and C17, which are found to be associated with the A β plaques regions in AD brains based on their spatial concentration profiles. The summary of key Raman vibrational bands, reflecting the presence of A β pathology and oxidative damage in AD human brains, as retrieved from this research study is given in Table 5.3.

The spectrum of C4 displays a numerical number of characteristic bands, such as the Raman bands at 1657 cm⁻¹ (Amide I, α -helix), 1554 cm⁻¹ (Amide II), 1338 cm⁻¹ (CH₂ wagging vibrations from glycine (Gly) backbone and proline (Pro) side chain), 1267 cm⁻¹ (Amide III), 1206 cm⁻¹ (hydroxyproline (Hyp) and tyrosine (Tyr)), 1031 cm⁻¹ (Pro), 1002 cm⁻¹ (phenylalanine), 934 cm⁻¹ (C-C backbone), 852 cm⁻¹ (Pro, Hyp, Tyr), which are all assigned to the Raman bands of collagen (Movasaghi *et al.*, 2007). Additionally, the Raman spectrum exhibits a unique band at 1705 cm⁻¹, indicative for the C=O stretching vibration in amino acids. I suggest that this Raman band observed in C4 spectrum might be originated from the Gly-Pro-X and Gly-X-Hyp sequence (where X is any amino acid), which are the most common motifs of collagen.

Indeed, there are convincing data that senile plaques extracted from AD human brains contain CLAC component, which was found to be associated with collagen XXV (Hashimoto *et al.* 2002). As

confirmed by *in vitro* studies, a collagen-like triple-helical peptide can attenuate the nucleation and fibril growth of the amyloidogenic peptide (Parmar et al. 2012). In relation to the C=O vibration observed in the Raman spectrum of C4, the same study suggested that the C=O moieties in repeating Gly-Pro-Hyp sequences within the triple-helix collagen can bind to the backbone amides or to the glutamine/asparagine side chains of the amyloidogenic peptide and reduce its nucleation. The further link between collagen and amyloid has been indicated with the observation of the neuroprotective potential of collagen VI against A β neurotoxicity, which is able to inhibit the association of A β oligomers with neurons, protect A β plaques from dissolving into toxic amyloid species (Cheng et al. 2009).

Table 5.3. The summary of key Raman vibrational bands indicative of A β pathology and oxidative damage resulting from the hyperspectral image unmixing analysis of Raman images of post-mortem AD human brains in the hippocampus and cortex.

Raman shift, cm ⁻¹	Molecular vibration	Chemical assignments	Potential role in AD pathogenesis, indicative of
1673	C=O (Amide I)	β -sheet proteins	pathogenic A β protein
	C=C	cholesterol	interaction with A β fibrils
	C=C	E-unsaturated FAs in <i>trans</i> -configuration	lipid peroxidation and induced pro-inflammatory cascade through ROS generation
1705	C=O	triple-helix in collagen	binding site to A β peptide (attenuate nucleation)
970	PO ₄ ³⁻	calcium phosphate crystals	mitochondria damage, activation of the NLRP3 inflammasome
1007, 1154 1518	C-CH ₃ , C-C, C=C	β -carotene	inflammation and oxidative stress
1320	Fe ₃ O ₄	ferritin	promotion of A β oligomer assembly and oxidative damage
2884, 2852	CH ₂ asymmetric and symmetric stretch	FAs	an acyl chain order (I_{2884}/I_{2852}), pronounced for saturated lipids

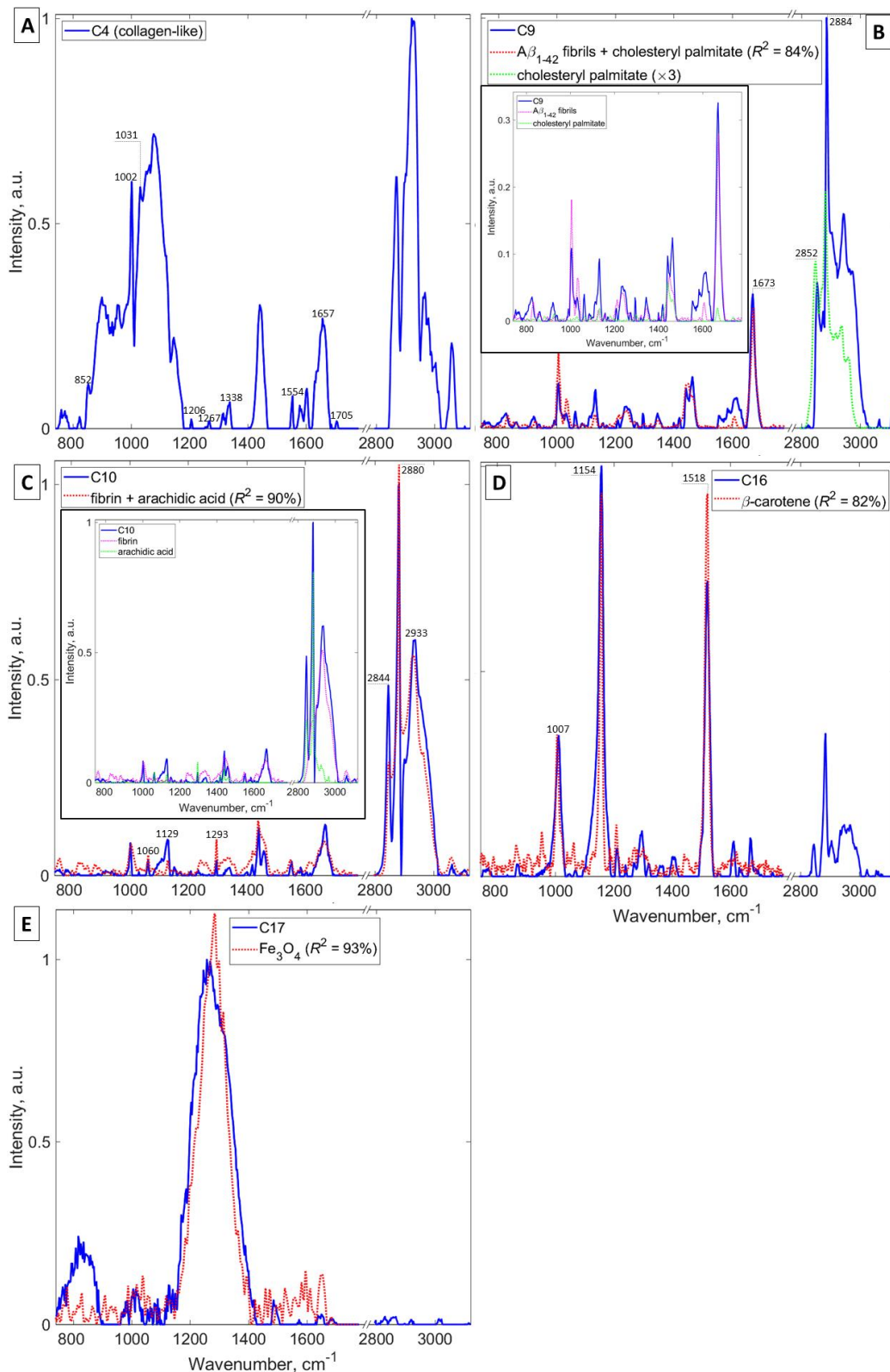


Fig. 5.3: Raman spectra of the chemical components (blue solid lines) colocalizing with hippocampal A β plaques, obtained from the simultaneous Q-US/PS-NMF analysis of 30 hippocampal A β plaques (5 AD patients) together with 10 control Raman maps (2 elderly humans without AD). C4 (A) has spectral characteristics resembling collagen XXV (see text). C9 (B) is a mixture of aggregated A β ₁₋₄₂ peptides and saturated lipids with cholesteryl derivatives. C10 (C) is a mixture of fibrin and arachidic acid. C16 (D) is attributed to carotenoids. C17 (E) is attributed to iron oxide. The chemical attribution of components C9, C10, C16 and C17 is based on the comparison with analytical standard Raman spectra of pure chemical species. Fits are shown by the red dotted lines and found using NLS algorithm. Corresponding R^2 are also indicated. The fit in (B) is a superposition of the Raman spectrum of synthetic A β ₁₋₄₂ fibrils (magenta line) and cholesteryl palmitate (green line); the contributions are separately shown in the inset for the fingerprint region. The fit in (C) is a superposition of fibrin (magenta line) and arachidic acid (green line); the contributions are shown in the inset. The red line in (D) is the Raman spectrum of β -carotene. The red line in (E) is the Raman spectrum of Fe₃O₄.

The spectra of C9 and C10 exhibit several bands in both the fingerprint and CH-stretch regions, which are assigned to a mixture of proteins and lipids with different molecular structure. Specifically, the fingerprint region of C10 displays Raman bands at 1060, 1129, and 1293 cm^{-1} , assigned to the C-C skeletal stretching vibrations, and the CH_2 twisting mode of fatty acids, respectively (Krafft *et al.* 2005; Czamara *et al.* 2015). Its attribution to a saturated lipid in the solid phase is supported by co-presence of a strongly pronounced 2880 cm^{-1} band in the CH-stretch region, which is represented by the asymmetric CH_2 stretch enhanced by the Fermi resonance interaction with the overtones of CH_2 and CH_3 deformations, compared with a relatively weak band around 2933 cm^{-1} , which is attributed to a combination of CH_3 and CH_2 asymmetric vibrations enhanced by the broadening and shift of the CH deformations in the liquid phase (DiNapoli *et al.*, 2014). These observations combined with the assignment with the Raman spectra of analytical standards using NLS fitting algorithm allowed me to assign the spectrum of C10 to a mixture (red dotted line) of 79% fibrin (magenta line) (Jain *et al.* 2014) and 21% arachidic acid (green line) (Czamara *et al.* 2015) in both the fingerprint and CH-stretch regions. This assignment is consistent with the previous studies revealing deposition of fibrin in $\text{A}\beta$ plaques of AD mouse brains (Paul *et al.* 2007). Furthermore, the same study has indicated that fibrin can promote neuroinflammation in AD brains, possibly accelerating neuronal damage. Similarly, my study reveals the co-presence of arachidic acid, indicative of oxidative damage in tissue, with fibrin within the $\text{A}\beta$ plaque regions of human AD brains.

I was able to identify an acyl chain order (i.e., an estimate of the lipid viscosity) in the Raman spectrum of C9 according to the ratio between the intensity at 2884 cm^{-1} (the CH_2 asymmetric stretch) and 2852 cm^{-1} (the CH_2 symmetric stretch) (Kiskis *et al.* 2015). I found that this ratio for C9 was twice as high as that for C10, thereby indicating a high proportion of saturated lipids in C9. Importantly, Raman spectrum of C9 has a strong band at 1673 cm^{-1} , which can be assigned to the superposition of the C=O stretching vibration of the protein backbone (Amide I band) from a β -sheet protein structure (Czamara *et al.* 2015), with the C=C stretching vibration of cholesterol (Krafft *et al.* 2005), and the FA chain of *E*-unsaturated FAs in *trans*-configuration (Movasaghi *et al.* 2007). Interestingly, the generation of *trans* double bonds (near 1670 cm^{-1}) occurs as a result of conversion of *cis* double bonds (near 1655 cm^{-1}), that are not present in C9, in the process of lipid peroxidation (Muik *et al.* 2005). Together with the assignment with the Raman spectra of analytical standards using NLS fitting algorithm, the Raman spectrum of C9 in the fingerprint region can be well represented (red dotted line) by a mixture of 81% synthetic $\text{A}\beta_{1-42}$ fibrils (spectrum is available only in the fingerprint region (Dong *et al.* 2003)), which is a well-known aggregated component of $\text{A}\beta$ plaques with predominately β -sheet

protein structure (magenta line), and 19% cholesteryl palmitate (green line) (Czamara *et al.* 2015). For the CH-stretch region, the Raman spectrum of C9 is found to be consistent with the reference spectrum of cholesteryl palmitate, which also conform with its high acyl chain order typical for saturated lipids as I showed above. Therefore, I assigned C9 to a mixture of A β ₁₋₄₂ aggregated protein with a high-content of the β -sheet structures, and cholesteryl derivatives with saturated long-chain FA chains, representing lipid aggregates. The co-presence of pathogenic fibrillar A β ₁₋₄₂ protein with saturated cholesteryl esters within one resolved chemical component might indicate the interaction of these species in AD brain tissues.

The fingerprint region of C16 exhibits three sharp bands at 1007 cm⁻¹, 1154 cm⁻¹, and 1518 cm⁻¹, which can be attributed to the methyl rocking vibrational mode, C-C, and C=C in-phase stretch vibrations of the polyene chain, respectively, all indicative of carotenoids (Radu *et al.*, 2016). Furthermore, the relative intensities of these Raman bands are similar to those for pure β -carotene (red dotted line), therefore confirming its attribution to β -carotene. It is important to note that this component is strongly pronounced in cortical plaques, as will be discussed in the next sections. According to the current stage of knowledge, average carotenoid concentrations in AD and non-demented control tissues from the frontal lobe and occipital cortex have been measured, and for β -carotene these concentrations were 4.5 ng/g in AD brains and 5.5 ng/g in normal elderly ones. However, the information about its spatial distribution and correlation with A β plaques is still missing. Furthermore, the ultimate role of β -carotene and other carotenoids in free radical-affected diseases, including AD has not yet been elucidated (Stocker and Keaney 2004; Lloret *et al.* 2009). Despite being considered as a well-known anti-oxidant, *in vitro* studies reveal that β -carotene can show either anti- or pro-oxidant properties depending on its concentration and the oxygen partial pressure in tissue (Burton and Ingold 1983).

The Raman spectrum of C17 is found to be consistent with Fe₃O₄ (Glasscock *et al.*, 2008) (see red dotted line). According to the literature, the redox metal ions including iron has been detected in AD brains (Ramos *et al.* 2014). Since metal ions are chemically overactive with other molecules, they make the tissues significantly predisposed to oxidative damage. Furthermore, the recent study using electron holography showed that iron nanoparticles colocalize with the A β plaque cores (Plascencia-Villa *et al.*, 2016). Additionally, convincing data indicate a high binding affinity of metal ions to A β peptides (Zatta *et al.* 2009). This property of metal ions provides easy binding to A β species with formation of A β -metal complexes. Once the complex is generated, the A β -bound metal particles might influence the oligomerization of A β peptides (Zatta *et al.* 2009).

5.3.2. Spatial distributions of key chemical components in hippocampal A β plaques

In this section, I inspect and compare Raman concentration maps of the chemical components (C4, C9, C10, C16 and C17) across AD and non-demented patient groups in the hippocampal brain region. Fig. 5.4- Fig. 5.8 provide overview results of all unmixed Raman images, retrieved from the simultaneous Q-US/PS-NMF analysis of 30 hippocampal A β plaques (5 AD patients) together with 10 control Raman maps (2 elderly humans without AD). In order to investigate the spatial correlation of C4, C9, C10, C16 and C17 in A β plaques of different morphologies together with controls, I show representative examples of A β plaques of the following types: fibrillar (Fig. 5.9A, 70 \times 70 μm^2 from Ah1_001), cored neuritic (Fig. 5.9B, 60 \times 60 μm^2 from Ah2_001), core-only (Fig. 5.9C, 40 \times 40 μm^2 from Ah3_001) and diffuse neuritic (Fig. 5.9D, 50 \times 50 μm^2 from Ah4_001) plaques, together with two control regions (Fig. 5.9E, 64 \times 64 μm^2 from Ch1_001, and Fig. 5.9F, 50 \times 50 μm^2 from Ch2_001). Row 1 demonstrates fluorescence images acquired after staining with Th-S, and Row 2 shows DIC images of the same plaques collected before Raman measurements, with the white squares representing the areas of Raman imaging. Rows 4 to 8 show the Raman concentration maps of C4, C9, C10, C16 and C17, respectively, and Row 3 gives a blue-green-red overlay of the concentration maps of C4, C9, and C10. Note, relative Raman concentrations are obtained from the Q-US/PS-NMF analysis, by applying the normalization such that the mean total concentration is equal to unity (see Section 5.2.3 and Section 3.4 (Chapter 3) for details).

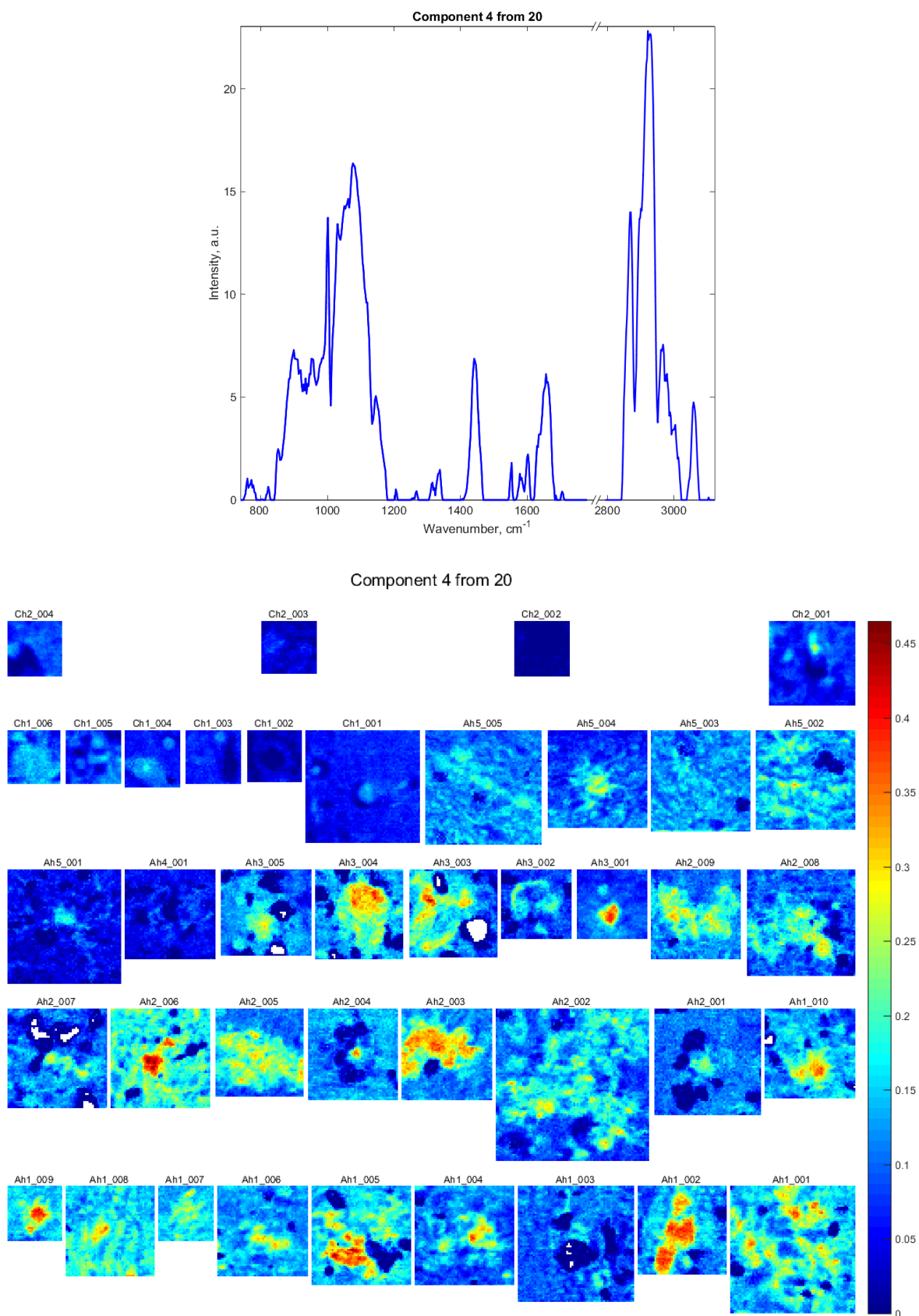


Fig. 5.4: Spatial distributions of the Raman concentration and the corresponding component spectra of $\mathbb{C}4$ for the measured AD hippocampal brain regions together with controls (labelled according to the sample source as Ah1,..., Ah5, and Ch1, Ch2, respectively) on colour scales as indicated, retrieved from the simultaneous Q-US/PS-NMF unmixing analysis of 30 hippocampal $A\beta$ plaques (5 AD patients) together with 10 control Raman maps (2 elderly humans without AD).

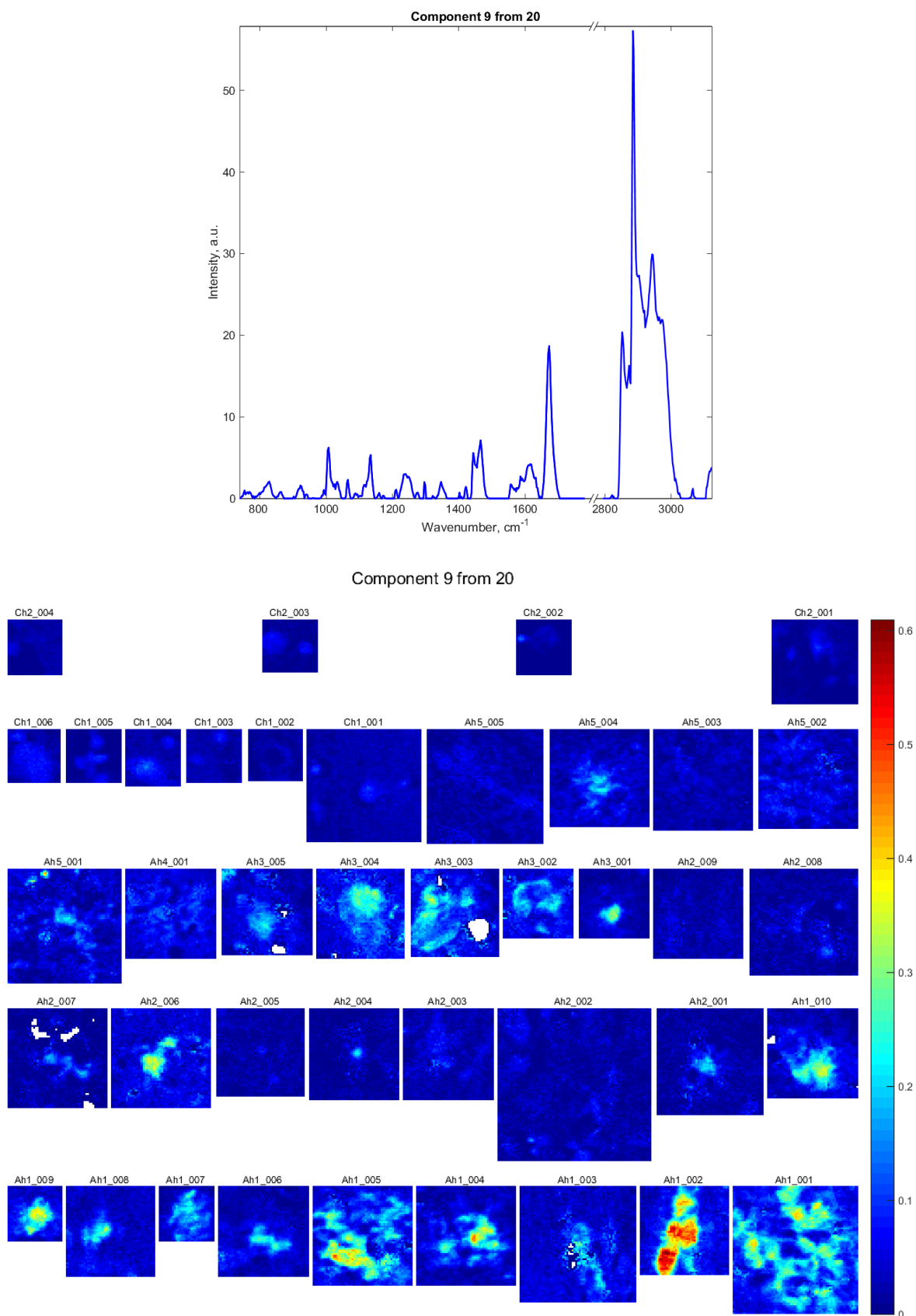


Fig. 5.5: Spatial distributions of the Raman concentration and the corresponding component spectra of C9 for the measured AD hippocampal brain regions together with controls (labelled according to the sample source as Ah1,..., Ah5, and Ch1, Ch2, respectively) on colour scales as indicated, retrieved from the simultaneous Q-US/PS-NMF unmixing analysis of 30 hippocampal A β plaques (5 AD patients) together with 10 control Raman maps (2 elderly humans without AD).

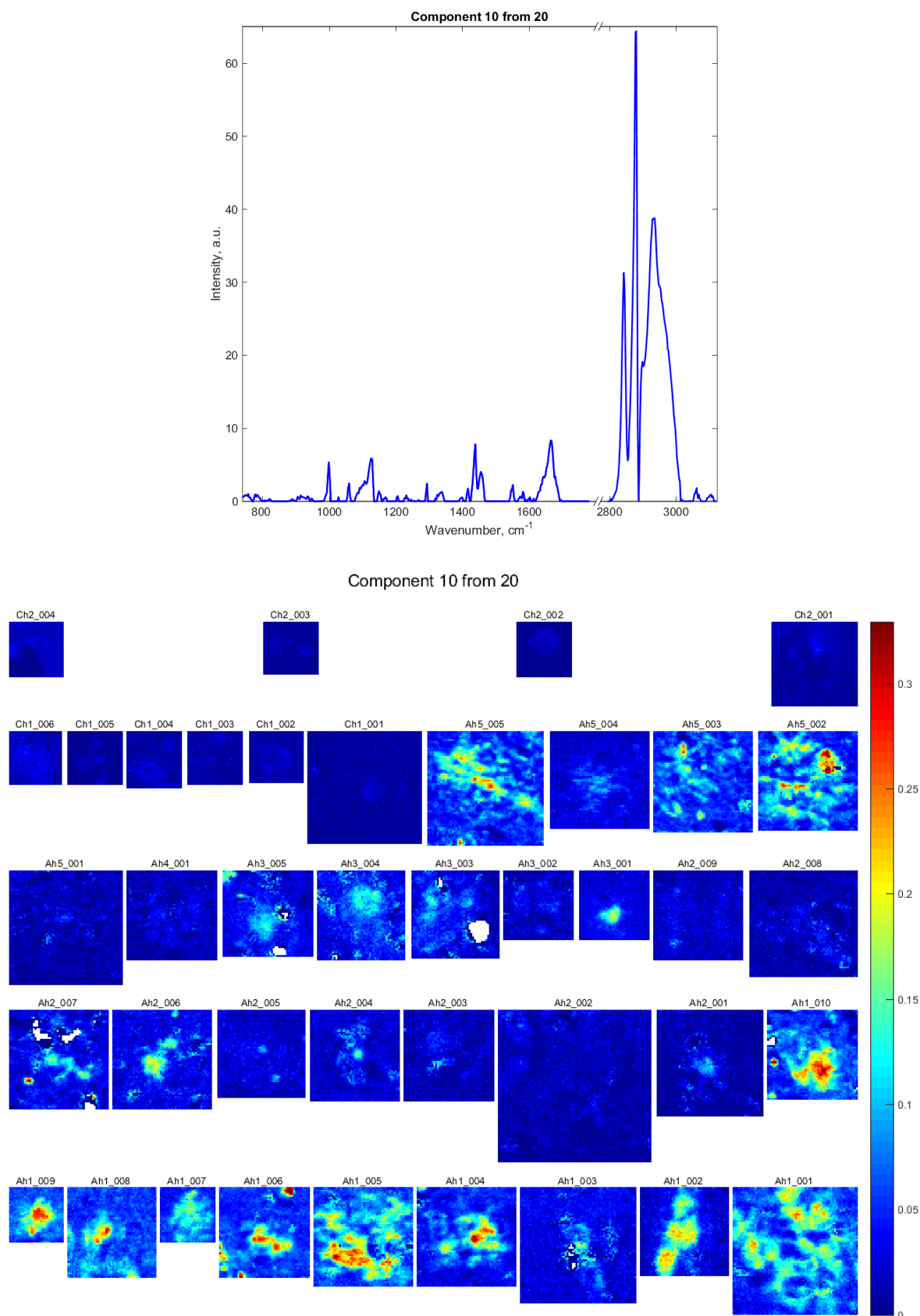


Fig. 5.6: Spatial distributions of the Raman concentration and the corresponding component spectra of C10 for the measured AD hippocampal brain regions together with controls (labelled according to the sample source as Ah1,..., Ah5, and Ch1, Ch2, respectively) on colour scales as indicated, retrieved from the simultaneous Q-US/PS-NMF unmixing analysis of 30 hippocampal A β plaques (5 AD patients) together with 10 control Raman maps (2 elderly humans without AD).

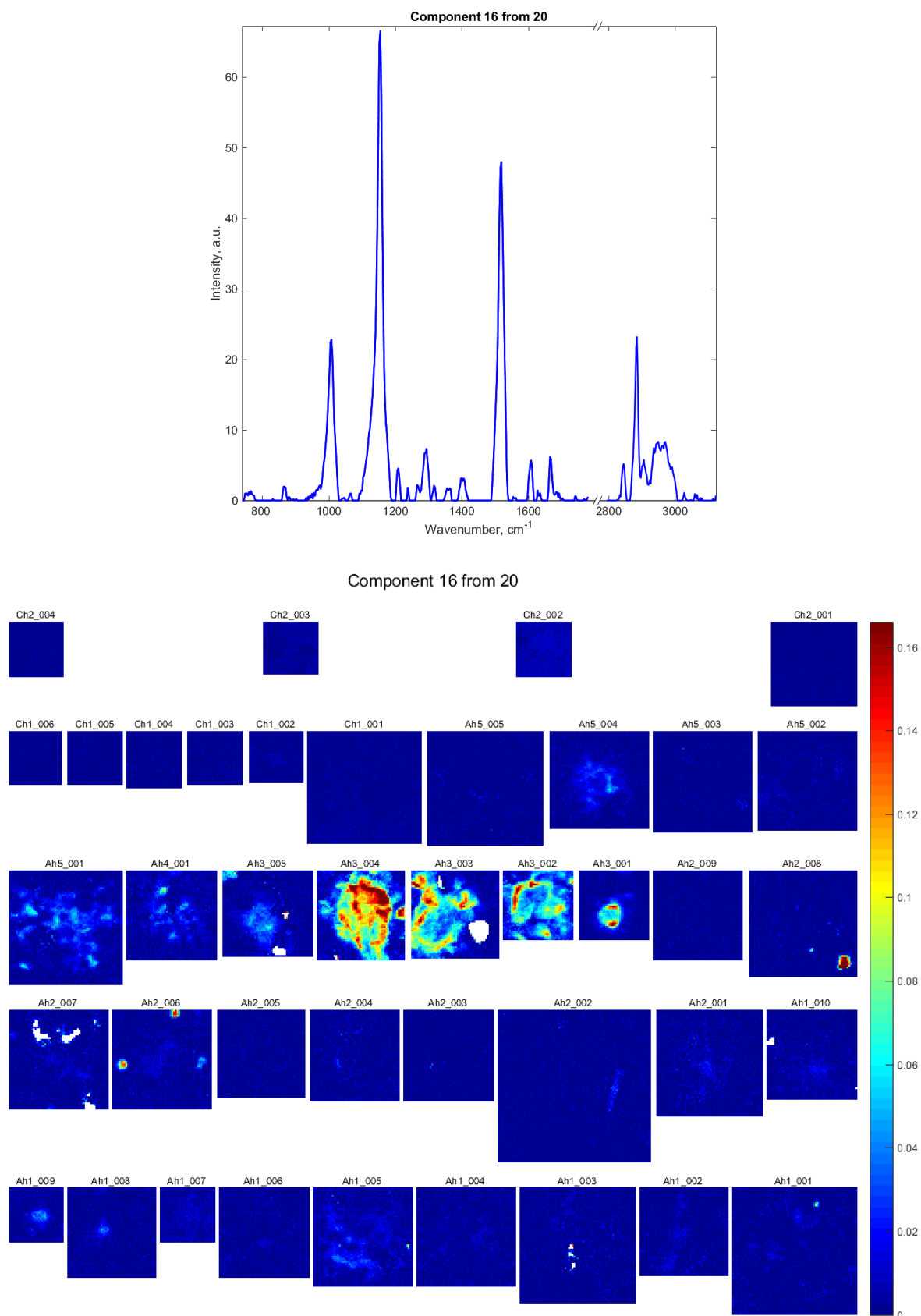


Fig. 5.7: Spatial distributions of the Raman concentration and the corresponding component spectra of C16 for the measured AD hippocampal brain regions together with controls (labelled according to the sample source as Ah1,..., Ah5, and Ch1, Ch2, respectively) on colour scales as indicated, retrieved from the simultaneous Q-US/PS-NMF unmixing analysis of 30 hippocampal A β plaques (5 AD patients) together with 10 control Raman maps (2 elderly humans without AD).

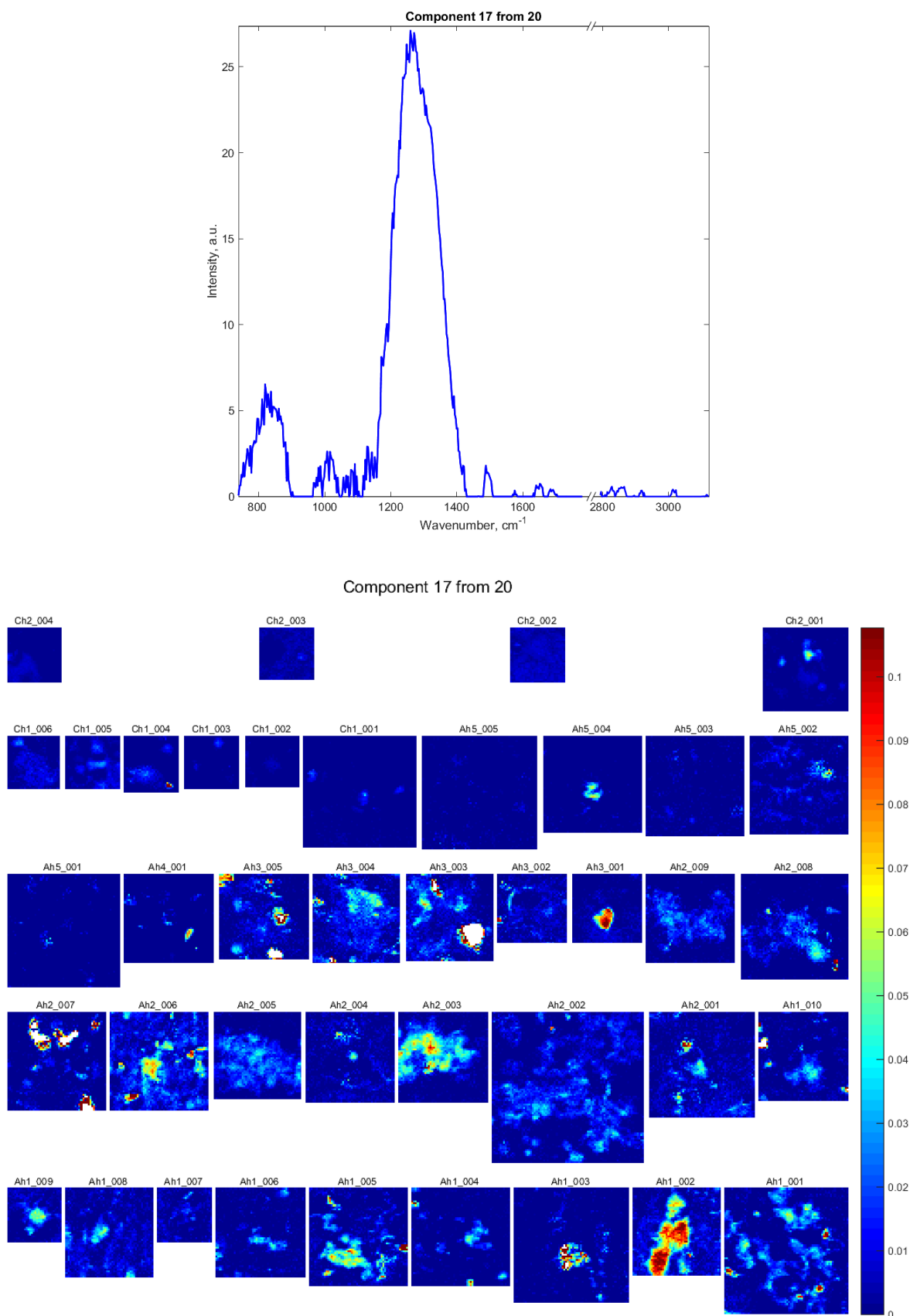


Fig. 5.8: Spatial distributions of the Raman concentration and the corresponding component spectra of C17 for the measured AD hippocampal brain regions together with controls (labelled according to the sample source as Ah1,..., Ah5, and Ch1, Ch2, respectively) on colour scales as indicated, retrieved from the simultaneous Q-US/PS-NMF unmixing analysis of 30 hippocampal A β plaques (5 AD patients) together with 10 control Raman maps (2 elderly humans without AD).

In general, the spatial concentration profiles indicate the increased accumulations of these components in the plaque areas compared to the control regions.

Notably, CLAC (C4) is found to be one of the main constituents of A β plaques with maximum concentrations of about 40%, 40%, 30%, and 20% for fibrillar, core-only, cored neuritic and diffuse neuritic plaques, respectively. This component is clustered in micro-domains of various sizes, which are linked to each other, forming one large structure of shape similar to the plaque. This can be clearly seen on the fibrillar plaque by comparing the concentration map of C4 (Fig. 5.9A4) with the fluorescence image of this plaque (Fig. 5.9A1). Notably, this collagen component is not observed in the oligomeric halo of the cored neuritic plaque, as seen by the void areas in its concentration map (Fig. 5.9B4). Similarly, fibrillar A β_{1-42} species and saturated lipids with high cholesteryl ester content, representing C9, are observed to be packed in multi-clusters, which in turn are bundled to each other, forming macro-aggregate, templating fibrillar plaque (Fig. 5.9A5-D5) (Kiskis *et al.* 2015). This amyloid/lipid compound is another main constituent of A β plaques with maximum concentrations of about 35%, 30%, 25%, and 20% for fibrillar, core-only, cored and diffuse neuritic plaques, respectively. C10, which is assigned to a mixture of fibrin and arachidic acid, is found to be specific to A β plaques in AD samples (Fig. 5.9A6-D6), since it is not observed for any control region corresponding to non-demented elderly brains (Fig. 5.9E6, F6). This protein-lipid component is strongly present in fibrillar and core-only plaques, where it accounts for 25% maximum concentration, compared to cored and diffuse neuritic plaques, where its concentration exhibits a peak of 15% just in a few pixels. As can be visually observed for the fibrillar plaque (Fig. 5.9A6), this mixed component is assembled in multi-domains, which co-localise with the plaque. β -carotene component (C16), in turn, accumulates in micro-scale clusters throughout the entire core-only (Fig. 5.9C7) and diffuse neuritic plaques (Fig. 5.9D7) only, where it accounts for about 25% and 15% maximum concentrations, respectively, compared to negligible concentrations for control regions (Fig. 5.9E7, F7). As can be seen from the concentration maps of iron oxide (C17) in fibrillar (Fig. 5.9A8) and core-only plaques (Fig. 5.9B8), this component is accumulated in uni-clusters ($\sim 2 \mu\text{m}$ in size), which are more pronounced at the outer rim of A β plaque.

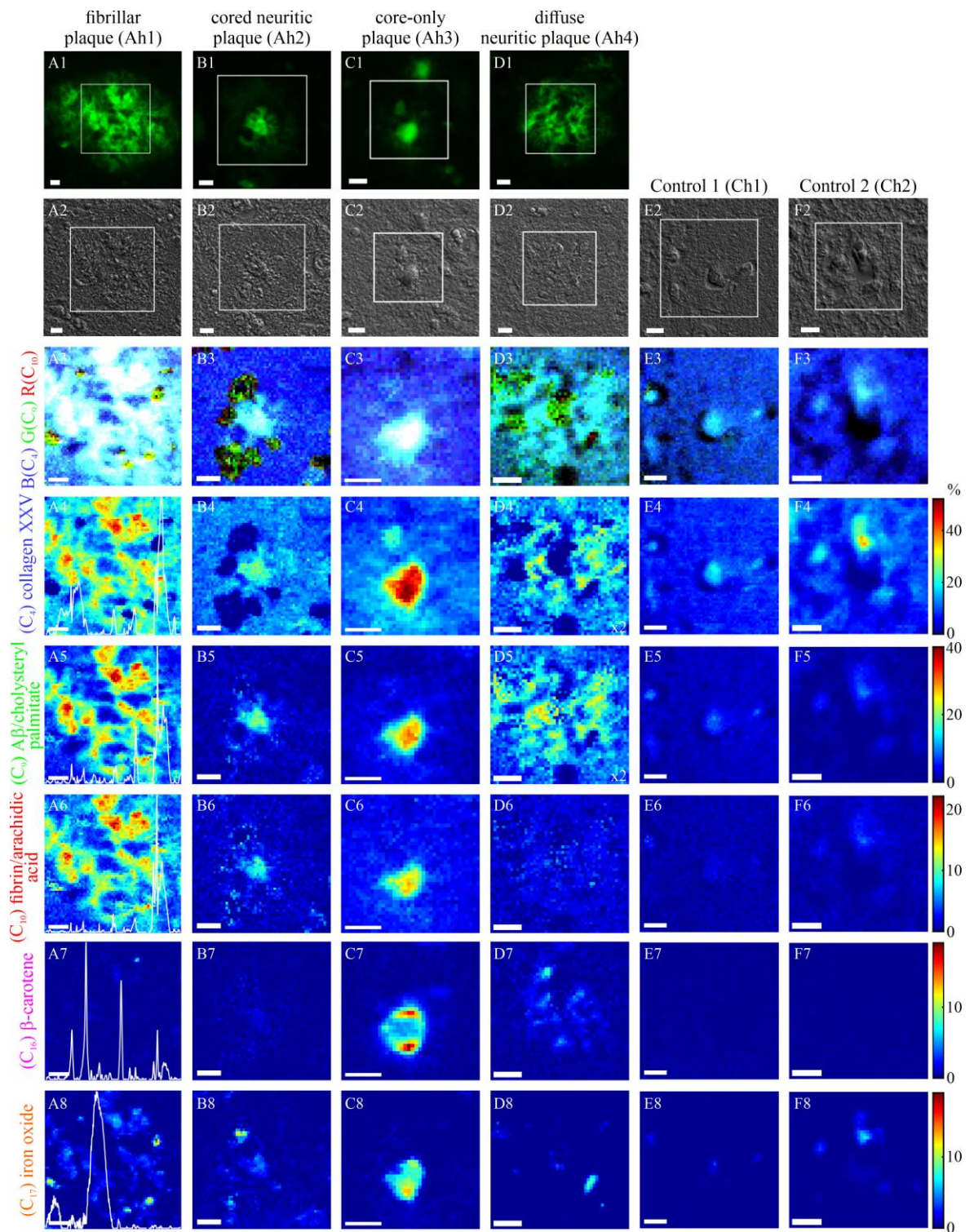


Fig. 5.9: Images of hippocampal A β plaques with different morphologies and non-demented control regions shown in jet colour scale: the fibrillar (A), cored neuritic (B), core-only (C) and diffuse neuritic (D) plaques referring to AD samples, labelled as Ah1_001, Ah2_001, Ah3_001, Ah4_001, respectively, and two control regions (E,F), corresponding to non-demented elderly individuals marked as Ch1_001, Ch2_001. Rows 1-2: the regions of Raman measurements, indicated by white square and visualized by DIC microscopy of the unlabelled samples (A2-F2) and by fluorescence microscopy of the plaque areas (A1-D1) after staining with Th-S. Row 3: pseudo-colour images for the A β plaques and control regions using C4 (collagen XXV) as blue, C9 (a mixture of fibrillar A β ₁₋₄₂ and saturated cholesteryl esters) as green, and C10 (a mixture of fibrin and arachidic acid) as red, scaled to saturate at 25% of maximum colour channel. Rows 4-8: spatial concentration profiles of the selected components, on colour scales as indicated. The Raman concentrations in panel D4, D5 is rescaled by a factor of two for visibility. The corresponding component spectra are indicated as white lines in the first column (see also Fig. 5.3). Scale bars: 10 μ m.

A pseudo-color image encoding the concentrations of $\mathbb{C}4$ in blue, $\mathbb{C}9$ in green, and $\mathbb{C}10$ in red provides a good rendering of the components' correlation in plaques of different morphologies, as shown in Fig. 5.9 (row 3). For example, each of these components colocalize with the fibrillar core of $A\beta$ plaque, but there is a lack of fibrin-arachidic acid structures ($\mathbb{C}10$) at the outer rim (Fig. 5.9A3) of the fibrillar plaque. On the other hand, the oligomeric halo of $A\beta$ plaque is found to be enriched in $A\beta$ -saturated cholesteryl ester domains ($\mathbb{C}9$), which can be clearly observed for the cored neuritic plaque (Fig. 5.9B3).

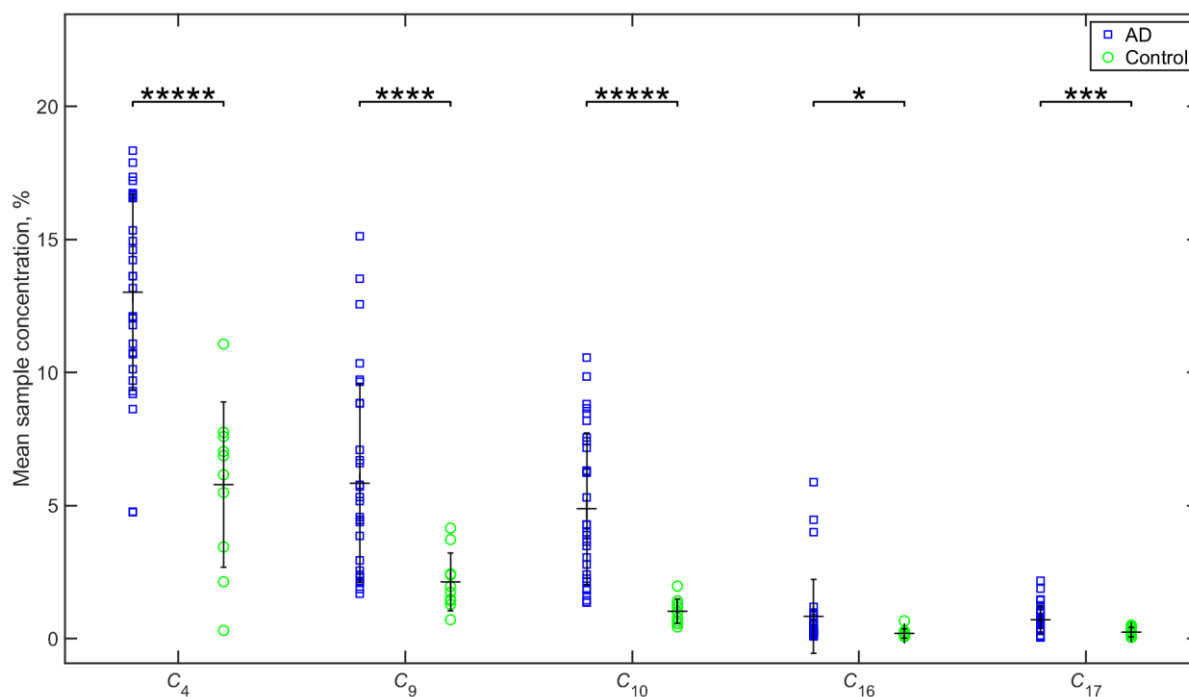


Fig. 5.10: A scatter plot of the sample mean concentrations is given for 30 hippocampal $A\beta$ plaques (5 AD patients) and 10 control (2 elderly humans without AD) Raman images versus component number ($\mathbb{C}4$, $\mathbb{C}9$, $\mathbb{C}10$, $\mathbb{C}16$, and $\mathbb{C}17$). The mean and standard deviation of each cohort are indicated by the error bars. The significance in pairwise difference in the concentration levels between AD and control groups was determined by two-sample two-tailed t -test with unequal variances. * $p < 0.05$, *** $p < 0.001$, **** $p < 0.0001$, ***** $p < 0.00001$. Here, AD = Alzheimer's disease; C = control.

To investigate the significance of the received concentration levels, I have statistically analysed the mean (see Fig. 5.10) and median (Fig. 5.11) concentrations of $\mathbb{C}4$, $\mathbb{C}9$, $\mathbb{C}10$, $\mathbb{C}16$, and $\mathbb{C}17$ found from AD and control populations over the imaged regions. For each component, the mean (or the median) and the STD are given separately for AD and control groups, and a t -test (or the Wilcoxon rank sum test) was used to determine the significance of the observed differences. The probability of the null-hypothesis, revealing whether the statistical distributions corresponding to diseased and control samples are significantly different, which will be reflected by the small p -values. For both mean and median concentrations of $\mathbb{C}4$, $\mathbb{C}9$, $\mathbb{C}10$ and mean concentration of $\mathbb{C}16$, $\mathbb{C}17$, I found p -values below a few percent, which confirms a significant increase in the levels of these components in plaque regions of AD tissues compared to the control group. However, the difference in median

concentration for C16 and C17 between diseased and control cohorts was found insignificant as reflected by the p -values higher than a 5% (Fig. 5.11). It is important to note that the distribution of C16 and C17 for the AD group appears to be shifted to higher levels of median concentration for 3 diseased samples as could be clearly observed for C16 in Fig. 5.11, implying the high variation and heterogeneity in the concentration of these components from patient to patient.

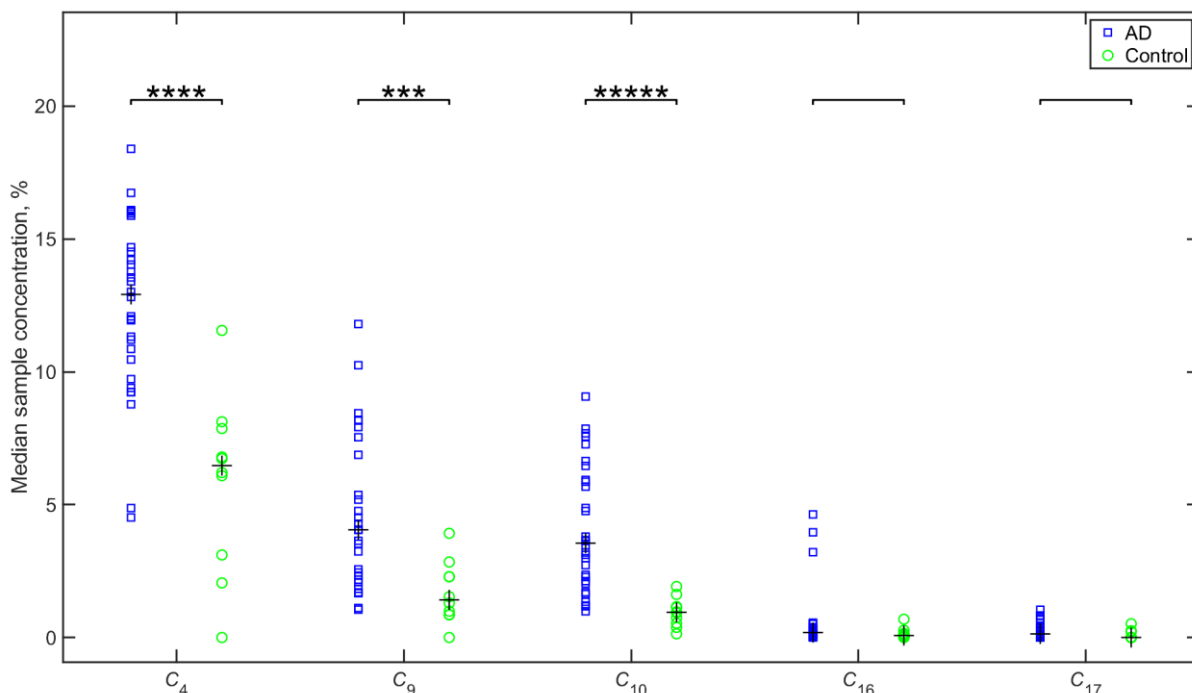


Fig. 5.11: A scatter plot of the sample median concentrations is given for 30 hippocampal A β plaques (5 AD patients) and 10 control (2 elderly humans without AD) Raman images versus component number (C4, C9, C10, C16, and C17). The median of each cohort is indicated by the plus sign. The significance in pairwise difference in the concentration levels between AD and control groups was determined by the Wilcoxon rank sum test. *** $p < 0.001$, **** $p < 0.0001$, ***** $p < 0.00001$. Here, AD = Alzheimer's disease; C = control.

Fig. 5.12 demonstrates the colocalization histograms for the concentration distributions of C9 - C10 (top row) and C9 - C4 (bottom row) for AD and control groups, representing the statistics on 10, 9, 5, 1, 5 plaques from Ah1, Ah2, Ah3, Ah4, Ah5, and 6, 4 control Raman images from Ch1, Ch2 individuals, respectively. A typical size of each Raman image was about $50 \times 50 \mu\text{m}^2$. The Pearson's correlation coefficients R for each case subject are also shown in Fig. 5.12, indicating a positive linear correlation between concentration distributions of the selected paired components, except for the pair C9 - C10 from subject Ah5. The colocalization histogram for Ah4 sample representing a Raman image of just one measured plaque is also given. These histograms show a significant difference in the concentration distributions of collagen, A β_{1-42} fibrils-saturated cholesteryl ester and fibrin-arachidic acid complexes between AD and control groups, and therefore might be beneficial for the discrimination of patients' classes. Specifically, a cut-off of concentration levels at 15%, 5%, and 15%, 28% for components 9, 10 (top row) and components 9, 4 (bottom row) in the colocalization histograms of Fig. 5.12, respectively, results in *only* the

histograms for the AD cohort exhibiting concentrations higher than these levels. Therefore, I have been able to separate hippocampal AD samples from the non-AD controls using the information from the components' concentration distributions of unmixed Raman images, which is in line with the results using the mean concentration (Fig. 5.10).

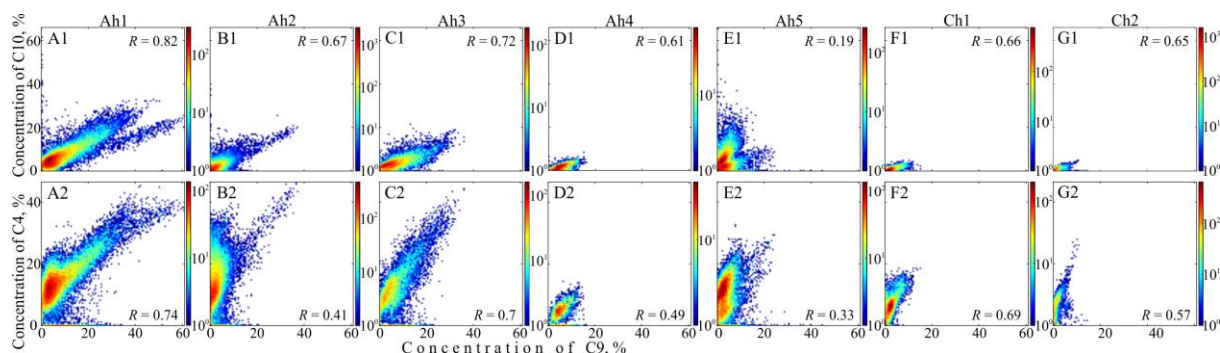


Fig. 5.12: Colocalization histograms of concentration (%) for C9 - C10 (upper row) and for C9 - C4 (lower row) for each diseased (5 AD patients) and control (2 individuals) hippocampal samples, which refer to AD and non-demented elderly individuals, labelled as Ah1 (A), Ah2 (B), Ah3 (C), Ah4 (D), Ah5 (E) and Ch1 (F), Ch2 (G). Statistics on these samples was determined by the analysis of 10 (from Ah1), 9 (from Ah2), 5 (from Ah3), 1 (from Ah4), 5 (from Ah5) plaques, and 6 (Ch1), 4 (Ch2) control regions with a typical size of each Raman image of about $50 \times 50 \mu\text{m}^2$. The Pearson's correlation coefficients R for each case subject are shown.

5.3.3. Chemical composition of cortical A β plaques: key chemical components

Similar to the hippocampal brain region, I have measured 31 unstained cortical A β plaques from 6 AD patients, and 7 control regions from 2 elderly humans without AD. The same framework of the Q-HIU analysis as for the hippocampus samples was applied. The results of this analysis reveal five key chemical components found colocalizing with cortical A β plaques, with four of these exhibiting Raman spectra similar to C9, C10, C16, and C17 found in the hippocampus and sorted by their mean concentration, from largest to smallest. These are: a mixture of fibrillar A β_{1-42} and saturated lipids with cholesteryl derivatives (C4, $R^2 = 78\%$), a mixture of fibrin and arachidic acid (C11, $R^2 = 90\%$), β -carotene (C16, $R^2 = 86\%$) and Fe_3O_4 (C20, $R^2 = 89\%$) (see Table 5.2 on components' attribution). Importantly, collagen component (C4 in the hippocampus) was not found in the cortical plaque regions, whereas a new component appears, in spectral characteristics resembling calcium phosphate crystals (C7, $R^2 = 93\%$) (see Fig. 5.13). Specifically, the spectrum of this component has a very strong Raman band near 970 cm^{-1} , attributed to the symmetric stretching mode of the phosphate group, indicative of whitlockite (Haskin *et al.* 1997).

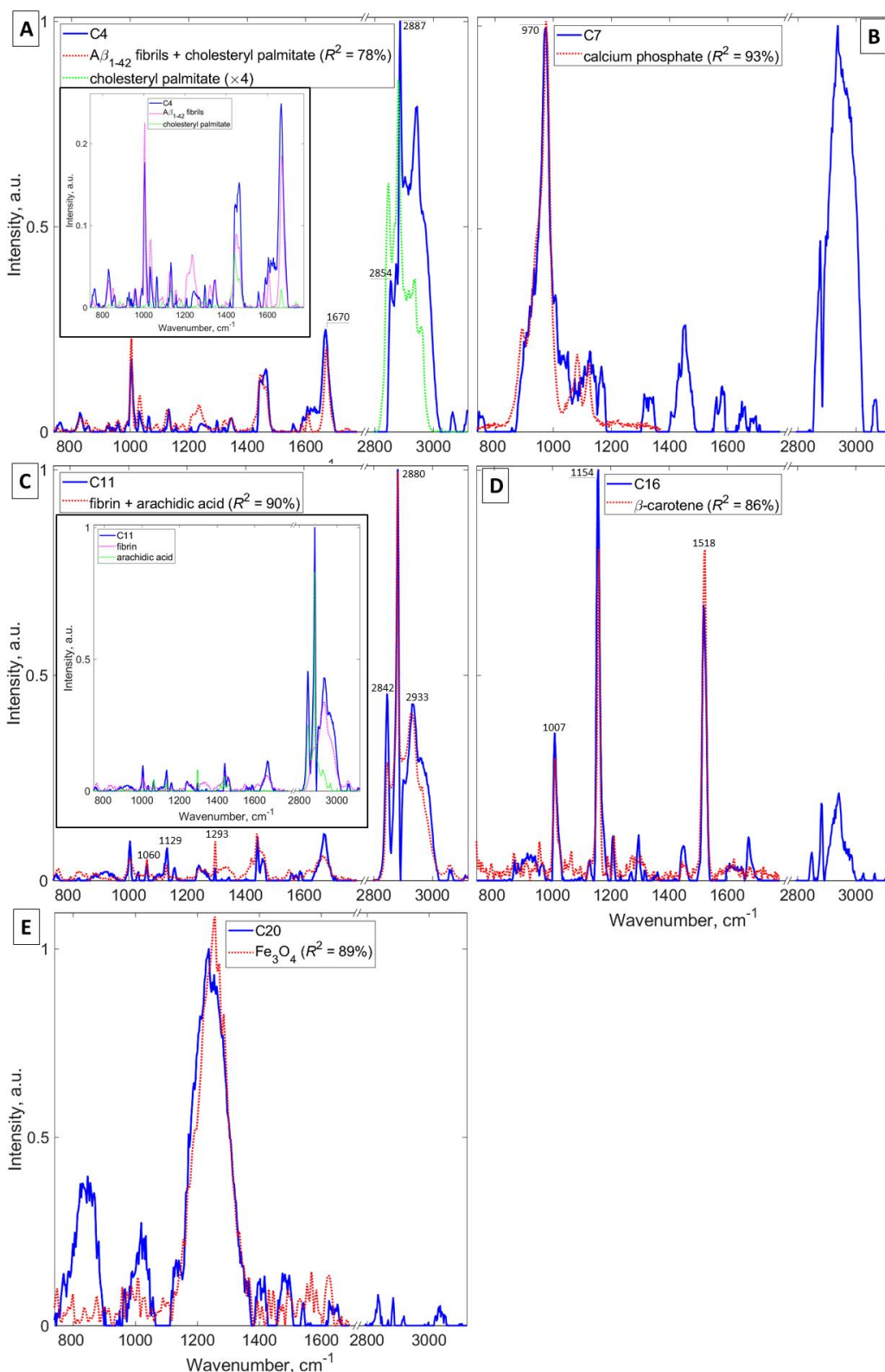


Fig. 5.13: Raman spectra of the chemical components (blue solid lines) colocalizing with cortical A β plaques, obtained from the simultaneous Q-US/PS-NMF analysis of 31 cortical A β plaques (6 AD patients) together with 7 control Raman maps (2 elderly humans without AD). C4 (A) is a mixture of A β ₁₋₄₂ fibrils and saturated lipids with cholesteryl derivatives. C7 (B) is assigned to calcium phosphate crystals. C11 (C) is a mixture of fibrin and arachidic acid. C16 (D) is attributed to carotenoids. C20 (E) is attributed to iron oxide. The chemical attribution of components C4, C7, C11, C16 and C20 is based on the comparison with analytical standard Raman spectra of pure chemical species. Fits are shown by the red dotted lines and found using NLS algorithm. Corresponding R^2 are also indicated. The fit in (A) is a superposition of the Raman spectrum of synthetic A β ₁₋₄₂ fibrils (magenta line) and cholesteryl palmitate (green line); the contributions are separately shown in the inset for the fingerprint region. The red line in (B) is the Raman spectrum of calcium phosphate. The fit in (C) is a superposition of fibrin (magenta line) and arachidic acid (green line); the contributions are shown in the inset. The red line in (D) is the Raman spectrum of β -carotene. The red line in (E) is the Raman spectrum of Fe₃O₄.

5.3.4. Spatial distributions of key chemical components in cortical A β plaques

In this section, I examine and compare the spatial concentration profiles of the 5 components, identified in the previous section over AD and non-demented populations in the frontal cortical brain region. Similarly to the hippocampal brain region, I show an overview results of all unmixed Raman images, as retrieved from the simultaneous Q-US/PS-NMF analysis of unstained 31 cortical A β plaques (6 AD patients) together with 7 control Raman maps (2 elderly humans without AD) in Fig. 5.14-Fig. 5.18.

In order to examine in detail the spatial correlation of C4, C7, C11, C16 and C20 in the cortical A β plaques of various types, I show the spatial concentration profiles of the plaques with three different morphologies (see rows 4-8 of Fig. 5.19), namely two neuritic ($40\times 40\ \mu\text{m}^2$ from Ac1_001, $64\times 64\ \mu\text{m}^2$ from Ac2_001), core-only ($55\times 55\ \mu\text{m}^2$ from Ac2_007) and cored neuritic ($64\times 64\ \mu\text{m}^2$ from Ac3_001) plaques supplemented by two control regions ($64\times 64\ \mu\text{m}^2$ from Cc1_001, and $32\times 32\ \mu\text{m}^2$ from Cc2_001). The DIC and fluorescence images of the same plaque and control areas are given in row 1 and 2 of Fig. 5.19, where white squares indicate the regions of Raman measurements. To note, white areas in panels B4-B8 represent pixels, which were excluded from the analysis as noise-dominated (see Section 5.2.3 for details).

By examining Fig. 5.19, I found that the spatial concentration profiles of C4 (the A β fibrils and saturated lipids with high cholesteryl ester content) (Fig. 5.19A4-D4) and C7 (calcium phosphate) (Fig. 5.19A8-D8) in the plaque areas mimic the contours of Th-S stained plaques in the corresponding fluorescence images (Fig. 5.19A1-D1). In particular, C4 and C7 (indicative of calcium mineralization) accumulate throughout the A β plaque areas tending to have higher concentrations at the core of plaques and lower ones at the plaque periphery, except for the cored neuritic plaque (the upper one only, Fig. 5.19D8). Also, the concentration images of C11 (a mixture of fibrin and arachidic acid), C16 (β -carotene) and C20 (Fe_3O_4) reveal the increased micro-accumulations of these species in A β plaques. Notably, β -carotene component is clustered within the plaques and tends to wrap their core. It appears that the smaller the plaque the higher its coverage by β -carotene. Similarly, iron oxide (C20) shows clear specks observed inside the plaques, whereas a fibrin/arachidic acid complex accumulates not only inside but also outside of plaque regions.

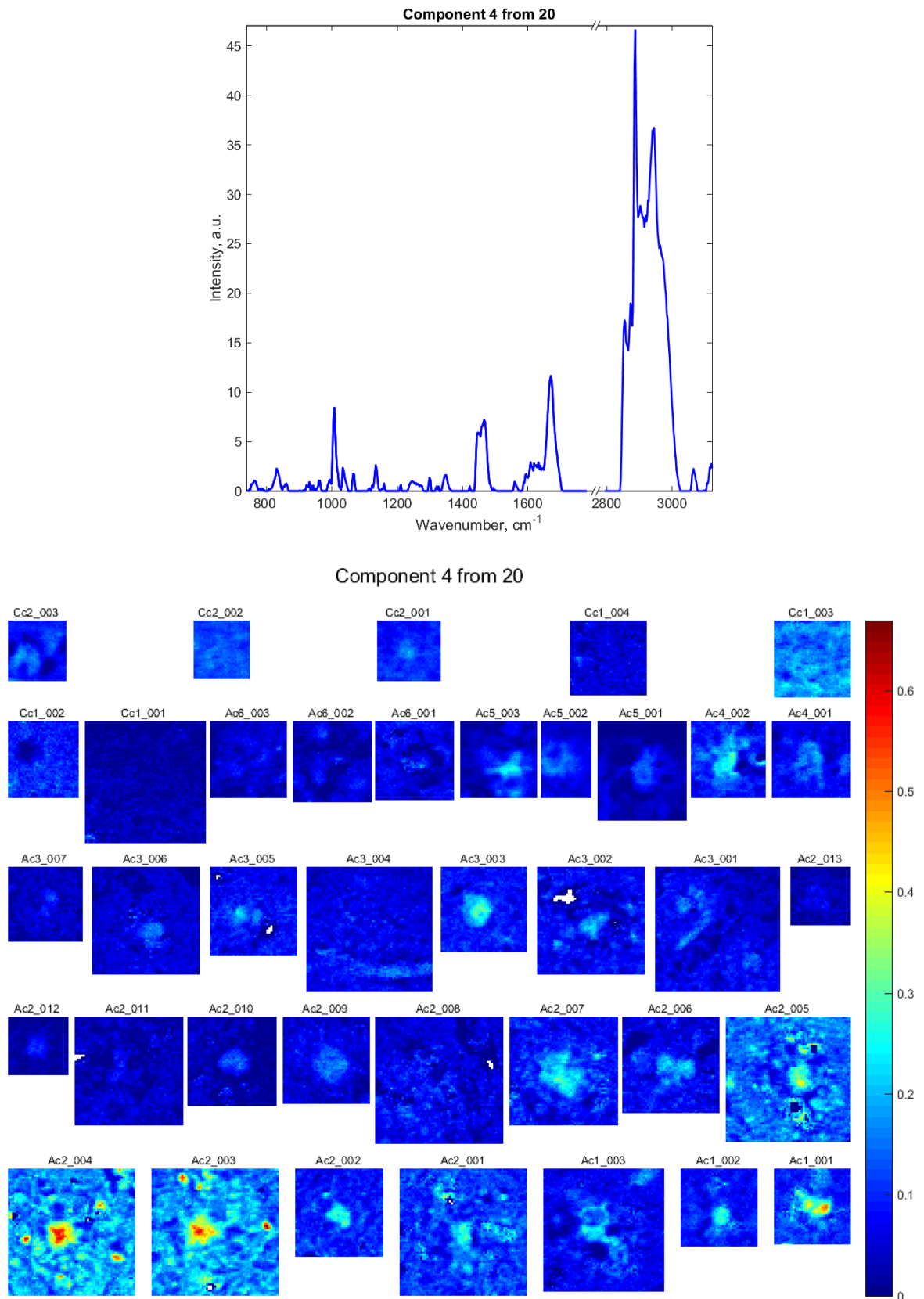


Fig. 5.14: Spatial distributions of the Raman concentration and the corresponding component spectra $\mathbb{C}4$ for the measured AD cortical brain regions together with controls (labelled according to the sample source as Ac1,...,Ac6, and Cc1, Cc2, respectively) on colour scales as indicated, retrieved from the simultaneous Q-US/PS-NMF unmixing analysis of 31 cortical A β plaques (6 AD patients) together with 7 control Raman maps (2 elderly humans without AD).

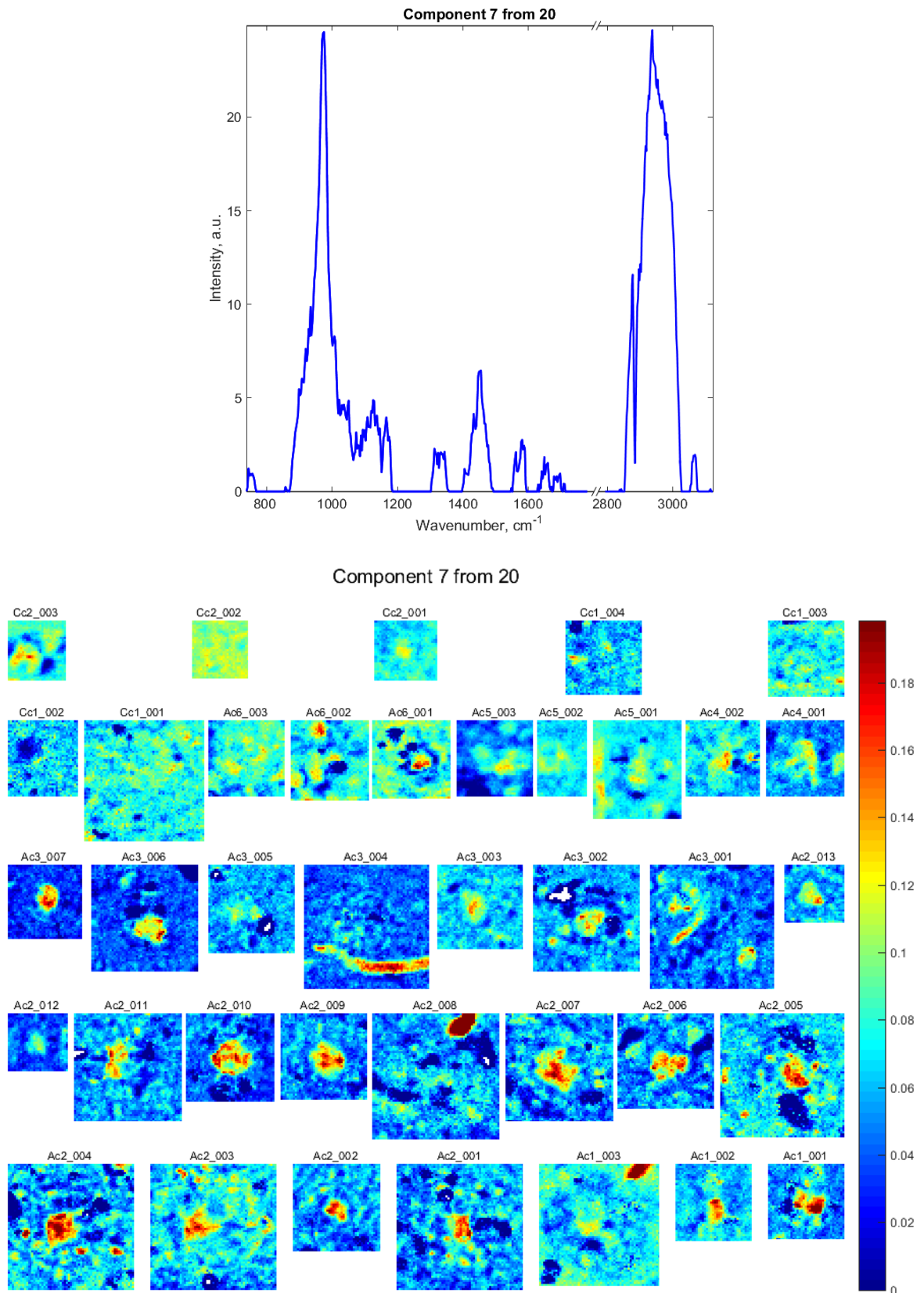


Fig. 5.15: Spatial distributions of the Raman concentration and the corresponding component spectra $\mathcal{C}7$ for the measured AD cortical brain regions together with controls (labelled according to the sample source as Ac1,...,Ac6, and Cc1, Cc2, respectively) on colour scales as indicated, retrieved from the simultaneous Q-US/PS-NMF unmixing analysis of 31 cortical A β plaques (6 AD patients) together with 7 control Raman maps (2 elderly humans without AD).

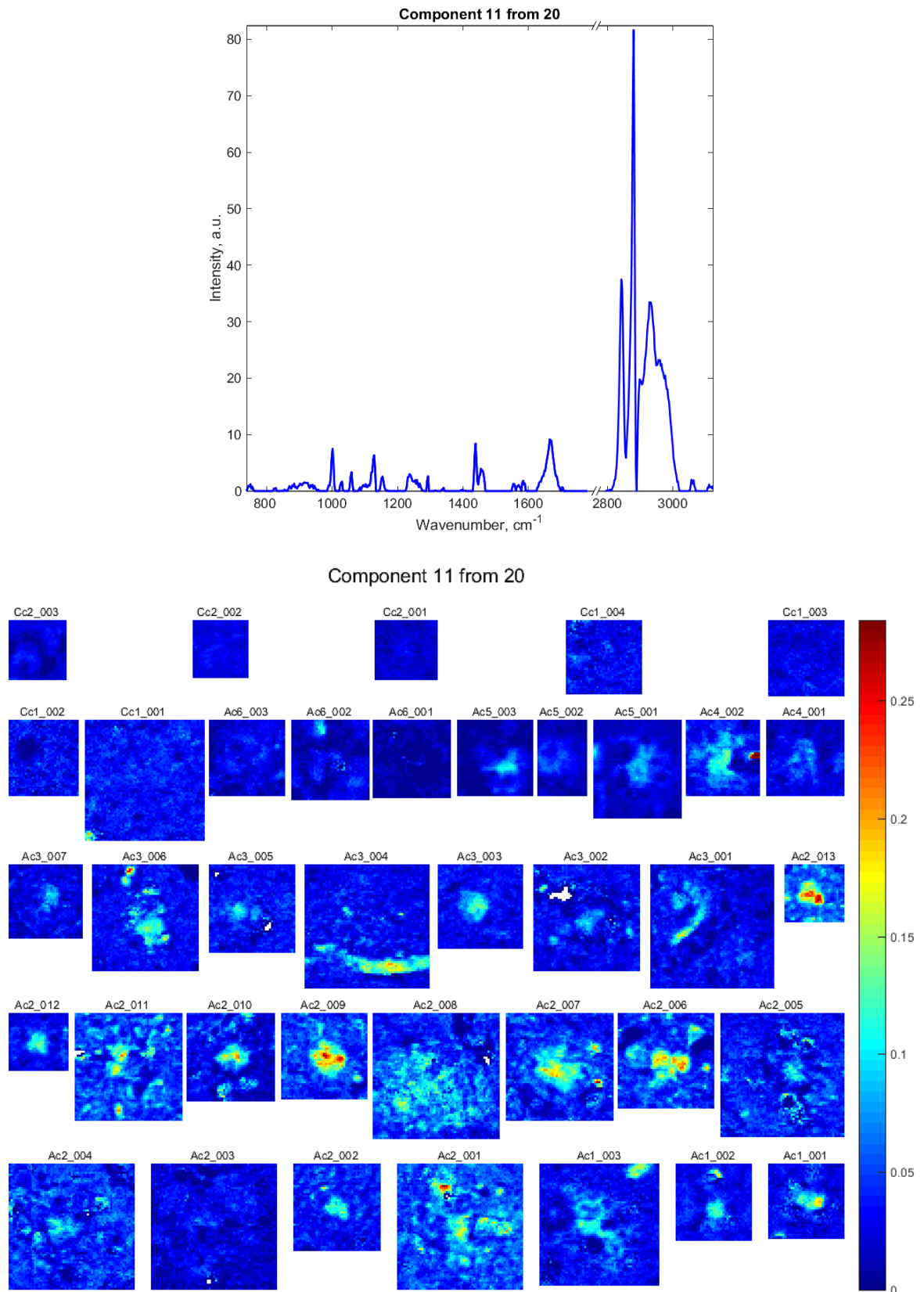


Fig. 5.16: Spatial distributions of the Raman concentration and the corresponding component spectra C11 for the measured AD cortical brain regions together with controls (labelled according to the sample source as Ac1,...,Ac6, and Cc1, Cc2, respectively) on colour scales as indicated, retrieved from the simultaneous Q-US/PS-NMF unmixing analysis of 31 cortical A β plaques (6 AD patients) together with 7 control Raman maps (2 elderly humans without AD).

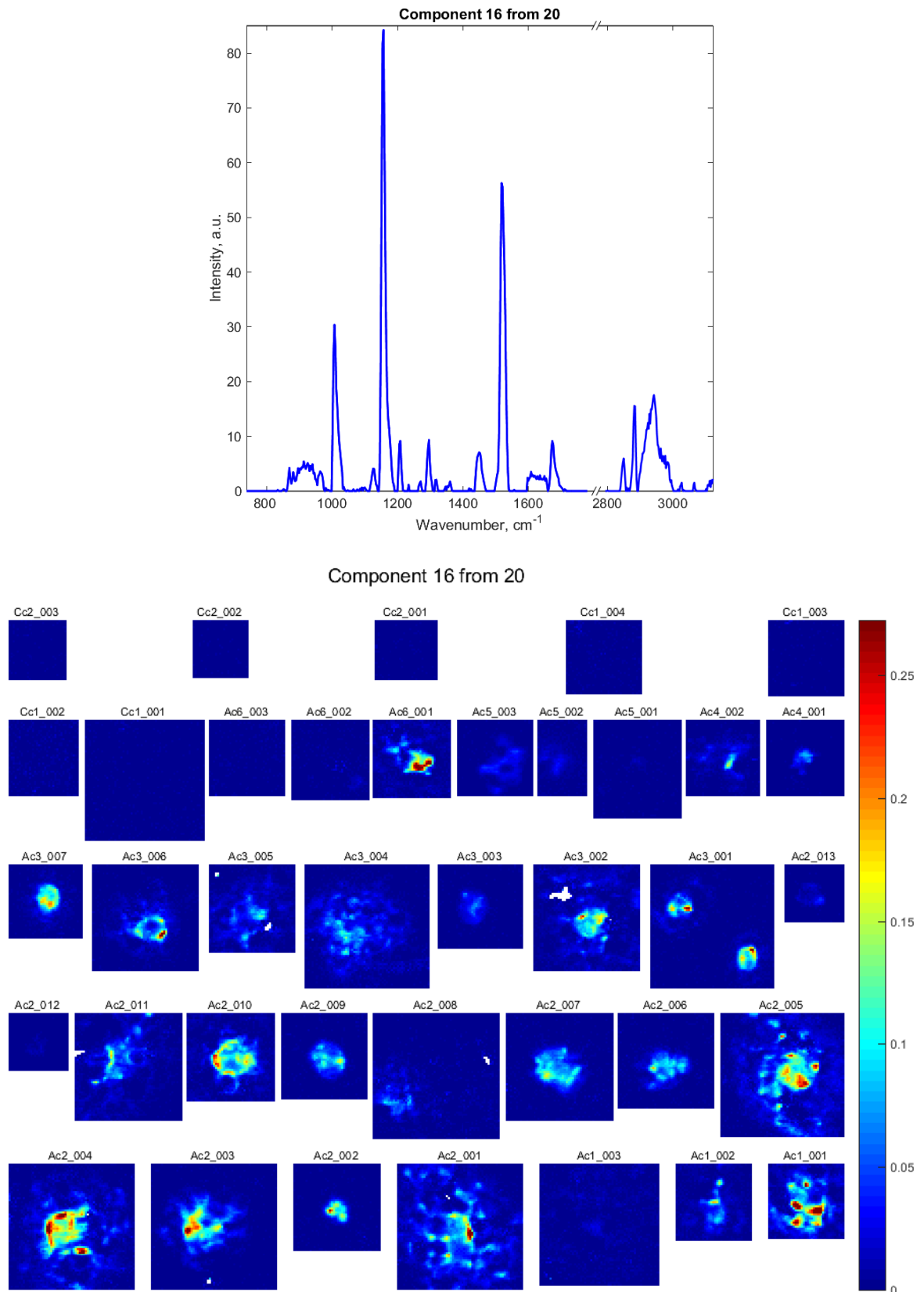


Fig. 5.17: Spatial distributions of the Raman concentration and the corresponding component spectra C16 for the measured AD cortical brain regions together with controls (labelled according to the sample source as Ac1, ..., Ac6, and Cc1, Cc2, respectively) on colour scales as indicated, retrieved from the simultaneous Q-US/PS-NMF unmixing analysis of 31 cortical A β plaques (6 AD patients) together with 7 control Raman maps (2 elderly humans without AD).

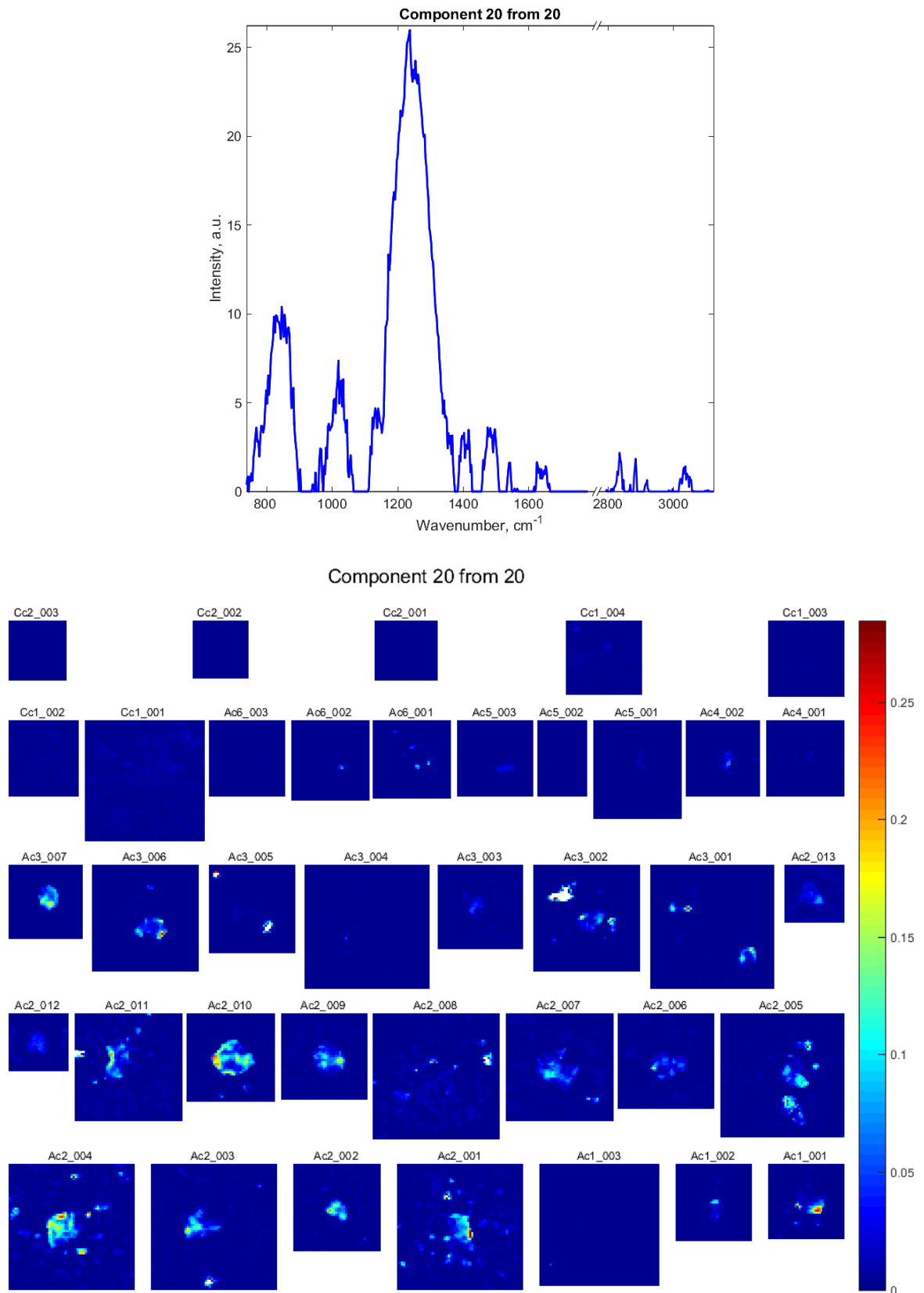


Fig. 5.18: Spatial distributions of the Raman concentration and the corresponding component spectra C20 for the measured AD cortical brain regions together with controls (labelled according to the sample source as Ac1, ..., Ac6, and Cc1, Cc2, respectively) on colour scales as indicated, retrieved from the simultaneous Q-US/PS-NMF unmixing analysis of 31 cortical A β plaques (6 AD patients) together with 7 control Raman maps (2 elderly humans without AD).

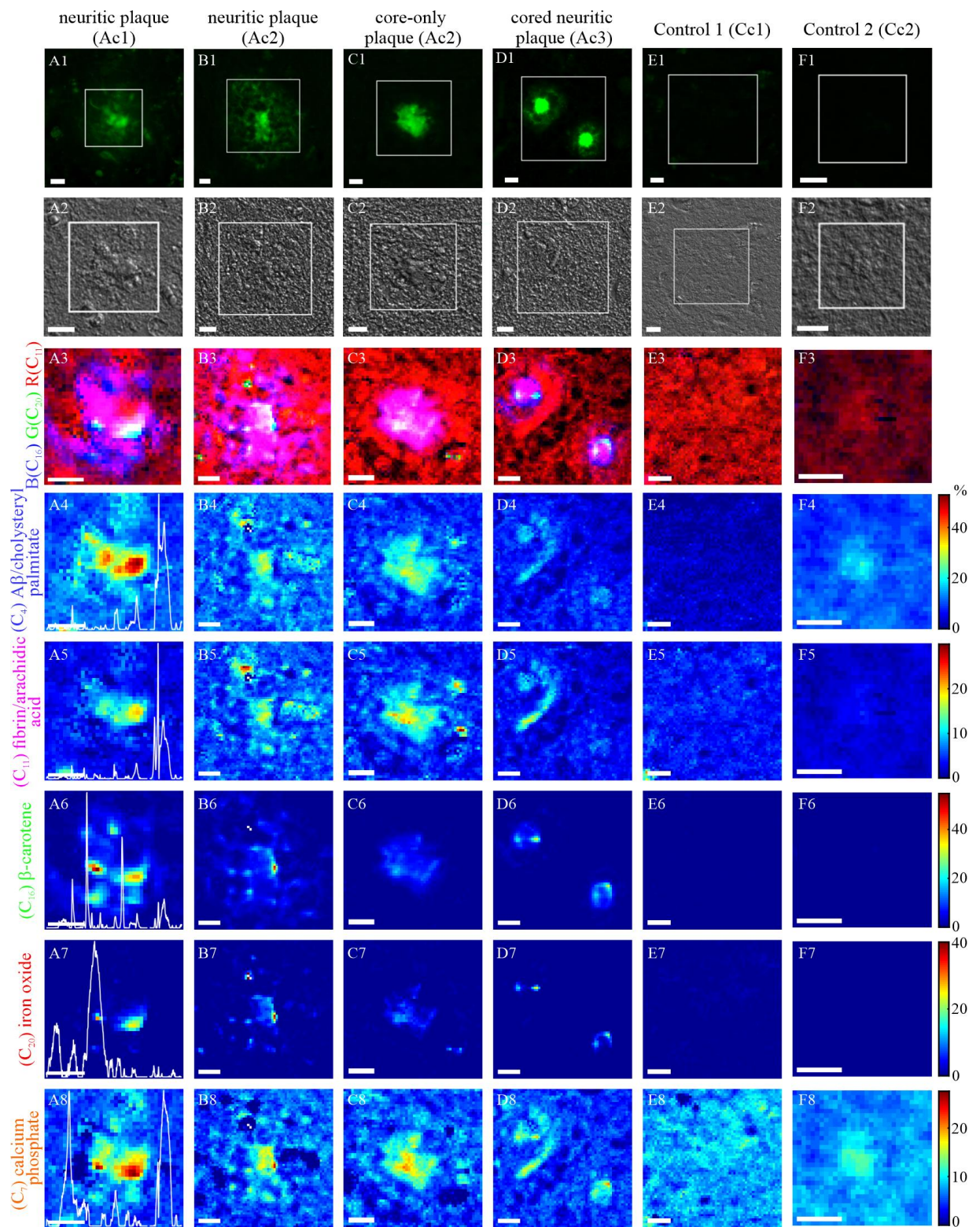


Fig. 5.19: Images of cortical A β plaques with different morphologies and non-demented control regions shown in jet colour scale: the neuritic (A, B), core-only (C) and cored neuritic (D) plaques referring to AD samples, labelled as Ac1_001, Ac2_001, Ac2_002, Ac3_001, respectively, and two control regions (E,F), corresponding to non-demented elderly individuals marked as Cc1_001, Cc2_001. Rows 1-2: the regions of Raman measurements, indicated by white square and visualized by DIC microscopy of the unlabelled samples (A2-F2) and by fluorescence microscopy of the plaque areas (A1-F1) after staining with Th-S. Row 3: pseudo-colour images for the A β plaques and control regions using C4 (a mixture of fibrillar A β_{1-42} and saturated cholesteryl esters) as blue, C20 (iron oxide) as green, and C11 (a mixture of fibrin and arachidic acid) as red, scaled to saturate at 25% of maximum colour channel. Rows 4-8: spatial concentration profiles of the selected components, on colour scales as indicated. The corresponding component spectra are indicated as white lines in the first column (see also Fig. 5.3). Scale bars: 10 μ m.

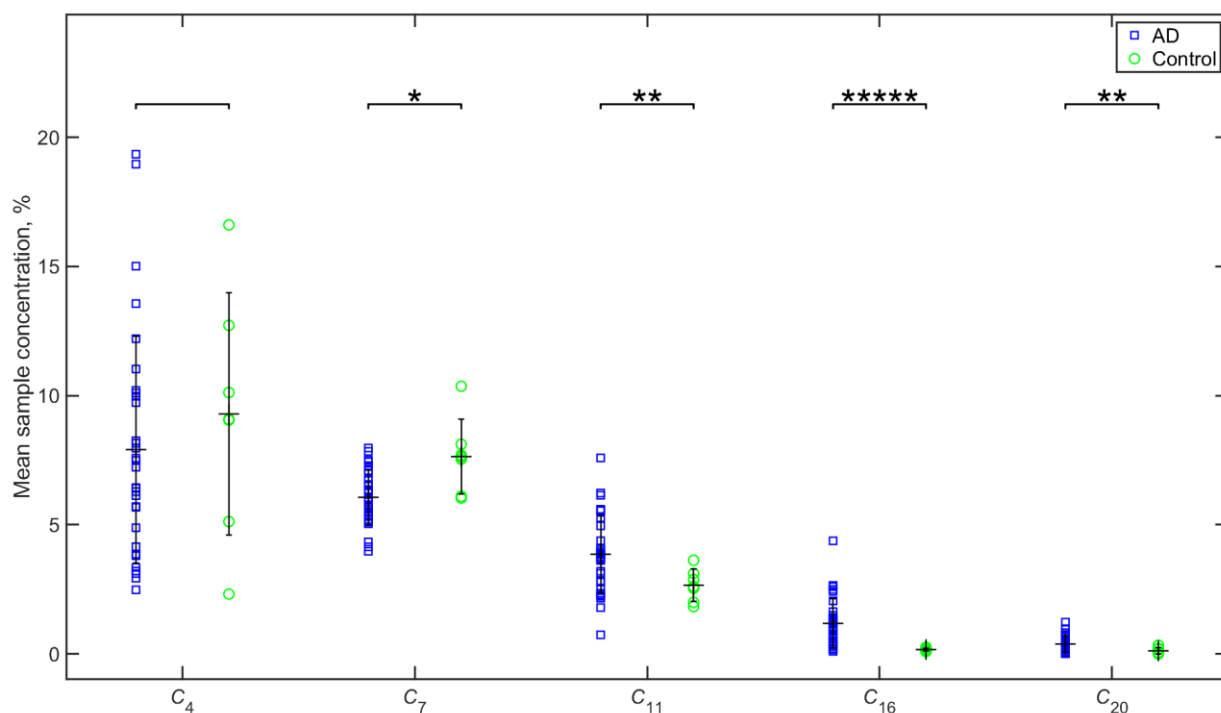


Fig. 5.20: A scatter plot of the sample mean concentrations is given for 31 cortical A β plaques (6 AD patients) and 7 control (2 elderly humans without AD) Raman images versus component number (C4, C7, C11, C16, and C20). The mean and standard deviation of each cohort are indicated by the error bars. The significance in pairwise difference in the concentration levels between AD and control groups was determined by two-sample two-tailed t -test with unequal variances. * $p < 0.05$, ** $p < 0.01$, **** $p < 0.00001$. Here, AD = Alzheimer's disease; C = control.

A statistical analysis of all cortical samples reveals the statistically significant changes (p -value less than 5%) in the mean concentration levels of C7, C11, C16, and C20, but not for C4, found from two-sample two-tailed t -test with unequal variances as evident from Fig. 5.20. Additional consideration of the median concentration for the same components (see Fig. 5.21) and their comparison with the corresponding mean values revealed the skew statistical distribution in individual component concentrations for the AD patient group (see, for example, the distribution of C16 in Fig. 5.21) reflected by the significant changes in p -values between the median and mean concentrations levels. The significance in pairwise difference for the median concentration levels between AD and control groups was determined by the Wilcoxon rank sum test (Fig. 5.21).

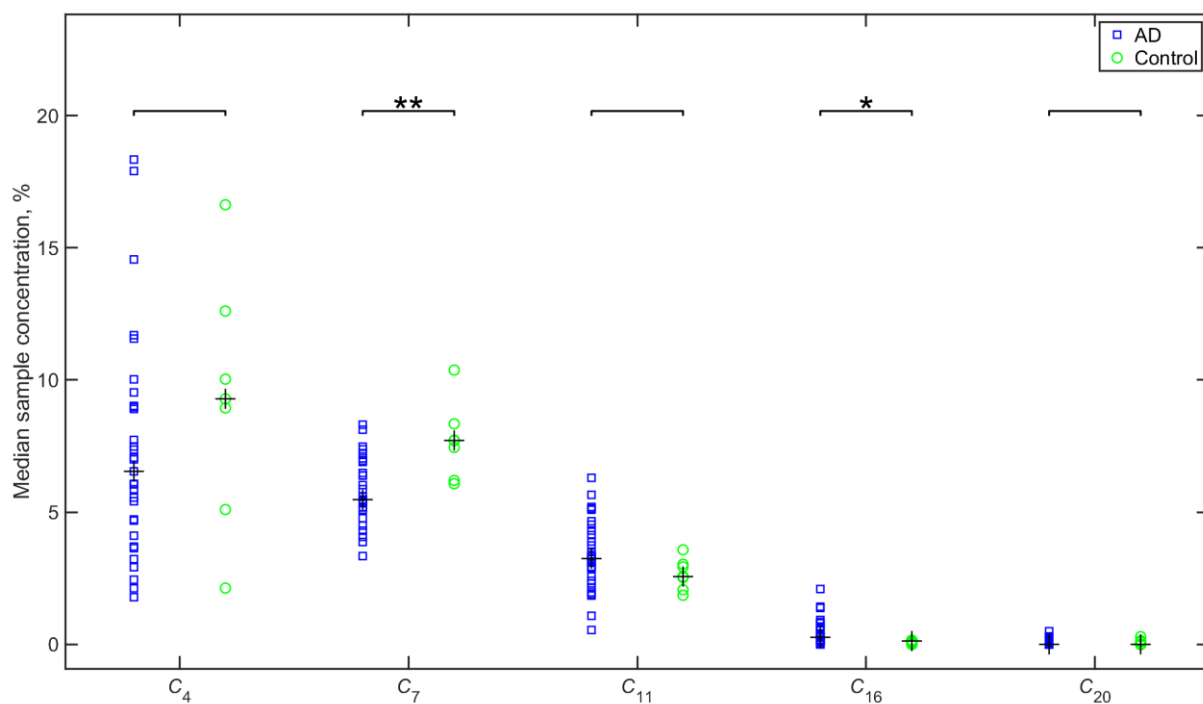


Fig. 5.21: A scatter plot of the sample median concentrations is given for 31 cortical A β plaques (6 AD patients) and 7 control (2 elderly humans without AD) Raman images versus component number (C4, C7, C11, C16, and C20). The median of each cohort is indicated by the plus sign. The significance in pairwise difference in the concentration levels between AD and control groups was determined by the Wilcoxon rank sum test. * $p < 0.05$, ** $p < 0.01$. Here, AD = Alzheimer's disease; C = control.

Fig. 5.22 shows the colocalization histograms for the concentration distributions of C16 (β -carotene) and C20 (iron oxide) of each diseased (4 AD patients) and control (2 elderly individuals without AD) samples, using data came from 3, 13, 7, 2, 3 and 3 plaques corresponding to Ac1 (A), Ac2 (B), Ac3 (C), Ac4 (D), Ac5 (E), and Ac6 (F) samples as well as 4, 3 control regions representing Cc1 (G), Cc2 (H) individuals. Each Raman image was about $50 \times 50 \mu\text{m}^2$ in size. The inspection of the distribution histograms reveals significant changes in the concentration levels of these components between AD and control groups, indicating their potential to be utilized for the patients' classes differentiation, similar to what observed for the hippocampal regions. Specifically, the cut-off value of the colocalization histograms at 5% and 3% Raman concentration levels for C16 and C20, respectively, results in only the AD group having Raman concentrations higher than these values, therefore implying the differentiation of the AD samples from the non-demented controls.

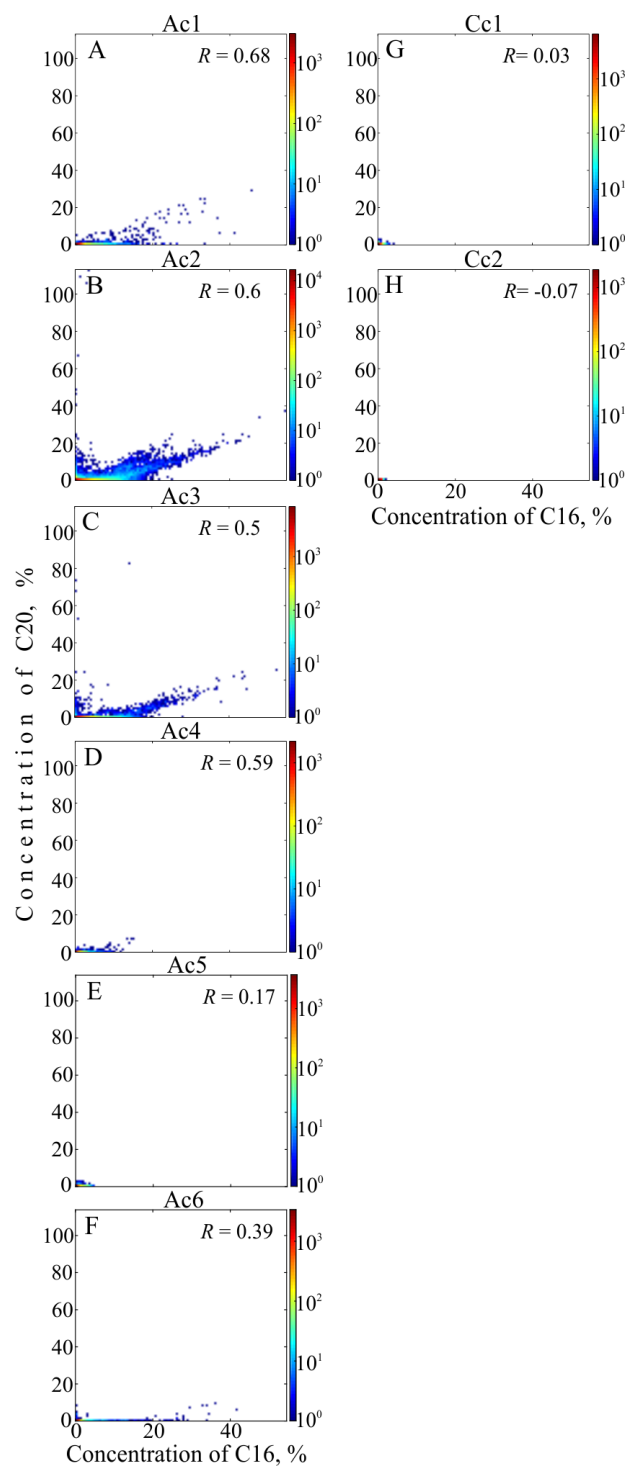


Fig. 5.22: Colocalization histograms of concentration (%) for C20 - C16 for each diseased (6 AD patients) and control (2 individuals) samples in the cortex, which refer to AD and non-demented individuals, labelled as Ac1 (A), Ac2 (B), Ac3 (C), Ac4 (D), Ac5 (E), Ac6 (F) and Cc1 (G), Cc2 (H). Statistics on these samples was determined by the analysis of 3 (from Ac1), 13 (from Ac2), 7 (from Ac3), 2 (from Ac4), 3 (from Ac5), 3 (from Ac6) plaques, and 4 (Cc1), 3 (Cc2) control regions with a typical size of each Raman image of about $50 \times 50 \mu\text{m}^2$. The Pearson's correlation coefficients R for each case subject are shown.

5.4. Findings

In this chapter, I reported the chemical composition of label-free A β plaques in the hippocampus and the frontal lobe regions of AD human brains using point-scan confocal Raman micro-spectroscopy. I showed that Raman micro-spectroscopy allowed to resolve and quantify pathogenic A β ₁₋₄₂ chemical component of plaques from completely label-free samples. Strikingly, these A β ₁₋₄₂ fibrils are found to form a co-aggregate with saturated lipids of high cholesteryl ester content, that spatially colocalize with the plaque core and spectrally representing one chemical component. This finding points to the close interaction between aggregated A β and cholesteryl derivatives with long-chain saturated FAs. Along with amyloid-lipid complex, the A β cores of AD human brains are observed to contain another mixed component, spectrally assigned to a combination of fibrin and arachidic acid, both indicative of tissue inflammation. As other important neuroinflammatory markers, β -carotene and iron oxide are found strongly colocalizing with A β aggregates and forming distinct multiple clusters within plaque regions. As a signature of cell damage, cortical plaque core is found to accumulate excessive amounts of calcium phosphate crystals, that might indicate about complete cellular membrane rupture due to neurotoxic A β interaction with lipid membranes of human cortical neurons. Collectively, the identified inflammatory markers found colocalizing with A β plaques and exhibiting significantly increased levels in AD tissues might suggest a conserved pattern of chronic immune system activation in response to A β neurotoxicity. Therefore, a detailed characterization of immunological pathways followed by accumulation of pro-inflammatory components in close proximity to A β plaque regions might provide new insight into A β amyloidosis implicated in human AD brains (Stefani 2012). To address this, Chapter 7 and Chapter 8 will be devoted to the fluorescence imaging of specific inflammatory markers in A β plaques of human AD brains with a focus on the investigation of A β colocalization with them.

In response to potential clinical application, the results of Raman micro-spectroscopy in the hippocampal and frontal lobe brain regions show a proof-of-principle for the biomolecular characterization and quantitative imaging of individual biochemical components of diseased tissues compared to non-diseased controls. Importantly, these identified components are found to exhibit significantly different Raman concentrations between AD and non-demented brains, highlighting their potential use as characteristic biomarkers of AD, beneficial for the disease diagnosis.

Chapter 6. Three-dimensional chemical imaging of thick frozen brain sections by line-scan Raman micro-spectroscopy

6.1. Introduction

My previous study chapter shows a proof of concept for Raman micro-spectroscopy combined with efficient multivariate hyperspectral image unmixing analysis to simultaneously detect individual spectral profiles and spatial distributions of three hallmarks of AD brains: A β fibrils, saturated lipids and inflammatory components of prolonged immune system activation (iron oxide, calcium crystals, β -carotene and fibrin) all colocalizing in the A β plaque. That study was performed on thin formalin-fixed-paraffin-embedded brain sections mounted on a standard glass slide, which is the gold standard for histological tissue examination used in research and clinical setting. However, it has been inferred from the previous study chapter that Raman imaging on this type of samples have three disadvantages due to (1) significant contribution of fluorescence and Raman scattering from the glass slide/coverlip to the Raman spectra of tissues complicating the extraction of relevant chemical information; (2) contribution of wax residuals to the Raman spectra of dewaxed tissues requiring a digital fixation of this component during analysis to avoid interference with meaningful components; (3) potential effects of dewaxing and paraffin wax itself on preservation of actual bio-chemical content of tissues. It is worth mentioning that based on my experience of work with paraffin brain sections these samples preserve good tissue architecture and solid structure after dewaxing making them easy to handle for Raman imaging and post-examination with fluorescence microscopy without destroying the sample.

In balance, this study chapter will present the spatially resolved chemical composition of frozen brain tissues without chemical fixatives and mounted on fluorescence-free CaF₂ Raman windows for Raman imaging. Furthermore, in this study chapter, 3D Raman imaging will be performed on thick brain sections using an advanced version of Raman micro-spectroscopy, line-scan Raman, (pros: improved scanning speed and smooth image distribution by scanning the laser beam over a region of interest line by line) coupled with an oil immersion objective of a higher magnification (pros: higher spatial resolution and better 3D sectioning).

6.2. Method

6.2.1. Human tissue samples and tissue preparation

As in Chapter 5, human brain tissue was sourced from the Thomas Willis Oxford Brain Collection (TWOBC), which is part of the Medical Research Council (MRC) Brain Bank Network, with the ethical approval of the Research Tissue Bank provided by the Oxford Brain Bank (OBB) Access Committee. A total of 4 hippocampal diseased samples were recruited from the hippocampus of three AD subjects, who at the time of death were affected by AD. As a control, 1 hippocampal control sample was investigated from the corresponding brain region of non-demented elderly subject, which was not diagnosed with AD based on histological tissue examination. Source brain sections arrived unfixed frozen and were packed in a box with a dry ice, that upon arrival were placed and kept in the freezer at $-80\text{ }^{\circ}\text{C}$ for later cryostat sectioning. Prior to cryostat sectioning, fresh brain block was removed from the freezer and immediately placed into a cryostat at $-20\text{ }^{\circ}\text{C}$ (thereby preventing tissue thawing), followed by a mounting of the tissue block in freezing media (that was pre-applied on top of a specimen disk (chuck)). Next, the chuck with the mounted cold brain block was positioned onto a specimen holder with a cutting blade in place. Then, a section of interest was sliced into adjusted thickness (in a range $20\text{-}40\text{ }\mu\text{m}$) and quickly caught with the brush, followed by its transfer to a CaF_2 window (25 mm in diameter and 0.5 mm in thickness) by sticking to the glass surface. To confirm the disease status by histochemistry, one additional tissue section adjacent to each brain slice to be imaged with Raman micro-spectroscopy was always cut and mounted on standard glass slide. Subsequently, these sections were stained with Th-S dye as described in Section 5.2.1 and tested for the presence of plaques via fluorescence microscopy (see Section 5.2.2). Immediately after cryostat sectioning, the mounted fresh brain samples were air dried for about 30 minutes at room temperature, and then were placed in a holder with another CaF_2 coverslip on top of the sample, in which the brain tissue stayed intact. Finally, the holder with the mounted brain section was transferred and kept in a freezer at $-80\text{ }^{\circ}\text{C}$ for further use. For Raman imaging, unfixed frozen brain samples were removed from the freezer and from the holder, and the sample was allowed to thaw at room temperature for 10 minutes. For $\text{A}\beta$ fibril visualization, $35\text{ }\mu\text{l}$ of a mixture solution consisting of a $10^{-4}\%$ Th-S in D_2O diluted in a 2% low melting point agarose liquid at 9:1 was pipetted into the sample mounted on CaF_2 window and another CaF_2 coverslip of the same size was attached on top. This sandwiched structure was squeezed and gripped between two plastic chambers. Similarly, control sample of a non-demented subject was stained with Th-S following the procedure above. To control the potential artefacts of staining on the chemical composition of brain, one AD sample was prepared completely label-free and covered with just D_2O .

6.2.2. Line-scan Raman micro-spectroscopy instrumentation

As in Chapter 5, Raman imaging was carried out using a home-built multimodal laser-scanning microscope based on an inverted Nikon Ti-U stand, coupled to a Horiba Jobin-Yvon iHR 550 imaging spectrometer (300 grooves/mm grating) and an Andor CCD Newton DU-971N-BV detector (1600 × 400 pixels, 16 μm pixel size). A laser source (Laser Quantum GEM 532 nm, 2W) was used for excitation. The 532 nm laser excitation was filtered by a Semrock LL01-532 clean-up filter and coupled into the microscope by a dichroic mirror (Semrock LPD01-532RS). Raman scattering was collected in epi-direction, filtered with a long pass filter (Semrock BLP01-532R), and dispersed by the imaging spectrometer. The spectral resolution of the system was 4.9 cm⁻¹ with 20 μm width of the spectrometer entrance slit, and the detector length enabled to cover a spectral range (330, 4050) cm⁻¹. For line-scan Raman imaging, all brain samples were collected by scanning the laser beam line by line (129 μm in length) over a region of interest with a step size of 0.64 μm in y-direction resulting in a 129×129×1600 points hyperspectral Raman with typically a 5 second exposure time per line. A z-stack Raman image was acquired by sequential scanning of each focal plane with a step size of 3 μm. All Raman images were taken with a nominal laser power of 1W at the sample. Note that during data processing each image was normalized according to its laser energy which is (the laser power) × (the exposure time), making the Raman intensities comparable between samples. All images were collected using a 40× 1.15 NA oil objective and a 1× tube lens. Line-scan confocal Raman imaging was provided by a cylindrical lens allowing to project the laser beam into a line subsequently coupled with the vertical input slit of the spectrometer, and a horizontal slit (Thorlabs VA100), that was widely open (set at nominal 0.8 units in width) enabling to transfer the whole laser line containing Raman signal for detection. The estimated spatial resolution was 0.5 μm in-plane and 1 μm axially.

6.2.3. Hyperspectral Image Unmixing analysis

As in Chapter 5, I used the same approach (see a flowchart of the Q-HIU data analysis methodology in Fig. 3.5) for the unsupervised hyperspectral image analysis of the biomedical Raman data from frozen unfixed AD brain samples together with non-demented controls to be investigated in this study chapter. Like in Chapter 5, all acquired images were analysed together, enabling the comparison of the unmixing biochemical content between samples. As detailed in Section 5.2.3 and Chapter 3, the analysis to be presented in this chapter consisted of 3 major consecutive steps: (1) subtraction of a short noise from the data using the SVD-ADC method with the 50% cut-off for scores and loadings; (2) removal of a broad background from the denoised data using the BGF method with a STD of 900 cm⁻¹; (3) hyperspectral image unmixing for chemical composition retrieval from the noise-filtered background-subtracted data using the

efficient quantitative unsupervised/partially supervised non-negative matrix factorization (Q-US/PS-NMF) method via a fast combinatorial alternating non-negativity-constrained least squares algorithm. The Q-US/PS-NMF algorithm (Lobanova and Lobanov 2019) factorizes the spectrally and spatially resolved data into a linear expansion of direct products of non-negative spatial concentration (matrix **C**) and corresponding non-negative spectral (matrix **S**) profiles, resolving the individual biochemical components of the samples' composition. For analysis reproducibility, 2 repetitions with 20 000 iterations each were utilised during Q-US/PS-NMF. Each repetition converged to the same local minimum of the factorization error. The final factorization expansion was selected as a pair of matrices (**C** and **S**) with minimum factorization error. In the factorizations to be presented in this chapter, the relative factorization error was about 2%. To compare the Raman concentrations of resolved chemical components between samples, I normalize each component spectrum and concentration map in such a way that mean spectra of the chemical components are equal and the total mean spatial concentration is one.

It is important to note that, unlike the analysis for paraffin-embedded samples investigated in Chapter 5, the analysis of the unfixed frozen tissues was fully unsupervised, i.e. the composition of frozen brain tissues was retrieved without any prior information of its biochemical content.

Of note, from experimental point of view, correlative Raman imaging of A β plaques using frozen brain sections is a challenging task due to the lack of contrast in these wet tissues with DIC microscopy and inability to reopen the sample for histochemical examination of the areas imaged with Raman without destroying the tissues. To help with A β plaque identification, the brain samples were stained with Th-S (the well-established dye for identifying amyloid fibrils (Kelenyi, 1967)) of a very low concentration (10^{-4} % m/v Th-S solution) prior Raman measurements. To avoid the washing out of the lipid content, ethanol washing cycles were not used during the procedure. To check whether the staining with a very small concentrated Th-S dye affects the Raman biochemical composition of the brain samples, one completely label-free sample covered with water was participated in this study for comparison. For the final results, 3D Raman images acquired from the label-free sample and shown spectrally and spatially resembling the A β plaque were included in the analysis of all tissues. In the analysis, the Raman images of the hippocampal brain samples from 3 AD individuals and 1 non-demented control (C) individual are named as **AD1_01z1-z3** (label-free sample from AD patient AD1), **AD1_02z1-z7** (Th-S stained sample from AD patient AD1), **AD2_01z01-z11** (Th-S stained sample from AD patient AD2), **AD3_01z1-z5** (Th-S stained sample from AD patient AD3) and **C1_01z01-z10** (Th-S stained sample from control subject C1 without AD). All z-stacks were acquired sequentially with a 3 μ m step in z-direction except for **AD1_01z1-z3** stack, where a 5 μ m step was used.

6.3. Results

Confocal Raman micro-spectroscopy was used to investigate the biochemical composition and 3D spatial distribution of A β plaques and their bioenvironment in frozen human AD brain tissues from the hippocampus. Compared to formalin-fixed-paraffin-embedded brains studied in the previous study chapter, the frozen brain samples were prepared without chemical fixative and paraffin preservation, which allows to study the actual content of brain tissues. The Q-HIU data analysis was performed simultaneously on all data, allowing a direct comparison of spatial concentration profiles of chemical components in diseased and control samples.

Intermediate steps of the Q-HIU data analysis on acquired Raman micro-spectroscopy images of hippocampal brain tissues in AD together with non-demented controls are shown in Fig. 6.1. Specifically, Fig. 6.1D shows the autocorrelation coefficients map for singular vectors received from SVD-ADC analysis of all Raman images, labelled according to the sample source and representing consequent planes of the representative z-stack composite image as z1, z2 and etc. The dotted diagonal line represents a decision line of a 50% cut-off for mean autocorrelation coefficients, that separates the coefficients above the line (circled cross signs – meaningful components) from those below it (cross signs – noise) as shown in Fig. 6.1D. Note that read-noise and shot noise are localized around zero, whereas physically meaningful components show high mean autocorrelation. For these data, SVD-ADC with a 50% cut-off of mean autocorrelation coefficients has defined an approximating matrix, consisting of 40 singular components. To verify this number, I consider the spatial distribution and corresponding spectra for two singular vectors with the autocorrelation coefficients that are lower and higher 50% (Fig. 6.1E-F). For a pair of discarded singular vectors, corresponding to 28% mean autocorrelation, spatial maps do not show any recognised pattern, and spectrum resembles noise, whereas for a pair of meaningful singular vectors with 80% mean autocorrelation, spatial maps show some colocalized features, and spectrum exhibits several clear Raman bands. To show the accuracy of SVD-ADC, I give the results of this method for two points from a Raman image of A β plaque (**AD1_01z1**) with low (right) and high (left) fluorescent background in Fig. 6.1B-C. As can be seen in detail in the inset of Fig. 6.1B, SVD-ADC method allows to significantly reduce the noise from the image.

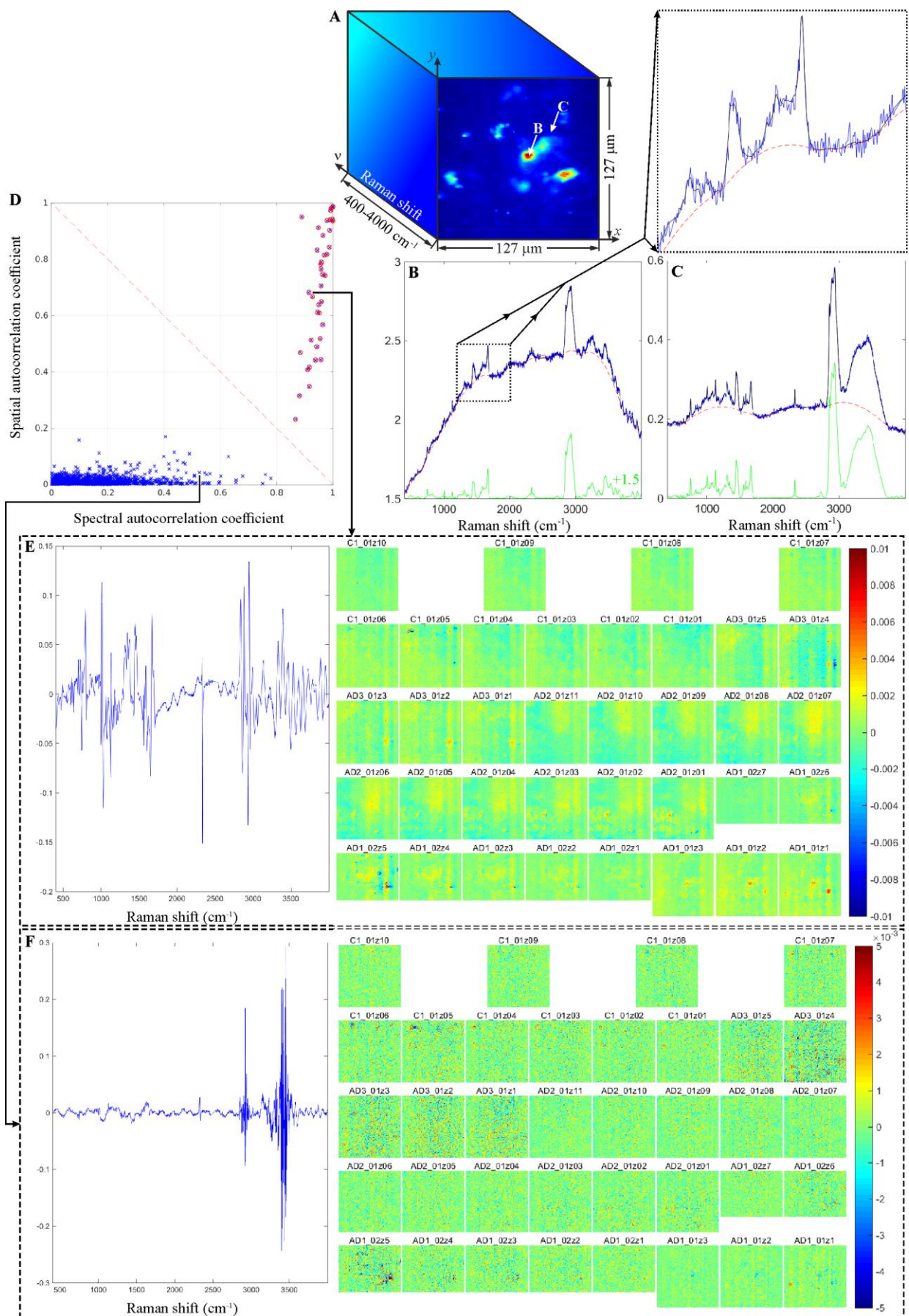


Fig. 6.1: Schematic of a hyperspectral Raman cube (A). The arrows with letters B and C mark two pixels, Raman spectra of which are shown on the panels B and C, respectively. The input Raman spectrum (blue line) before the SVD-ADC and the corresponding noise-filtered Raman spectrum (black line) after this procedure (B-C). The results

of background subtraction using the bottom Gaussian fitting is shown by the green line: the bottom Gaussian fit (red dashed line) is subtracted from the noise-filtered Raman spectrum, giving background-free Raman spectrum. Spatio-spectral autocorrelation coefficients map of singular vectors resulted from SVD-ADC (D). The dotted diagonal line represents a decision line of $R_{th} = 50\%$ cut-off for mean autocorrelation coefficients R_i , separating the coefficients above the line (circled cross signs – meaningful components) from those below it (cross signs – noise). The spatial distribution and corresponding spectra of two singular vectors with the mean autocorrelation coefficients with values $\cong 80\%$ and $\cong 28\%$ as indicated on the panel D (E-F). On both panels, Raman images are labelled according to the sample source and represents hippocampal regions.

Also, Fig. 6.1B, C show an example of BGF algorithm applied to the same Raman image, received from the SVD-ADC. The Raman spectra at two spatial pixels with high (Fig. 6.1B) and low (Fig. 6.1C) fluorescent background before (blue line) and after (green line) background removal with the representative bottom Gaussian fit (red line) are demonstrated in Fig. 6.1B-C. A zoom of the amide I, II bands of the Raman spectrum in Fig. 6.1B shows that the BGF algorithm allows to accurately subtract a fluorescent background from the spectra.

The final step of the Q-HIU data analysis is Q-US/PS-NMF. Applied to factorization analysis of the acquired Raman images of frozen brain tissues, I identified that all Raman images are well represented using 11 separate components giving a factorization error of 2.36%. When selecting 12 components, the Q-US/PS-NMF analysis was checked to show a similar factorization error of 2.22% and retrieved a significantly modified key component of A β pathology lesions exhibiting a noisy spatial distribution and significantly less meaningful Raman spectrum ($R^2 = 80\%$) compared to that for 11 components' analysis that was assigned to a mixture of saturated CEs and fibrin protein ($R^2 = 92\%$). Similarly, the same component in the analysis using 10 components with a factorization error of 2.72% shows a Raman spectrum that significantly less resembles the chemical signatures of proteins and lipids, and spatial distributions having a high background concentration. As deduced from the 11 components' analysis, the chemical components, which attribution has been identified, are summarised in Table 6.1.

The results reveal that one component exhibiting spectrum that resemble a specific type of lipid, whereas another component can be attributed to a cytoskeleton protein. Other 2 components are observed to contain a series of Raman bands characteristic of both proteins and lipids. Three of these four assigned components are found significantly localizing with A β plaques. The other 7 components were found not significantly colocalizing with A β plaques or their chemical attribution has not been established based on available spectral databases. Of identified components, C3 was found consistent with the Raman spectrum of water ($R^2 = 97\%$) using an ID expert tool of Bio-Rad's KnowItAll Vibrational Spectroscopy software with Raman Spectral Libraries. The Raman spectra and corresponding concentration profiles of all 11 components in the brain samples as retrieved from the Q-US/PS-NMF analysis are given in Appendix B. In the course of the next sections, I will focus on the description and attribution of the chemical

components, which are found significantly colocalizing with A β plaques. Specifically, I will examine in detail C1, C2, C6, C9. Note, in the following, I will sort these components by decreasing mean Raman concentration.

Table 6.1: Chemical component attribution retrieved from the Q-US/PS-NMF analysis with 11 components on Raman images of frozen brain tissue.

Chemical component attribution	R^2 for component number C# retrieved from the Q-US/PS-NMF analysis with 11 components
phosphatidylcholine	93% (C1)
actin	76% (C2)
water	97% (C3)
fibrin + cholesteryl palmitate	92% (C6)
A β_{1-42} fibrils + oxidized arachidonic acid in <i>trans</i> configuration	76% (C9)

6.3.1. Chemical composition of frozen human brain tissues in Alzheimer’s disease: key chemical components

Fig. 6.2 shows the Raman spectra of the 4 chemical components colocalized with A β plaques, as obtained from the Q-US/PS-NMF data analysis of AD human brain tissues together with non-demented controls in the fingerprint (736-1780 cm^{-1}) and CH-stretch (2793-3122 cm^{-1}) regions. The range above 3200 cm^{-1} is dominated by Raman scattering of water, and therefore was excluded from the Q-US/PS-NMF analysis to avoid its interference with the chemical components, which are relevant for my study. To identify chemical components’ assignments, I used Bio-Rad’s KnowItAll Vibrational Spectroscopy software with the Raman Spectral Libraries as a guide. Once I found the chemical attribution with this software, I compared the Raman spectra of the identified standards with the representative component spectra retrieved from my analysis using NLS algorithm as shown in Fig. 6.2. These comparisons revealed that 4 components can be spectrally assigned to phosphatidylcholine (PC) (C1, $R^2 = 93\%$, Fig. 6.2A); actin (C2, $R^2 = 76\%$, Fig. 6.2B); a mixture of fibrin and saturated CEs such as cholesteryl palmitate at a ratio of about 1:1 (C6, $R^2 = 92\%$, Fig. 6.2C); a mixture of fibrillar A β_{1-42} and oxidized polyunsaturated acid in *trans* chemical configuration such as *trans* isomer of arachidonic acid (AA) at a ratio of about 1:1 (C9, $R^2 = 76\%$, Fig. 6.2D). The summary of key Raman vibrational bands, reflecting the presence of A β pathology and oxidative stress implicated in AD human brains, as retrieved from this research study is given in Table 6.2.

Table 6.2. The summary of key Raman vibrational bands indicative of A β pathology and oxidative stress resulting from the hyperspectral image unmixing analysis of Raman images of frozen AD human brains in the hippocampus.

Raman shift, cm ⁻¹	Molecular vibration	Chemical assignments	Potential role in AD pathogenesis, indicative of
1668	C=O (Amide I) stretch	β -sheet proteins	pathogenic A β protein
	C=C stretch	E-unsaturated FAs in <i>trans</i> -configuration	oxidation of lipid membranes by free radicals, triggering the pro-inflammatory cascade and pyroptotic cell death
548, 703, 1700	C=C stretch	cholesterol	interaction with A β fibrils
1740	C=O stretch	cholesteryl ester	
718, 875	N ⁺ (CH ₃) ₃ symmetric and asymmetric stretch	phosphatidylcholine	a major constituent of the grey matter of healthy brain tissue (30%)
1068, 1088, 1132, 1177	C-C stretch	saturated FAs	a pronounced feature of AD brain tissues, diagnostic of oxidative modification of lipid membranes
3004	=CH stretch	unsaturated FAs	a lacking feature of AD brain tissues, diagnostic of oxidative modification of lipid membranes

To further justify the chemical components' assignments, I characterised the marker Raman bands of the identified chemical components C1, C3, C6 and C9, that were found in a good agreement with the assignments using the respective Raman spectra of analytical standards based on NLS fitting algorithm. In particular, the attribution of C1 (Fig. 6.2A) to PC was confirmed by the presence of two marker bands at 718 cm⁻¹ and 875 cm⁻¹ assigned to the symmetric and asymmetric stretching modes of the choline N⁺(CH₃)₃ (Krafft *et al.* 2005; Czamara *et al.* 2015). Of the FA content, the presence of the unsaturated carbon (C=C) chains and *cis* conformation of lipid C1 is indicated by the characteristic Raman bands at 1268 cm⁻¹ and 1662 cm⁻¹, respectively (Krafft *et al.* 2005; Czamara *et al.* 2015).

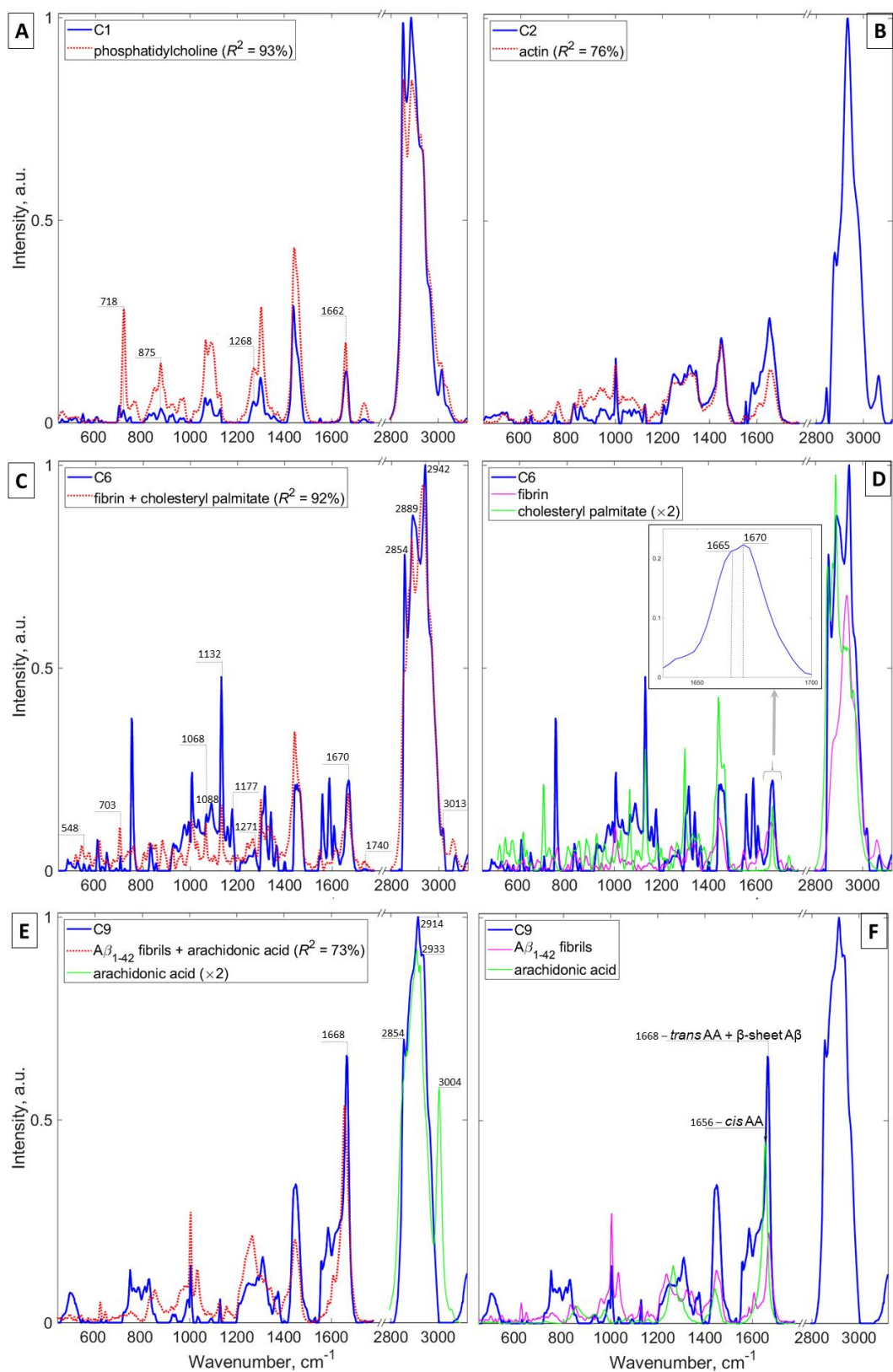


Fig. 6.2: Raman spectra of the chemical components (blue solid lines) colocalizing with hippocampal A β plaques, obtained from the Q-US/PS-NMF analysis of AD human brain tissues together with non-demented controls. C1 (A) has spectral characteristics resembling phosphatidylcholine. C2 (B) resembles actin. C6 (C) is attributed to a mixture of fibrin and saturated lipids with cholesteryl derivatives. C9 (E) can be represented as a mixture of aggregated A β peptide and *trans* lipids such as a *trans* isomer of arachidonic acid. The chemical attribution of components C1, C2, C6 and C9 is based on the comparison with analytical standard Raman spectra of pure chemical species. Fits are shown by the red dotted lines and found using NLS algorithm. Corresponding R^2 are also indicated. The fit in (A) is the Raman spectrum of phosphatidylcholine. The fit in (B) is the Raman spectrum of actin. The fit in (C) is a superposition of fibrin (magenta line) and cholesteryl palmitate (green line); the contributions are shown in the separate figure D. The fit in (E) is a superposition of the Raman spectrum of synthetic A β_{1-42} fibrils (magenta line) and arachidonic acid (green line); the contributions are separately shown in the figure F for the fingerprint region.

The Raman spectrum of C6 exhibits the several diagnostic bands of cholesterol (CHL) backbone and CEs. Specifically, the presence of the CHL backbone is indicated by the co-occurrence of distinct hallmark bands at 548 cm^{-1} , 703 cm^{-1} and 1670 cm^{-1} (the C=C stretch of the cholesterol ring) (Krafft *et al.* 2005; Czamara *et al.* 2015). CE attribution is confirmed by the appearance of characteristic small-intensity band centred at 1740 cm^{-1} assigned to the C=O stretching vibrations of the ester group (Krafft *et al.* 2005). The dominated presence of saturated FAs chains in the composition of C6 is reflected by the occurrence of high/medium intensity bands at 1068 , 1088 , 1132 and 1177 cm^{-1} due to the C-C stretching vibrations that are profound for saturated FAs, compared to a relatively low intensity band at 1271 cm^{-1} and an apparently small shoulder at 3013 cm^{-1} , that are both characteristic features of unsaturated FAs (Krafft *et al.* 2005; Czamara *et al.* 2017). The presence of protein in the composition of C6 is indicated by the occurrence of the amide-like shoulder band at 1665 cm^{-1} typical for the α -helix structured proteins such as collagen and fibrin combined with the band at 2942 cm^{-1} assigned to the CH_3 stretching vibrations of proteins. Possibly, fibrin protein can be present in the chemical composition of C6, which Raman spectrum shows a good similarity in both the positions and shapes of the bands with its pure chemical reference based on NLS algorithm reflected by a high correlation similarity coefficient as well as the presence of characteristic vibrational bands of α -helix structures as discussed above.

For C9 (Fig. 6.2D), the structural hallmark of aggregated amyloid peptide assembled into the cross- β structured fibrils is confirmed by the profound high intensity amide band at 1668 cm^{-1} (Kiskis *et al.* 2015), assigned to the C=O stretching vibrations of the protein backbone, and the missing shoulder located between 1662 – 1655 cm^{-1} , characteristic of the α -helix structured proteins (Rygula *et al.* 2013). For the lipid content, Raman spectrum of C9 spectrally resembles that of AA, which is an essential polyunsaturated FA in the composition of cellular membranes accounting for about 15% of total polyunsaturated FAs content of the phospholipid membranes in brain grey matter (Crawford and Sinclair 1971). Related to disease-associated pathology, AA has been suggested to maintain the fluidity of the cellular membranes (Tremi *et al.* 2018). Importantly, presence of polyunsaturated fats in the *trans* isomerization in C9, known to be massively generated during oxidation of lipid membranes by free radicals (Tremi *et al.* 2018), is indicated by the high intensity band at 1668 cm^{-1} assigned to the C=C stretching vibrations of FAs in the *trans* isomerization (Sadeghi-Jorabchi *et al.* 1991) combined with the lack of the neighbouring band near 1656 cm^{-1} originated from the C=C stretch of FAs in the *cis* configuration (Czamara *et al.* 2015). The oxidation modification of polyunsaturated acid in the composition of C9 is also reflected by the missing band around 3004 cm^{-1} , that is a diagnostic band of unsaturated FAs originated from the =CH stretching vibrations (Krafft *et al.* 2005). Together with the spectral

assignments to a superposition of fibrillar $A\beta_{1-42}$ and AA, my findings suggest the attribution of C9 to a mixture of $A\beta_{1-42}$ fibrils and oxidized *trans* isomer of AA (ox-*trans*-AA).

6.3.2. Spatial distributions of key chemical components in frozen human Alzheimer's disease brains

In this section, I analyse the spatial concentration profiles of the chemical components (C1, C2, C6 and C9) across AD and non-demented patient groups in the hippocampal brain region. Fig. 6.3- Fig. 6.6 show overview results of all unmixed 3D Raman images, retrieved from the simultaneous Q-US/PS-NMF analysis that allowed to retrieve the chemically specific 3D concentration maps of AD human brain tissues affected by $A\beta$ pathology and non-demented controls. In order to illustrate 3D distribution of C1, C2, C6 and C9 in human brains, each unmixed z-stack composite has been imaged into the representative planes as AD1_01z1, AD1_01z2, AD1_01z3;...; C1_01z01-z10 (see Section 6.2 for details on the acquired images) for each resolved component as shown in Fig. 6.3 - Fig. 6.6. A typical step between neighbour planes was 3 μm , except for the AD1_01z1-z3 stack, where a 5 μm step was used. Note, relative Raman concentrations are obtained from the Q-US/PS-NMF analysis, by applying the normalization such that the mean total concentration is equal to unity (see Section 6.2.3 and Section 3.4 (Chapter 3) for details).

In general, the spatial concentration profiles of unmixed Raman images revealed the high lipid content of the human brain tissues distributed throughout the brain regions. In particular, C1, representing unsaturated PC-rich lipid bodies, is found to be one of the main constituents of the hippocampus (see Fig. 6.3). Its representative concentration maps show a rather uniform distribution over the human non-demented brains that remind the cell morphology (see the C1_01z01-z10 images in Fig. 6.3) compared to a more dispersed spatial pattern for the AD tissues with distinct accumulations of individual lipid droplets as clearly observed from the AD1_02z1-z4 images of Fig. 6.3. Another lipid-rich component (C6), representing a lipoprotein with a high CE content, appears to be the plaque-associated one that tightly envelopes the plaque core as visually observed from the spatial distribution of the AD1_01z1 image in Fig. 6.5.

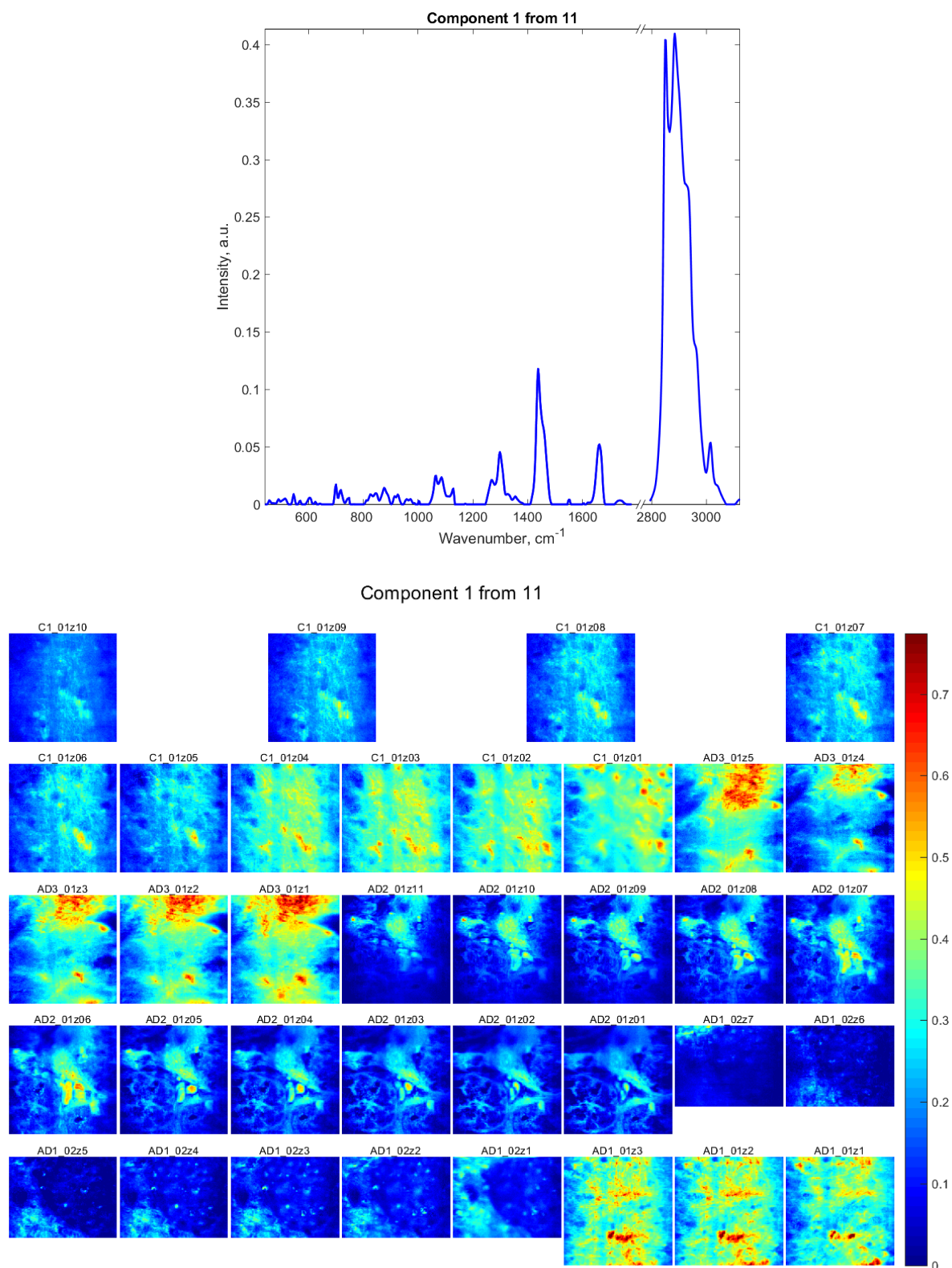


Fig. 6.3: 3D spatial distributions of the Raman concentration and the corresponding component spectra of C1 from the measured AD hippocampal brain regions and non-demented controls labelled according to the sample source as AD1, AD2, AD3, and C1 on colour scales as indicated, retrieved from the simultaneous Q-US/PS-NMF unmixing analysis of 3D Raman images of the human AD tissues affected by A β pathology together with non-demented control regions. 3D distribution is shown by a sequential representation of each image plane of a representative z-stack as AD1_01z1, AD1_01z2, AD1_01z3;...; C1_01z01-z10. A typical step between neighbour planes was 3 μm , except for the AD1_01z1-z3 stack, where a 5 μm step was used. In all panels, a typical image size is 127 \times 127 μm^2 , except for the AD1_02z1-z7 images of a 127 \times 98 μm^2 in size.

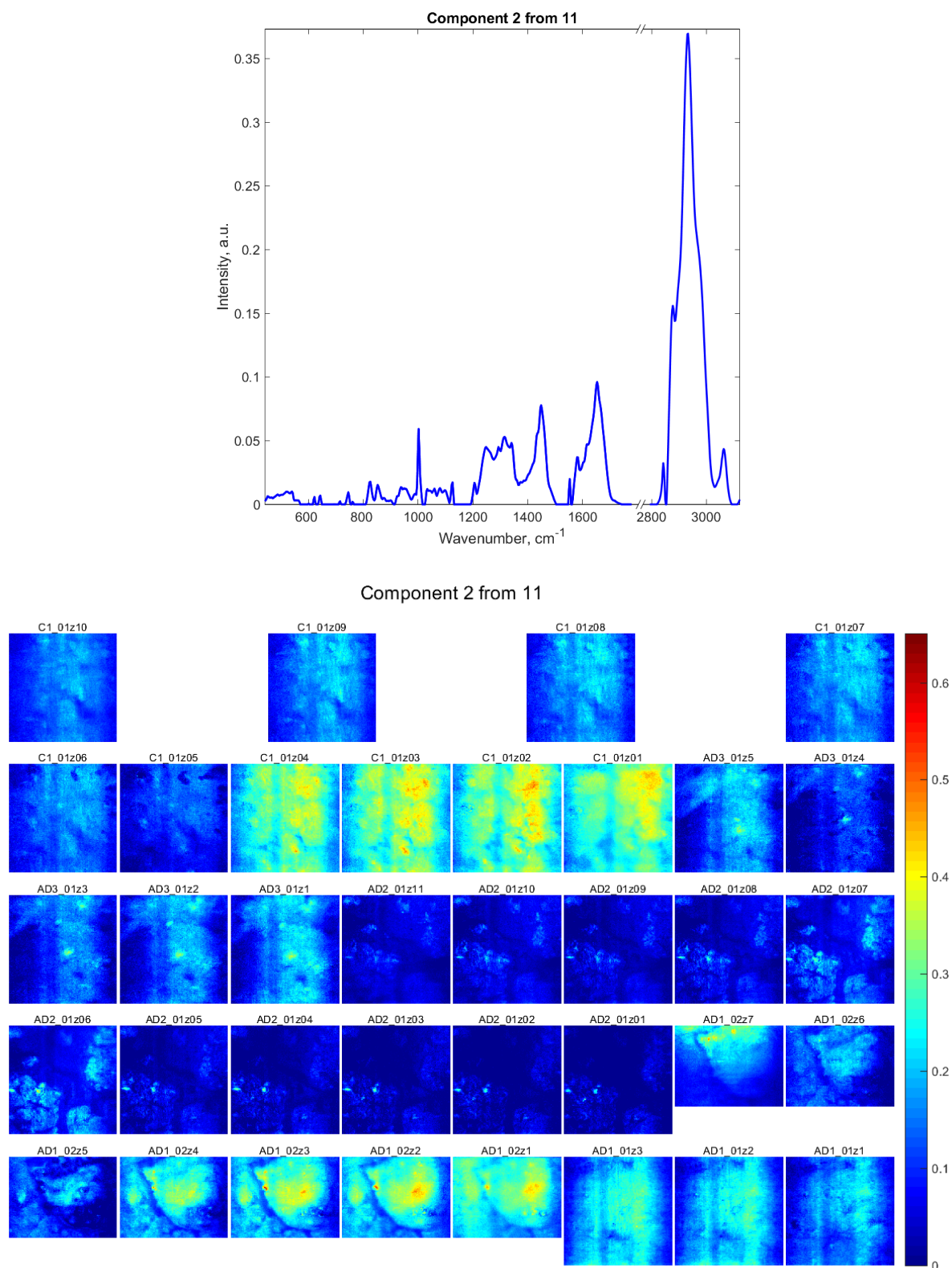


Fig. 6.4: 3D spatial distributions of the Raman concentration and the corresponding component spectra of C2 from the measured AD hippocampal brain regions and non-demented controls labelled according to the sample source as AD1, AD2, AD3, and C1 on colour scales as indicated, retrieved from the simultaneous Q-US/PS-NMF unmixing analysis of 3D Raman images of the human AD tissues affected by A β pathology together with non-demented control regions. 3D distribution is shown by a sequential representation of each image plane of a representative z-stack as AD1_01z1, AD1_01z2, AD1_01z3;...; C1_01z01-z10. A typical step between neighbour planes was 3 μ m, except for the AD1_01z1-z3 stack, where a 5 μ m step was used. In all panels, a typical image size is 127 \times 127 μ m², except for the AD1_02z1-z7 images of a 127 \times 98 μ m² in size.

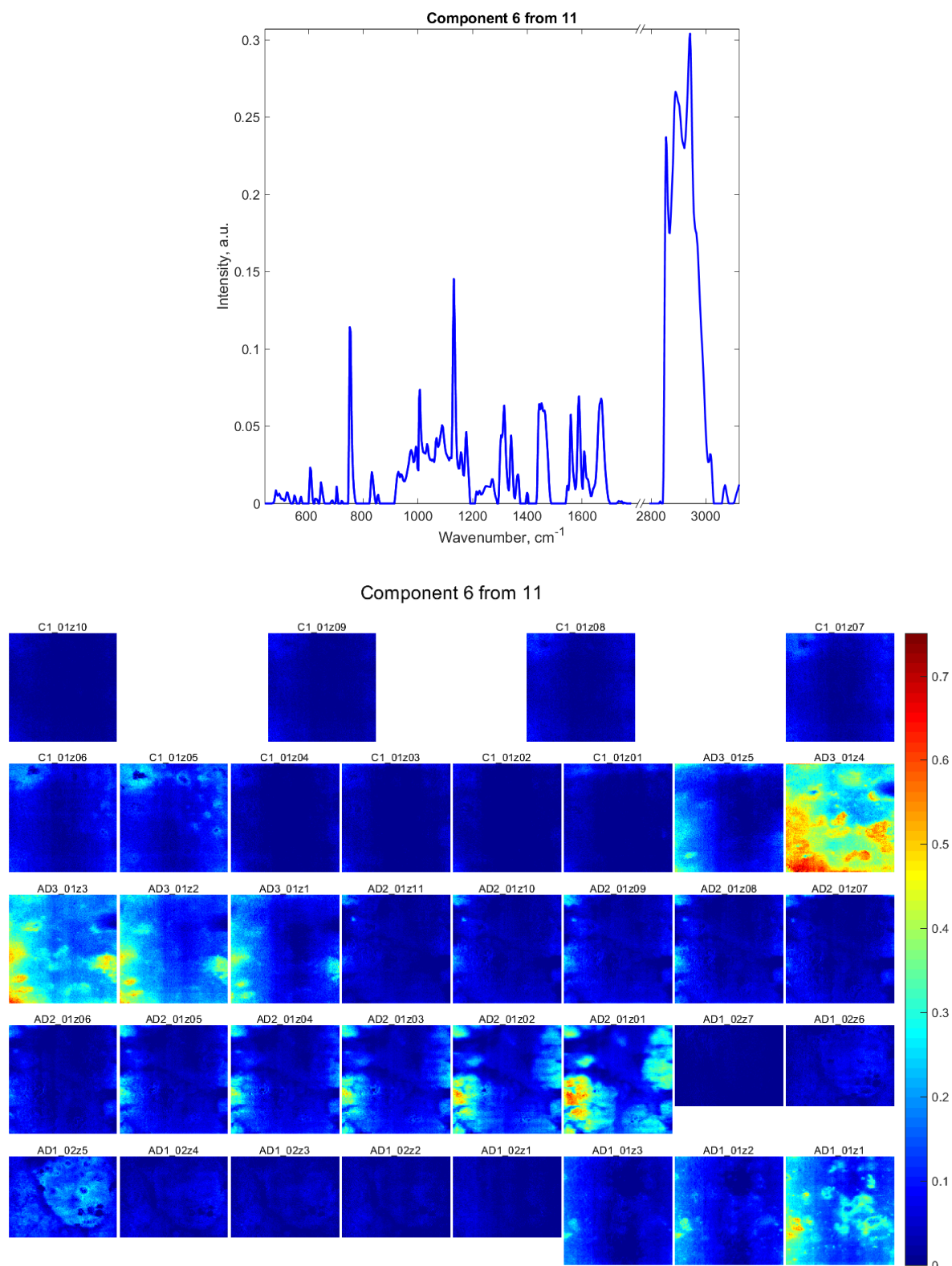


Fig. 6.5: 3D spatial distributions of the Raman concentration and the corresponding component spectra of C6 from the measured AD hippocampal brain regions and non-demented controls labelled according to the sample source as AD1, AD2, AD3, and C1 on colour scales as indicated, retrieved from the simultaneous Q-US/PS-NMF unmixing analysis of 3D Raman images of the human AD tissues affected by A β pathology together with non-demented control regions. 3D distribution is shown by a sequential representation of each image plane of a representative z-stack as AD1_01z1, AD1_01z2, AD1_01z3;...; C1_01z01-z10. A typical step between neighbour planes was 3 μm , except for the AD1_01z1-z3 stack, where a 5 μm step was used. In all panels, a typical image size is 127 \times 127 μm^2 , except for the AD1_02z1-z7 images of a 127 \times 98 μm^2 in size.

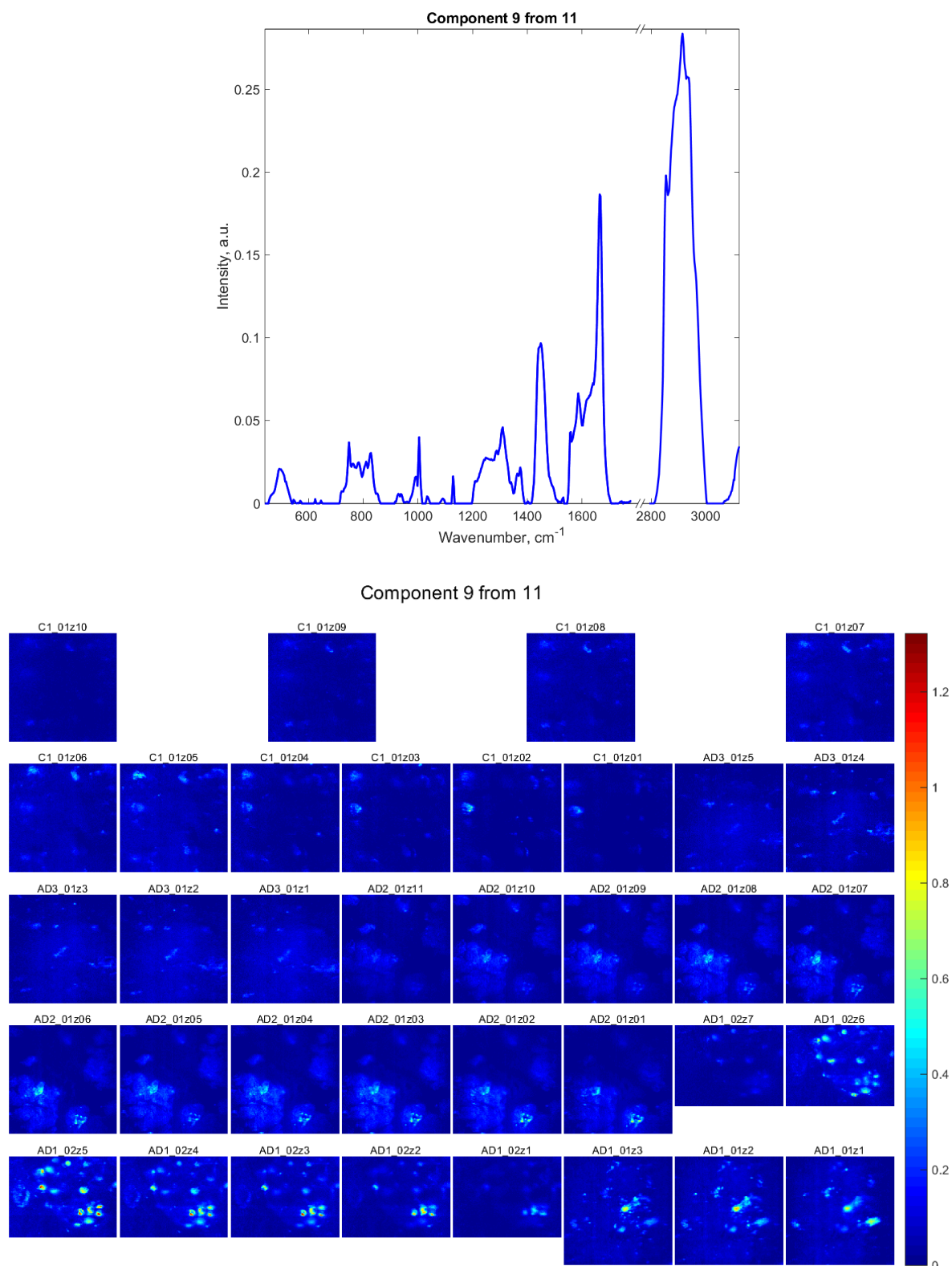


Fig. 6.6: 3D spatial distributions of the Raman concentration and the corresponding component spectra of C9 from the measured AD hippocampal brain regions and non-demented controls labelled according to the sample source as AD1, AD2, AD3, and C1 on colour scales as indicated, retrieved from the simultaneous Q-US/PS-NMF unmixing analysis of 3D Raman images of the human AD tissues affected by A β pathology together with non-demented control regions. 3D distribution is shown by a sequential representation of each image plane of a representative z-stack as AD1_01z1, AD1_01z2, AD1_01z3;...; C1_01z01-z10. A typical step between neighbour planes was 3 μm , except for the AD1_01z1-z3 stack, where a 5 μm step was used. In all panels, a typical image size is 127 \times 127 μm^2 , except for the AD1_02z1-z7 images of a 127 \times 98 μm^2 in size.

As for the amyloid component, C9 that is assigned to a mixture of fibrillar A β_{1-42} species and oxidized polyunsaturated *trans* lipids is observed to form the highly concentrated plaque core with condensed, densely packed content of these co-aggregated components (see Fig. 6.6). For example, the spatial distribution of this component for the images the AD1_01z1-z3 representing AD group shows the classical morphology of the so-called “dense core A β plaque” (D’Andrea and Nagele 2010). This type of plaque is believed to have an increased ability to attract immune cells such as microglia compared to other ones (D’Andrea and Nagele 2010). As an example of intracellular A β deposits, the concentration maps of C9 for the images AD1_02z1-z7 show significant accumulations of these amyloid-lipid species apparently within the cell bodies of neurons. In the supplementary material I included a 3D volume view of chemical C9 (red) and C1 (blue) generated based on the AD1_02z1-z7 Raman images, projecting the spatial volumetric distribution of intracellular A β protein aggregated with oxidised polyunsaturated *trans* lipids (C9) within the neuronal cells that colocalize with the phosphatidylcholine-rich lipid droplets (C1).

In the non-demented control regions, the concentration map of this mixed component (C9) show some non-zero Raman concentrations (see the C1_01z01-z10 images in Fig. 6.6) which values are comparable to that for the AD3 sample. This might be due to a dominated content of the oxidized lipids in a mixed C9 for the non-demented control sample compared to the amyloid fraction. Therefore, the Raman concentrations observed in the control sample represent largely the accumulations of lipids. Furthermore, these oxidized polyunsaturated lipid domains in the composition of C9 show granular distribution that is colocalized to the cellular membranes outlining the cell shape as can be deduced from the C1_01z03 image in Fig. 6.6. Of note, these evident changes observed as amyloid-lipid micro-domains deposited in the cells of the non-demented tissues might possibly indicate early signs of AD pathology, that can be important for early diagnosis of AD.

For C2, found to be rich in actin, the spatial distributions of this component across AD and non-demented tissues exhibit relatively uniform spatial pattern of Raman concentrations (Fig. 6.4). Interestingly, the concentration maps of this component for the AD1_02z1-z7 images show the significant accumulations of actin that form the ellipsoid-shape cloud of possibly cell lysis material, surrounding the A β -positive neurons. This accumulation material of actin content might be originated from the dead cells that underwent the pro-inflammatory programmed cell death (pyroptosis) involving the release of lytic cellular content.

To show colocalization of the A β and lipid components with the pro-inflammatory ones in human AD brain tissues, I show absolutely label-free Raman image, encoding the concentrations of C9

(A β species co-aggregated with oxidized *trans* isomers of AA) in green and C6 (the CE-rich lipid domains) in red, in comparison to the high-resolution fluorescence images of the A β stained (green) plaques co-labelled for either microglia (Iba1, blue) and gasdermin D (GSDMD) (red) (see Fig. 6.7A) or ASC specks (red) (see Fig. 6.7C). The inspection of these images together indicates that the CE-rich lipid bodies in the label-free Raman image localize to the pro-inflammatory microglia that tightly envelop the plaque core. Together with colocalization to the microglial processes, the CE halo is observed spatially correlating with the accumulations of the pore-forming GSDMD, characteristic of cell pyroptosis, and ASC specks, indicative of the canonical inflammasome activation such as NLRP3, both colocalizing to the microglial membranes. These observations indicate the link between the abnormal accumulations of CE lipids around the plaque core and the pro-inflammatory processes both induced by the A β pathology in human AD brains.

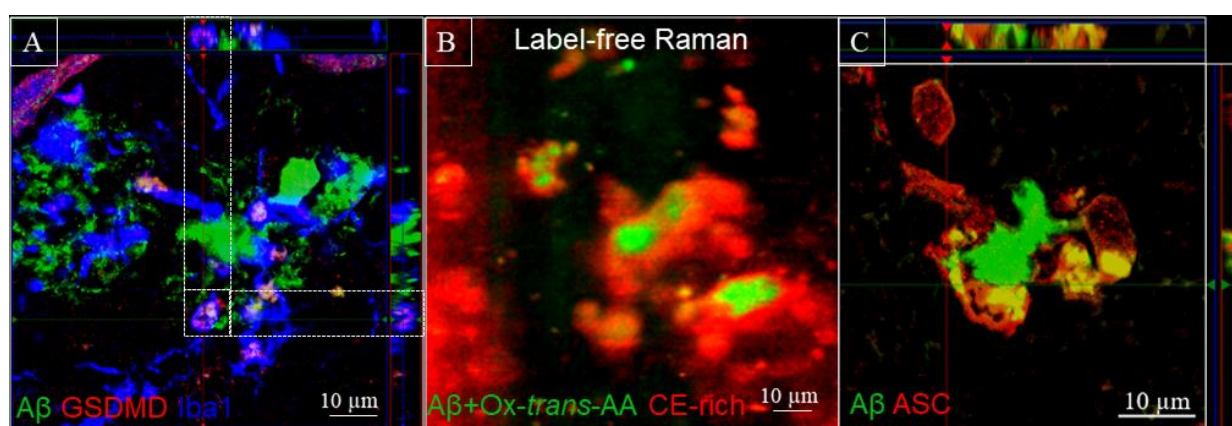


Fig. 6.7: Unmixed label-free Raman image of the plaque composition (B) in human AD brains: the core enriched with A β fibrils and oxidized *trans* polyunsaturated lipids such as AA (green) and the surrounding halo composed of lipoproteins with high CEs content (red). Combined fluorescence images of A β -stained (green) plaques co-labelled for GSDMD (red) and microglia (blue) (A) as well as ASC specks (red) (C), showing the localization of ASC specks and pore-forming GSDMD (indicated by white square) to the microglial membranes all correlated to the sites of the CE-rich plaque halo in the representative Raman image (B), indicating pyroptotic cell death of highly inflammatory immune response around the plaque. In panel B, Ox-*trans*-AA = oxidized trans isomer of arachidonic acid.

6.4. Findings

Frozen human brain tissues in AD were investigated using label-free confocal Raman microspectroscopy. 3D Raman images of A β deposits surrounded by lipidomic environment were measured and chemically unmixed to retrieve individual biochemical profiles of the pathological brain composition. In relation to extracellular amyloid, my results revealed that the plaque core mainly consists of a mixture of aggregated A β ₁₋₄₂ protein and oxidatively-modified arachidonic

acid in the *trans* isomerization, representing one component. Similarly, my analysis allowed to resolve the accumulations of intracellular A β_{1-42} aggregates co-depositing with oxidised polyunsaturated *trans* lipid bodies within the cell bodies of neurons. Also here, Raman imaging enabled to distinguish the ellipsoid-shaped cloud surrounding the A β -positive neurons consisting of actin, possibly representing the lytic material of dead cells underwent the programmed pro-inflammatory cell death (pyroptosis).

Importantly, co-deposition of A β_{1-42} fibrils with oxidised polyunsaturated lipids in one component possibly indicate a close interaction between these two. Importantly, oxidation status of the lipids within the A β aggregate is confirmed by the presence of the enhanced Raman band at 1668 cm⁻¹, implicated during lipid peroxidation (Muik *et al.* 2005), combined with the lack of the Raman band around 3004 cm⁻¹, indicative of unsaturated FAs or the loss/absence of C=C double bonds (Brozek-Pluska *et al.* 2012), occurring during oxidation with generation of saturated lipid bio-products. The significant accumulations of the oxidatively-modified arachidonic acid with pathogenic A β fibrils shown in this study might point to unresolved neuroinflammation and oxidative damage implicated in human AD brains in response to the chronic A β deposition. It is important to note that the results showing the accumulation of the oxidation lipid products derived from AA colocalizing with the aggregated A β protein within the plaque core and neuronal cell bodies, revealed the strong dysregulation of AA lipid pathways previously documented to be implemented in the AD pathogenesis. Indeed, a natural *cis* isomer of AA is known as a key component of phospholipid cellular membranes that maintains their fluidity and integrity whereas the *trans* configuration of AA embedded into the cell membranes was suggested to cause the decreased membrane fluidity and permeability with a more rigid packing, that might be detrimental for the cell survival (Tremi *et al.* 2018). In the healthy brain, AA shows anti-oxidative properties by activating a peroxisome proliferator-activated receptor gamma (Wang *et al.* 2006) and a syntaxin-3 (STX-3) protein implicating in the neuron growth and repair (Darios and Davletov 2006). To that end, the disturbance of AA pathways possibly through peroxidation induced by toxic A β accumulation in the human brain might trigger the AD pathogenesis, which is consistent with my findings.

The halo of the plaque is revealed to consist of predominantly lipids in spectral characteristics resembling CEs, that tightly envelope the A β core. Using high-resolution fluorescence microscopy in combination with confocal Raman micro-spectroscopy, I demonstrate that the CE-rich lipid aggregates localize to the pro-inflammatory microglia processes surrounding the plaque core and are found to spatially correlate with numerous pore-forming GSDMD, indicative of pyroptosis, and ASC specks, reflecting the canonical inflammasome activation such as NLRP3, both colocalizing to the microglial membranes. This finding of the significant accumulation of CE lipids

within microglia colocalizing with pro-inflammatory oligomerized proteins such as GSDMD and ASC specks around the plaque core might point to a cross-talk between these neuroinflammatory cell death-inducing proteins and aberrant lipid aggregates together able to strongly amplify neuroinflammation and oxidative damage in human AD brains, ultimately causing neurodegeneration. One possible mechanism of their relationship might be suggested, representing the hypothetic chronic cycle of AD pathogenesis. To begin with, it is widely accepted that AD pathogenesis started from the deposition of aggregated A β proteins, that are sensed by the NLRP3 inflammasome as a pathogenic danger signal (Halle *et al.* 2008). Indeed, the receptors of the innate immune system have been evolutionally programmed to sense surface amyloid, that is abundant in many bacteria (Sleutel *et al.* 2017). Applied to AD-associated amyloidosis, assembly of the NLRP3 inflammasome triggered by pathogenic A β leads to accumulation of pro-inflammatory cytokines, that are believed to shift a microglia state to the pro-inflammatory one with decreased phagocytic capacity (Cherry *et al.* 2014). Consequently, this results in impaired A β clearance by these pro-inflammatory microglia processes, that significantly contribute to accumulation of damage-associated molecular patterns (DAMPs) signals and lysosomal damage (evident by aberrant intracellular lipid build-up of lysosomal membrane oxidation material), that are in turn able to further alarm the NLRP3 inflammasome and therefore amplify neuroinflammation (Sarlus and Heneka 2017). Here, the unresolved neuroinflammation represent a conserved pattern of A β -induced toxicity, which all together lead to neurodegeneration. It is also important to note that the mechanism of neuronal cell death implicated in AD pathogenesis possibly can be driven by lysosomal membrane rupture (Aits and Jaattela 2013), evident by aberrant intracellular build-up of lipids from oxidised lysosomal membranes within enlarged, swollen neurons and immune cells (Jerome *et al.* 1998). Lysosomal membrane oxidation can be in turn initiated through either the interaction of A β oligomers with lipid cellular membranes or the A β -induced inflammatory bio-products such as ROS with lysosomal membranes (Oku *et al.* 2017). To that end, the distinct CE lipid halo around the A β core revealed by label-free Raman micro-spectroscopy in this chapter colocalizing with strongly activated pro-inflammatory components of human AD brains might reflect lysosomal membrane oxidation of surrounding the plaque cells, leading to their death and contributing to unresolved neuroinflammation. To link A β accumulation to specific inflammatory pathways my next two study chapters will present the results of correlative fluorescence imaging of immuno-stained inflammatory components in A β plaques of post-mortem human AD brains.

Chapter 7. Correlative fluorescence imaging of amyloid- β with ASC speck and microglia in human Alzheimer's disease brains: inflammatory response to amyloid- β aggregation

7.1. Introduction

Despite the long-standing model for A β -associated pathogenesis in AD, inflammatory and immunological processes are considered by many of not just mere bystanders but the central players in the initiation and progression of AD (Weiner and Frenkel 2006).

The innate immune response to accumulation of pathogenic A β protein in AD brain begins with activation of resident phagocytic cells such as microglia (Sarlus and Heneka 2017). To induce phagocytosis of misfolded A β aggregates, microglia express a variety of cellular PRRs including but not limited to cytosolic NOD-like receptors such as NLRP3 (Halle *et al.* 2008; Heneka *et al.* 2013). On molecular level, the recognition of amyloid- β by the NLRP3 domain induce its assembly with ASC and pro-caspase-1 proteins into the large protein complex called the NLRP3 inflammasome (Latz 2010). NLRP3 activation initiates processing of pro-caspase-1 into active caspase-1 through interaction with ASC filaments. Active caspase-1 in turn cleaves pro-IL-1 β and pro-IL-18 into the mature cytokines known as key mediators of neurotoxicity in “inflamed” brain (Latz 2010). Caspase-1 activation also produces a fragment of pore-forming gasdermin D that enables the release of the mature IL-1 β , IL-18 and ASC specks through the gasdermin pores in the membrane of affected cells in the process of a pyroptotic cell death (Shi *et al.* 2015). In the extracellular space, ASC specks preserve their capability to mature pro-IL-1 β following their ingestion by macrophages, from where ASC specks initiate a pro-inflammatory cascade (Franklin *et al.* 2014). Therefore, targeting molecules of the innate immune system that are involved in the regulation of the pro-inflammatory cascade are of great interest to therapy, as that could shift the immune response into the neuroprotective one preventing neurodegeneration.

Not only do ASC specks responsible for caspase-1 activation during the NLRP3 inflammatory signalling serve as a key regulator of inflammatory responses but they are also believed to promote A β aggregation. Recent discovery using an AD mouse model (Venegas *et al.* 2017) proposed a new model of AD pathogenesis according which extracellular ASC micro-domains spread A β

toxicity by seeding a new A β nucleation. The consistence with this hypothesis has been shown in the same study demonstrating the effectiveness of anti-ASC speck immunotherapy tested in the FAD mice for blockage of A β pathology spreading.

The aim of this chapter is to link A β pathology spreading and defective microglial A β phagocytosis to specific inflammatory pathways in human AD brains. Spatial colocalization and 3D distribution patterns of the three AD hallmarks at the sites of A β plaques will be examined and quantified using high-resolution fluorescence microscopy. For this, co-immunostaining of the ASC speck neuroinflammatory complex, pathogenic A β protein and microglia will be performed in post-mortem human AD brain and non-demented control to determine the significance of a pro-inflammatory microglia phenotype in the areas of A β pathology and a degree of colocalization of ASC specks with A β .

7.2. Method

7.2.1. Human tissue samples

Human brain tissue was sourced from the Thomas Willis Oxford Brain Collection (TWOBC), which is part of the Medical Research Council (MRC) Brain Bank Network, with the ethical approval of the Research Tissue Bank provided by the Oxford Brain Bank (OBB) Access Committee. Formalin-fixed-paraffin embedded brain slices of 5 μ m thickness were participated in this study. The diseased cohort was represented by the samples of two brain regions (hippocampus and frontal lobe) collected from 5 AD patients. For control experiment, the non-demented control samples from the subjects without AD were also included in the study.

7.2.2. Immunohistochemistry

For immunofluorescent staining of formalin-fixed-paraffin-embedded brain sections, the following protocol has been used:

1. Formalin fixed brain tissue (5 μ m thick) slides were deparaffinized using a standard dewaxing protocol consisting of three consecutive steps: 1) heating at 60-70 °C in a pre-heated oven for 1 hour; 2) removing the paraffin in xylene (two cycles for 20 minutes each); 3) rehydrating in a sequence of 100%, 90% and 70% ethanol for 5 minutes each, followed by three times washing in distilled water for 5 minutes each.
2. Heat-induced epitope retrieval in boiling DAKO solution: deparaffinized brain sections were transferred to 1X DAKO/PBS (pH 6.2) target retrieval solution (REF S1699 – 10X

concentrate) and then incubated in a preheated to and maintained at 90 °C water-bath for 45 minutes, followed by cooling down in the solution for 20 minutes;

3. Sections were washed three times for 5 min each in 1X PBS (pH 7.4) and blocked in 1X PBS/1% BSA/0.1% Triton X-100 (or 0.1% Saponin) (Blocking Buffer) for 30 min followed by 2 hours incubation with all primary antibodies in Blocking Buffer.
4. Sections were washed three times in 1X PBS/0.1% Triton X-100 (Wash Buffer), and incubated with Alexa- 488, 546 and 633 conjugated donkey secondary antibodies (Invitrogen, 1:400, 5 µg/ml) diluted in Blocking Buffer for 90 min, followed by three times washing in Wash Buffer for 5 min each.
5. Sections were mounted using Immu-Mount (Thermo).

The following combination of primary antibodies for triple immunofluorescence staining of A β , ASC speck and Iba-1 was used with respective concentrations:

- mouse monoclonal anti-A β (6E10, BioLegend Catalog# 803004, 1:200, 5 µg/ml)
- rabbit polyclonal anti-ASC (AL177, AdipoGen, 1:200, 5 µg/ml),
- goat monoclonal anti-Iba1 (AIF-1/Iba1, Novus Biologicals, 1:200, 2.5 µg/ml)

7.2.3. Laser-scanning confocal fluorescence microscopy instrumentation

High-resolution fluorescence microscopy was performed on a LSM 710 inverted confocal laser scanning microscope (Zeiss) using 100X/ NA 1.46 oil objective (0.23 µm lateral resolution at $\lambda = 0.550$ µm). Images were acquired with an 8-bit colour depth, a view of 512×512 pixels, and 0.17 µm pixel size, which results in an 85×85 µm² image size. All images were taken using a z-stack mode with a step of 0.5 µm in z-direction. Emission of fluorescently labelled antibodies were acquired sequentially.

7.2.4. Analysis

Z-stack images were processed using Zen 2.5 lite imaging software. The regions of A β , microglial processes and ASC speck immunoreactivity were determined using a threshold at 20% value of the deviation from a representative exponentially decaying distribution histogram of A β , microglia and ASC speck fluorescence intensities. For comparison of results, the threshold at 3 STD, 1.5 STD and 3 STD of A β , microglia and ASC speck total distribution histograms, respectively, were used as described in (Condello *et al.* 2015). The results of both methods are checked to produce

equivalent results. The example of the areas representing the plaque core and halo, determined as a difference of the whole plaque and its core diameters, for one cortical and one hippocampal plaque is shown in Fig. 7.1A, B. The images of the thresholded A β , microglia and ASC speck fluorescence intensities for the same plaques are also given in Fig. 7.1.

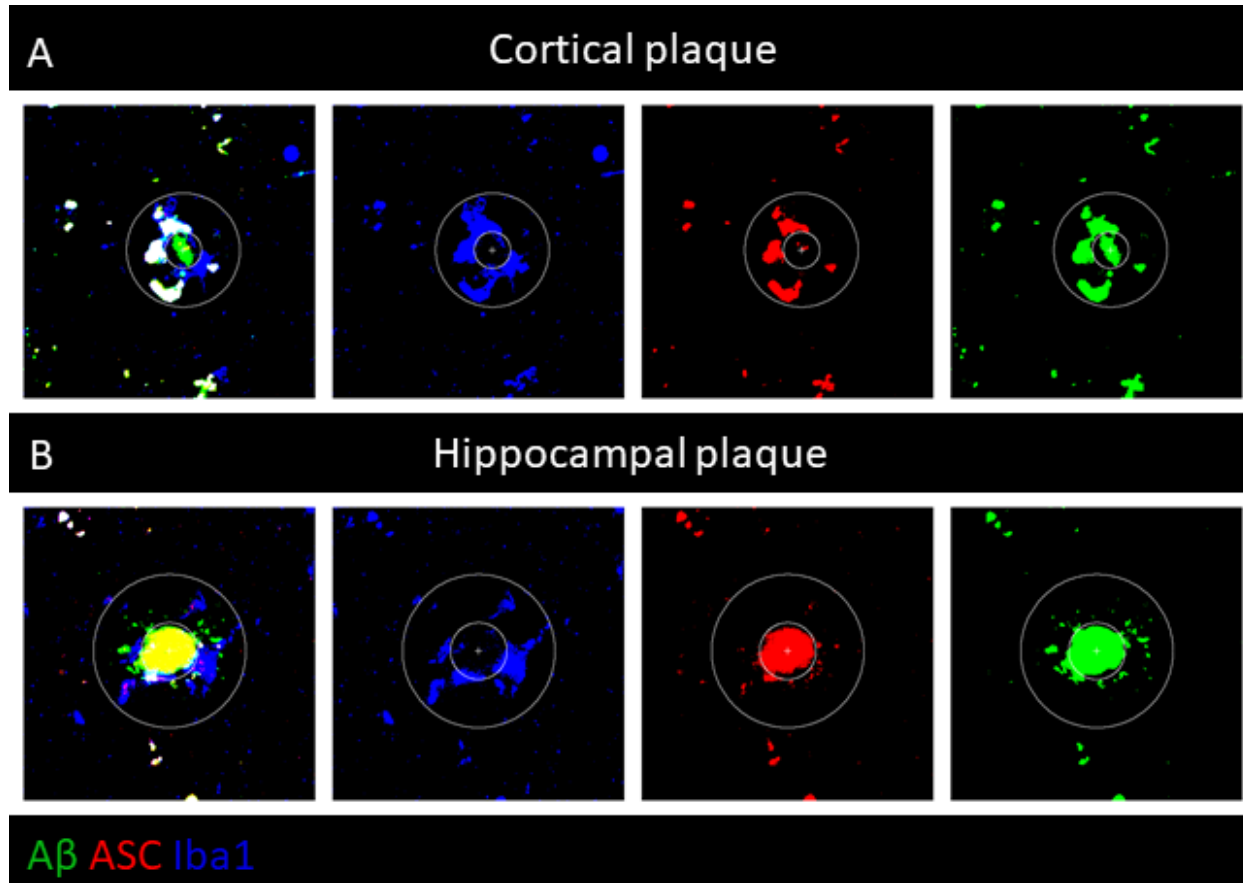


Fig. 7.1: Individual and merged channels fluorescence images of the thresholded A β , microglia and ASC speck fluorescence intensities for one cortical (A) and one hippocampal (B) plaques. In all panels, the white circles of smaller and larger radius indicate the area of plaque core and halo, respectively, selected for the quantification.

For AD group of samples, the relative volume of antibody reactivity inside the whole plaque/plaque core or its halo was determined as a sum of the representative pixel intensities above the threshold within the corresponding plaque area divided by this area were calculated. For non-demented hippocampal controls, the equivalent approach was used. The comparison of the relative volumes between AD and non-demented samples was performed through quantification of plaque (AD) versus non-plaque control (non-AD) regions using two-sample two-tailed *t*-test with unequal variances. To examine correlation/colocalization of the immunolabelled A β , ASC specks, and Iba-1-labeled microglia, the following quantities were calculated for each plaque region:

1. As a measure of how A β plaques are covered by microglia processes, the volume of the A β covered by microglia within the whole plaque, the plaque core and its halo normalised on the microglia-positive volume in the corresponding region ($V_{\text{microglia+A}\beta}^{\text{plaque}}/V_{\text{microglia}}^{\text{plaque}}$)

- versus the volume of the A β un-covered by microglia within the same area normalised on the microglia-negative volume within this area ($V_{A\beta\text{-microglia}}^{plaque}/1 - V_{\text{microglia}}^{plaque}$).
2. As a measure of ASC speck colocalization with A β , the volume of the ASC specks colocalizing with A β within the whole plaque, the plaque core and its halo normalised on the A β -positive volume in the corresponding region ($V_{ASC+A\beta}^{plaque}/V_{A\beta}^{plaque}$) versus the volume of the ASC specks non-colocalizing with A β within the same area normalised on the A β -negative volume within this area ($V_{ASC-A\beta}^{plaque}/1 - V_{A\beta}^{plaque}$).
 3. As a measure of A β colocalization with ASC specks, the volume of the A β colocalizing with A β within the whole plaque, the plaque core and its halo normalised on the ASC speck-positive volume in the corresponding region ($V_{ASC+A\beta}^{plaque}/V_{ASC}^{plaque}$) versus the volume of the A β non-colocalizing with A β within the same area normalised on the ASC speck-negative volume within this area ($V_{A\beta-ASC}^{plaque}/1 - V_{ASC}^{plaque}$).
 4. As a measure of correlation/colocalization among microglia, A β and ASC specks: correlation coefficient of microglia-A β -ASC specks colocalization within the selected region according to the formula: $V_{\text{microglia}+A\beta+ASC}^{plaque}/\sqrt[3]{V_{\text{microglia}}^{plaque} V_{A\beta}^{plaque} V_{ASC}^{plaque}}$.
 5. As a measure of a shifted microglia state to the pro-inflammatory phenotype with decreased phagocytic capacity (i.e. the reduced A β clearance function): (1) the volume of microglia processes colocalized with A β and ASC specks within the whole plaque, the plaque core and its halo divided by the volume of microglia colocalized with A β in the same area (indicative of pro-inflammatory phenotype), determined as $V_{\text{microglia}+A\beta+ASC}^{plaque}/V_{\text{microglia}+A\beta}^{plaque}$, $V_{\text{microglia}+A\beta+ASC}^{core}/V_{\text{microglia}+A\beta}^{core}$ and $V_{\text{microglia}+A\beta+ASC}^{halo}/V_{\text{microglia}+A\beta}^{halo}$.

To confirm the statistical significance of the observed effect, the representative quantities has been investigated between the hippocampal versus cortical plaque regions of AD brain tissues. A total of 42 cortical and 61 hippocampal plaques from four AD patients were included in the quantification. As a control group, 13 fluorescence images of the hippocampus from one non-demented control subject were also included in the analysis.

7.3. Results

In general, the A β plaque regions of the human AD brain tissues are found to be enveloped by activated microglia processes, which are strongly correlated with the co-deposits of the A β -ASC specks of about 4 μ m average size within the microglial soma (see Fig. 7.2, for example).

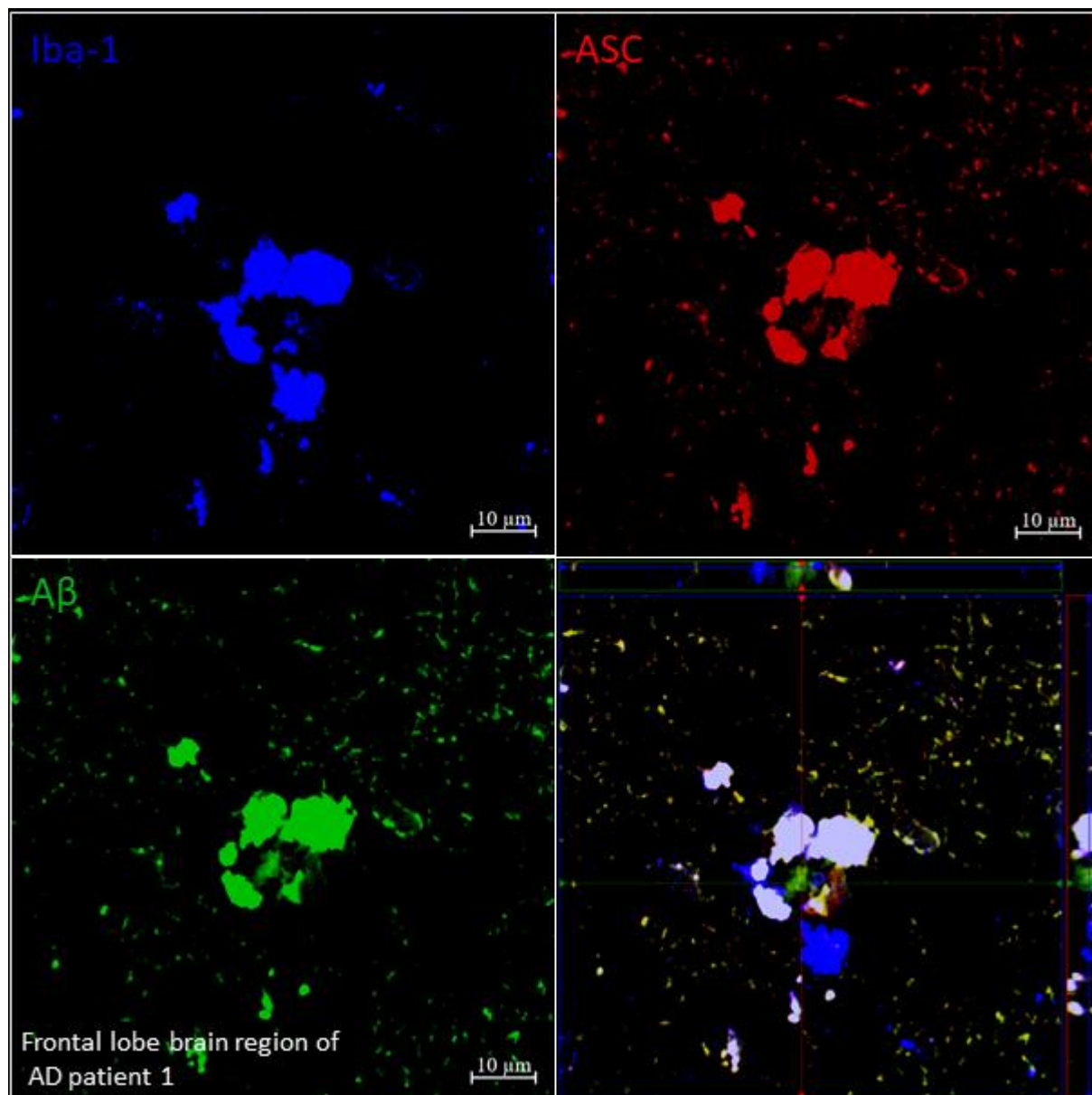


Fig. 7.2: Individual and merged channels fluorescence images of activated microglia (Iba1, blue) and ASC specks (AL177, red) around A β plaque (6E10, green) in the frontal lobe brain region of a patient with AD. Colocalization of anti-A β /ASC specks within Iba1-positive microglia supports the hypothesis of inflammasome activation in response to A β aggregation. Scale bars, 10 μ m.

In particular, activated microglia found in a close proximity to the A β plaque regions contain numerous assembled ASC (see Fig. 7.3), therefore indicating that the microglial phagocytosis of A β aggregates triggers the inflammasome activation within the microglia in the human AD brains, involving the formation of the ASC specks in their soma.

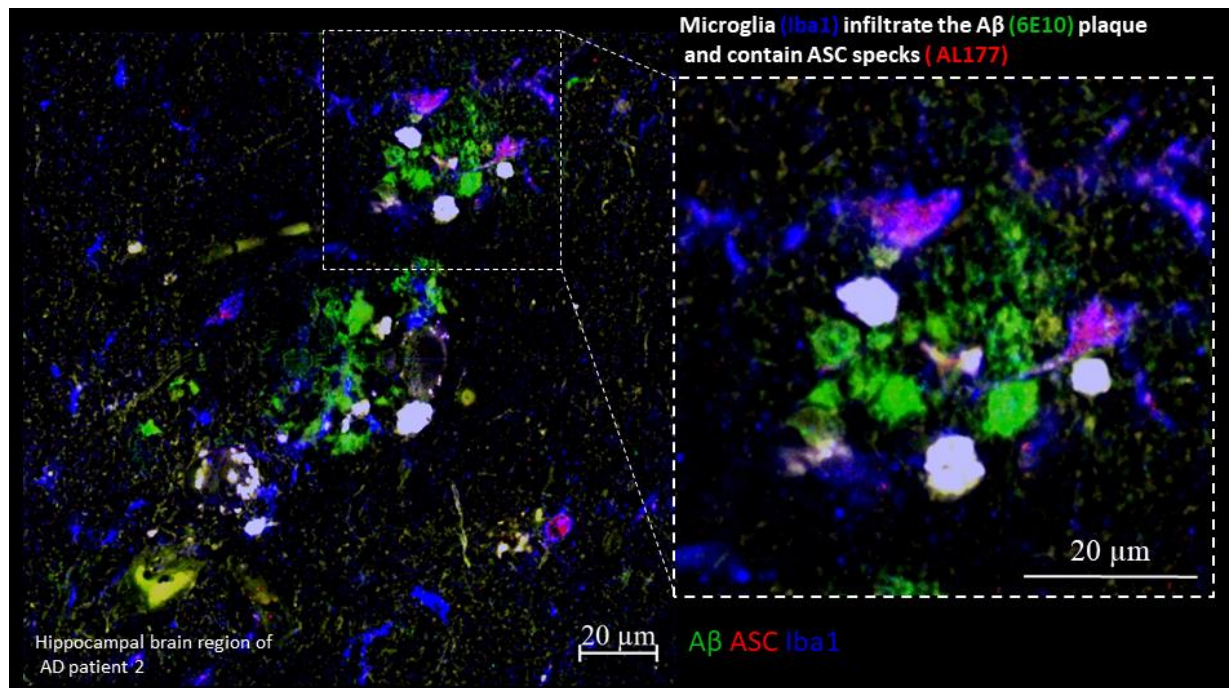


Fig. 7.3: Representative fluorescence image of co-deposition of A β with ASC speck-positive microglia in the hippocampal brain region of a patient with AD. The zoom of the outlined image area is shown on the right and indicates the inflammasome activation within microglia in close proximity to the A β plaque resulting in the distinct ASC speck formations. Scale bars, 20 μ m.

The cores of A β plaques appear to contain multiple micro-scale clusters of the ASC specks of various sizes, which are integrated into the plaque core and surrounded by the A β fibrils (see Fig. 7.4A-C).

To quantify the observed effects, the comparisons of the relative microglia, ASC speck and A β -positive volumes within the plaque core, halo and whole plaque for cortical versus hippocampal plaques of AD human brains are performed using histogram distributions (upper panels) and two-sample two-tailed *t*-test with unequal variances (Fig. 7.5A-C). The results of *t*-test represented as mean \pm the standard error of mean (SEM) are shown in the lower panels of Fig. 7.5A-C. The significant difference of each antibody reactivity for hippocampal plaque (AD) versus non-demented control (non-AD) regions is also demonstrated in Fig. 7.5A-C (lower panels) indicated by *p*-values of $2.1 \cdot 10^{-10}$, $9.7 \cdot 10^{-11}$ and $1.6 \cdot 10^{-13}$ for microglia, ASC speck and A β channels, respectively. The analysis was based on the quantification of 42 hippocampal and 61 cortical plaques from four AD patients. Control regions were represented by 13 fluorescence images from one non-demented control subject. As can be deduced from Fig. 7.5, cortical plaques have significantly more compact core and a stronger activation of microglia processes and ASC specks in the halo compared to the hippocampal plaques. However, the microglial coverage throughout A β plaque regions is found to be extremely low accounting for about 5% and 4.5% in the core and 8% and 5% in the halo in average for the cortical and hippocampal plaques, respectively (see Fig. 7.5A).

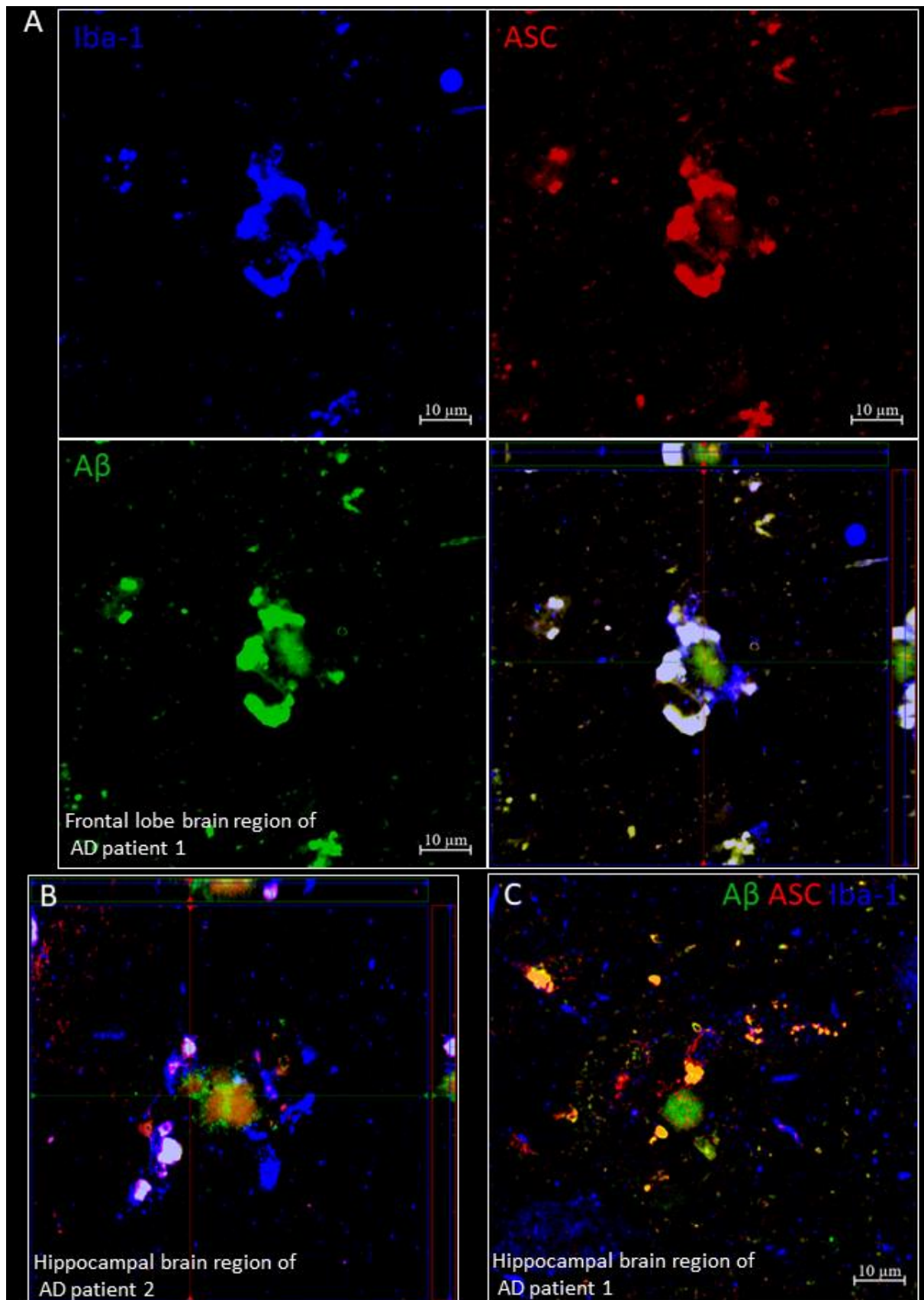


Fig. 7.4: Individual and merged channels fluorescence images of ASC specks (AL177, red) integrated into the A β cores and microglia (Iba1, blue) around in the frontal lobe (A) and hippocampal (B, C) brain regions of two patients with AD. Scale bars, 10 μ m in all panels.

To elucidate the degree of A β -microglia and A β -ASC speck colocalization in hippocampal and cortical plaques regions, I compared (i) the relative volume of A β covered versus uncovered by

microglia processes (Fig. 7.6A), (ii) the relative volume of ASC specks colocalizing versus non-colocalizing with A β (Fig. 7.6B), and (iii) the relative volume of A β colocalizing versus non-colocalizing with ASC specks (or in other words, in regions containing and non-containing ASC specks) (Fig. 7.6C) within the core, halo and whole plaque. The quantification using *t*-test reveals that microglia is significantly colocalized with A β in the plaque halo and core, except hippocampal plaques with a relatively high proportion of microglia-uncovered A β cores, indicative of inefficient microglial A β phagocytosis in these locations. As evident from Fig. 7.6B for the plaque core and halo, the volume of free ASC specks, which do not colocalize with A β , is negligible compared to the ASC volume bound to A β . Furthermore, according to Fig. 7.6C, about 80% of ASC specks is bound with A β in average for both hippocampal and cortical plaques, whereas the amount of A β non-colocalizing with ASC specks accounts for less than 35% and 15% for the hippocampal and cortical plaques in average. Altogether, these observations might indicate that the interaction of ASC with A β at the sites of plaque core and halo is a statistically significant process for both hippocampal and cortical A β plaques.

To elucidate to what extent the pro-inflammatory microglia activation associated with the A β accumulations and diverse for different brain regions with AD pathology, the activated pro-inflammatory microglial state was quantified within the plaque areas in the hippocampus and cortex, by calculating the volume ratio of microglia processes colocalized with A β and ASC specks in this area to that colocalized with A β . The results are shown in Fig. 7.7A. Specifically, the distribution histograms testifying the shifted microglia phenotype reveals that the cortical plaques are characterized by microglia processes containing both A β and ASC specks and statistically showing that ASC specks are present in about 90% of A β -positive microglia in average, therefore indicating a significant upregulation of the pro-inflammatory microglial phenotype in response to aggregated A β in the cortical plaques of human AD brains. In contrast, the hippocampal plaque cores appear to be associated with the less reactive microglial state, which does not accumulate the significant amounts of ASC specks in their somas compared to the cortical plaque ones ($p = 6.2 \cdot 10^{-11}$).

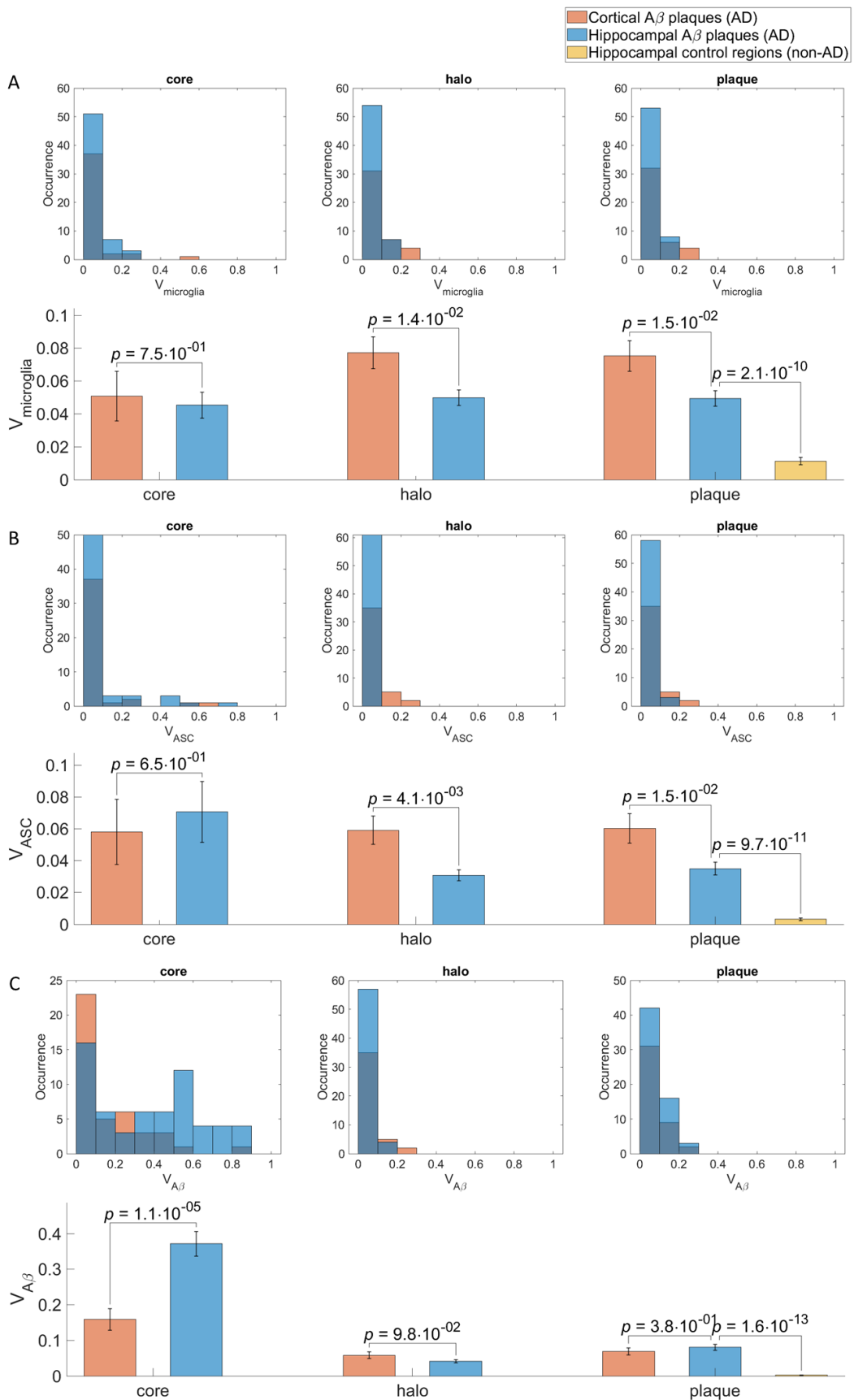


Fig. 7.5: (A-C) Quantification of relative microglia, ASC speck and A β -positive volumes within the plaque core, halo and whole plaque for cortical versus hippocampal plaques of AD human brains. Data are represented as histogram distributions (top panels) and mean \pm SEM (bottom panels). The examination of each antibody reactivity for hippocampal plaque (AD) versus non-demented control (non-AD) regions is also given, confirming a statistically significant increase of microglia, ASC and A β immunoreactivity in plaque regions.

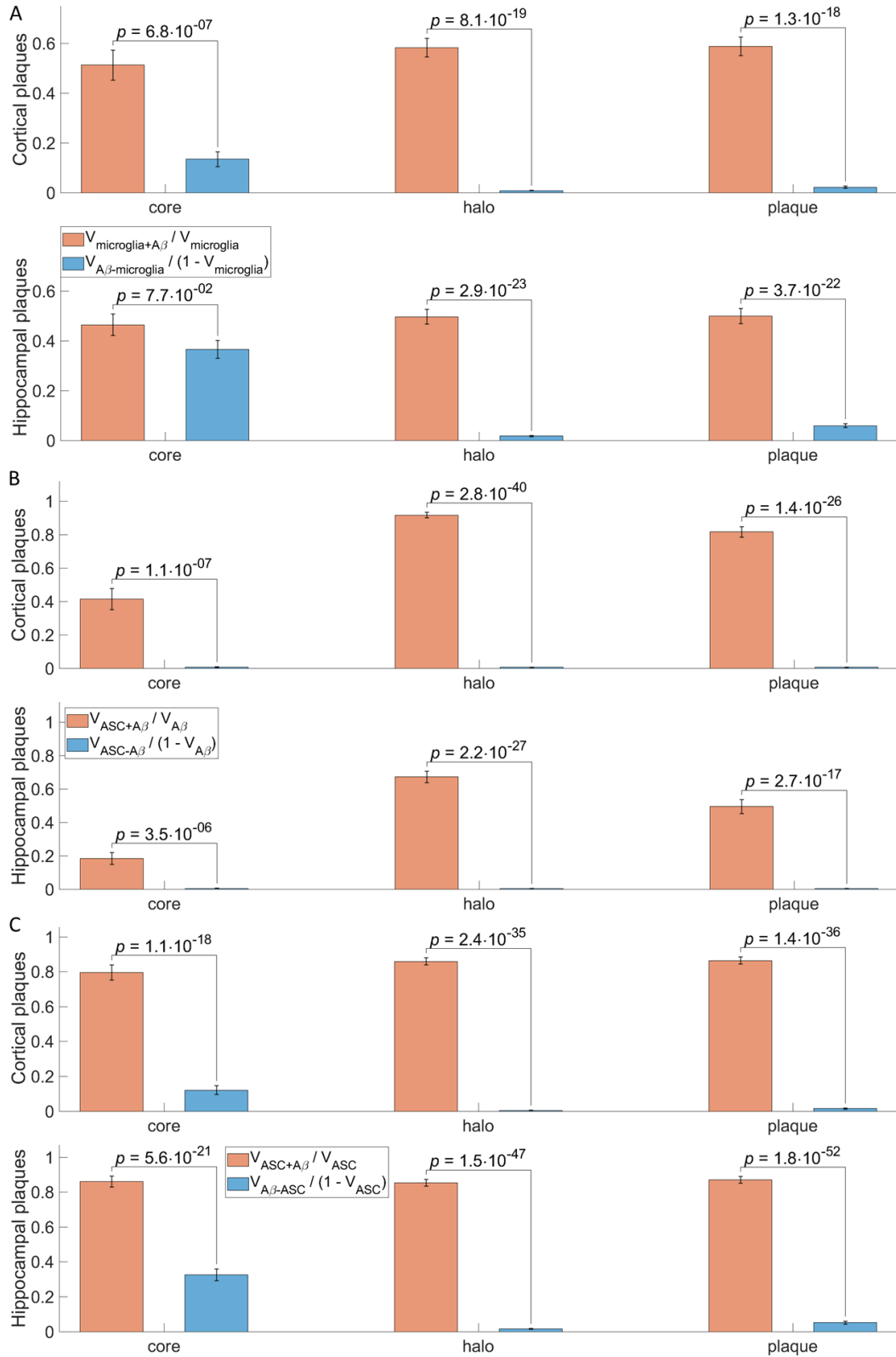


Fig. 7.6: Quantification of cortical and hippocampal plaques revealing a high degree of the A β -microglia (A) and A β -ASC speck (B) colocalization in the plaque core, halo and whole plaque, except hippocampal core with a statistically non-significant microglial A β coverage. Data are represented as mean \pm SEM.

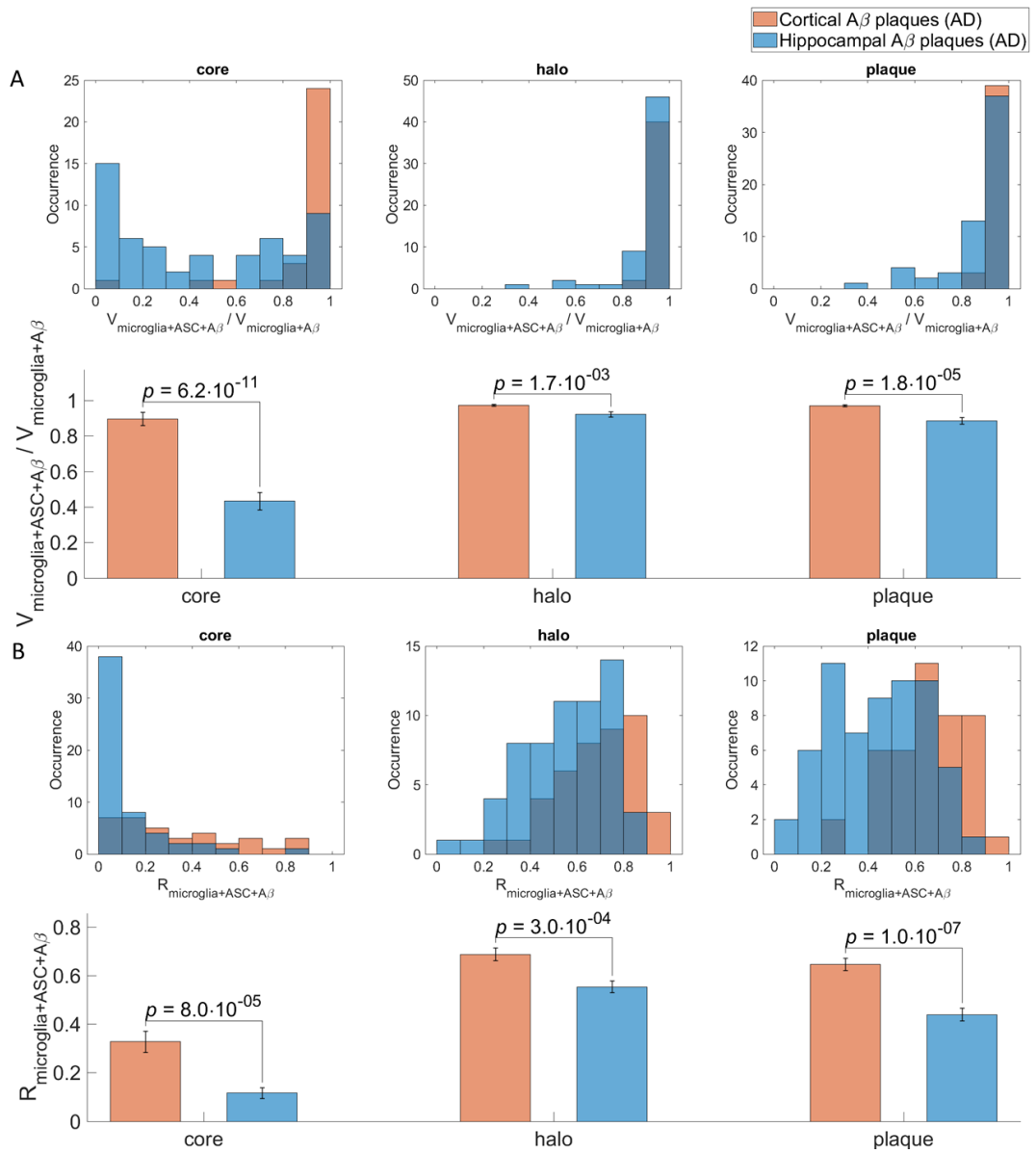


Fig. 7.7: (A-B) Quantification of the A β -ASC speck-microglia immunolabelled fluorescence images revealing a significant shift of the microglial activation to the pro-inflammatory state in the cortical plaque cores compared to the hippocampal ones. Data are represented as mean \pm SEM.

7.4. Findings

The analysis of correlative fluorescence images of the immunolabelled with A β /ASC specks/microglia AD brain sections and corresponding non-demented controls shows that ASC specks strongly colocalize with A β in the plaque cores of AD human brains and the statistical significance of this effect has been demonstrated. As shown in this chapter, the relative volume of the microglia-associated A β , indicative of microglial A β phagocytosis, is found to be similar between the cortical and hippocampal A β plaques accounting for about 50% in average for both plaque core and halo. However, the quantification reveals that the cores of hippocampal plaques contain significant amount of A β accumulations, which are not covered by microglia processes. Furthermore, colocalization of the A β -ASC specks within microglia, that might be a hallmark of a pro-inflammatory microglial A β phagocytosis, is found to be high for the sites of plaque halos. The extent of this colocalization is more pronounced for the cortical plaques accounting for about 65% average correlation value. In contrast, the pro-inflammatory microglial A β phagocytosis in the A β core is several times less efficient compared to that in the halo as evident from a 2- and 5-fold decrease in microglia-A β -ASC speck correlation value for the cortical and hippocampal core, respectively. Importantly, the cortical plaques are observed to be associated with a significantly upregulated pro-inflammatory microglia phenotype containing the largely increased accumulations of ASC specks compared to the hippocampal plaques. The degree of this effect is markedly greater for the A β plaque cores as evident by a surprisingly small p -value ($p = 6.2 \cdot 10^{-11}$). My findings suggest that the microglial phagocytosis of A β aggregates triggers the inflammasome activation within microglia in the human AD brains, resulting in the formation of the ASC specks in their soma. Then, the ASC specks possibly undergo the release from the microglia to the extracellular space, where they promote A β oligomer assembly. Possibly, accumulations of pro-inflammatory cytokines, resulted from the inflammasome activation within microglia, in the place of intensive A β aggregation polarize the microglial phenotype to a pro-inflammatory state with impaired phagocytic capacity of aggregated A β .

Chapter 8. Correlative fluorescence imaging of amyloid- β with ASC speck and complement component 9 in human Alzheimer's disease brains: inflammatory response to amyloid- β aggregation

8.1. Introduction

It has been reported that the activation of the complement system pathway in response to A β aggregation results in the reduction of A β plaque burden in AD brains. Specifically, the studies in AD transgenic mouse models have found that the treatment with transforming growth factor β 1 (TGF- β 1), stimulating upregulation of the complement C3 (Hogasen *et al.* 1995) protein, enhances the microglial phagocytosis of C3b-opsonized A β deposits, resulting in a 50% reduction of the A β plaque burden (Wyss-Coray *et al.* 2001; D'Andrea *et al.* 2004). Thus, it is not far-fetched to hypothesize that MAC can also possibly help to clear A β load by creating MAC pores on the A β plaque surface containing lipid vesicles, that are shown to be a major component of the A β plaque (see Chapter 5-6), thereby facilitating the MAC incorporation. Upon assembly of MACs on the amyloid-lipid plaque complex, they might destabilise the plaque chemical structure and induce its dissociation into less toxic forms that are more sensitized for brain phagocytic cells of the innate immune system. On the other hand, the recent studies in human lung epithelial cells show that accumulation of MAC pores in the cell membranes disturb calcium homeostasis resulting in Ca²⁺ efflux in the mitochondrial matrix, that in turn induces the NLRP3 activation, thereby initiating a pro-inflammatory response and cell apoptosis (Triantafilou *et al.* 2013). Applied to AD brains, the detrimental pro-inflammatory role of MAC on adjacent to plaque neuronal cells might be also associated with the activated NLRP3 inflammasome and formation of ASC specks. It is important to note that chronic A β aggregation occurring in the course of AD results in an excessive generation of the NLRP3 pathway products including ASC specks, leading to unresolved inflammation with fatal consequences for the activated cells and surrounding tissues. In response to NLRP3 activation by A β pathogen, gasdermin D of the NLRP3 inflammatory signalling induces the pyroptosis of activated cell (Shi *et al.* 2015), allowing the release of ASC specks into extracellular space (Latz 2010). As identified by recent *in vitro* studies, extracellular ASC specks play an important role in A β pathology spreading due to their unique ability to seed A β oligomer assembly (Venegas *et al.* 2017). This finding is also in line with the results of the

previous chapter, where I showed the significance of the ASC speck incorporation into the A β plaque cores.

The aim of this chapter is to better characterise lethal and pro-inflammatory effects of the MAC complex of the late stage complement cascade on A β clearance and the propagation of neuroinflammation in human AD brains. Quantification and correlation of spatial distribution patterns of the three AD hallmarks at the sites of A β plaques will be investigated using high-resolution fluorescence microscopy. For this, co-immunostaining of the ASC speck (indicative of the NLRP3 inflammasome assembly), pathogenic A β protein and the complement component 9 of MAC pores will be performed in post-mortem human AD brain and non-demented control to determine the significance of the inflammasome activation effect in conjunction with activated MAC pores in the areas of A β pathology and assess a potential capability of MAC pores to facilitate A β clearance.

8.2. Method

8.2.1. Human tissue samples

As in Chapter 7, human brain tissue was obtained from the Thomas Willis Oxford Brain Collection (TWOBC), which is part of the Medical Research Council (MRC) Brain Bank Network, with the ethical approval of the Research Tissue Bank provided by the Oxford Brain Bank (OBB) Access Committee. Correlative fluorescence imaging study of this chapter was performed on formalin-fixed-paraffin embedded brain slices of 5 μ m thickness. The diseased group is originated from the samples of two brain regions (hippocampus and frontal lobe) coming from 5 AD patients. For control experiment, the non-demented control cohort of samples from the individuals without AD were also participated in the study.

8.2.2. Immunohistochemistry

For immunofluorescent staining of the formalin-fixed-paraffin-embedded tissue brain sections, the following protocol has been used:

6. Formalin fixed brain tissue (5 μ m thick) slides were deparaffinized using a standard dewaxing protocol consisting of three consecutive steps: 1) heating at 60-70°C in a pre-heated oven for 1 hour; 2) removing the paraffin in xylene (two cycles for 20 minutes each); 3) rehydrating in a sequence of 100%, 90% and 70% ethanol for 5 minutes each, followed by three times washing in distilled water for 5 minutes each.

7. Heat-induced epitope retrieval in boiling DAKO solution: deparaffinized brain sections were transferred to 1X DAKO/PBS (pH 6.2) target retrieval solution (REF S1699 – 10X concentrate) and then incubated in preheated to and maintained at 90 °C water-bath for 45 minutes, followed by cooling down in the solution for 20 minutes;
8. Sections were washed three times for 5 min each in 1X PBS (pH 7.4) and blocked in 1X PBS/1% BSA/0.1% Triton X-100 (or 0.1% Saponin) (Blocking Buffer) for 30 min followed by 2 hours incubation with the primary antibodies in Blocking Buffer.
9. Sections were washed three times in 1X PBS/0.1% Triton X-100 (Wash Buffer), and incubated with Alexa- 488, 546 and 633 conjugated donkey secondary antibodies (Invitrogen, 1:400, 5 µg/ml) diluted in Blocking Buffer for 90 min, followed by three times washing in Wash Buffer for 5 min each.
10. As an indicator of A β plaque regions, Th-S dye was used for detection in green channel. For Th-S staining, after immunofluorescent labelling or prior mounting with an anti-fade media, brain slides were incubated in 1x PBS/0.01 % Th-S solution for 20 minutes, followed by differentiation cycles with 80%, 95% ethanol for 2 minutes each and subsequent three times washing in PBS for 5 minutes each.
11. Sections were mounted using Immu-Mount (Thermo).

The following combination of primary antibodies were used with respective concentrations for triple immunofluorescence staining of A β , ASC speck and C9/C5b-9 of the MAC complex:

- A β (Th-S dye, 0.01 % (m/v) solution in PBS)
- rabbit polyclonal anti-ASC (AL177, AdipoGen, 1:200, 5 µg/ml),
- mouse C9 neoantigen (mAb WU13-15, Hycult Biotech, 1:25, 4 µg/ml) *or* mouse monoclonal anti-C5b-9 (ab66768, Abcam, 1:50, 20 µg/ml).

8.2.3. Laser-scanning confocal fluorescence microscopy instrumentation

As in Chapter 7, high-resolution fluorescence microscopy was performed on a LSM 710 inverted confocal laser scanning microscope (Zeiss) using 100X/ NA 1.46 oil objective (0.23 µm lateral resolution at $\lambda = 0.550 \mu\text{m}$). Images were acquired with an 8-bit colour depth, a view of 512×512 pixels, and 0.17 µm pixel size, which results in an 85×85 µm² image size. All images were taken

using a z-stack mode with a step of 0.5 μm in z direction. Emission of fluorescently labelled antibodies were acquired sequentially.

8.2.4. Analysis

Similar to **Chapter 7**, z-stack images were processed using Zen 2.5 lite imaging software. The regions of $\text{A}\beta$, microglia processes and ASC speck immunoreactivities were determined using a threshold at 20% value of the deviation from a representative exponentially decaying distribution histogram of $\text{A}\beta$, C9 and ASC speck fluorescence intensities. For comparison of results, the threshold at 3 STD, 1.5 STD and 3 STD of $\text{A}\beta$, C9 and ASC speck total distribution histograms, respectively, were used as described in (Condello *et al.* 2015). The results of both methods are checked to produce equivalent results. The example of the areas representing the plaque core and halo, determined as a difference of the whole plaque and its core diameters, for one hippocampal and one cortical plaque is shown in Fig. 8.1. The images of the thresholded $\text{A}\beta$, C9 and ASC speck fluorescence intensities for the same plaques are also given in Fig. 8.1.

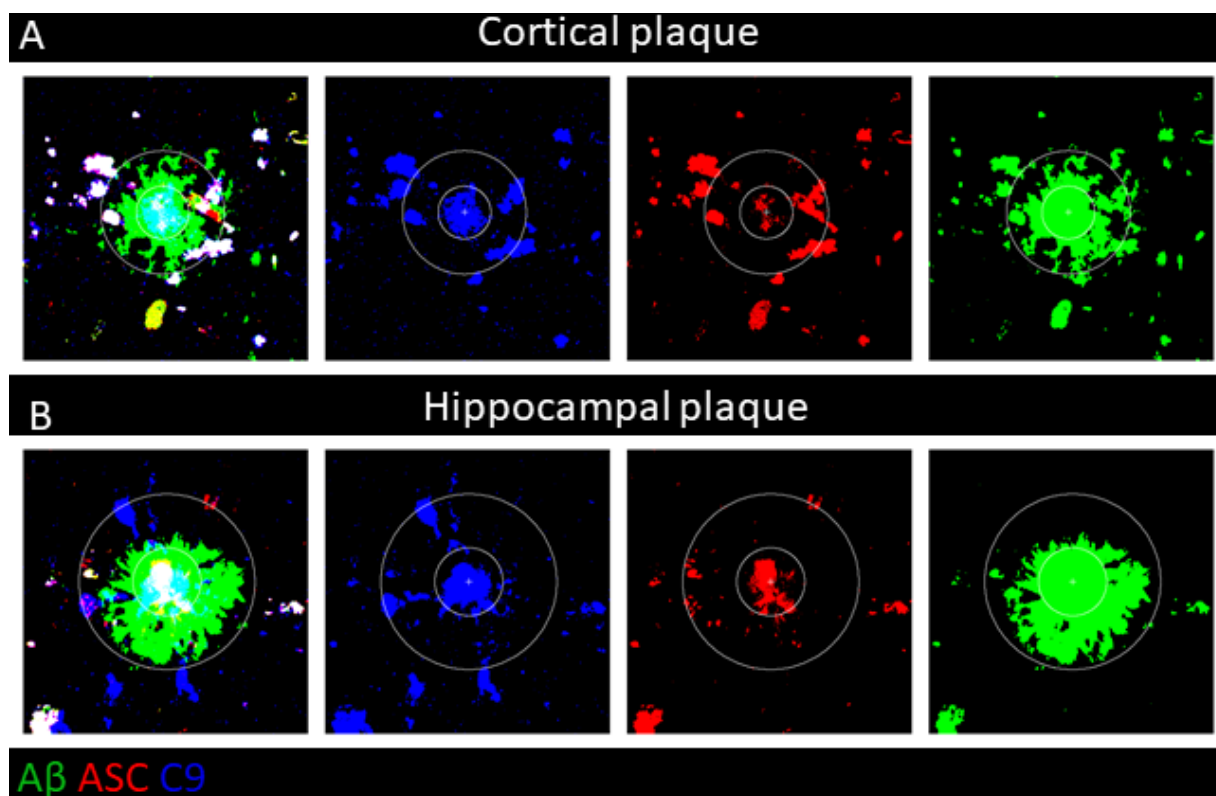


Fig. 8.1: Individual and merged channels fluorescence images of the thresholded $\text{A}\beta$, C9 and ASC speck fluorescence intensities for one cortical (A) and one hippocampal (B) plaques. In all panels, the white circles of smaller and larger radius indicate the area of plaque core and halo, respectively, selected for the quantification.

As in Chapter 7, an equivalent methodology was used for the analysis of C9-ASC speck- $\text{A}\beta$ labelled fluorescence images of $\text{A}\beta$ plaques in hippocampal and frontal lobe regions of AD human brains. The comparison of the fluorescence images between the hippocampal plaques (AD patients) and control regions (non-AD subjects) was also included. Characteristic quantities were

calculated using the same approach as for microglia-ASC speck-A β labelled fluorescence images. A total of 35 cortical and 43 hippocampal plaques from four AD patients were included in the quantification. As a control group, 16 fluorescence images of the hippocampal regions of brain from one non-demented control subject were also participated in the analysis. Two-sample two-tailed t -test with unequal variances was used to demonstrate the significance of the observed effect. To examine correlation/colocalization of the immunolabelled ASC specks, C9 and Th-S stained A β , the following quantities were calculated for each plaque region:

1. As a measure of C9-A β colocalization: (1) the volume of C9 colocalizing with A β within the whole plaque, the plaque core and its halo normalised on the A β -positive volume in the corresponding region ($V_{C9+A\beta}^{plaque} / V_{A\beta}^{plaque}$) versus the volume of the C9 non-colocalizing with A β within the same area normalised on the A β -negative volume within this area ($V_{C9-A\beta}^{plaque} / V_{1-A\beta}^{plaque}$); (2) correlation coefficient of C9-A β colocalization within the selected region according to the formula: $R = V_{C9+A\beta}^{plaque} / \sqrt{V_{C9}^{plaque} V_{A\beta}^{plaque}}$.
2. As a measure of ASC-A β colocalization: (1) the volume of A β colocalizing with ASC specks within the whole plaque, the plaque core and its halo divided by the ASC-positive volume in the same area ($V_{ASC+A\beta}^{plaque} / V_{ASC}^{plaque}$) versus the volume of the A β non-colocalizing with ASC within the same area normalised on the ASC-negative volume within this area ($V_{A\beta-ASC}^{plaque} / 1 - V_{ASC}^{plaque}$).
3. As a measure of C9-ASC speck colocalization: the volume of ASC specks colocalizing with C9 within the whole plaque, the plaque core and its halo divided by the C9-positive volume in the same area ($V_{C9+ASC}^{plaque} / V_{C9}^{plaque}$) versus the volume of the ASC specks non-colocalizing with C9 within the same area normalised on the C9-negative volume within this area ($V_{ASC-C9}^{plaque} / 1 - V_{C9}^{plaque}$).
4. As a measure of potential difference between A β areas colocalizing with C9 compared to that with ASC, possibly testifying the significance of the neuroprotective effect of MAC pores on the shrinkage of the A β plaque area versus the neurotoxic effect of ASC on the A β plaque growth: the volume of A β colocalized with C9 within the whole plaque, the plaque core and its halo divided by the A β -positive volume in the same area ($V_{C9+A\beta}^{plaque} / V_{A\beta}^{plaque}$) versus the volume of the A β colocalized with ASC within the same area normalised on the A β -positive volume within this area ($V_{ASC+A\beta}^{plaque} / V_{A\beta}^{plaque}$);

To confirm the statistical significance of the observed effect, the representative quantities has been investigated in the hippocampal and cortical plaque regions of AD brain tissues using two-sample two-tailed t -test with unequal variances.

To check whether C9 and A β levels are inversely correlated at the sites of plaque cores, I used Pearson's correlation coefficient (R) calculated for the core areas and determined according to the formula:

$$R = \frac{\text{cov}(I_{C9}, I_{A\beta})}{\sigma(I_{C9})\sigma(I_{A\beta})}, \quad (8.1)$$

where cov is the covariance and $\sigma(I_{C9})$, $\sigma(I_{A\beta})$ are the standard deviation of the fluorescence intensities of C9 (I_{C9}) and A β ($I_{A\beta}$), respectively.

In this quantification, the pixels with 'zero' fluorescence intensity of A β or C9 were excluded from the analysis. For each plaque with the negative correlation of C9 with A β , the dependence of the A β intensities from the C9 ones within the plaque core was investigated. For this, one plane from a z -stack fluorescence image of A β plaque was used. The data were represented as mean \pm SEM.

8.3. Results

To investigate the balance between potential neuroprotective and neurotoxic role of MAC against plaque toxicity, the confocal fluorescence images of the anti-A β -stained plaques co-immunolabelled for C9 and ASC specks in AD human brains of two regions (hippocampus and frontal lobe) together with non-demented controls were examined. The co-immunofluorescence images show that MAC components appear to create multiple pores within the A β plaque core by arranging in deposits of small (colocalized with the A β core in the centre) and large (colocalized with the inner perimeter of the A β core in the ring) diameters. MAC accumulations of larger diameter tend to form the ring-shaped accumulations within the A β core (Fig. 8.3), whereas the smaller-scale MAC deposits appear to colocalize with the A β core in the centre (Fig. 8.2). The presence of the MAC deposits inserted into the A β plaque core (Fig. 8.2, Fig. 8.4) might suggest that the MAC pores formed during the A β aggregation.

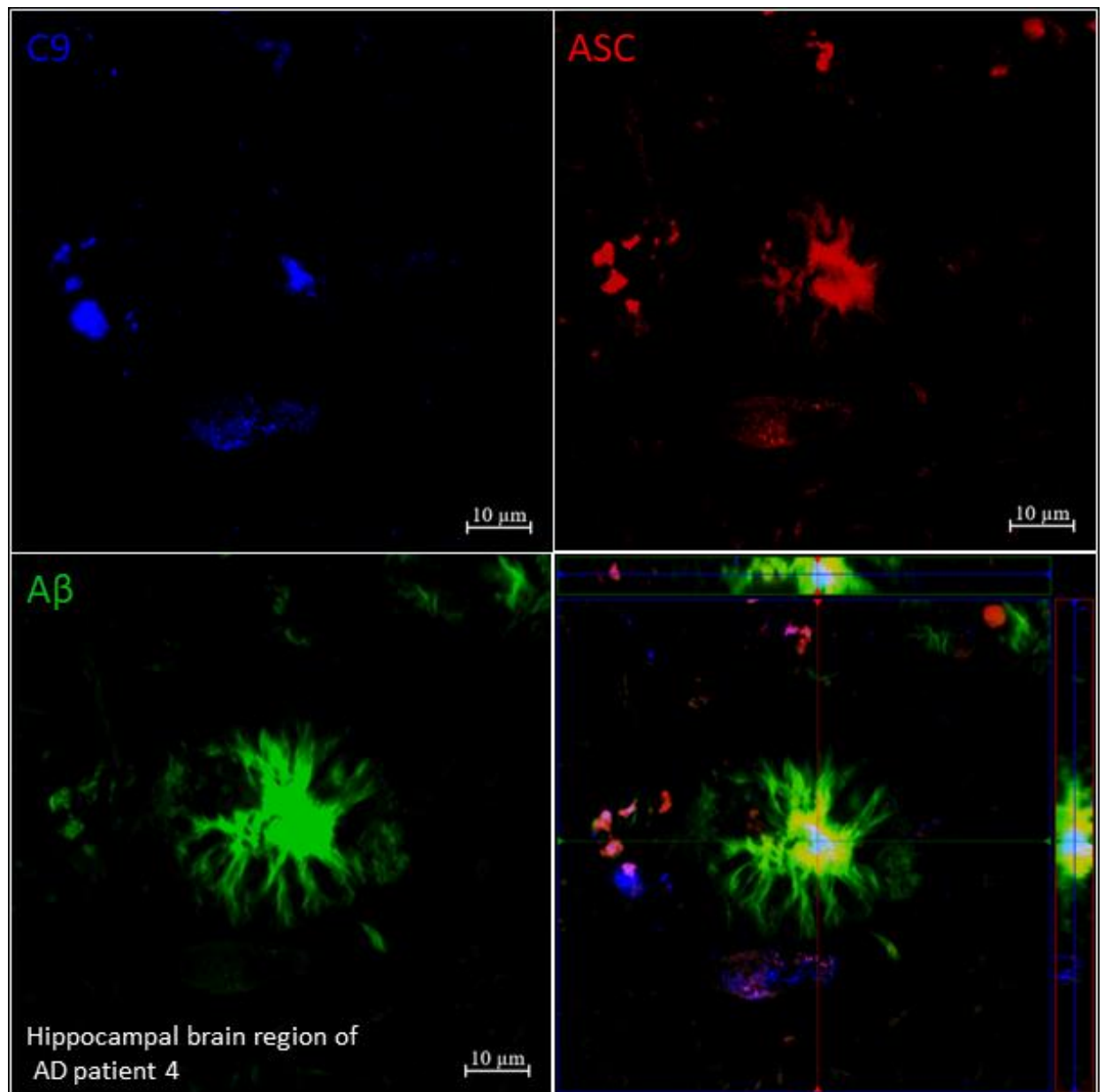


Fig. 8.2: Individual and merged channels fluorescence images of the MAC pores (C9, blue) integrated into the A β core (Th-S, green) and ASC specks (AL177, red) around in the hippocampal brain region of AD patient. Scale bars, 10 μ m.

The inspection of the MAC-ASC speck correlation reveals the accumulation of numerous ASC speck deposits, indicative of NLRP3 inflammasome activation, around the MAC pores at the sites of A β plaque cores (Fig. 8.2-Fig. 8.7), and therefore reflecting the MAC as a possible driver of the pro-inflammatory inflammasome activation in response to A β aggregation in human AD brains. It has been observed that the spatial distribution of the ASC specks in some MAC-positive plaque cores tend to be more uniform (Fig. 8.2 and Fig. 8.3), whereas other plaque cores accumulate distinct ASC specks and MAC pores both co-localizing to the apoptotic cell membrane (Fig. 8.5 and Fig. 8.7).

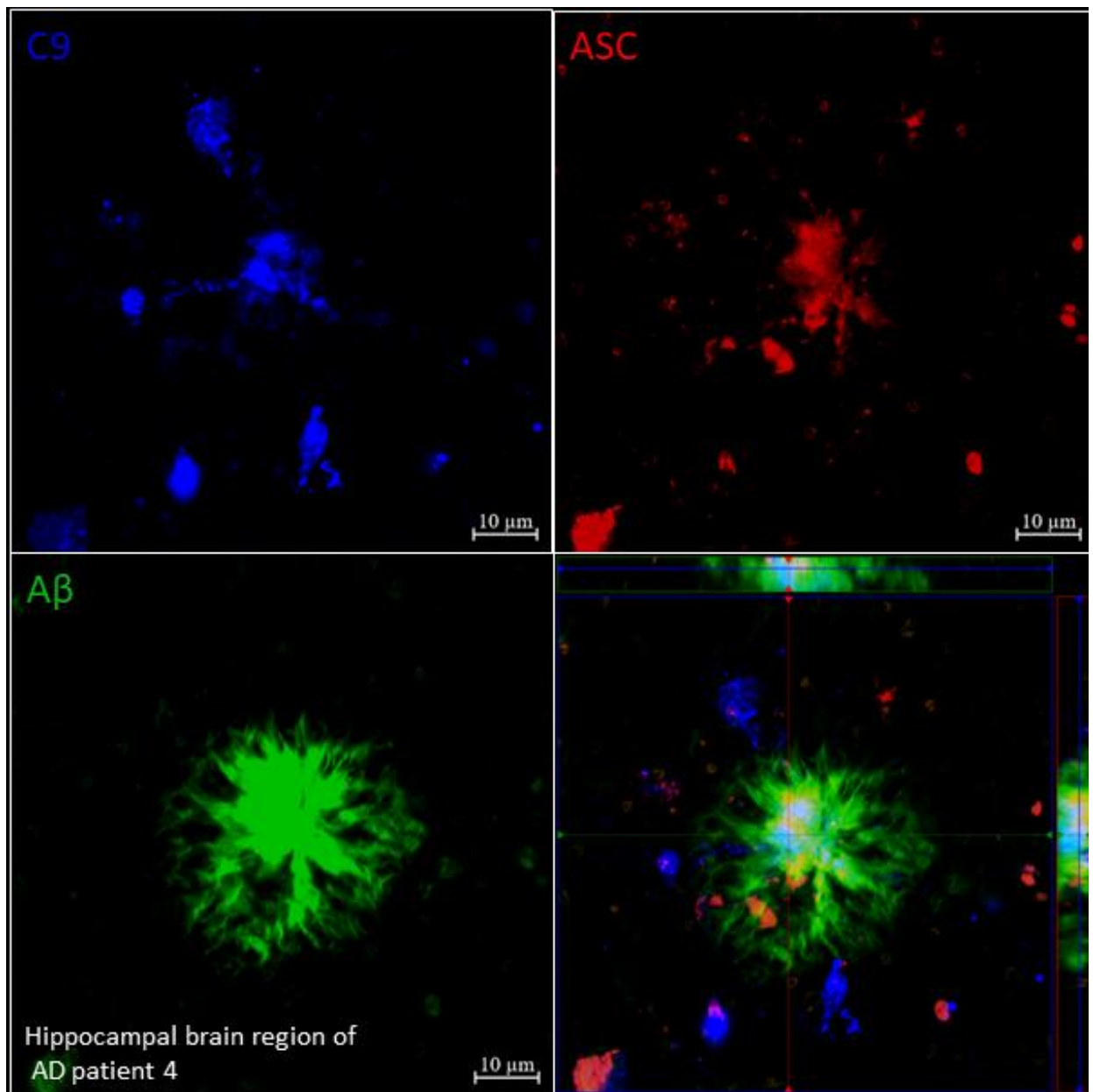


Fig. 8.3: Individual and merged channels fluorescence images showing the ring-shaped deposits of MAC pores (C9, blue) within the A β core (Th-S, green) and ASC specks (AL177, red) around in the hippocampal brain region of AD patient. Scale bars, 10 μ m.

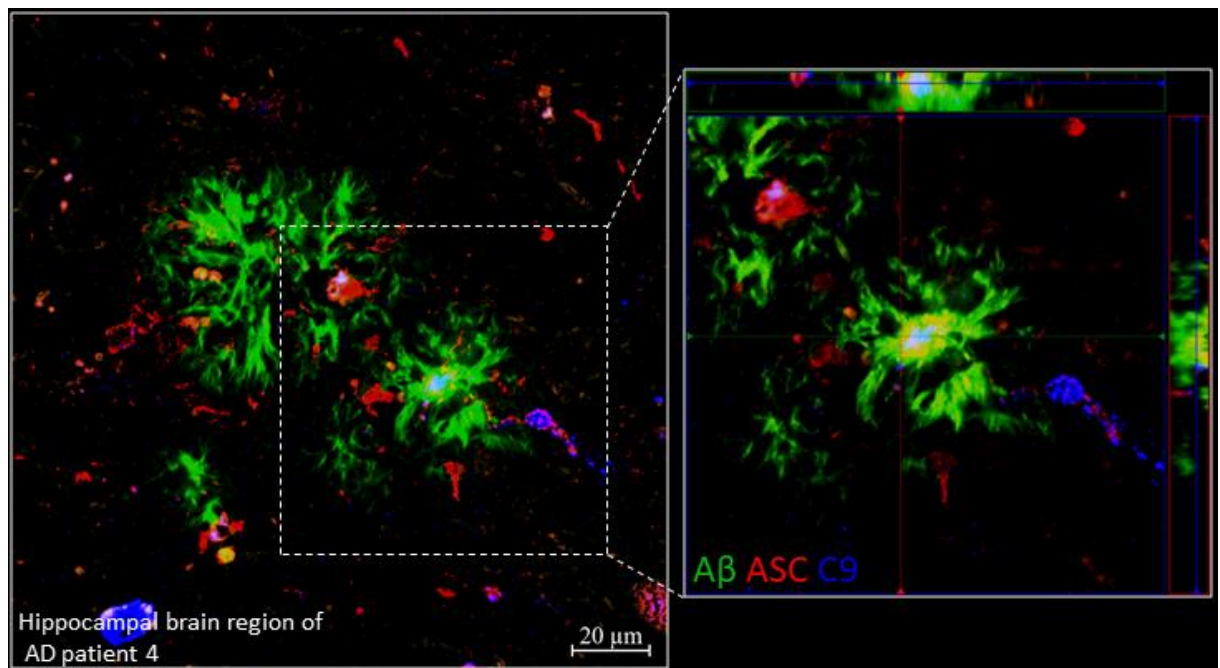


Fig. 8.4: Individual and merged channels fluorescence images revealing the presence of MAC pores (C9, blue) within the A β core (Th-S, green) with ASC specks (AL177, red) around in the hippocampal brain region of AD patient. Scale bars, 10 μ m.

To elucidate the degree of cross-correlation of C9, ASC specks and A β species, I compared (i) the relative volumes of C9 colocalizing versus non-colocalizing with A β (Fig. 8.9B), (ii) the relative volume of A β colocalizing versus non-colocalizing with ASC specks (Fig. 8.10A) as well as (iii) the relative volume of ASC specks colocalizing versus non-colocalizing with C9 complex (Fig. 8.10B) within the core, halo and whole plaque. The correlation coefficient for C9-A β complex has been also examined in Fig. 8.9A. In general, quantification of cortical and hippocampal plaques reveals a high degree of a pairwise colocalization of the investigated species within A β plaque cores, implying a direct link between these three. Analysis of A β -C9 correlation in both cortical and hippocampal plaques reveals that the pore-forming C9 strongly colocalize with A β at the sites of plaque cores as indicated by a high correlation value (Fig. 8.9A) and significant volume of C9-A β co-arrangements (Fig. 8.9B) within the A β -positive plaque regions. This observation implies the significance of MAC pore deposition within the A β plaque cores. Additionally, this effect is found to be strong at the sites of plaque halos, however it is less profound compared to the core based on *p*-values.

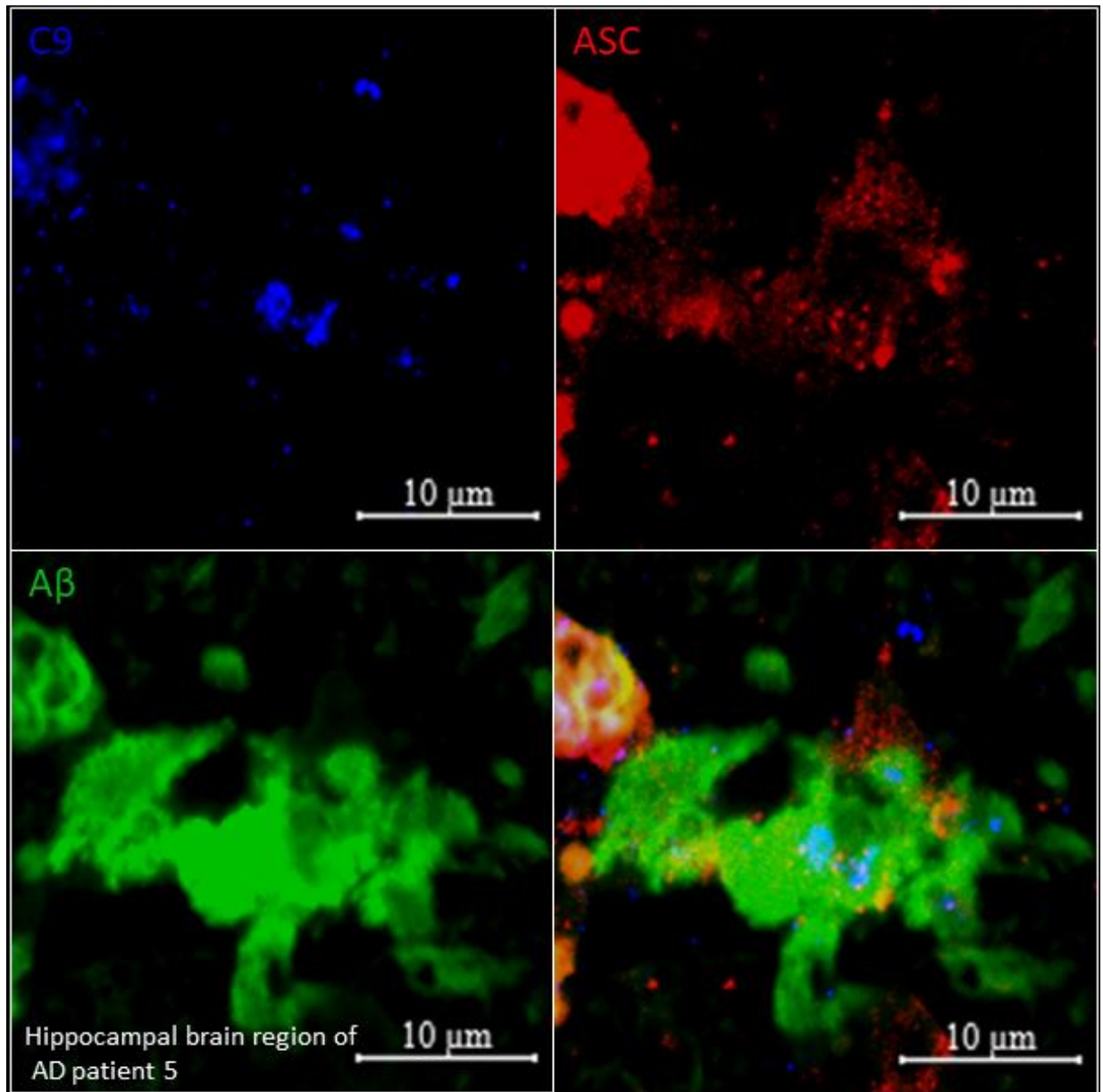


Fig. 8.5: Activation of the NLRP3 inflammasome and ASC speck assembly are triggered in response to sublytic MAC deposition in AD human brains. Figure shows the colocalization of the MAC (C-9, blue) and ASC specks (AL177, red) to the membranes of apoptotic cells activated within the core of the A β plaque (Th-S, green) in the hippocampal brain region of AD patient 5. Scale bars, 10 μ m.

In relation to A β -ASC speck quantification (Fig. 8.10A), almost all ASC specks are found to colocalize with A β fibrils at the sites of plaques ($V_{ASC+A\beta}^{plaque} \approx V_{ASC}^{plaque}$), indicating their interaction. Furthermore, the ASC specks are observed to colocalize with MAC pores (C9) at the sites of plaque core and halo, except the cortical plaque core, where the colocalization of ASC with C9 is found to be non-significant (Fig. 8.10B).

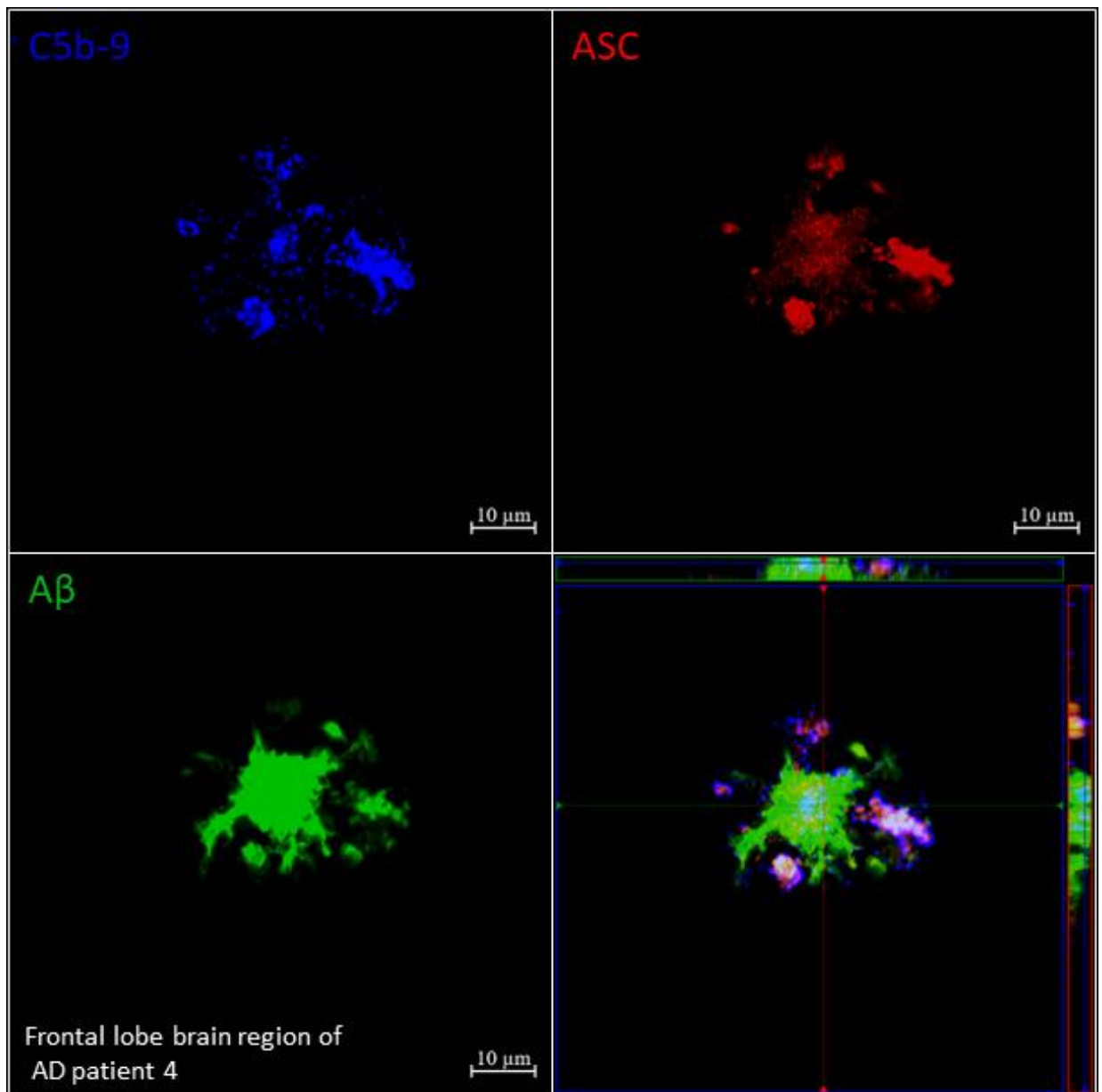


Fig. 8.6: Individual and merged channels fluorescence images showing the co-accumulation of MAC pores (C5b-9, blue) and ASC specks (AL177, red) throughout the cortical A β plaque (Th-S, green) in the frontal lobe brain region of AD patient 4. Scale bars, 10 μ m.

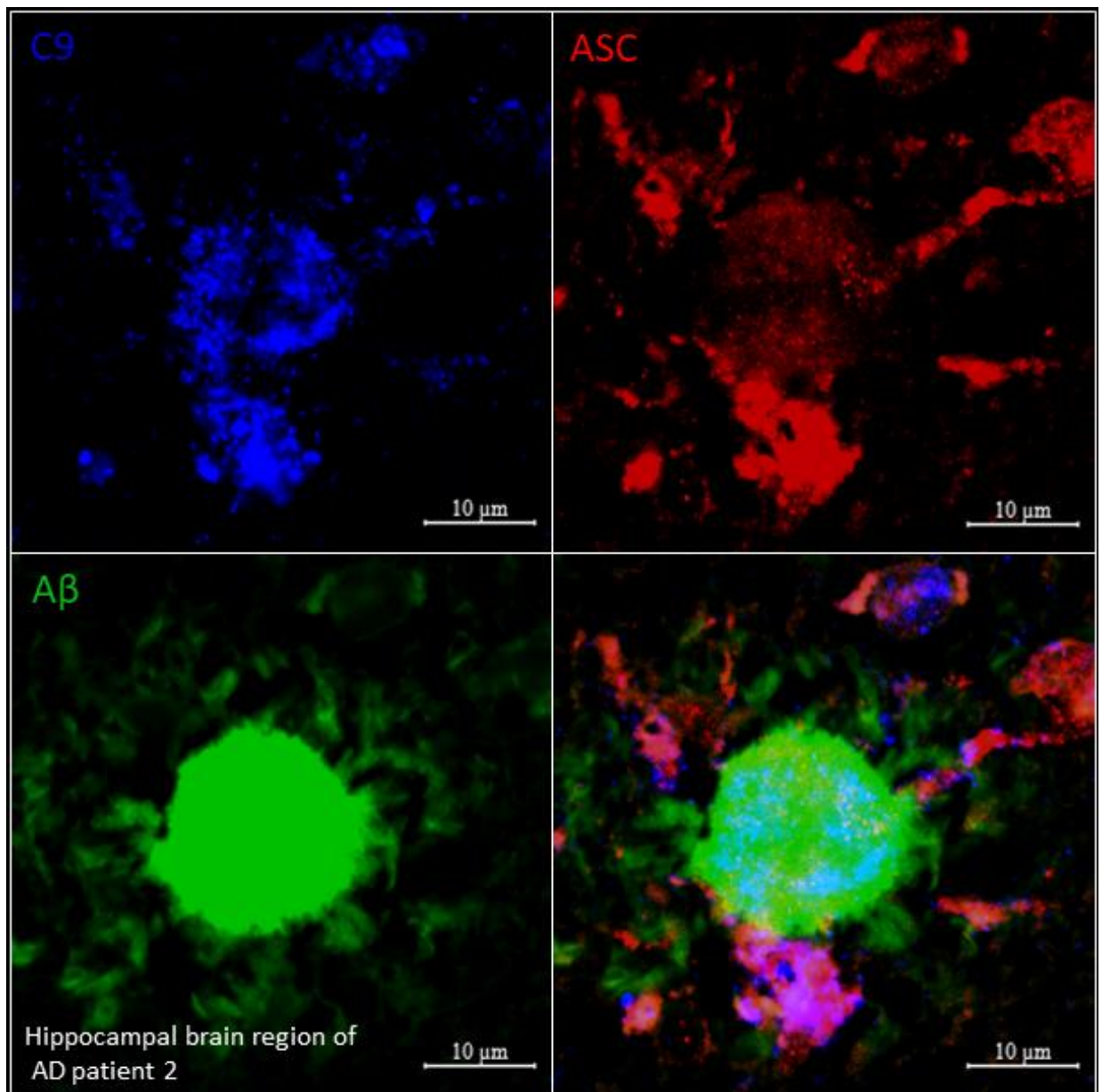


Fig. 8.7: Individual and merged channels fluorescence images showing the significant accumulations of MAC pores (C9, blue) and ASC specks (AL177, red) in the cortical A β plaque (Th-S, green) of the hippocampal brain region of AD patient 2. Scale bars, 10 μ m.

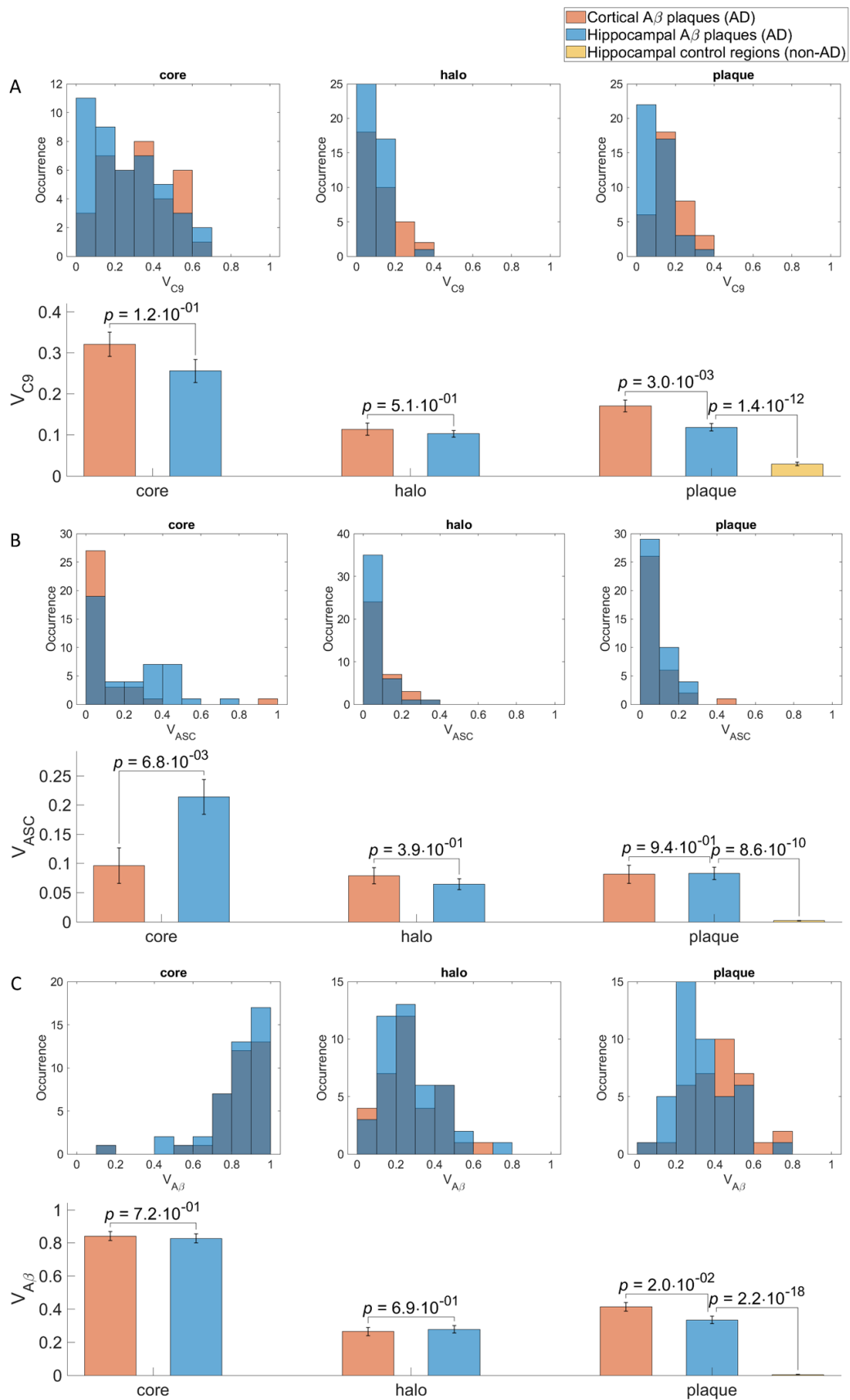


Fig. 8.8: (A-C) Quantification of relative C9, ASC speck and A β -positive volumes within the plaque core, halo and whole plaque for cortical versus hippocampal plaques of AD human brains. Data are represented as histogram distributions (top panels) and mean \pm SEM (bottom panels). The examination of each antibody reactivity for hippocampal plaque (AD) versus non-demented control (non-AD) regions is also given, confirming a statistically significant increase of C9, ASC and A β immunoreactivity in plaque regions and the specificity of the used antibodies.

Further examination of plaques regions reveals the subpopulation of the cortical plaques (15 plaques from a total population) that is characterized by the downregulated ASC activation and inverse correlation of C9 with A β levels at the sites of plaque core (see Fig. 8.11A,C,E). Specifically, colocalization histograms testifying the dependence of A β from C9 immunoreactivity reveals a marked reduction of A β -positive area of the plaque core, where C9 is upregulated (see Fig. 8.11B,D,F). Therefore, this observation might indicate that MAC clustering within the A β plaque cores can potentially stimulate the local clearance of A β burden in AD brains.

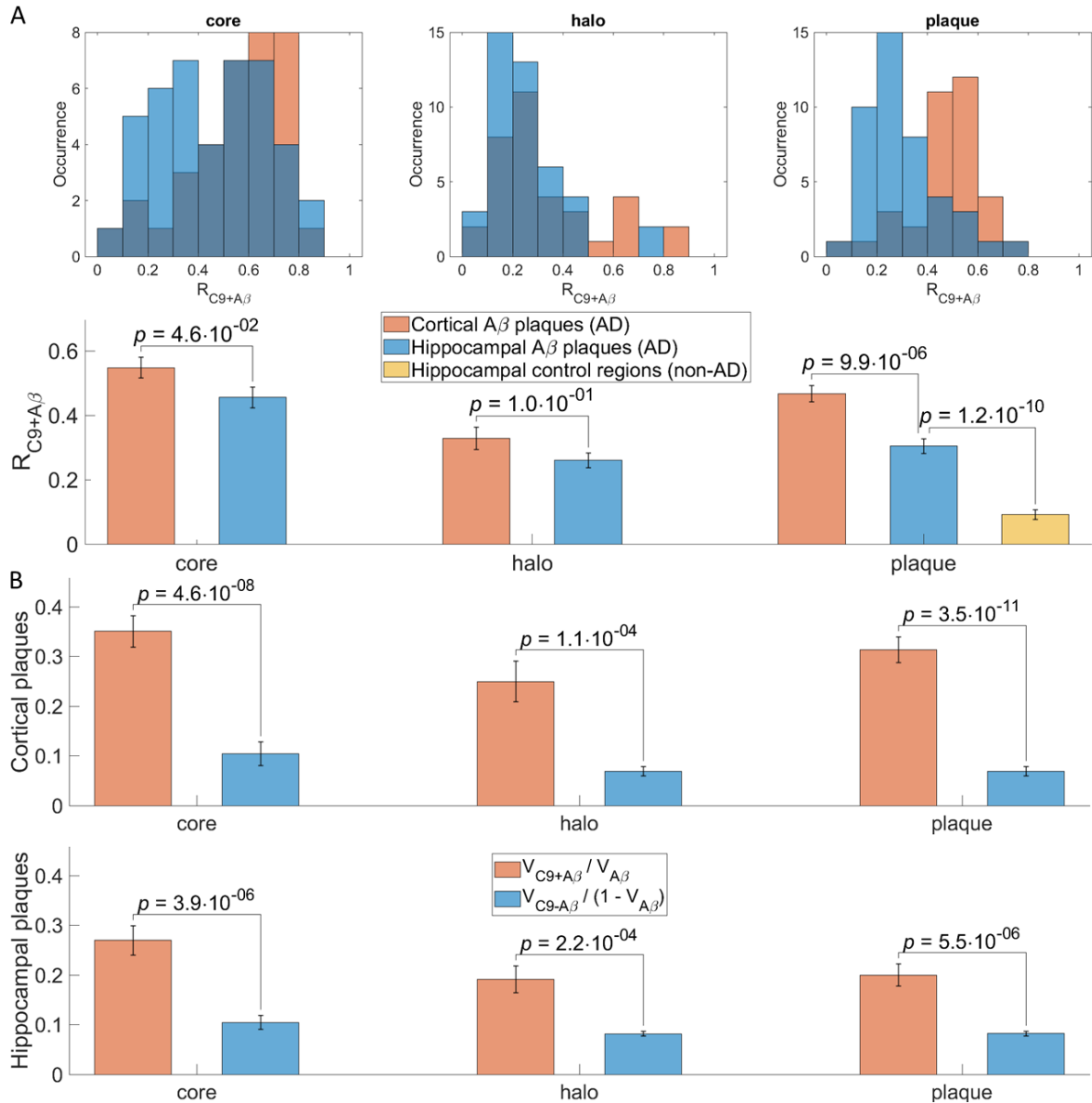


Fig. 8.9: (A-B) Quantification of cortical and hippocampal plaques revealing a high degree of the A β -C9 colocalization in the plaque core, halo and whole plaque that indicate the significance of the pore-forming C9 accumulation within the core and halo of the A β plaques. Data are represented as mean \pm SEM. The histogram distributions of the correlation value for C9-A β complex ($R_{C9+A\beta}$) are also included (A, top panel). For the hippocampal region, a comparison of $R_{C9+A\beta}$ between plaques and normal control regions coming from non-AD patients is given.

Collectively, my data show that the increased coverage of A β plaque cores by MAC pores might be associated with enhanced microglial A β phagocytosis lowering the local A β concentrations. In

contrast, the increased coverage of A β plaque cores with ASC specks has been shown in the previous chapter (Section 7.3) to be linked to the increased ASC-associated pro-inflammatory microglia phenotype that might lead to A β pathology spreading (Venegas *et al.* 2017).

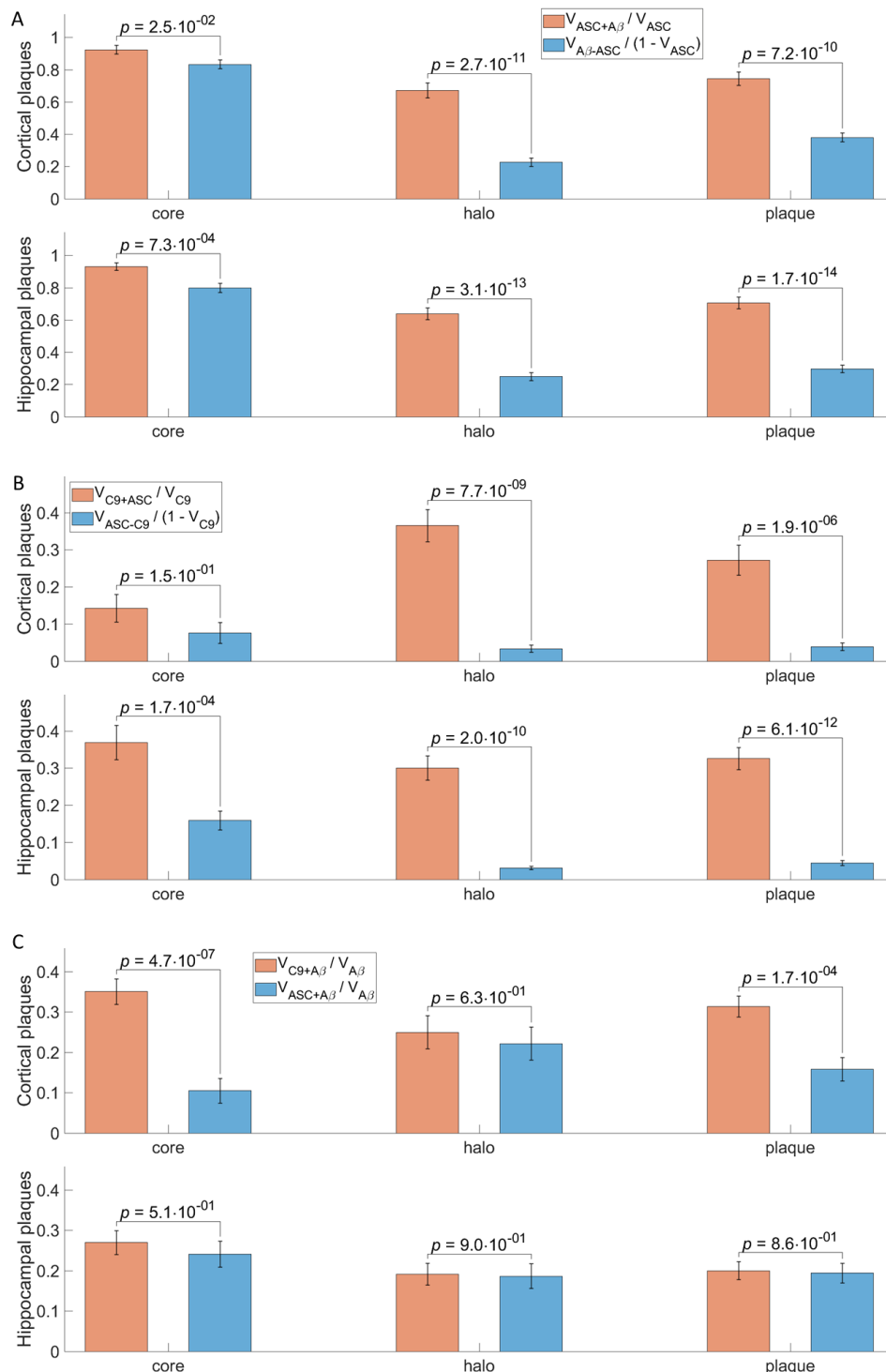


Fig. 8.10: Quantification of cortical and hippocampal plaques revealing a colocalization of ASC specks with A β (A) and C9 (B) in the plaque core, halo and whole plaque, except the cortical plaque core. (C) Quantification indicating the significance of the neuroprotective MAC effect on A β plaque shrinkage compared to the neurotoxic effect of ASC on A β plaque growth exclusively in the cortical plaque core. Data are represented as mean \pm SEM.

Therefore, the difference of relative MAC and ASC specks volumes colocalizing with A β within the plaque cores ($V_{C9+A\beta}^{core}$ versus $V_{ASC+A\beta}^{core}$) can possibly reveal whether the MAC-mediated A β

clearance is a more significant effect of AD brains compared to the ASC-induced A β assembly and toxicity. The results of this quantification confirm the significance of the pro-phagocytic effect of MAC pores on the shrinkage of the A β plaque area versus the neurotoxic effect of ASC on the A β plaque growth observed as a prominent feature of the cortical plaque core only (Fig. 8.10C).

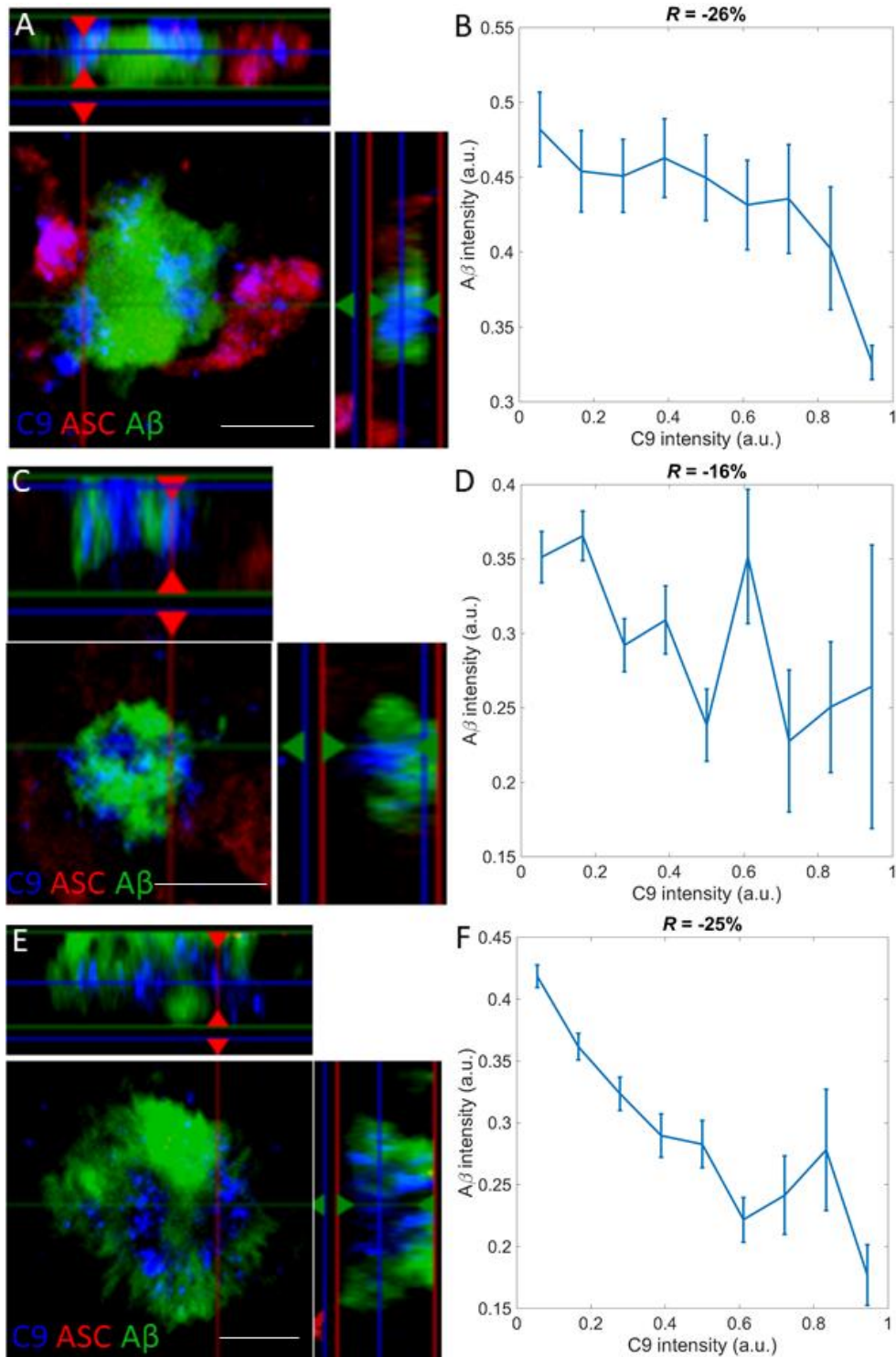


Fig. 8.11: Quantification of the C9-ASC-A β -stained cortical plaques revealing an inverse correlation of C9 with A β levels and therefore indicating the pore-forming C9 as a potential driver of A β phagocytosis able to lower A β concentration in AD brains: fluorescence images of the C9-positive plaques (A,C,E) and corresponding dependence of A β from C9 levels within the area of their colocalization at the sites of the plaque core (B,D,F). The representative Pearson's correlation coefficients R are also indicated on top. Scale bars in all panels, 10 μm .

The discriminative pattern of C9 and ASC speck co-activation within the A β plaque areas between the frontal lobe and hippocampal brain regions might depend from the plaque size. Statistically, cortical plaques are observed to be significantly more compact compared to the hippocampal ones as evident by small p -value ($p = 2.7 \cdot 10^{-11}$ in Fig. 8.12). Therefore, I hypothesize that cortical A β plaques of statistically smaller diameters are more prone to MAC-associated clearance. Indeed, quantification of C9 (indicative of MAC pores) correlation with the size of plaque core reveals that MAC pore coverage of cortical plaque cores decreases while the plaque core grow (Fig. 8.13A), whereas hippocampal plaques do not show a clear dependence of MAC activation from the plaque core diameter (Fig. 8.13B). This observation might imply that the pro-phagocytic MAC activity on local reduction of A β levels is inversely correlated with the size of cortical plaques. Analysis of ASC speck correlation with the size of plaque in turn shows that ASC speck coverage is greater for smaller plaques in the hippocampus (Fig. 8.13H). In contrast, cortical plaques do not exhibit a distinct dependence in a degree of ASC speck activation from the plaque diameter (Fig. 8.13G).

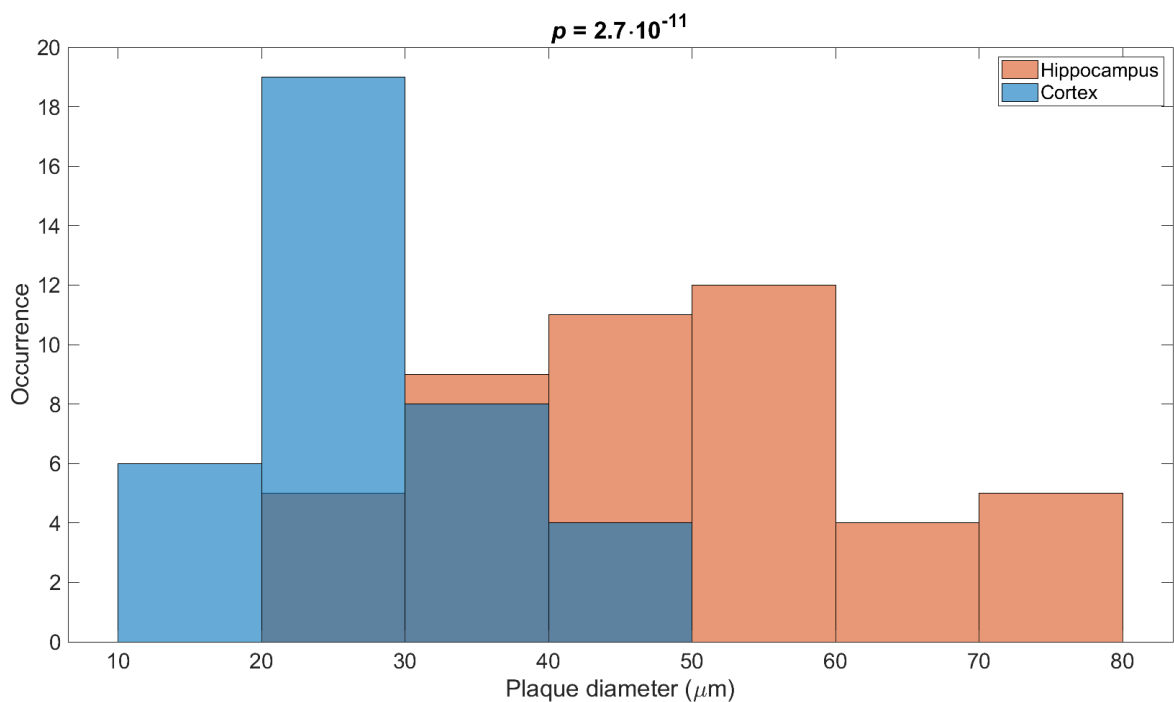


Fig. 8.12: Quantification of plaque diameter in two brain regions showing a striking difference in the size of cortical plaques compared to hippocampal ones. A resulting p -value is given.

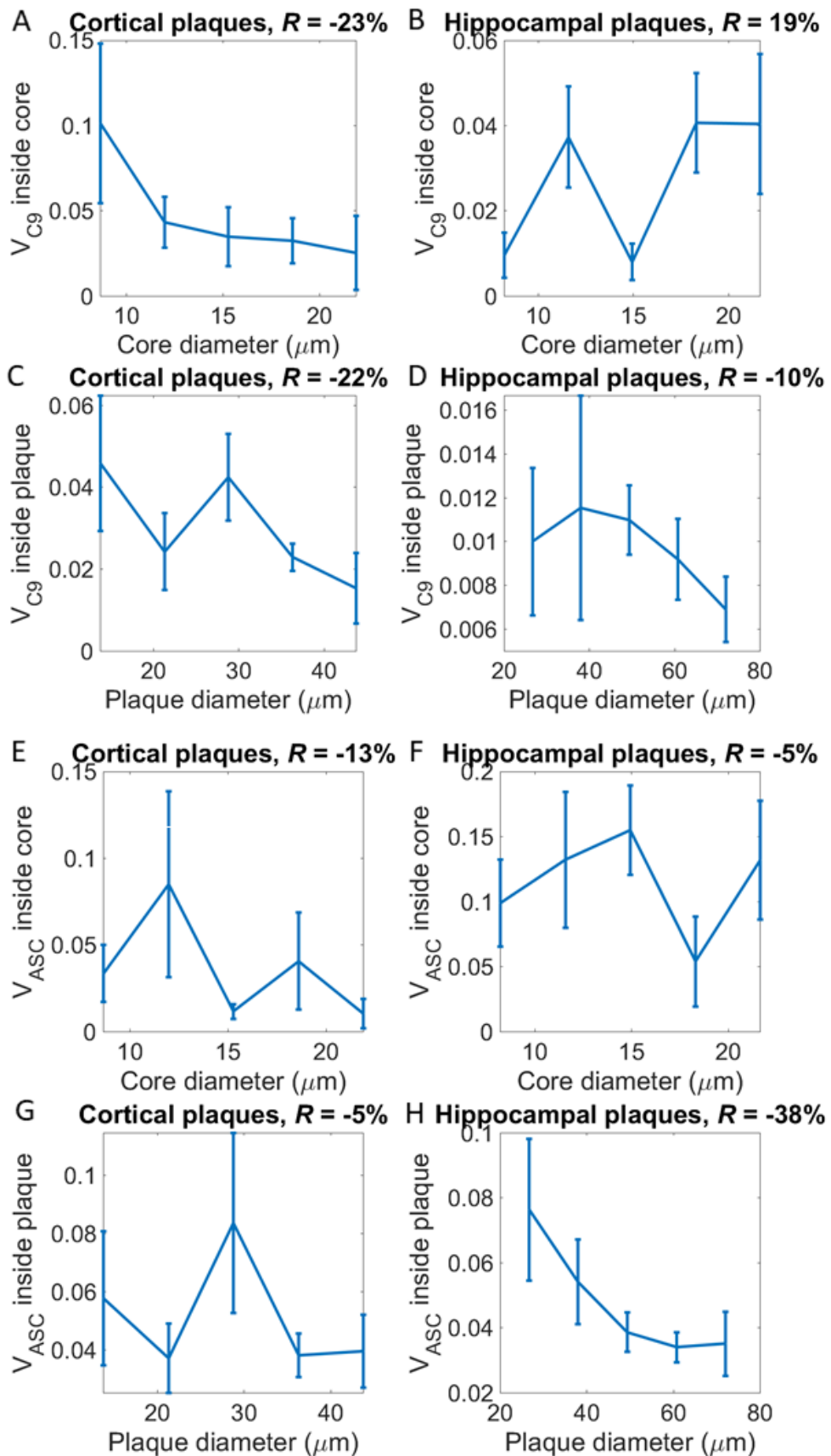


Fig. 8.13: (A-D) Quantification of C9 correlation with the size of plaque core (A,B) and whole plaque diameter (C,D) in the frontal lobe and the hippocampal brain regions revealing a reduced pore-forming C9 coverage of cortical plaques with larger core diameter. (E-H) Quantification of ASC speck correlation with the size of plaque showing a decreased ASC speck coverage of larger plaques in the hippocampus (H). Pearson's correlation coefficients R are also given.

8.4. Findings

The analysis of correlative fluorescence images of the Th-S stained A β plaques co-immunolabelled with the complement component 9 (representing MAC pores) and ASC specks (indicative of NLRP3 inflammasome activation) of AD brain sections shows that the MAC pores strongly colocalize with the A β plaque core of AD human brains, and the statistical significance of this effect has been demonstrated. ASC specks in turn are observed to cluster around the MAC pores, and therefore indicating the MAC as a trigger of the inflammasome activation at the sites of the A β accumulation. Quantitatively, the deposition of MAC pores and ASC specks within the hippocampal plaques are found to be a balanced effect with similar degree of activation. In contrast, the cortical plaque cores show a specific pattern. The plaque core in this brain region is found to be associated with the significantly upregulated activation of the MAC pores compared to ASC specks as evident by a surprisingly small p -value ($p = 4.7 \cdot 10^{-7}$). Along this observation, quantification of the plaque cores testifying an inverse correlation of C9 with A β intensities using a Pearson's correlation coefficient reveals the local decrease of A β levels at the sites of the cortical plaque cores, where MAC is upregulated. Collectively, these two observations might suggest that the MAC pores incorporated into the A β core can play a neuroprotective role by contributing to the A β phagocytosis, that results in shrinkage of the A β plaque areas. Strikingly, this possible MAC function with a potential A β clearance capacity is found to be inversely correlated with the plaque size as evident from the quantification of cortical plaques that are statistically more compact and therefore more prone to the MAC effect. My data might suggest that A β aggregation cause a persistent activation of the complement cascade followed by formation of the MAC pores within A β aggregate, that locally reduce A β levels through phagocytosis. While A β plaque grows, a pro-phagocytic function of MAC is decreasing, leading to an uncontrollable expansion of the A β plaque areas and thereby the amplified neurotoxicity in human AD brains.

Chapter 9. Discussion and conclusions

My thesis studied in detail spatially resolved chemical composition of A β plaques and their lipidomic and inflammatory microenvironment in post-mortem AD human brains using label-free confocal Raman micro-spectroscopy and high-resolution laser-scanning fluorescence microscopy. In the course of this chapter, I will summarise novel research outcomes of my thesis and emphasize its potential biomedical applications.

9.1. Raman micro-spectroscopy as a label-free tool for correlative 2D and 3D chemical imaging of A β plaques with both neuroinflammatory and lipidomic biomarkers of altered metabolism in AD human brains

In Chapter 5 and Chapter 6, I investigated in detail the chemical composition and performed correlative imaging of A β plaques with both neuroinflammatory biomarkers and lipids in post-mortem AD human brains by Raman micro-spectroscopy. For the formalin-fixed-paraffin-embedded brain sections studied in the hippocampal and frontal lobe brain regions by point-scan Raman micro-spectroscopy (Chapter 5), Raman micro-spectroscopy has been proven to detect striking differences in lipid composition as well as elevated concentration levels of oxidative stress and inflammatory bio-markers strongly colocalizing to the A β plaque areas of diseased tissues compared to controls. Specifically, A β plaque areas found spatially correlating with significant accumulations of chemical components assigned to a mixture of cholesteryl esters with saturated long-chain FAs and A β fibrils, a mixture of fibrin and arachidic acid, CLAC, β -carotene, magnetite, and calcium phosphate, that altogether and individually reflect oxidative damage of AD brains and neuroinflammation. Not only did I find the altered levels of lipid components between AD and non-demented control brains, but I also was able to detect the functional changes in lipid composition of AD tissues that are hallmarks of oxidative damage (Chapter 5). Specifically, human AD brains are observed to contain the abundant pathological signatures of lipid peroxidation as evident by presence of *trans* double bonds in the Raman spectrum of the saturated CE-A β fibril mixed component. Also, oxidative stress in AD brains was revealed by the accumulations of arachidic acid known to be generated through oxidative modification of AA. As another marker of oxidative damage, the significant accumulations of calcium phosphate are found to colocalize with the cores of cortical A β plaques, possibly reflecting the lethal neurotoxic and

pro-inflammatory effect of A β species on cells through the pathogenic formation of A β ion pores in the neuronal membranes of affected cells that is in turn linked to severe Ca²⁺ pathway disruption (Yatin *et al.* 1998; Kaye and Lasagna-Reeves 2013).

Altogether, Chapter 5 shows that AD brains accumulate excessive levels of the oxidative stress and inflammatory markers, spatially colocalized with amyloid and lipids in the A β plaques, thereby reflecting oxidative damage as a central player in the AD pathogenesis. Importantly, my data support the model that this plaque environment, shown to consist of the significant deposits of saturated cholesteryl esters, fibrin/arachidic acid, β -carotene and iron oxide, might contribute to plaque aggregation and A β pathology spreading.

Similarly, for the frozen AD human brain tissues without fixative artefacts studied by label-free line-scan Raman micro-spectroscopy in Chapter 6, 3D Raman images of A β plaque pathology lesions surrounded by lipidomic environment were acquired and chemically unmixed to produce individual biochemical profiles of the pathological brain composition. In agreement with the results of Chapter 5, the analysis on frozen AD brain samples also revealed that label-free Raman micro-spectroscopy is capable to distinguish significant intracellular and extracellular accumulations of pathogenic A β species assembled into the cross- β structured fibrils manifested by a profound marker band at 1668 cm⁻¹ combined with the missing band between 1662–1655 cm⁻¹, characteristic of the α -helix structured proteins (Rygula *et al.* 2013). For the lipid content, the analysis found two types of lipid deposits spatially colocalizing with the A β plaques. In particular, significant accumulations of polyunsaturated lipids, spectrally attributed to an oxidized form of a *trans* isomer of AA, that are co-deposited with the A β protein in one chemical component, were discovered colocalizing to the A β plaque core and the cell bodies of neurons. The abundant pathological signatures of lipid peroxidation in the composition of this amyloid-lipid component is evident by a high presence of *trans* double bonds in its Raman spectrum, which is consistent with the research findings of Chapter 5. These observations might manifest unresolved neuroinflammation and oxidative damage affected human AD brains in response to chronic A β accumulation. The results also revealed the halo tightly enveloping the A β core and composed of lipoproteins with a high CE content. This CE-rich halo is observed to colocalize with the activated microglial processes and spatially correlate with the pro-inflammatory immunolabelled components of the immune system such as the pore-forming gasdermin D protein, reflecting the cell pyroptosis, and the ASC specks, indicative of the NLRP3 inflammasome activation. Furthermore, the analysis found the ellipsoid-shaped cloud clustering around the A β -containing neurons consisting of the actin protein, possibly originated from the lytic material of the dead neuronal cells underwent the cell pyroptosis.

Importantly, as presented in Chapter 6, the A β and AA interplay can be possibly explained through their association with lipid cellular membranes. In particular, assembled A β oligomers are documented to disturb the integrity of neuronal membranes by creating the A β pores within them (Kayed and Lasagna-Reeves 2013), whereas AA as an essential polyunsaturated FA in the composition of the lipid bilayers is shown to facilitate growth/repair of new/damaged neurons (Darios and Davletov 2006). To that end, the co-existence of A β fibrils with the oxidatively modified *trans* isomer of AA in one complex at the sites of plaque core revealed by label-free 3D Raman imaging of human brains as presented in Chapter 6 might point to another possible mechanism of brain neurodegeneration through the conversion of AA to its peroxidized forms within lipid membranes induced by A β toxicity that lead to the dysregulation of the AA enzyme cascade and subsequent cell death.

Altogether, Chapter 5 and Chapter 6 show that Raman micro-spectroscopy is capable to distinguish spatially resolved chemically specific accumulations of lipid and proteins, composed of aggregated bioproducts of lipid peroxidation and protein signatures of the oxidative damage and neuroinflammation, that colocalize to A β plaque pathology lesions in label-free human AD brains. Therefore, my thesis suggests the use of non-destructive label-free Raman micro-spectroscopy as an imaging tool for the identification of the biochemical molecular signs of AD tissue pathology. Application of quantitative hyperspectral image analysis methods to large-scale Raman datasets from high-content human samples shown in my thesis will in turn stimulate further large-scale biomedical data analyses that could help to identify new imaging biomarkers and structural molecular features associated with various diseases.

9.2. Revealing novel brain imaging biomarkers for AD diagnosis

In Chapter 5 and Chapter 6, I showed that Raman micro-spectroscopy allowed to detect and quantify pathogenic A β_{1-42} chemical component of plaques from completely label-free brain tissue samples. Therefore, my thesis proposes the Raman spectral profile of A β as a brain imaging marker of AD pathology to be potentially used in clinical applications. As revealed in my thesis, this pathogenic A β protein is found in coupling with the lipid aggregate of the high oxidatively-modified FA content representing one chemical component, thereby supporting the model of a close interaction of A β with lipids. This lipid-bound A β complex is observed to be the main constituent of A β plaques. Therefore, my thesis utilizes the Raman spectral profile of oxidized FAs characterised by the significantly enhanced marker band of lipid peroxidation at 1668-1670

cm^{-1} together with the signatures of saturated lipids in the CH-stretch vibrational region (2700-3100 cm^{-1}) as an imaging lipidomic marker of AD human brains. The diagnostic signatures of lipids with saturated high-order FA chains in the CH-stretch region have been revealed by the increased 2880/2850 cm^{-1} intensity ratio by factor of 2 and above (Chapter 5) combined with the lacking Raman band near 3004 cm^{-1} (Chapter 5-6). It is important to note that recent studies already indicated the lipid effect on A β pathology spreading in the AD brains, elucidating that lipids can destabilise the A β aggregate by pulling out A β oligomers from its halo, thereby seeding a new neurotoxic A β nucleation (Kiskis *et al.* 2015). Specifically, it has been shown in the previous studies that both microglia-derived lipid micro-vesicles and ApoE-lipid complex, bind to fibrillar plaques, upon which they can either disintegrate the A β deposit into toxic A β oligomers (Joshi *et al.* 2014) or facilitate its aggregation and possibly clearance (Burns *et al.* 2003). The interplay of the A β protein with the CE-rich lipids as revealed in Chapter 5 is in line with the previous studies on cholesterol-mutant cell lines, indicating the positive correlation of A β production with the upregulated CE levels, controlled by acyl-coenzyme A:cholesterol acyltransferase (ACAT) (Puglielli *et al.* 2001). Additionally, these studies demonstrated that the pharmacological ACAT inhibitor efficiently suppressed the generation of both CE and A β , pointing to its potential use in AD treatment. To note, the animal trial of this strategy already gave encouraging results using an AD mouse model (Murphy *et al.* 2013).

Further to clinical impact, my thesis demonstrated that the statistical parameters of identifying biochemical components found from quantitative brain imaging with Raman micro-spectroscopy separate AD tissues from non-demented ones, that might be beneficial for AD diagnosis. In relation to inflammatory components of human AD brains, my data showed that the levels of β -carotene are significantly upregulated in AD human brains compared to the controls and these accumulations are strongly associated with A β plaque pathology lesions (Chapter 5). Therefore, my PhD thesis also propose the Raman spectral profile of β -carotene as an imaging marker of AD pathology, in which β -carotene might be a measure of neuroinflammatory response.

9.3. Revealing pro-inflammatory microglia phenotype as a signature of human AD brains affected by A β amyloidosis

As presented in Chapter 7, the analysis of fluorescence images with triple immunohistochemical staining of human AD brain sections for A β , ASC specks and microglia reveals the significance of the activated pro-inflammatory microglia phenotype in response to sustained A β accumulation, which is tightly linked to the greatly enhanced ASC speck assembly within microglial soma.

Therefore, the ASC speck-associated microglia state can be considered as a unique pro-inflammatory phenotype of AD brains with chronic A β aggregation. Importantly, these data might indicate that the therapeutic chemical agents which selectively block ASC speck formation within microglia have a great potential to tilt the ASC speck-specific pro-inflammatory microglia phenotype towards a neuroprotective state with increased A β clearance and reduced A β toxicity spreading capacities. It has been recently reported in the studies using cultured cells and mouse AD models that anti-ASC speck antibody treatment results in decreased levels of A β oligomers that in turn contribute to reduction of A β accumulations (Venegas *et al.* 2017). The results of my thesis support two mechanisms for a beneficial neuroprotective effect of anti-ASC antibody as previously suggested in recent studies (Venegas *et al.* 2017; Lee *et al.* 2019). One of these is targeting intracellular ASC. My data and previous studies indicate that, following A β aggregation, the inflammasome is activated in neuronal cells surrounding A β plaque lesions (Heneka *et al.* 2013) resulting in the ASC speck assembly within the inflammasome-activated cells. When ASC protein is polymerised into fibrils and ultimately to an assembled speck, it can initiate the maturation of IL-1 β cytokine through caspase-1 activation (Broderick *et al.* 2015). At this point, anti-ASC speck antibody binding to intracellular unassembled ASC will block caspase-1 activation and subsequent IL-1 β cytokine generation, which will suppress inflammatory response and reduce neurodegeneration. Indeed, caspase-1 has been recently established to activate pore-forming GSDMD that in turn was discovered to drive an inflammatory type of cell death known as pyroptosis (Rathkey *et al.* 2017). If the ASC speck assembly is not blocked by the selective antibody treatment, the inflammasome-activated cell undergoes pyroptosis, ultimately resulting in the release of ASC specks and IL-1 β cytokines into extracellular space, where IL-1 β cytokines can recruit new immune cells to the sites of infection and skew the microglial polarization towards the pro-inflammatory state (Cherry *et al.* 2014). Strikingly, when accumulated in the extracellular space, ASC specks show prion-like (prionoid) activities to recruit new ASC and caspase-1 in cells ingested ASC specks, thereby leading to continuous secretion of IL-1 β cytokines and unresolved inflammation (Franklin *et al.* 2014). At this point, anti-ASC speck antibody can also bind to extracellular ASC specks (Lee *et al.* 2019), thereby blocking maturation of new IL-1 β and contributing to switch to the anti-inflammatory microglial phenotype (Subramaniam and Federoff 2017) with increased A β phagocytic capacity, that results in decreased A β accumulations (Sarlus and Heneka 2017). If extracellular ASC specks are not neutralised by the antibody, ASC specks further induce inflammasome activation upon their phagocytosis by microglia, that result in the microglial pyroptosis (Sarlus and Heneka 2017), ultimately leading to uncontrollable growth of A β areas and neurodegeneration. In addition, anti-ASC speck antibody can block microglial

pyroptosis by binding to intracellular inflammasome and therefore suppressing/impeding its activation (Lee *et al.* 2019).

9.4. Pro-phagocytic effect of MAC pores on clearance of small A β plaques vs. pro-inflammatory potential of MAC pores on ASC speck-induced spreading of A β pathology in human AD brains: hypothetic cycle of AD pathogenesis

In Chapter 8, the analysis of fluorescence images with triple immunohistochemical staining of AD brain sections for A β , ASC specks and complement component 9 of MAC revealed a strong colocalization of MAC pores to the A β plaque core and ASC specks clustering around the MAC deposits, possibly implying the MAC as a driver of the inflammasome activation at the sites of A β accumulation. In view of these results, the hypothesis-driven cycle of AD pathogenesis can be proposed as follows. In immune system response to A β aggregation, the MAC pores are formed at the sites of A β plaques within membranes of surrounding cells. These MAC pores can permeabilize the A β -affected cell membranes, through which ASC specks undergo release into the extracellular space. Upon secretion of ASC specks through the MAC pore-containing membranes, free ASC specks can promote further A β oligomer assembly (Venegas *et al.* 2017), thereby contributing to A β pathology spreading. To note, my data are consistent with the model proposed in (Venegas *et al.* 2017). My results show a colocalization of ASC specks with A β in the plaque cores of AD human brains and the statistical significance of this effect is demonstrated.

Importantly, my data on 3D reconstruction of fluorescently labelled A β plaques co-immunostained for pore-forming C9 of MAC and ASC specks can indicate that C9 complex punches holes in the surface of A β plaque core and the site of C9 activation is observed to form a cavity with significantly decreased immunoreactivity levels of A β and ASC specks within the plaque core. Interestingly, this effect is more significant for the plaques of smaller diameter, that might represent newly formed deposits, that are more prone to the pro-phagocytic MAC effect with enhanced A β clearance capacity as clearly observed for cortical plaques. Therefore, my data suggest that activation of MAC to “small” A β plaque might trigger destabilization of A β aggregate resulting in its local clearance, thereby suppressing/impeding the pro-inflammatory inflammasome activation. It is plausible that this beneficial activity of MAC pores in response to A β aggregation that is a more pronounced effect for newly formed A β deposits of smaller diameter can be linked to activation of signalling pathways. Prevailing evidence from previous studies suggest that

activation of MAC is upregulated in AD brains (McGeer *et al.* 1989; Rogers *et al.* 1992; Itagaki *et al.* 1994; Shen *et al.* 1997; Webster *et al.* 1997). A lethal effect of MAC (C5b-9) on cells through assembly of a lytic pore, mainly consisting of numerous units of C9 protein, on cell surface is well-known (Emmerling *et al.* 2000). The effect of MAC on initiation of signalling pathways has been also documented showing that sublytic MAC pores on target cells can activate signal transduction pathways that might lead to cell proliferation/migration (Niculescu and Rus 2001; Fosbrink *et al.* 2006) and phosphorylation of tau protein (Britschgi *et al.* 2012). Here, the assembly of C5b-9 into MAC pore on the surface of pathogenic A β plaque might trigger specific cellular and immunological events that impede further A β aggregation and promote A β phagocytosis in human AD brains, thereby preventing the pro-inflammatory inflammasome activation. It is important to mention that the assembly of MAC into a pore requires lipid bilayers, into which the complements components C5b, C6, C7, C8, and C9 are incorporated (Serna *et al.* 2016). A β plaque appears not to have the lipid membrane, implying that MAC might not be able to create pores in the A β aggregate. However, in Chapter 5 and Chapter 6, I showed that A β fibrils spatially colocalize with lipid micro-vesicles of high saturated long-chain FAs content, representing one tightly bound complex of A β plaque chemical composition. Therefore, I am hypothesising that MAC can punch holes in A β plaque through interaction with A β -associated lipid micro-vesicles.

Taken together, the quantitative analysis shows that the MAC pores inserted into the A β core can support A β phagocytosis as evident by local reduction of A β immunoreactivity levels at the sites of MAC activation and these locations are also observed to have low ASC speck fluorescence intensities, implying the downregulation of the inflammasome activation at these sites. This observed effect of MAC is more profound for newly formed A β aggregates of smaller size (less than 25 μ m in average as evidenced in this thesis on the investigated population of cortical plaques), possibly implying that excessive aggregation of A β in the course of AD is difficult to overcome by clearance mechanisms of defensive immune system that is known to be downregulated/impaired in the elderly brains of decreased/defective repair function (Busse and Mathur 2012). On the other hand, the quantitative analysis also revealed the colocalization of the ASC specks to MAC pores within the A β cores of predominately the hippocampal plaques with 50 μ m average size, reflecting the MAC as a driver of neuroinflammatory processes in human AD brains. Therefore, my thesis indicates the MAC as a double-edged sword with distinct pro-phagocytic and pro-inflammatory effects on A β pathology, interrelation between which depends from the size of plaques and therefore from the relative area of human AD brains affected by A β accumulation.

9.5. Concluding remarks on the link between A β amyloidosis and neuroinflammation

All in all, my PhD thesis extensively investigated and characterised the inflammatory and lipidomic chemical environment of A β plaques in human AD brains using state-of-the-art high-resolution imaging techniques. The results show the sustained accumulations of oxidative stress and neuroinflammatory components of innate immune system colocalizing to A β plaque lesions, indicating inflammation as major contributor to AD pathology spreading. Specifically, quantitative imaging of chemical composition of A β plaque areas in human AD brains using two independent optical tools revealed spatial colocalization of numerous MAC pores with ASC specks (as shown by immunofluorescence) and calcium crystals (as shown by Raman microspectroscopy) in A β plaque cores, possibly indicating the link between these inflammatory signatures. The potential association of MAC pores with calcium deposits and ASC speck accumulations within the A β plaque cores can be explained by the previous study in human lung epithelial cells showing that the formation of MAC pores in the cell membranes leads to Ca²⁺ accumulations in the mitochondrial matrix, which recruits the NLRP3 assembly and ASC speck accumulation, thereby initiating further pro-inflammatory response and apoptosis (Triantafilou *et al.* 2013). As another important outcome, my PhD underlines a possible non-lethal beneficial effect of MAC complex on reduction of A β accumulations in AD brains, implying that MAC pores might act as a promoter of A β clearance. This activity of MAC which is exclusively applied to newly formed A β aggregates might indicate on the possibility that sustained growth of A β plaque areas in the course of AD may be linked to decreased/impaired phagocytic function mediated by the MAC.

Appendix A

Appendix A represents the results of two separate 20 component Q-US/PS-NMF analyses on the acquired Raman biomedical datasets of formalin-fixed-paraffin-embedded human AD brain tissues together with controls in hippocampal or cortical regions that report the biochemical composition of AD human brains as investigated in Chapter 5. In the analysis of the hippocampus, the datasets of 30 regions containing A β plaques from 5 AD individuals and 10 control regions from elderly humans without AD were included. In the analysis of the cortex, the datasets of 31 A β plaque areas from 6 AD subjects together with 7 control maps from 2 non-demented humans were participated. Each Fig. A-1 to A-20 (the hippocampus) and Fig. A-23 to A-42 (the cortex) in the given brain region provides the component spectra (on the left) and its corresponding spatial concentration profile (on the right) in the investigated samples, as retrieved from the factorization analysis. Figs. A-21 and 43 show the spatial (on the left) and spectral (on the right) mean absolute factorization error resulting from the factorization analysis of the hippocampal and cortical samples, respectively. The value for relative factorization error is also given on the top of each figure. Fig. A-22 and 44 illustrate the mean spatially resolved subtracted fluorescence intensity found by averaging over the same spectral regions as for the component spectra and normalizing on the component spectral integral for each respective hippocampal and cortical Raman image.

Chemical composition of the human hippocampus in AD presented below:

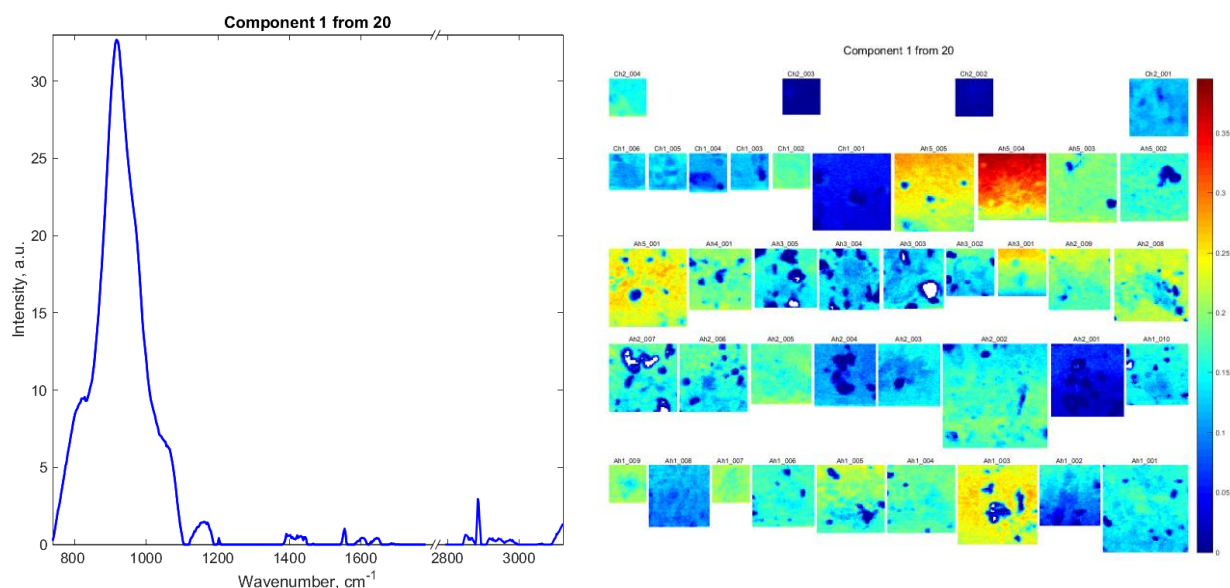


Fig. A-1: The component spectra C1 and its spatial distributions of the Raman concentration for the measured AD hippocampal brain regions together with controls (labelled according to the sample source as Ah1,..., Ah5, and Ch1, Ch2, respectively) on colour scales as indicated, retrieved from the simultaneous Q-US/PS-NMF unmixing analysis of 30 hippocampal A β plaques (5 AD patients) together with 10 control Raman maps (2 elderly humans without AD).

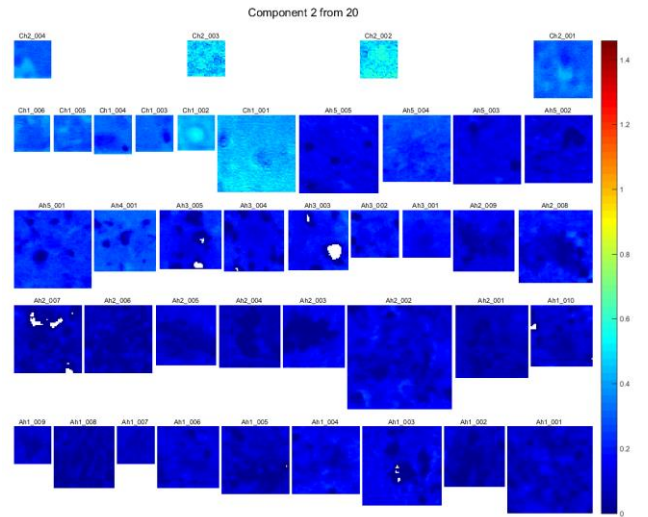
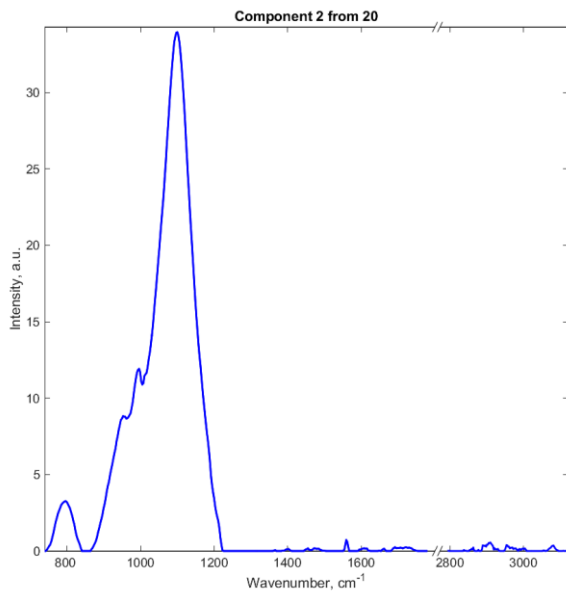


Fig. A-2: As Fig. A-1, but for C2.

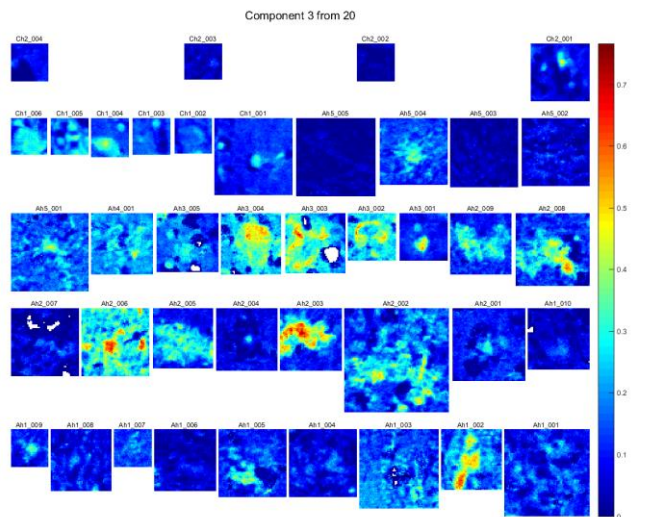
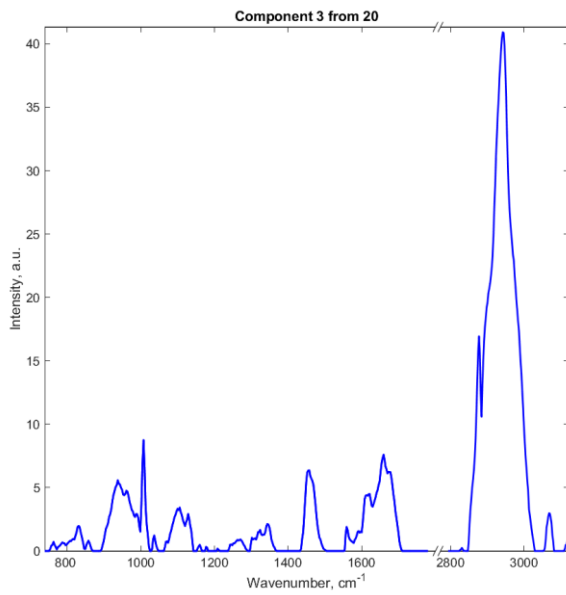


Fig. A-3: As Fig. A-1, but for C3.

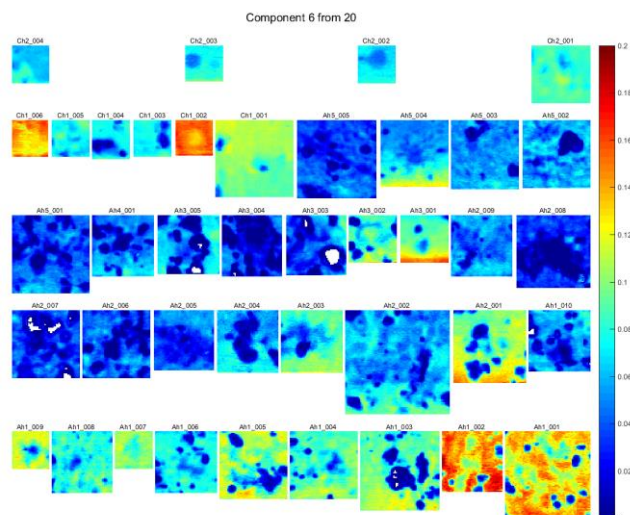
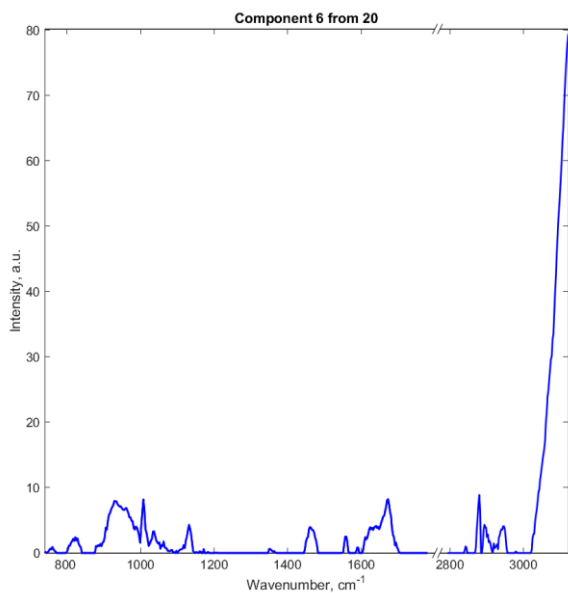


Fig. A-6: As Fig. A-1, but for C6.

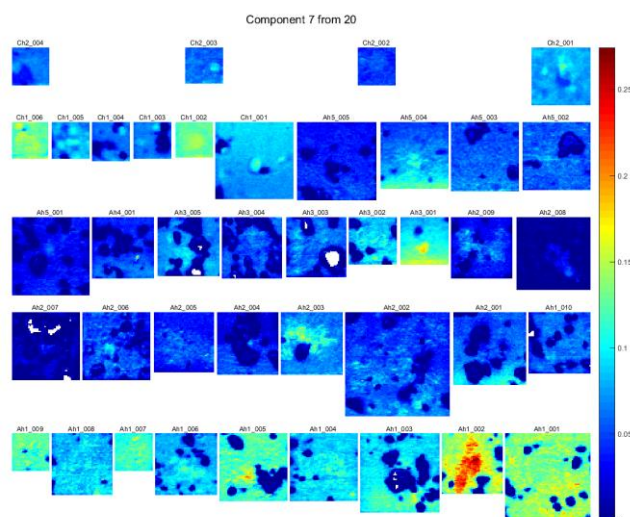
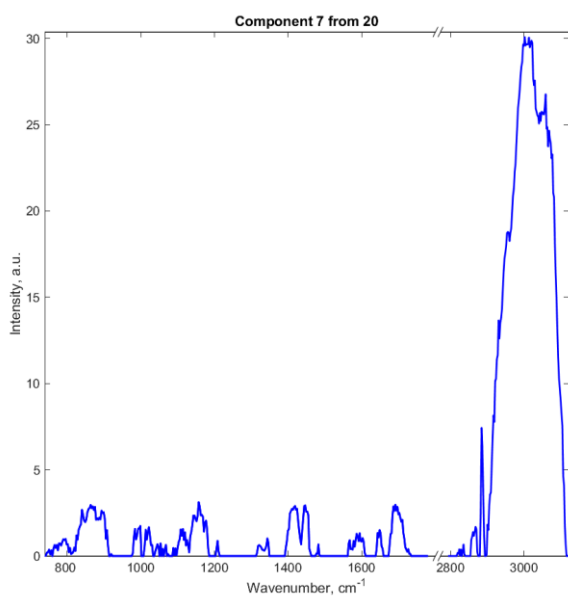


Fig. A-7: As Fig. A-1, but for C7.

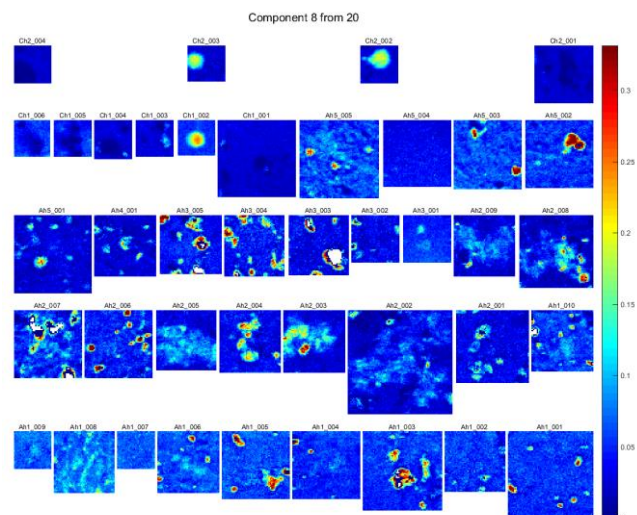
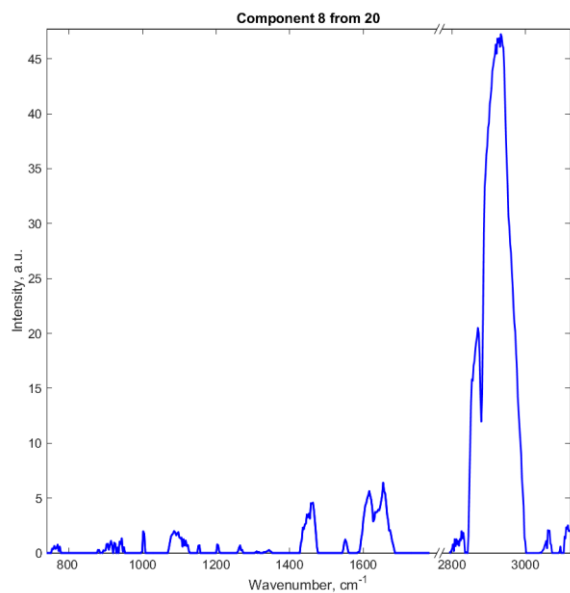


Fig. A-8: As Fig. A-1, but for C8.

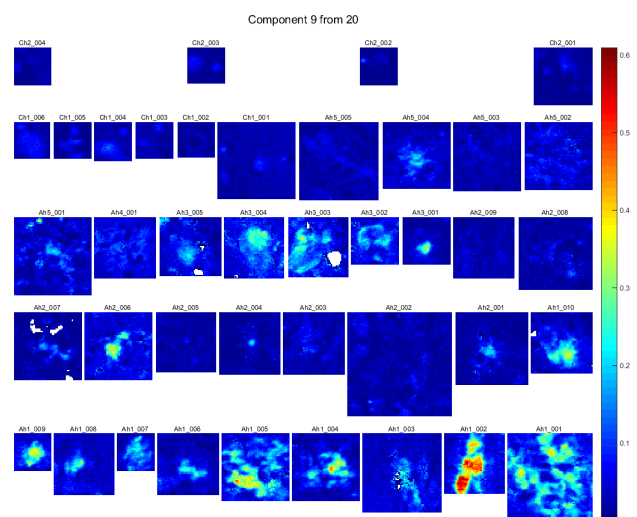
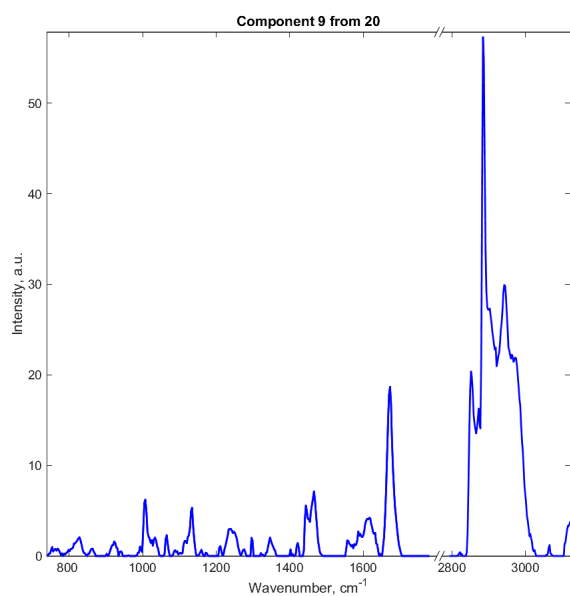


Fig. A-9: As Fig. A-1, but for C9.

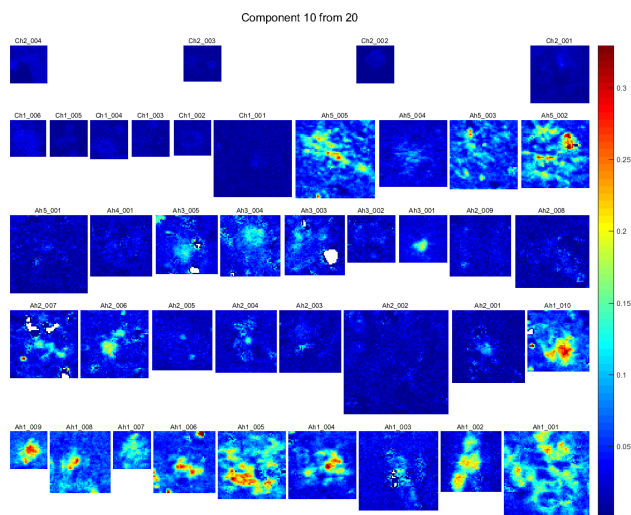
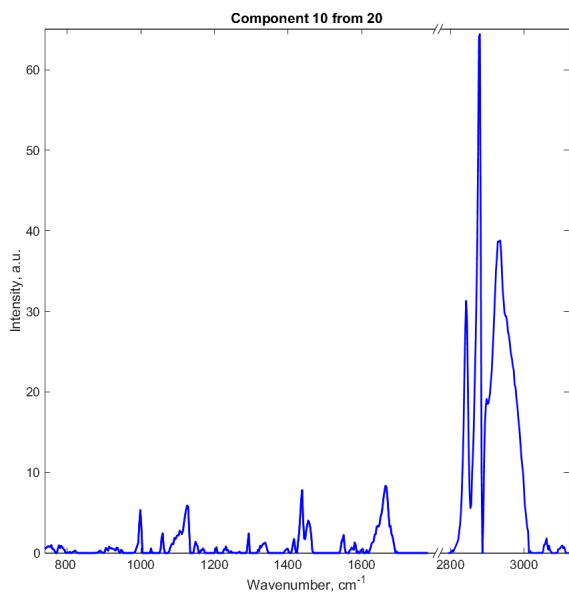


Fig. A-10: As Fig. A-1, but for C10.

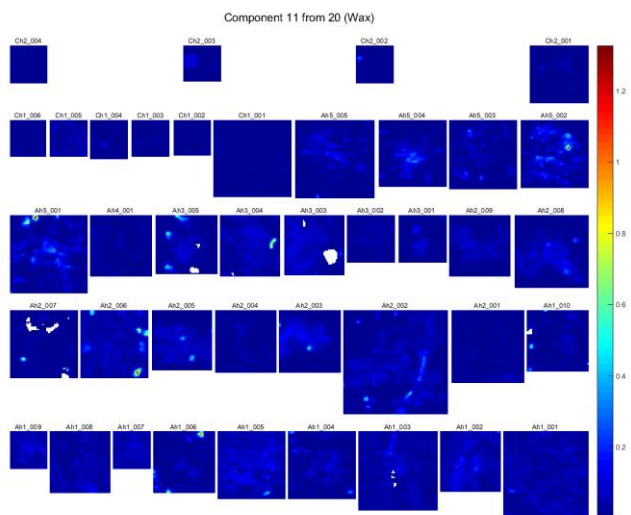
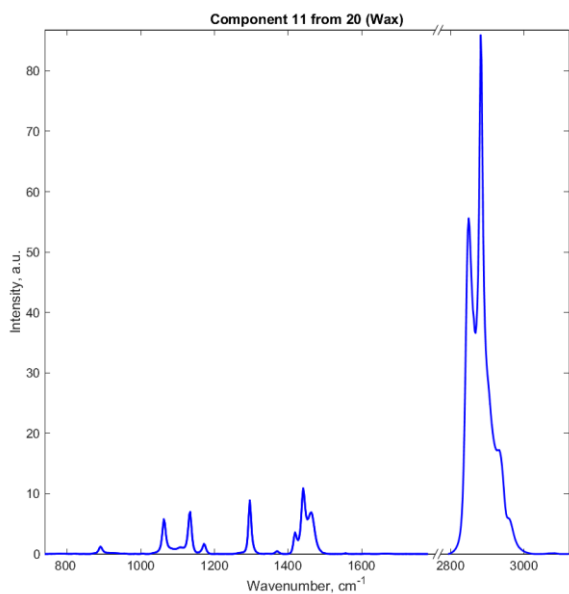


Fig. A-11: As Fig. A-1, but for C11.

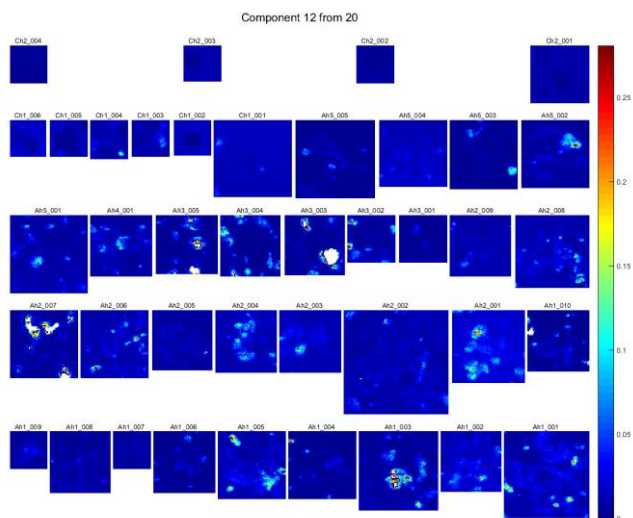
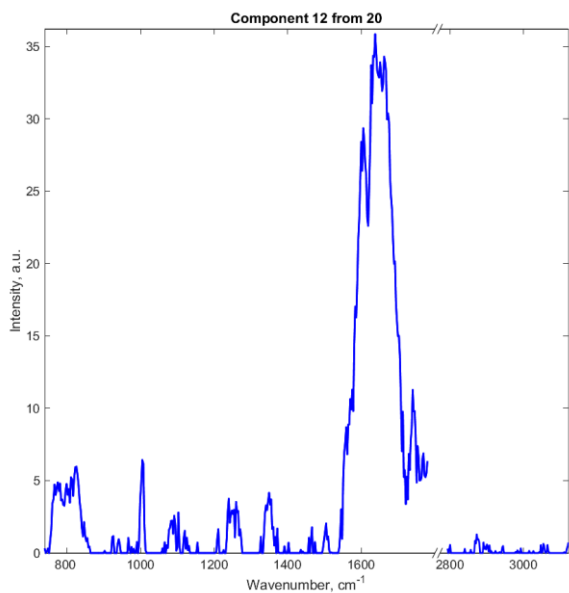


Fig. A-12: As Fig. A-1, but for C12.

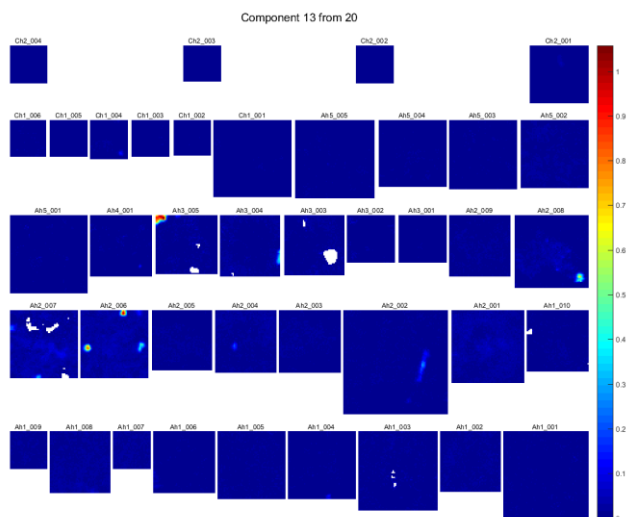
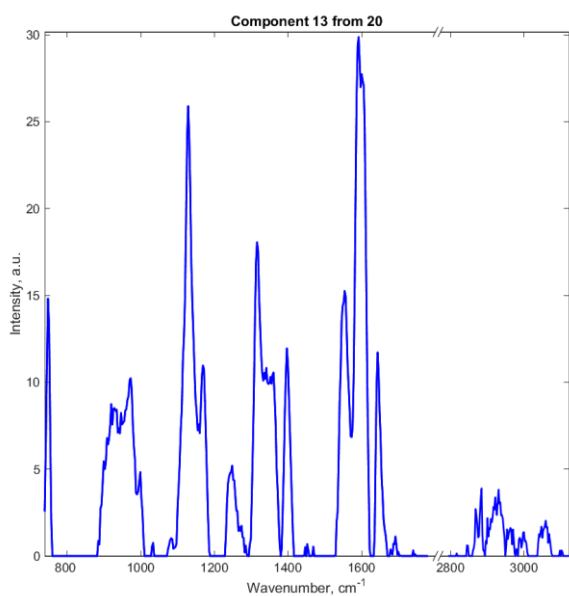


Fig. A-13: As Fig. A-1, but for C13.

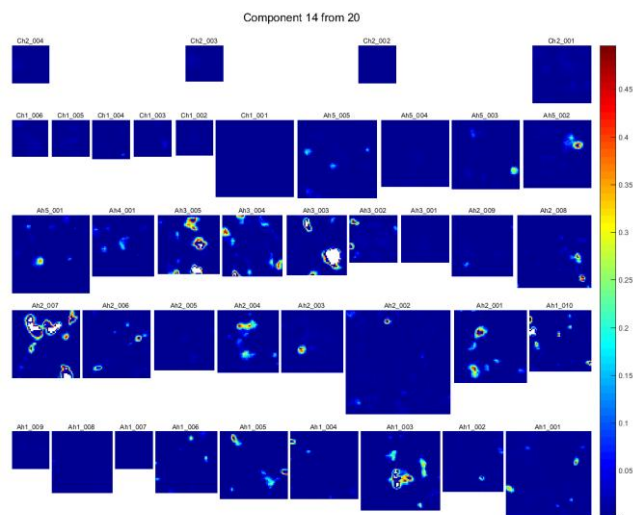
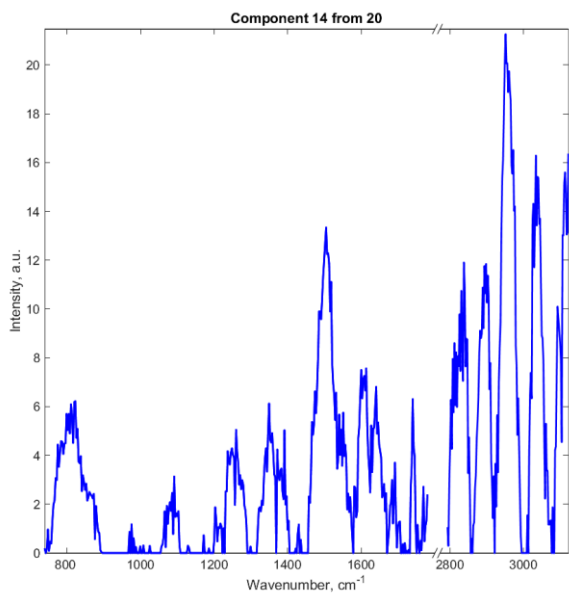


Fig. A-14: As Fig. A-1, but for C14.

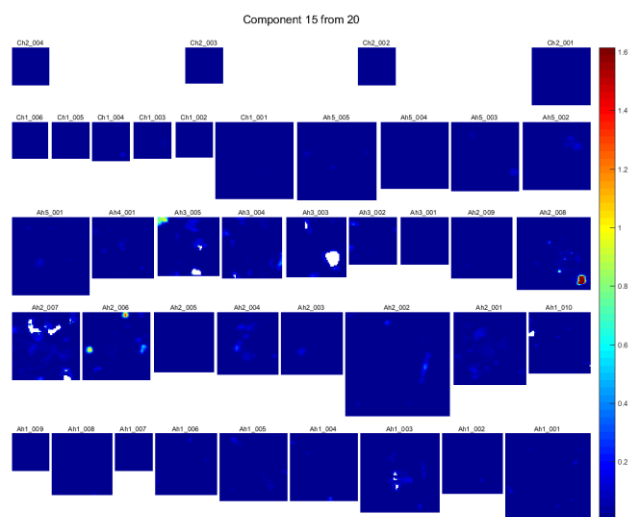
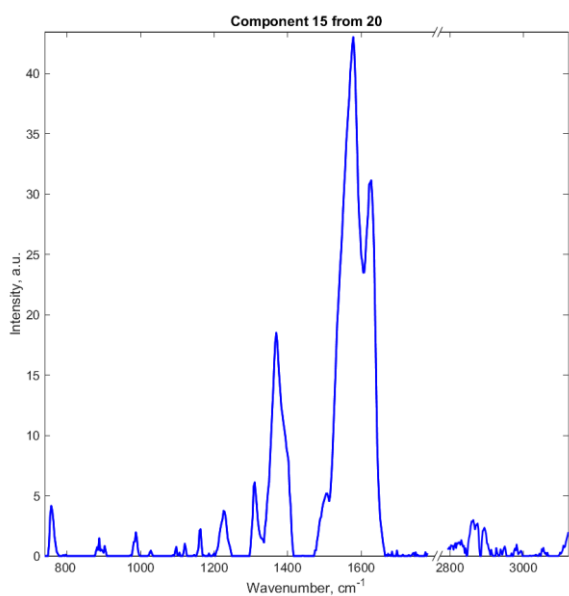


Fig. A-15: As Fig. A-1, but for C15.

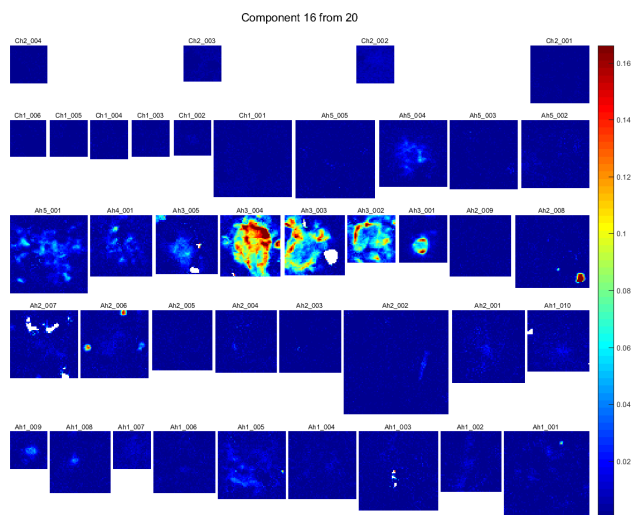
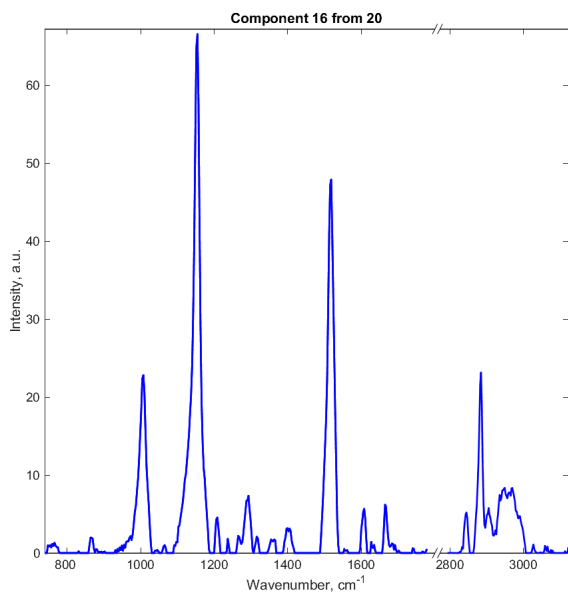


Fig. A-16: As Fig. A-1, but for C16.

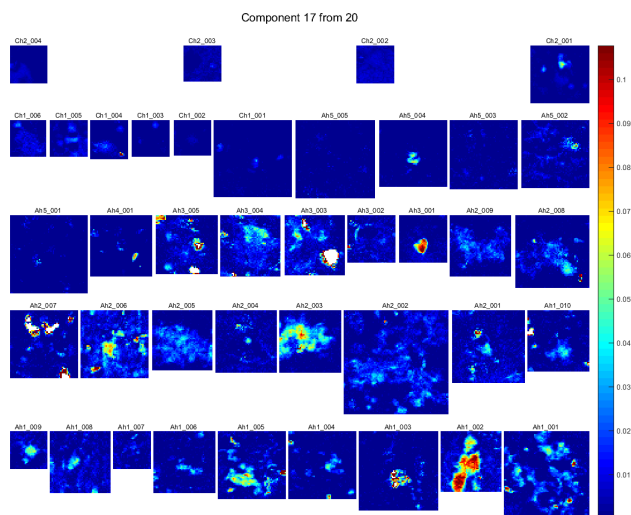
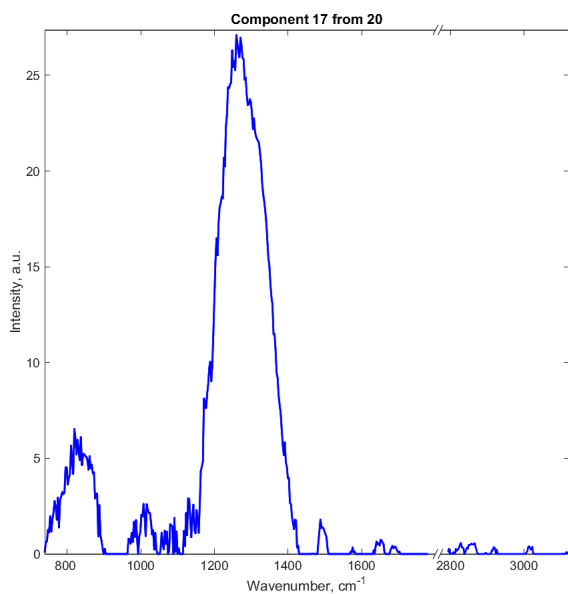


Fig. A-17: As Fig. A-1, but for C17.

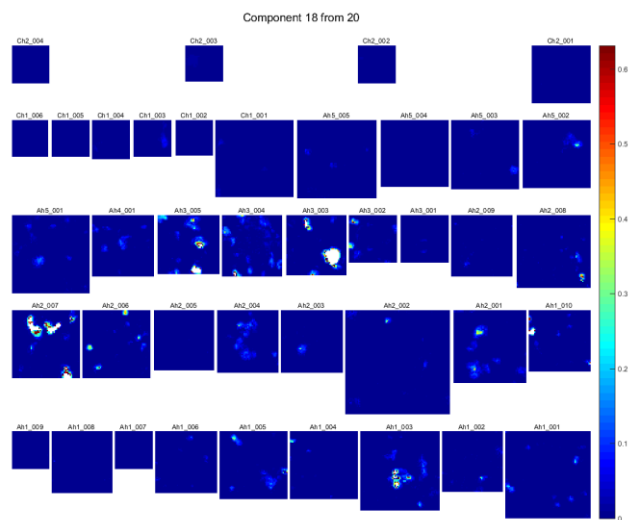
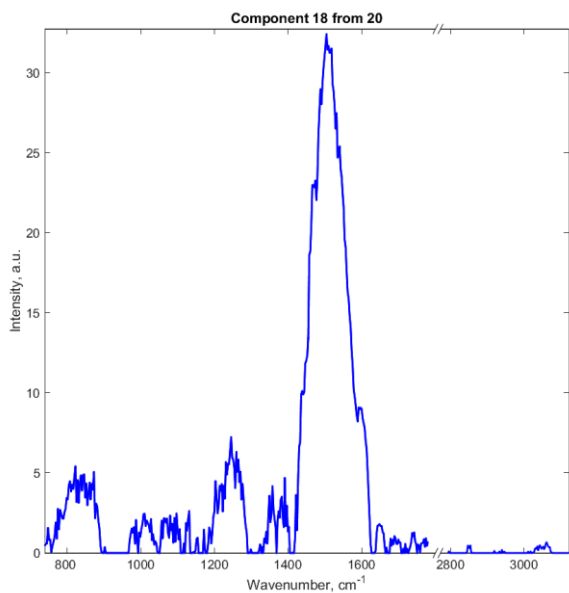


Fig. A-18: As Fig. A-1, but for C18.

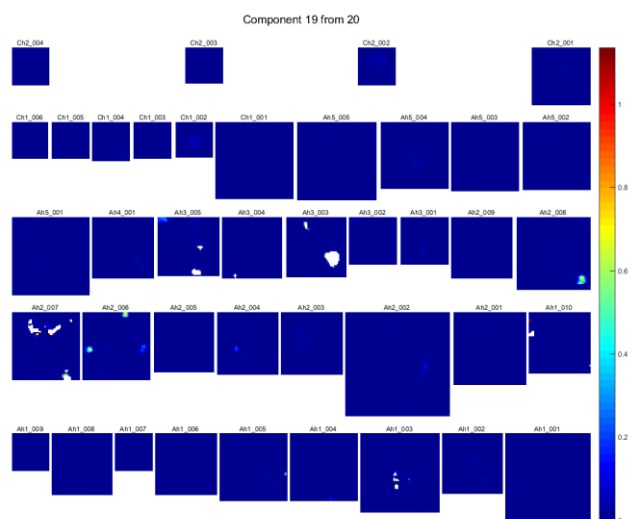
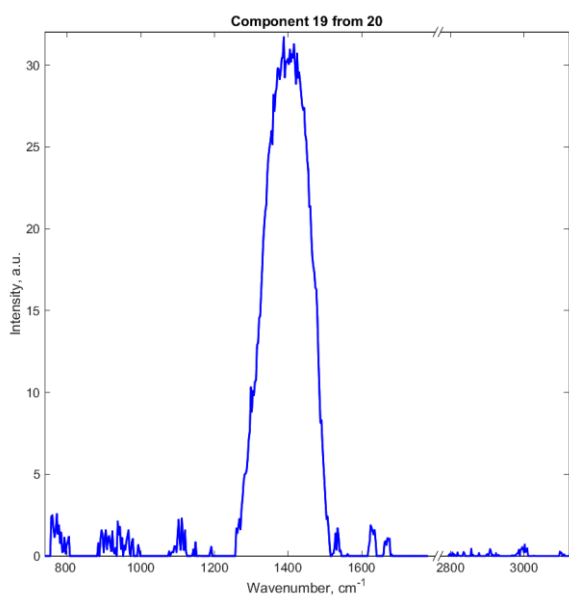


Fig. A-19: As Fig. A-1, but for C19.

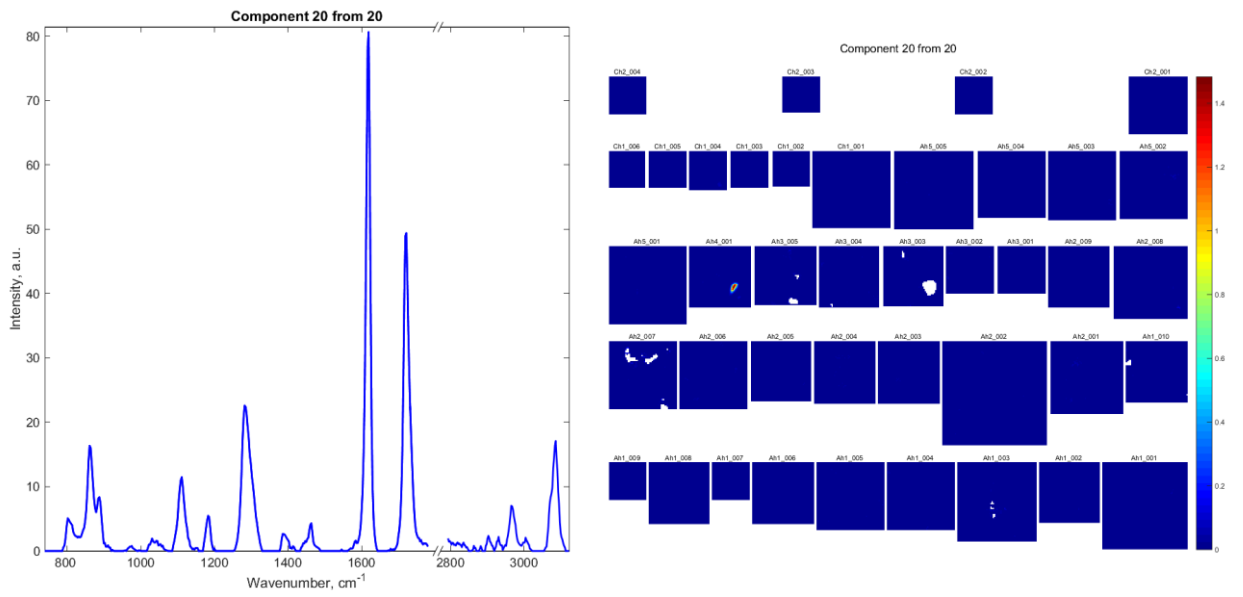


Fig. A-20: As Fig. A-1, but for C20.

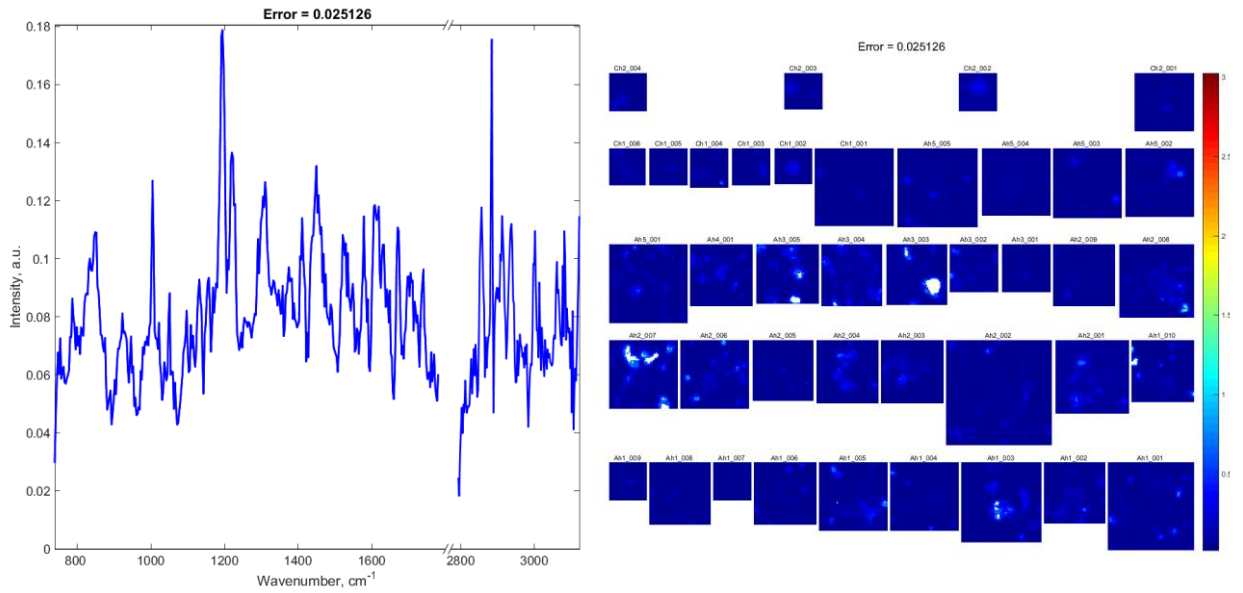


Fig. A-21: The spatial (on the right) and spectral (on the left) mean absolute factorization error resulting from the simultaneous Q-US/PS-NMF unmixing analysis of 30 hippocampal A β plaques (5 AD patients) together with 10 control Raman maps (2 elderly humans without AD).

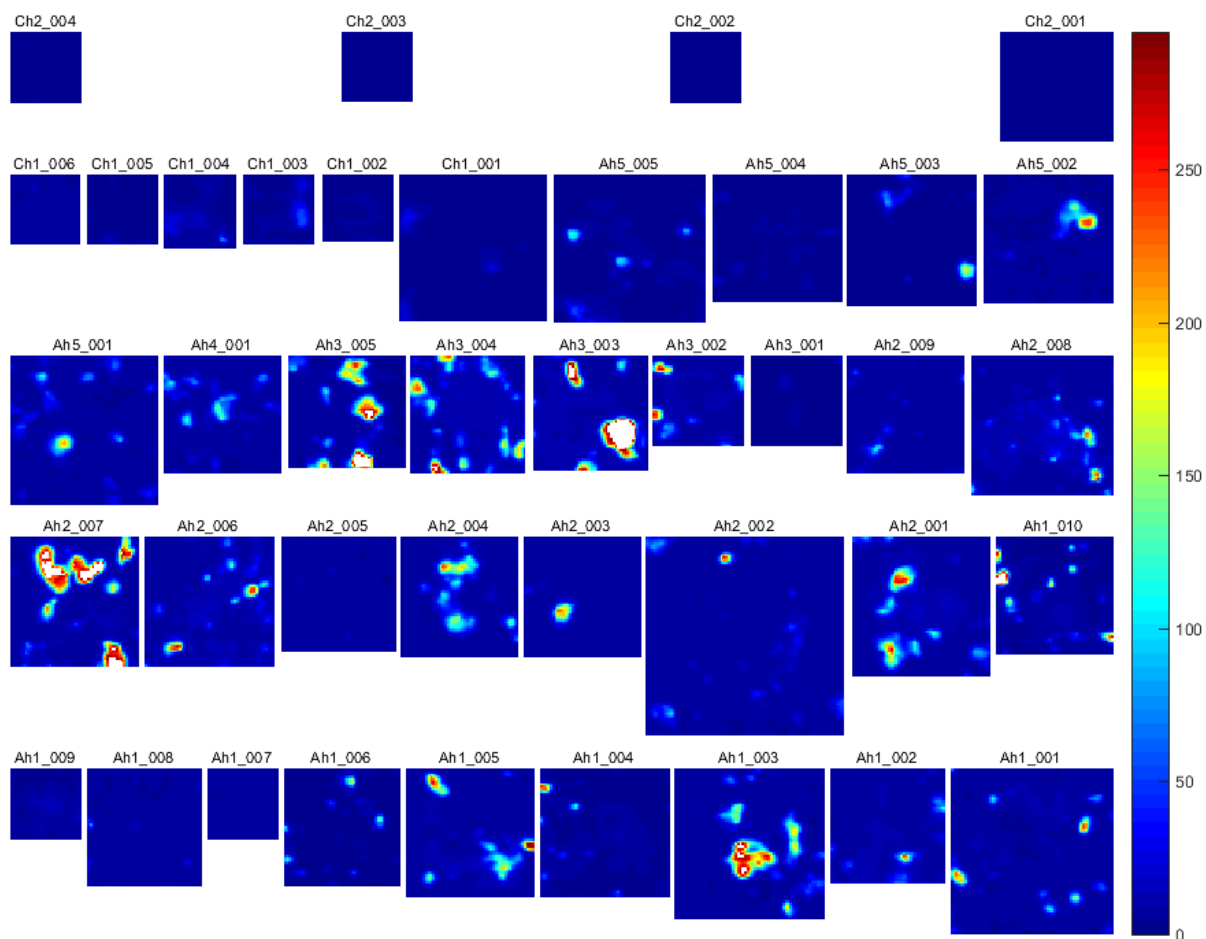


Fig. A-22: The mean spatially resolved subtracted fluorescence intensity of the same hippocampal samples found by averaging over the same spectral regions as for the component spectra and normalizing on the component spectral integral.

Chemical composition of the human cerebral cortex in AD presented below:

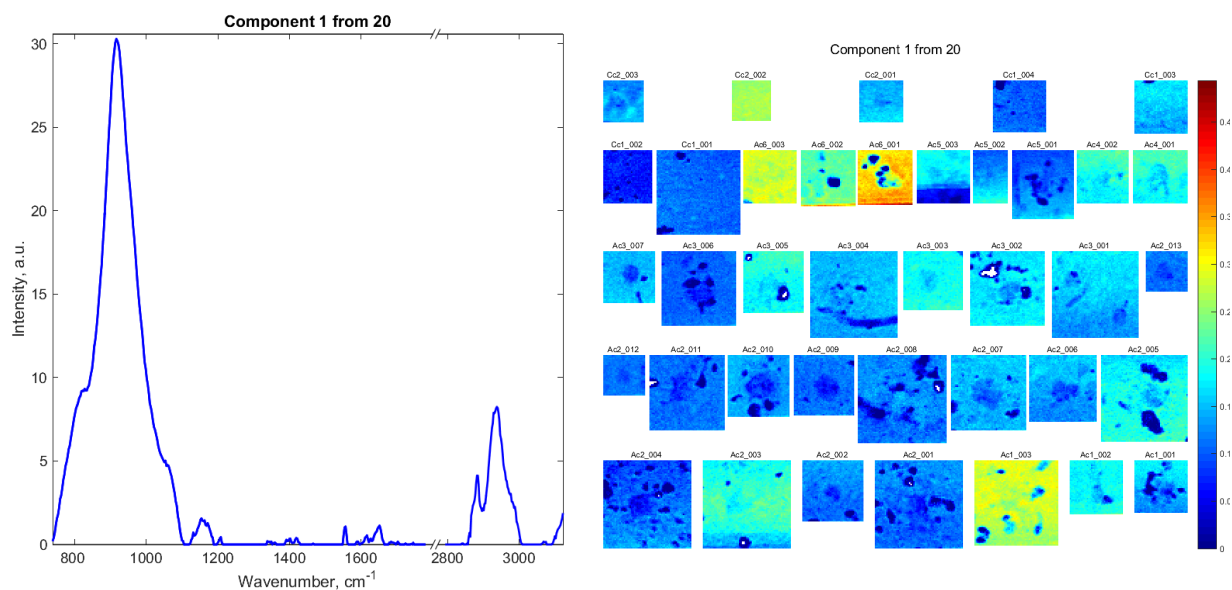


Fig. A-23: The component spectra C1 and its spatial distributions of the Raman concentration for the measured AD cortical brain regions together with controls (labelled according to the sample source as Ac1,..., Ac7, and Cc1, Cc2, respectively) on colour scales as indicated, retrieved from the simultaneous Q-US/PS-NMF unmixing analysis of 31 cortical A β plaques (7 AD patients) together with 7 control Raman maps (2 elderly humans without AD)

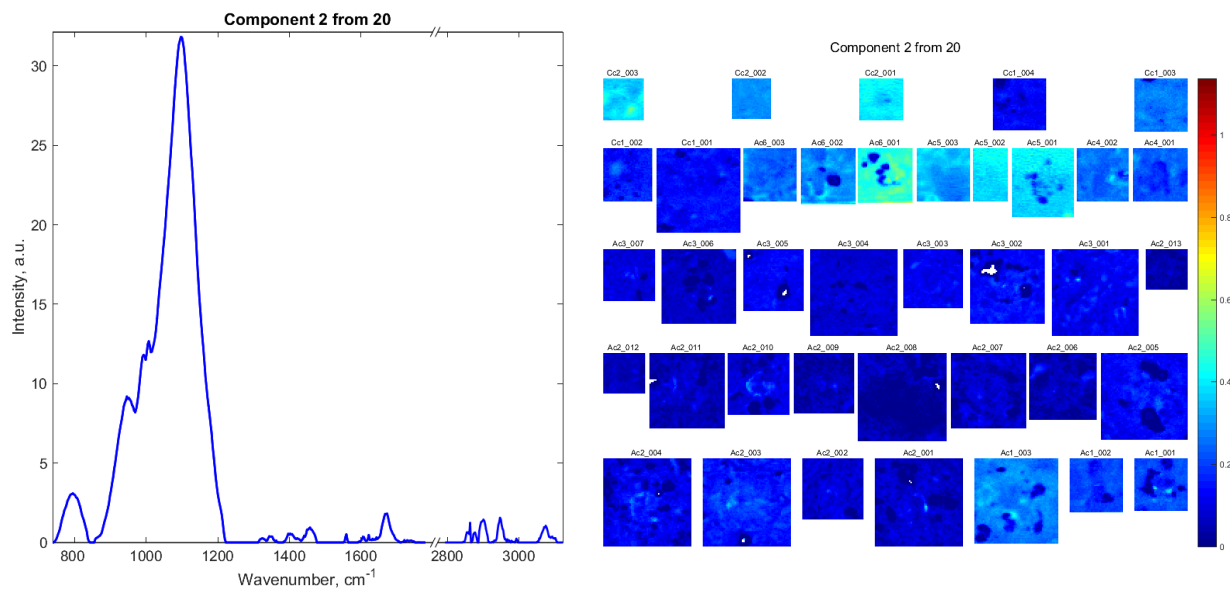


Fig. A-24: As Fig. A-23, but for C2.

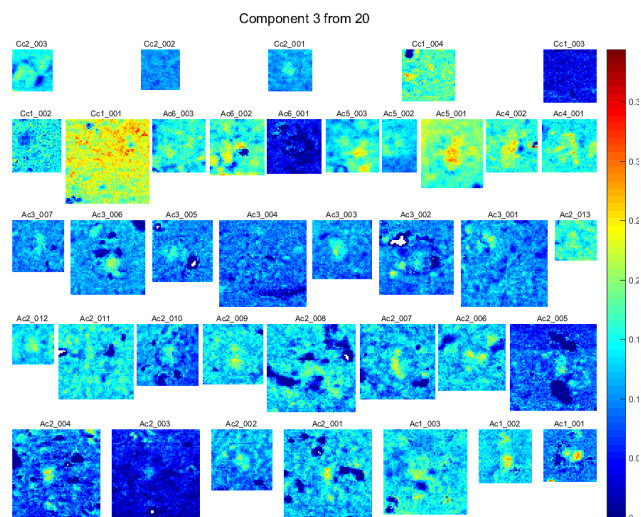
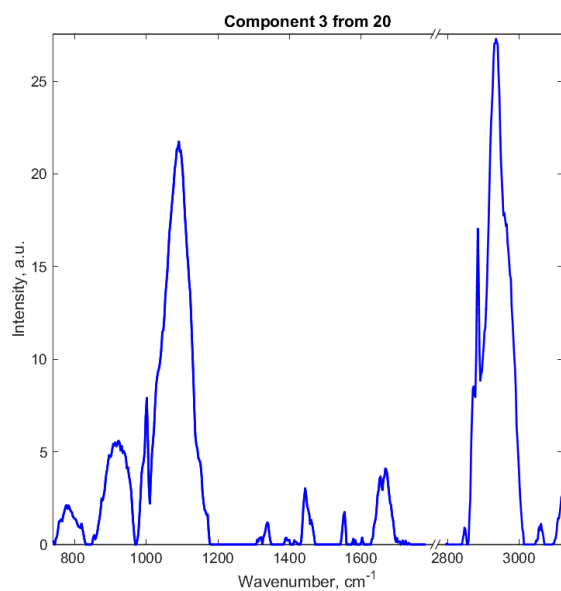


Fig. A-25: As Fig. A-23, but for $\mathbb{C}3$.

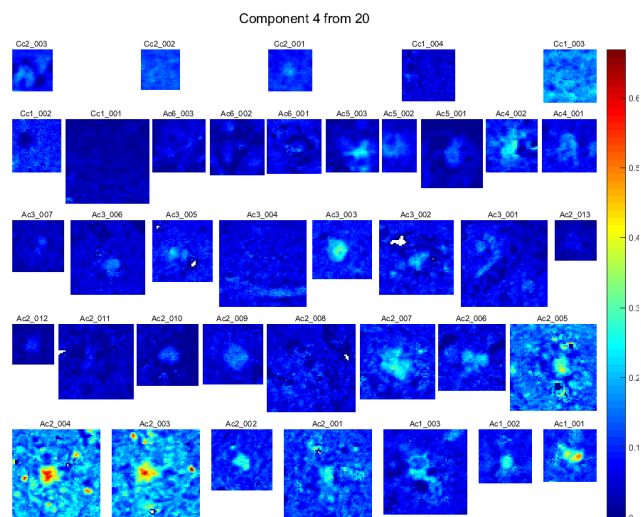
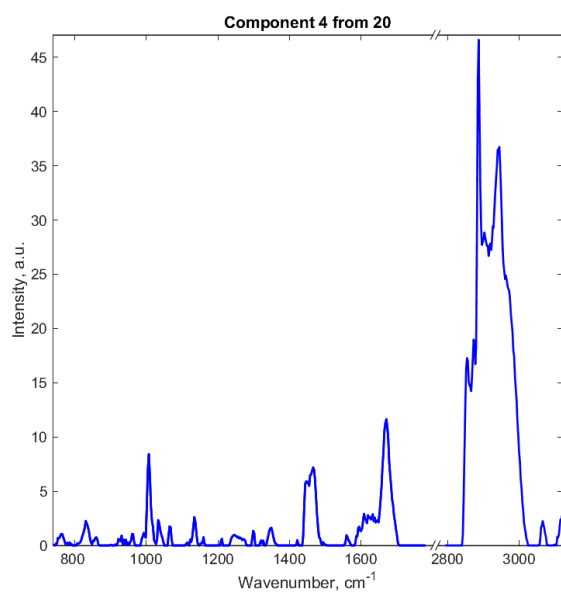


Fig. A-26: As Fig. A-23, but for $\mathbb{C}4$.

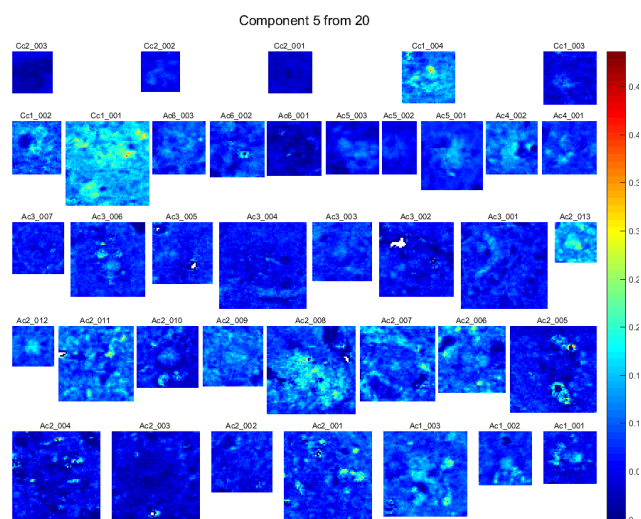
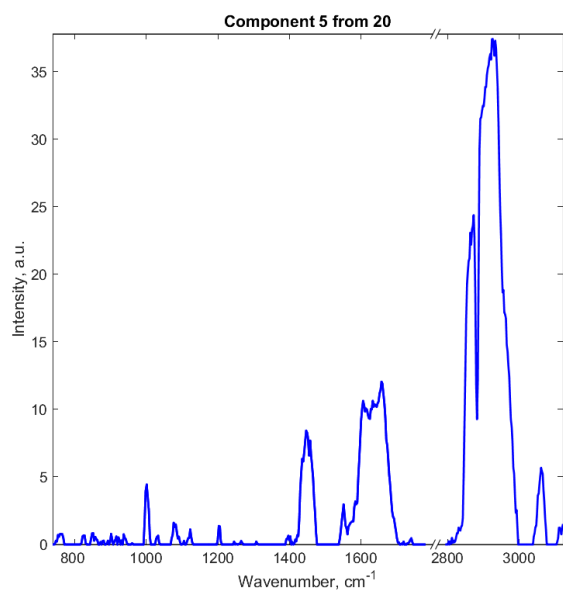


Fig. A-27: As Fig. A-23, but for $\mathbb{C}5$.

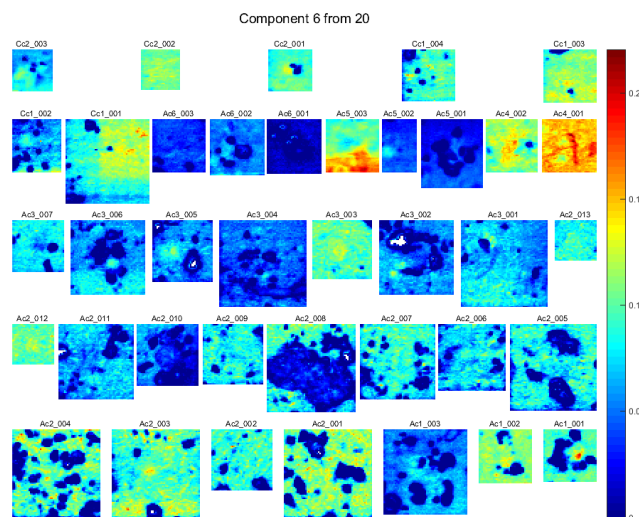
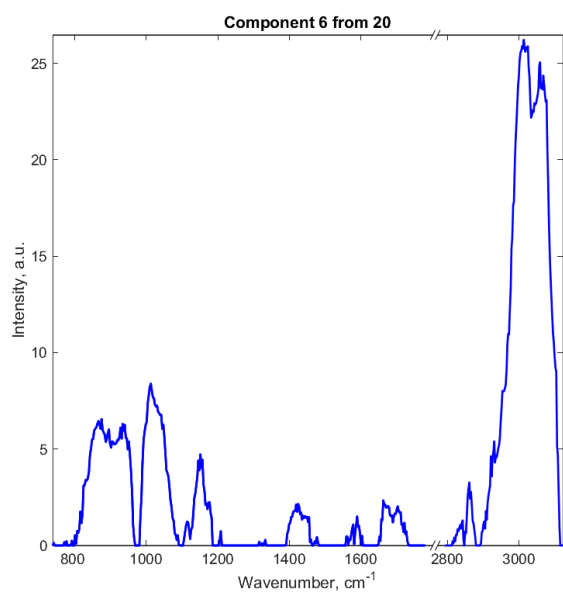


Fig. A-28: As Fig. A-23, but for $\mathbb{C}6$.

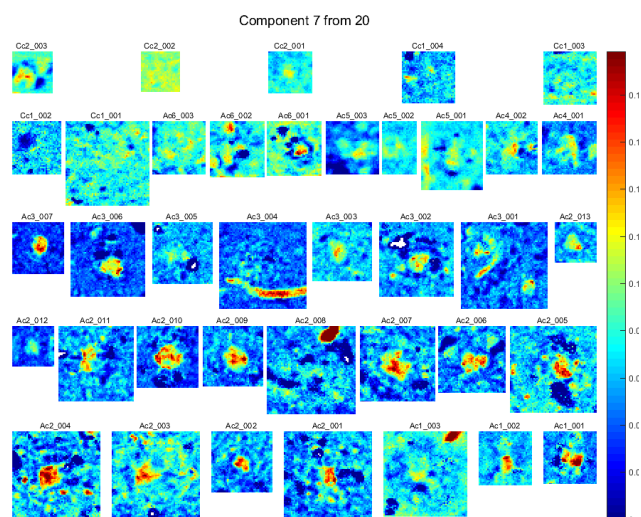
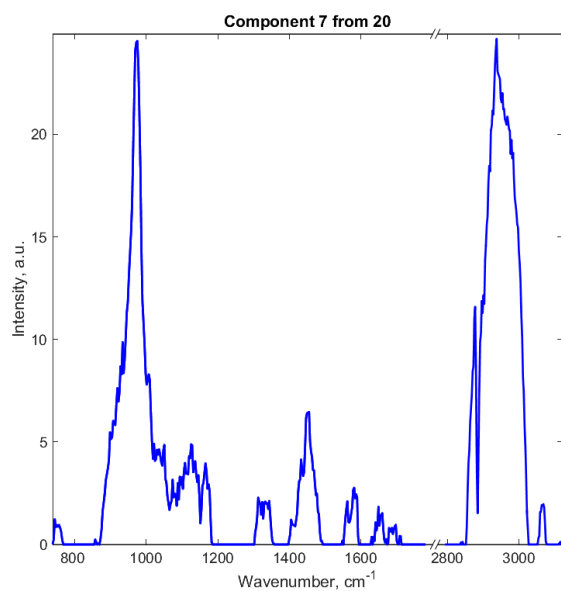


Fig. A-29: As Fig. A-23, but for $\mathbb{C}7$.

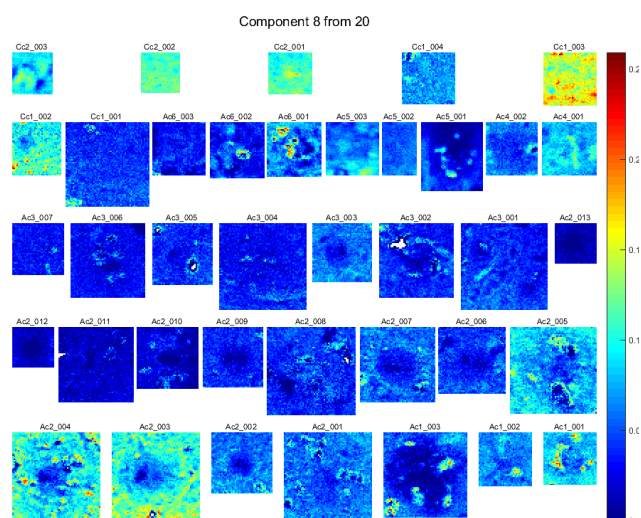
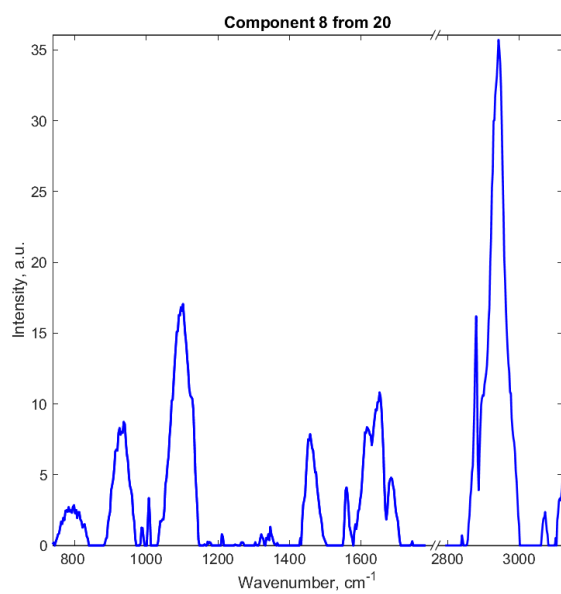


Fig. A-30: As Fig. A-23, but for $\mathbb{C}8$.

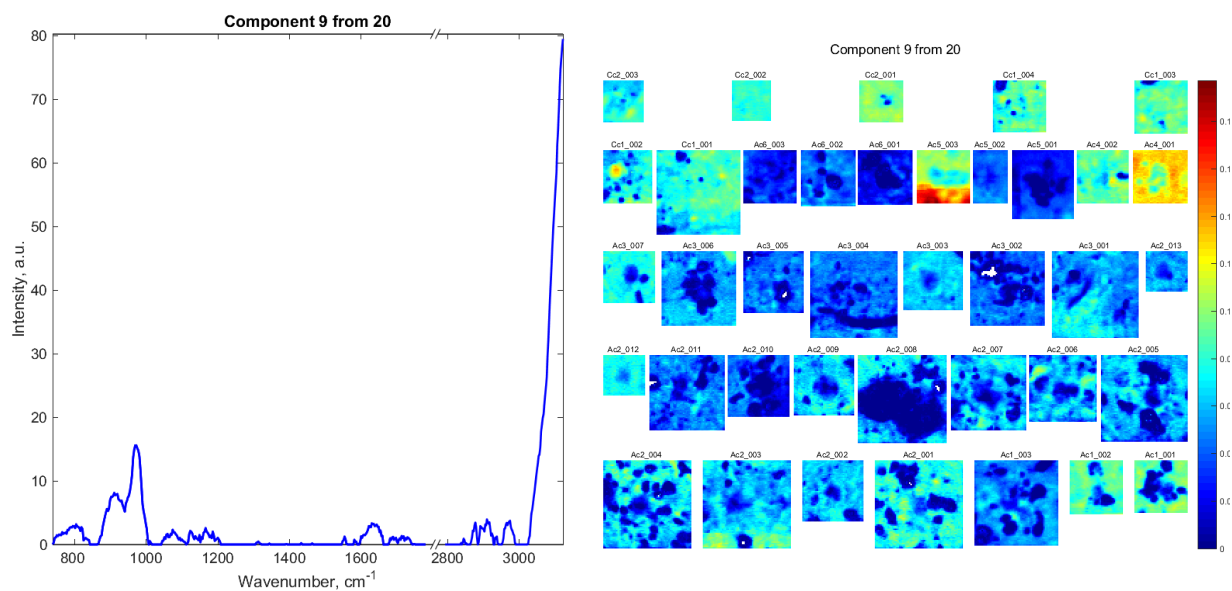


Fig. A-31: As Fig. A-23, but for $\mathbb{C}9$.

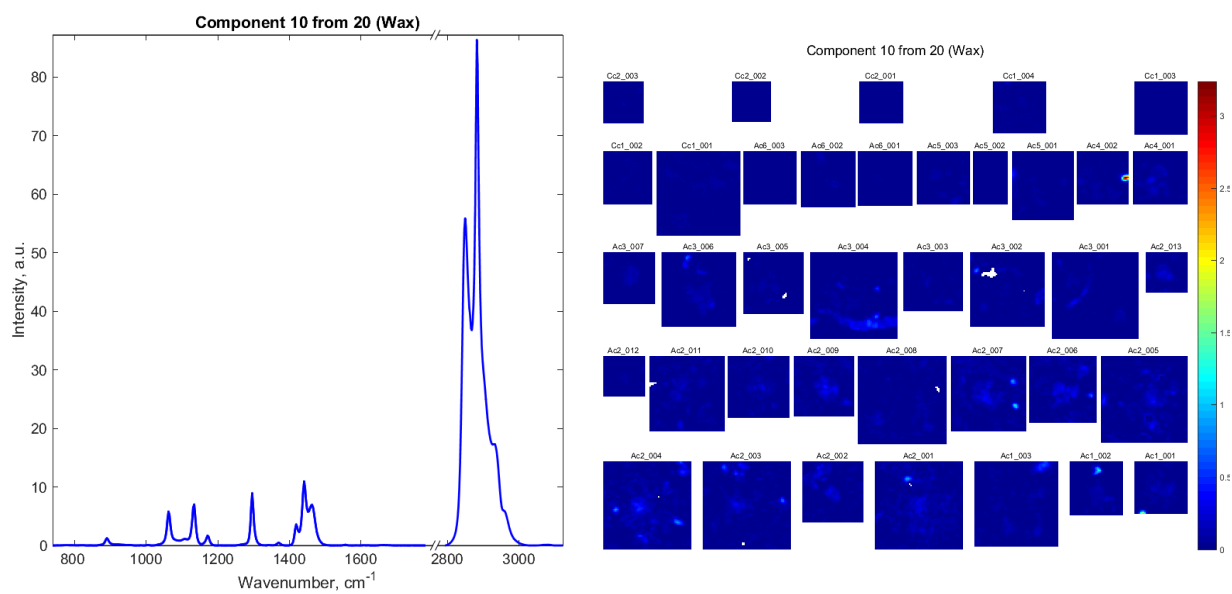


Fig. A-32: As Fig. A-23, but for $\mathbb{C}10$.

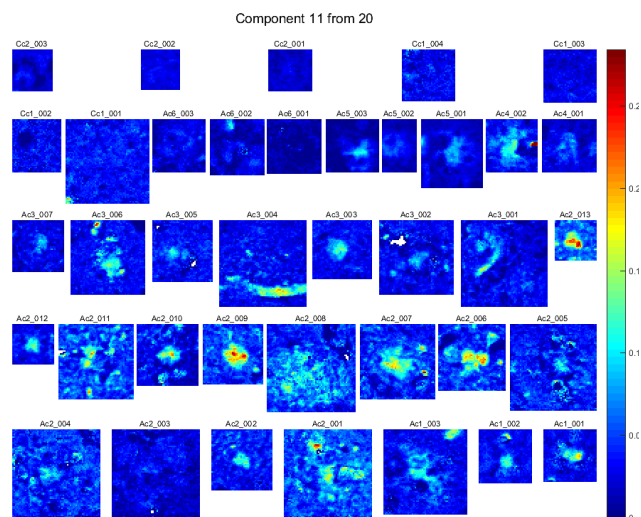
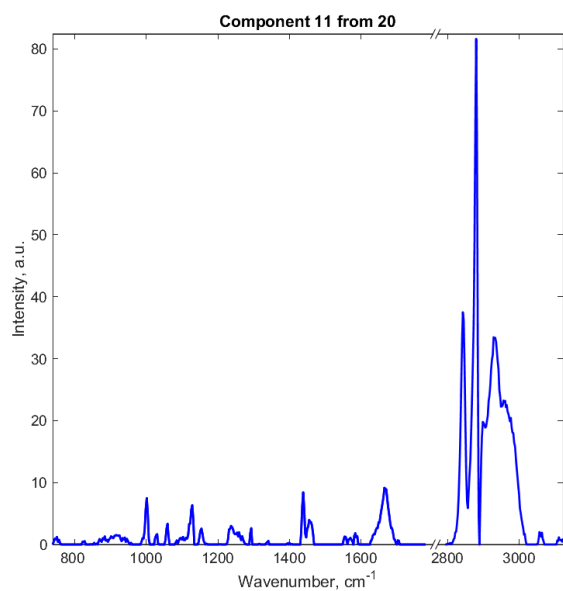


Fig. A-33: As Fig. A-23, but for $\mathbb{C}11$.

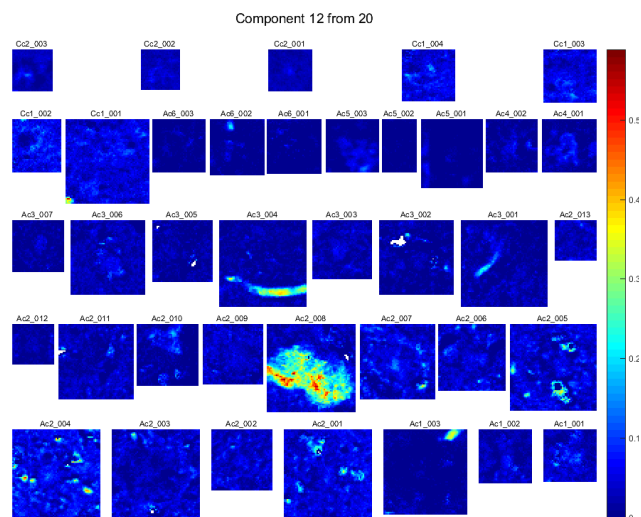
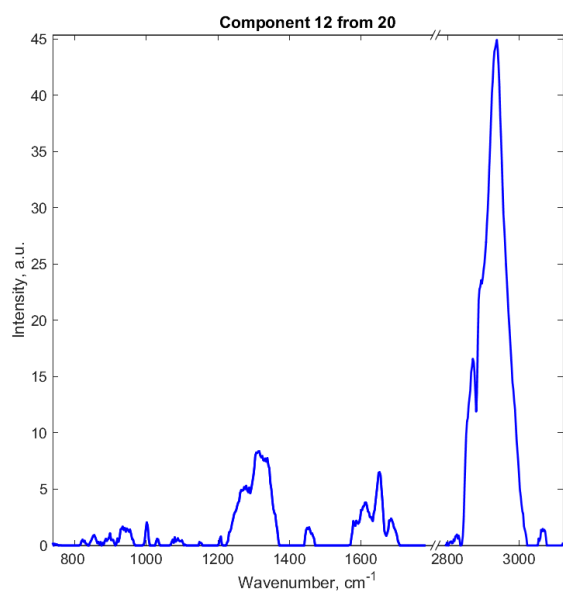


Fig. A-34: As Fig. A-23, but for $\mathbb{C}12$.

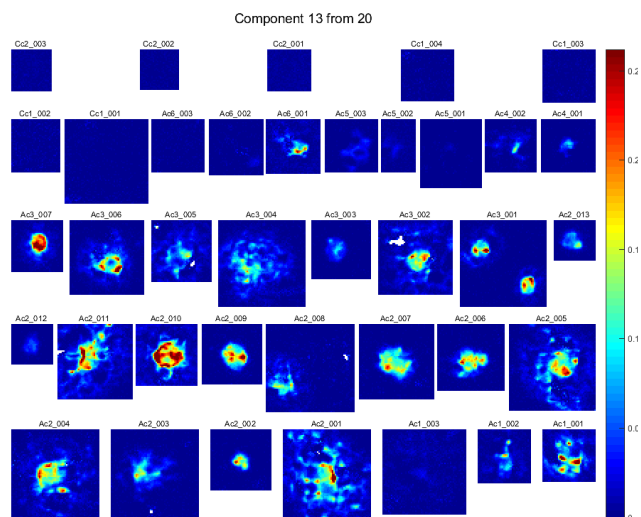
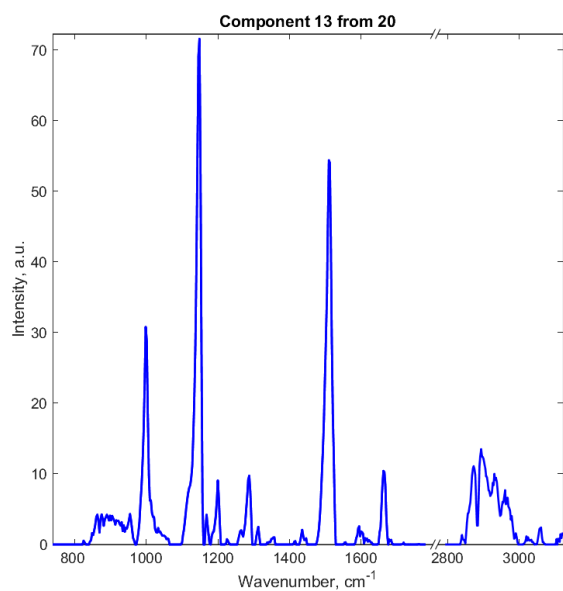


Fig. A-35: As Fig. A-23, but for $\mathbb{C}13$.

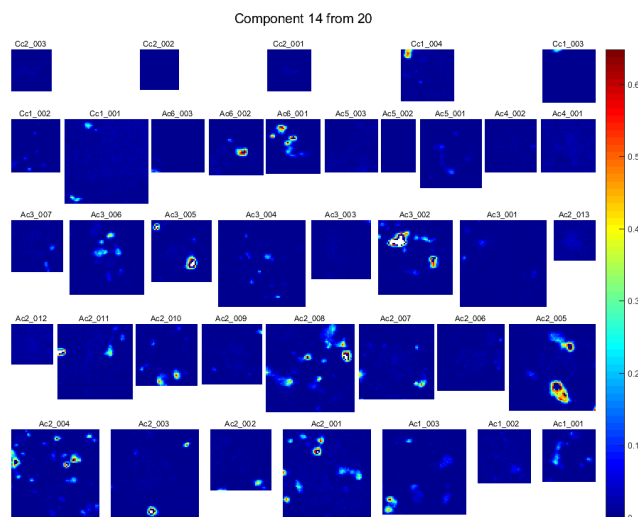
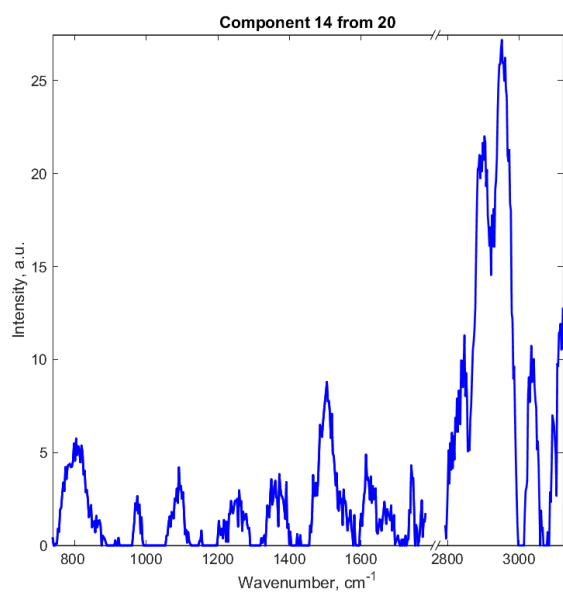


Fig. A-36: As Fig. A-23, but for $\mathbb{C}14$.

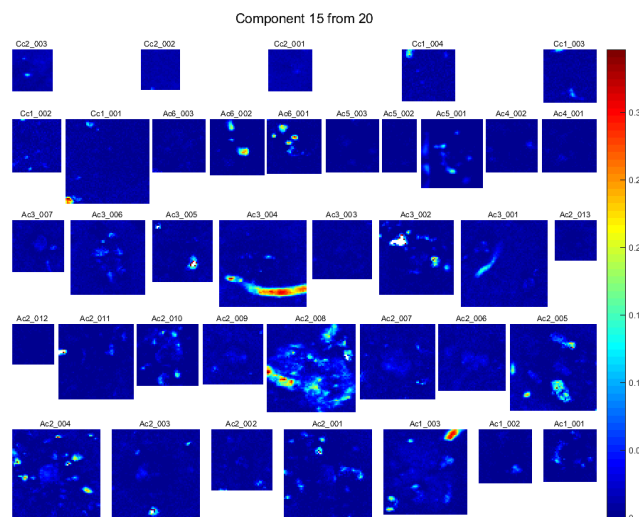
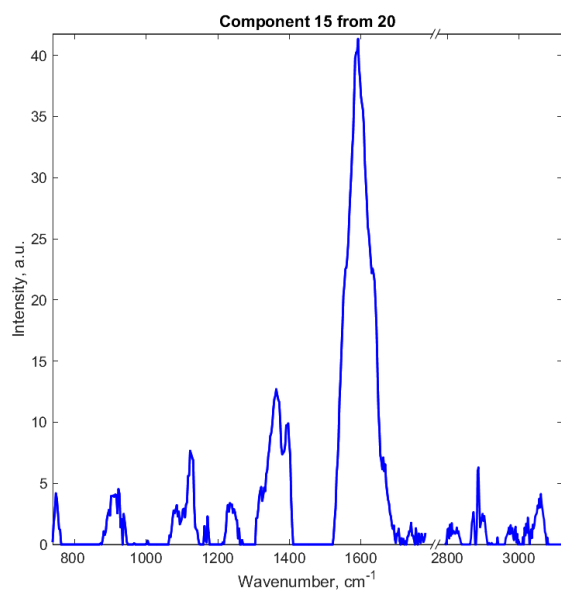


Fig. A-37: As Fig. A-23, but for $\mathbb{C}15$.

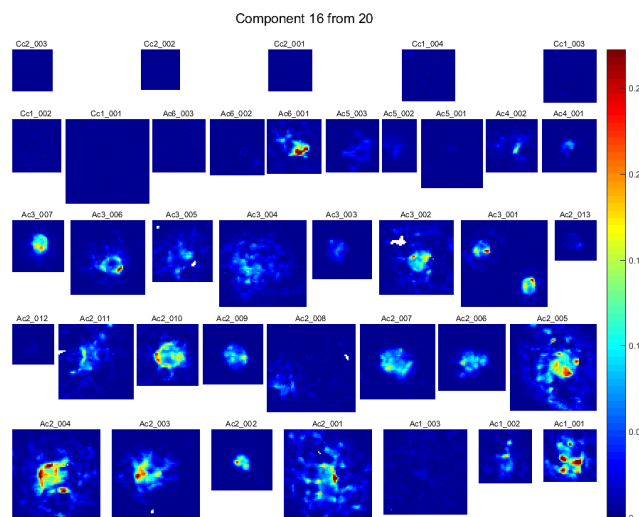
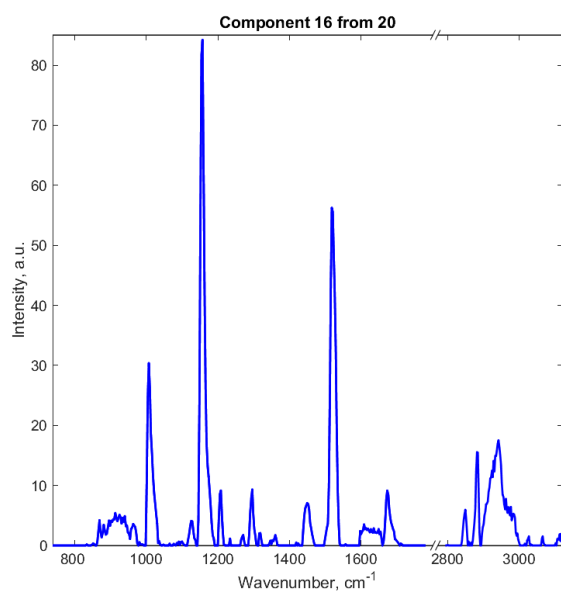


Fig. A-38: As Fig. A-23, but for $\mathbb{C}16$.

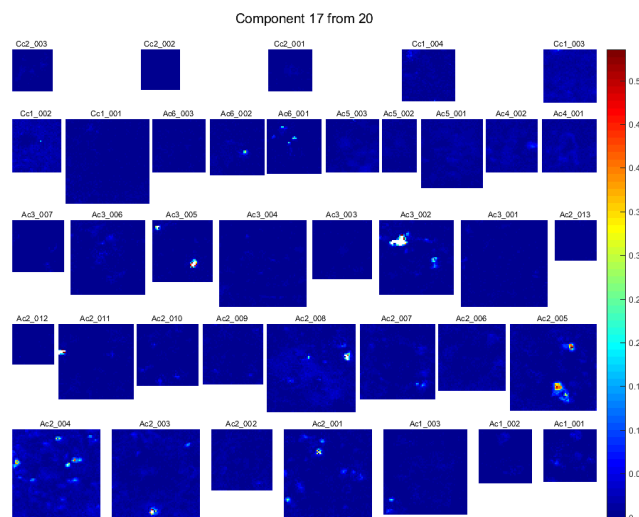
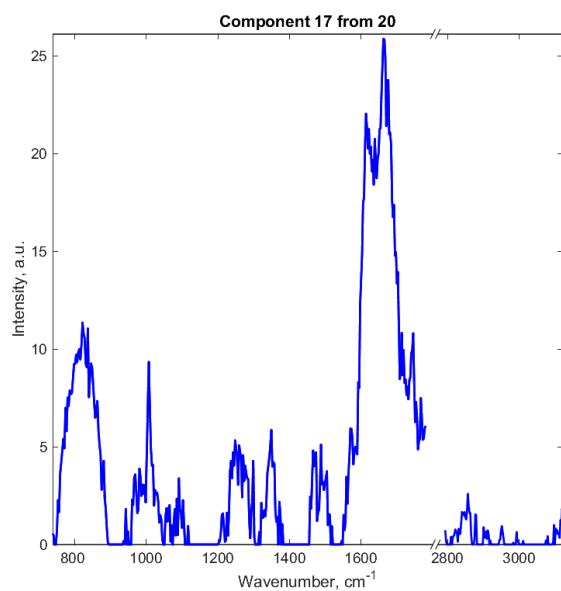


Fig. A-39: As Fig. A-23, but for $\mathbb{C}17$.

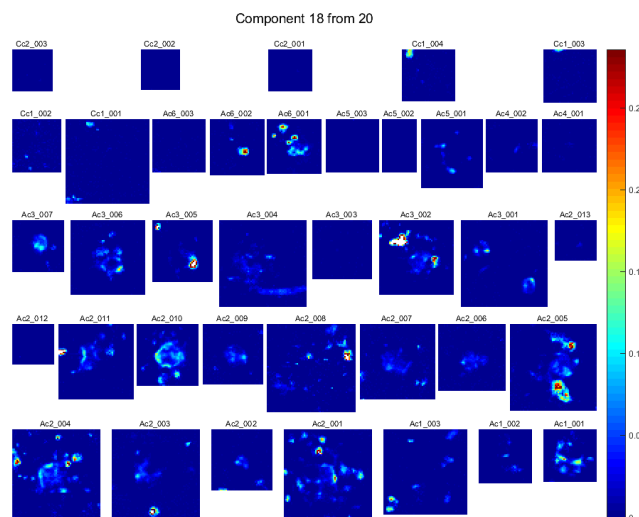
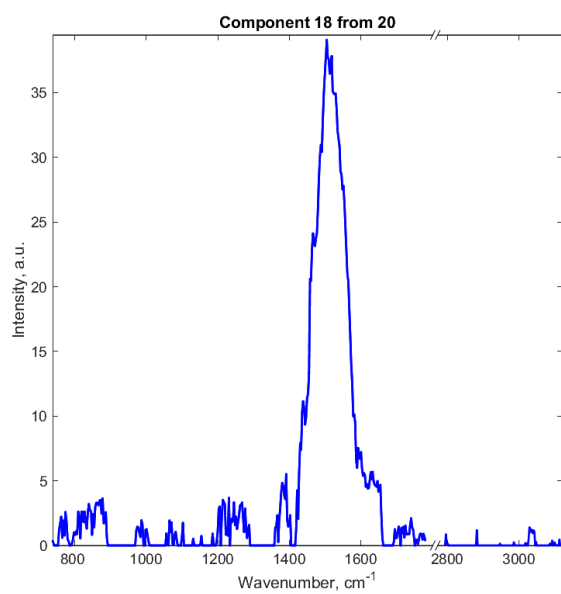


Fig. A-40: As Fig. A-23, but for $\mathbb{C}18$.

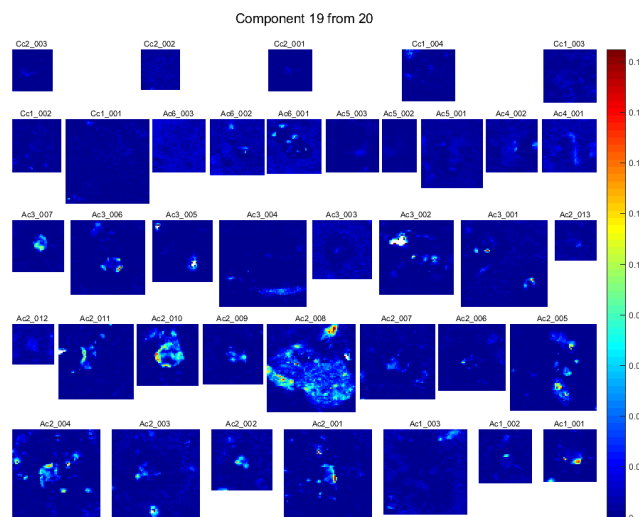
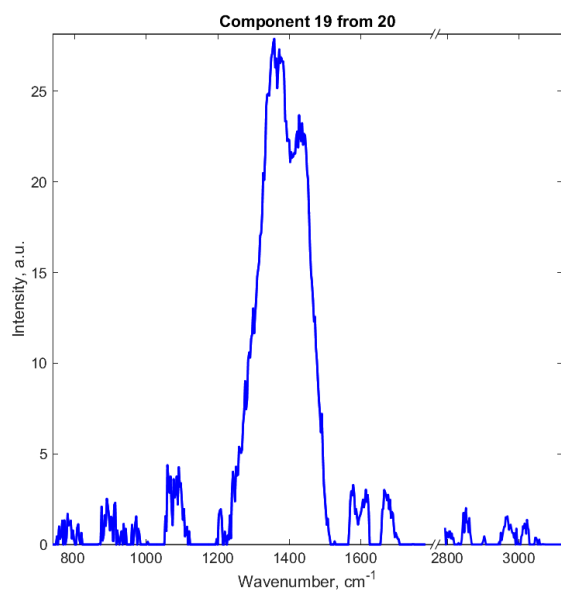


Fig. A-41: As Fig. A-23, but for $\mathbb{C}19$.

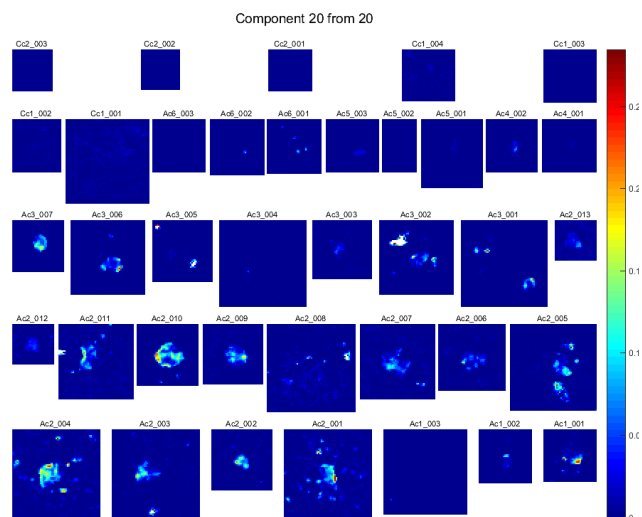
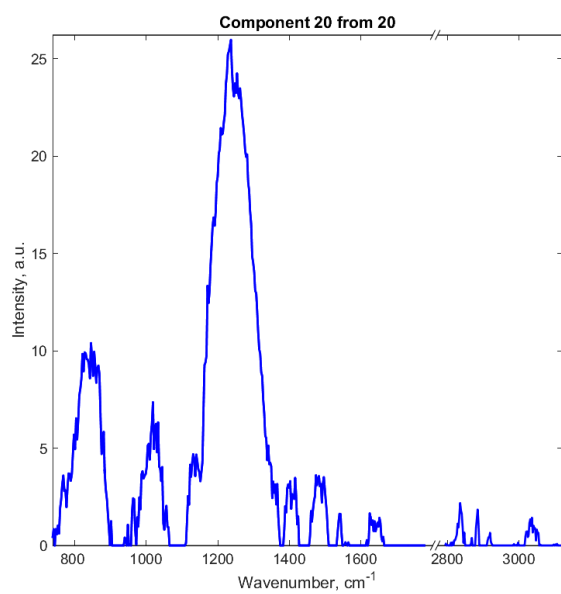


Fig. A-42: As Fig. A-23, but for $\mathbb{C}20$.

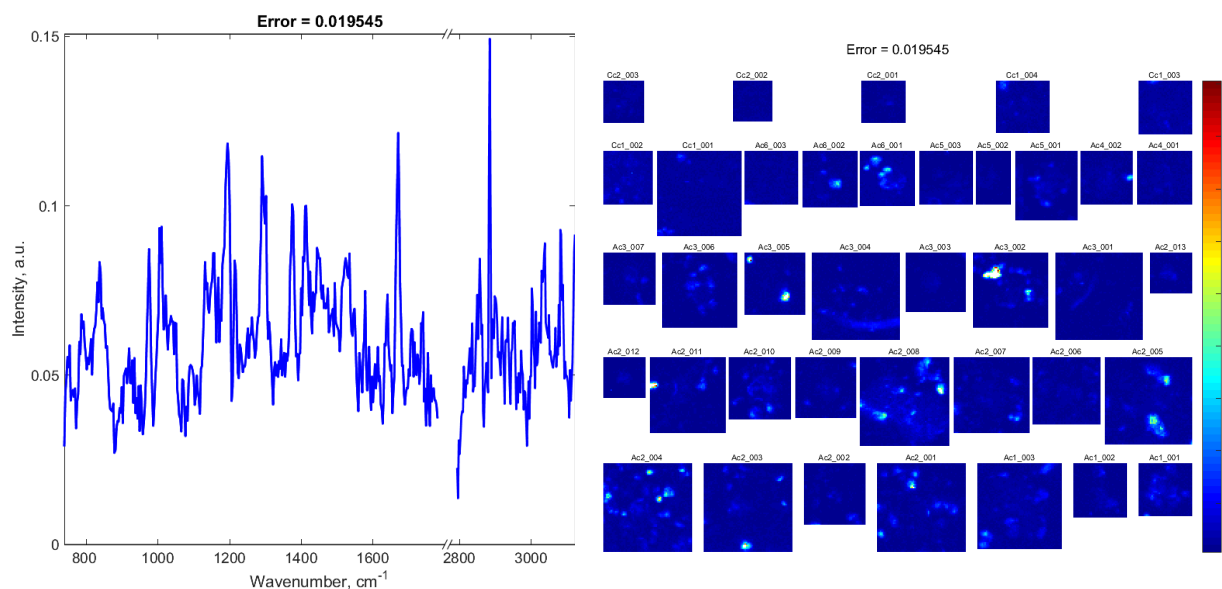


Fig. A-43: The spatial (on the right) and spectral (on the left) mean absolute factorization error resulting from the simultaneous Q-US/PS-NMF unmixing analysis of 31 cortical A β plaques (7 AD patients) together with 7 control Raman maps (2 elderly humans without AD).

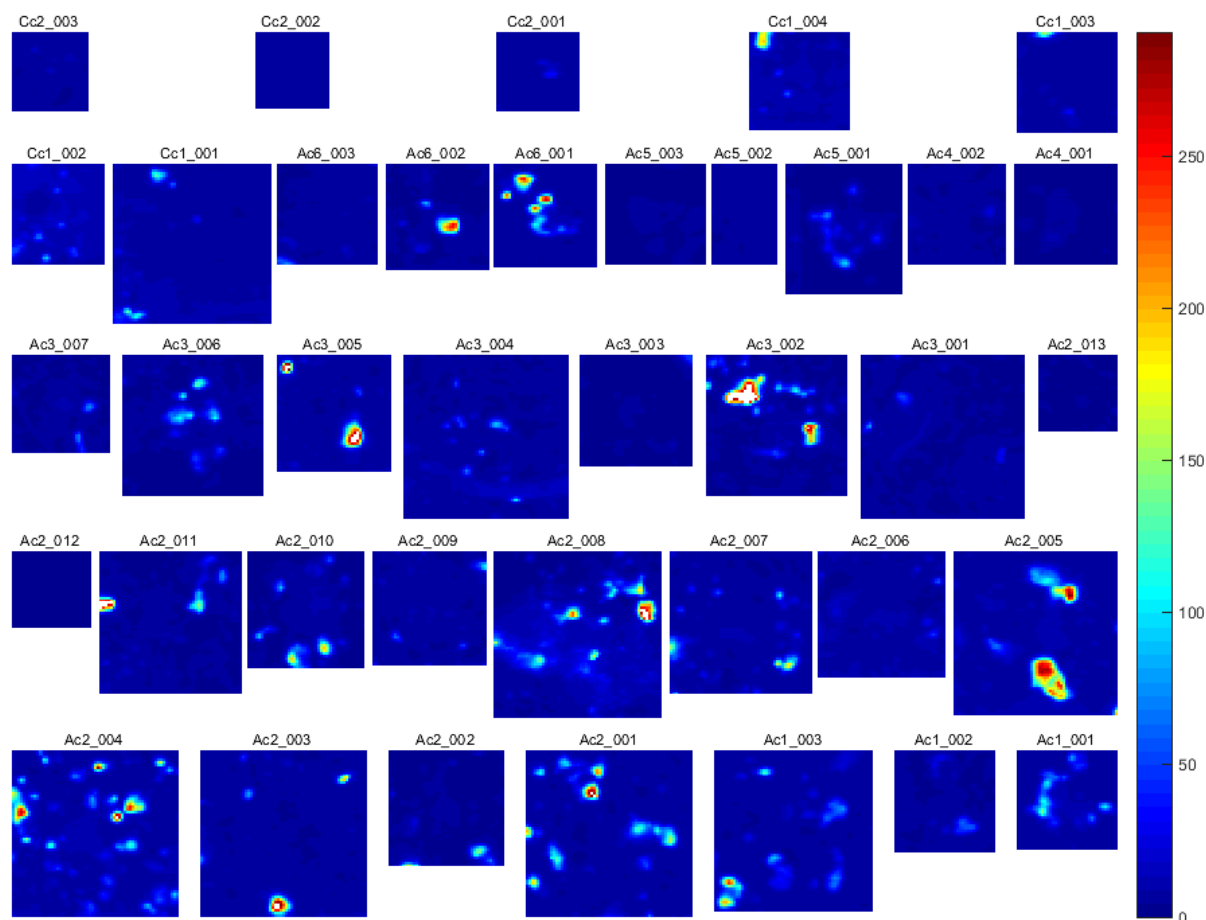


Fig. A-44: The mean spatially resolved subtracted fluorescence intensity of the same cortical samples found by averaging over the same spectral regions as for the component spectra and normalizing on the component spectral integral.

Appendix B

Appendix B represents the results of the 11 component Q-US/PS-NMF analysis on the acquired 3D Raman biomedical datasets of frozen human AD brain tissues and controls in the hippocampal brain region that report the biochemical composition of the AD human hippocampus without fixative artefacts as investigated in Chapter 6. Each Fig. B-1 to B-11 provides the component spectra (on the left) and its corresponding spatial concentration profile (on the right) in the investigated samples, as retrieved from the factorization analysis. Fig. B-12 shows the spatial (on the left) and spectral (on the right) mean absolute factorization error resulting from the factorization analysis. The value for relative factorization error is also given on the top of each figure.

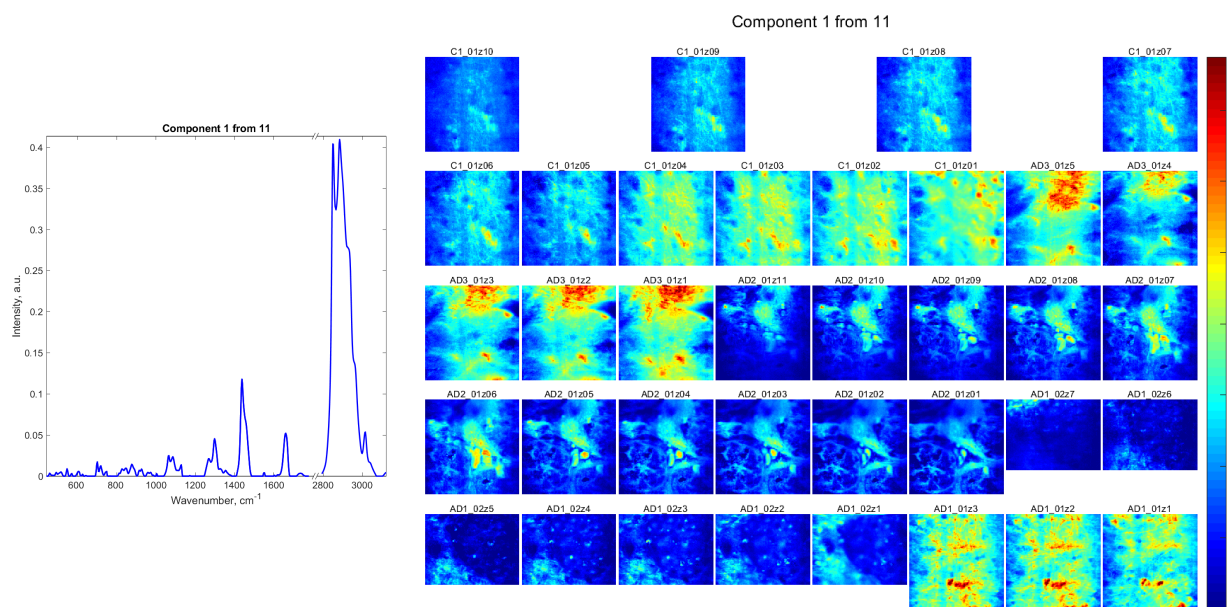


Fig. B-1: The component spectra C1 and its spatial distributions of the Raman concentration for the measured AD hippocampal brain regions together with controls (labelled according to the sample source as A1, A2, A3, and C1) on colour scales as indicated, retrieved from the simultaneous Q-US/PS-NMF unmixing analysis of frozen human brain tissues without fixative artefacts. In all panels, 2D Raman images from different focal planes of the representative z-stack were shown sequentially.

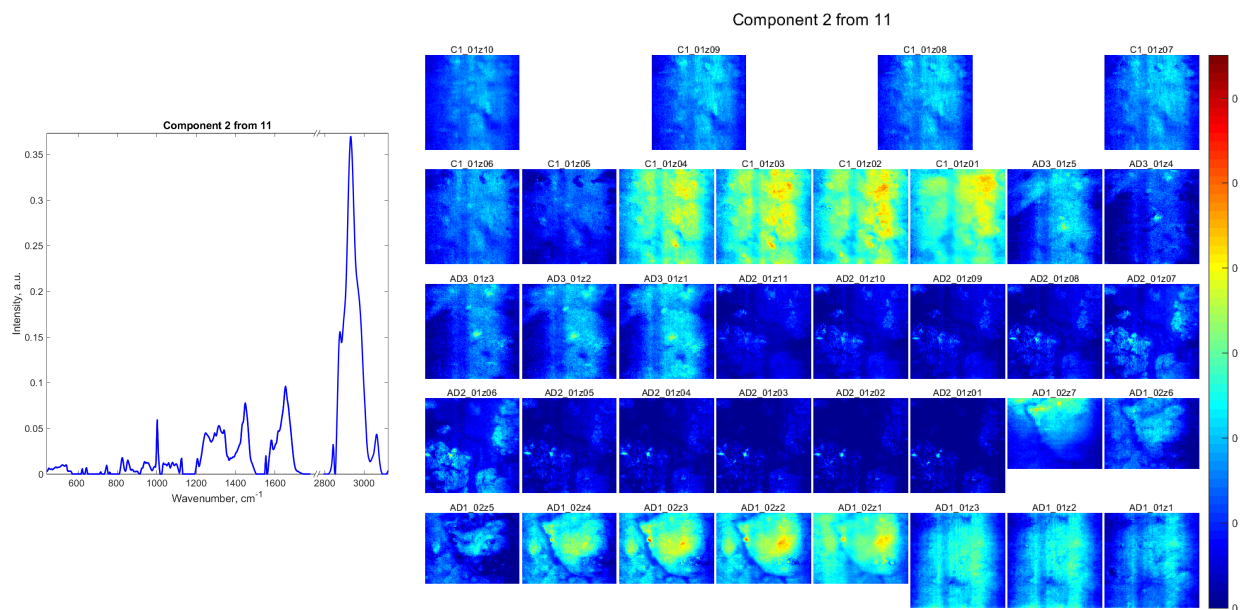


Fig. B-2: As Fig. B-1, but for C2.

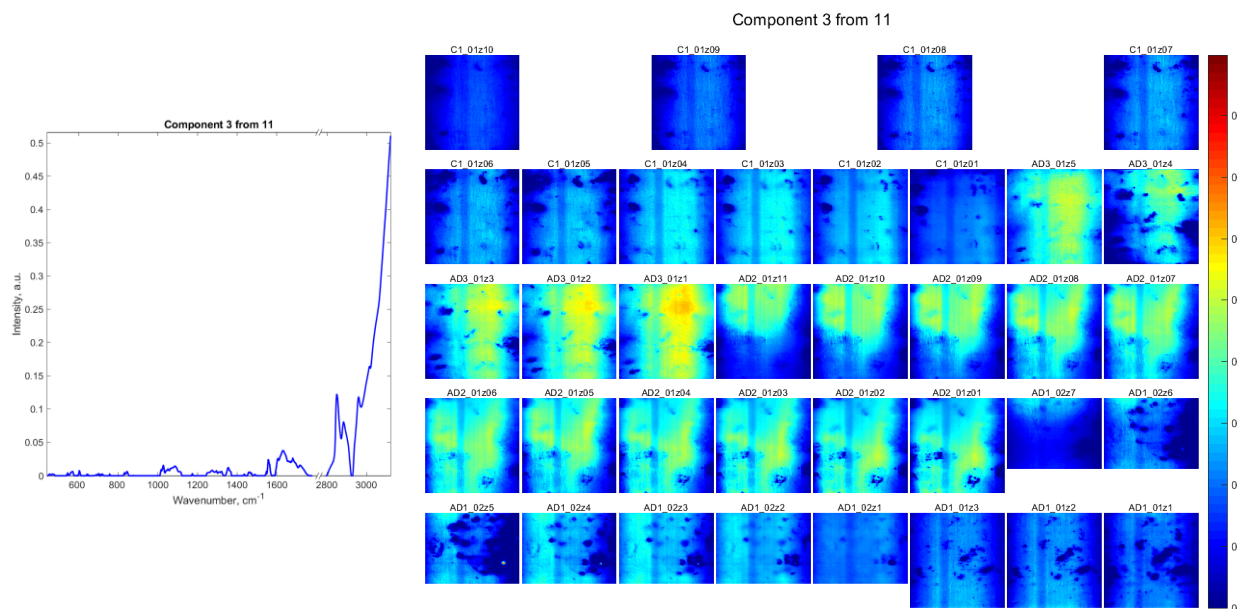


Fig. B-3: As Fig. B-1, but for C3.

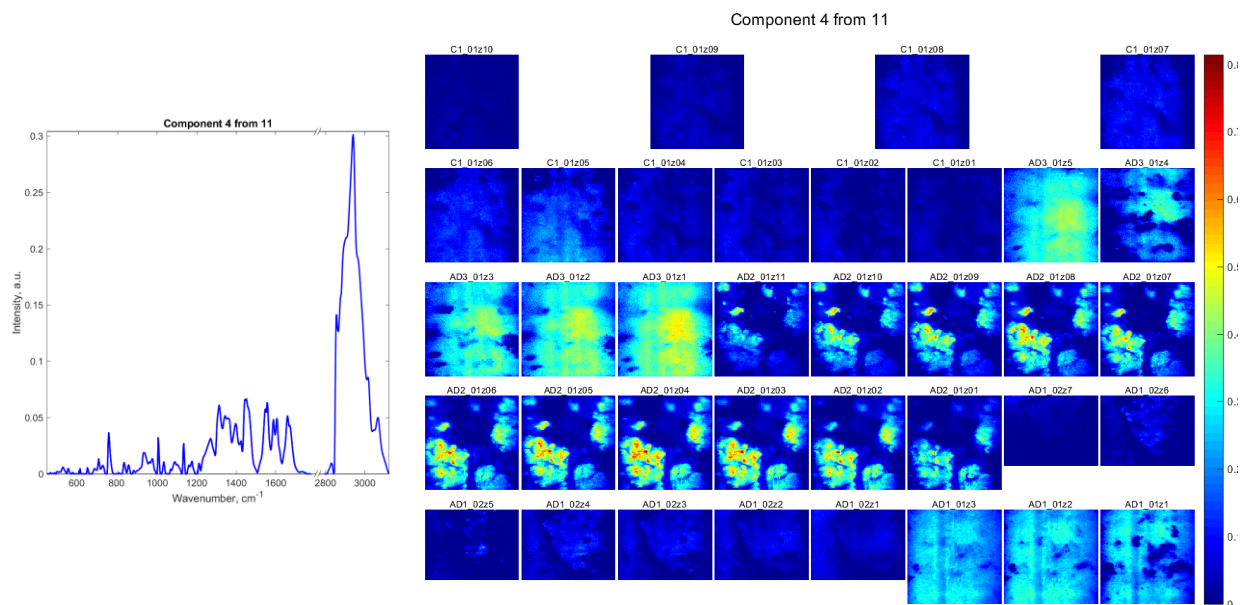


Fig. B-4: As Fig. B-1, but for C4.

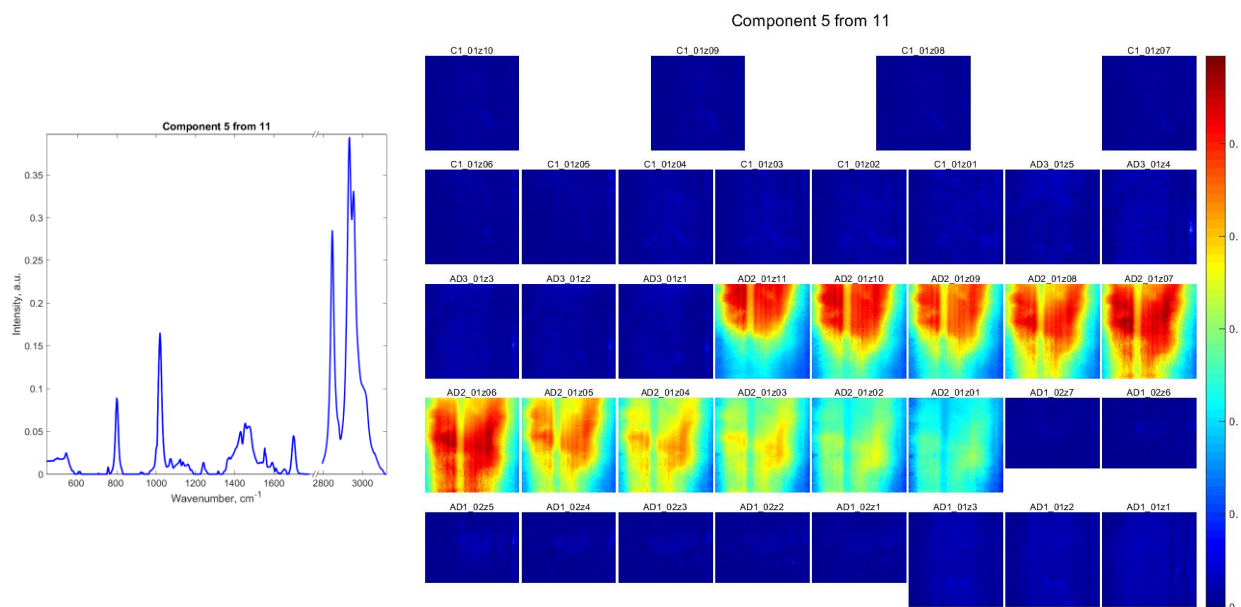


Fig. B-5: As Fig. B-1, but for C5.

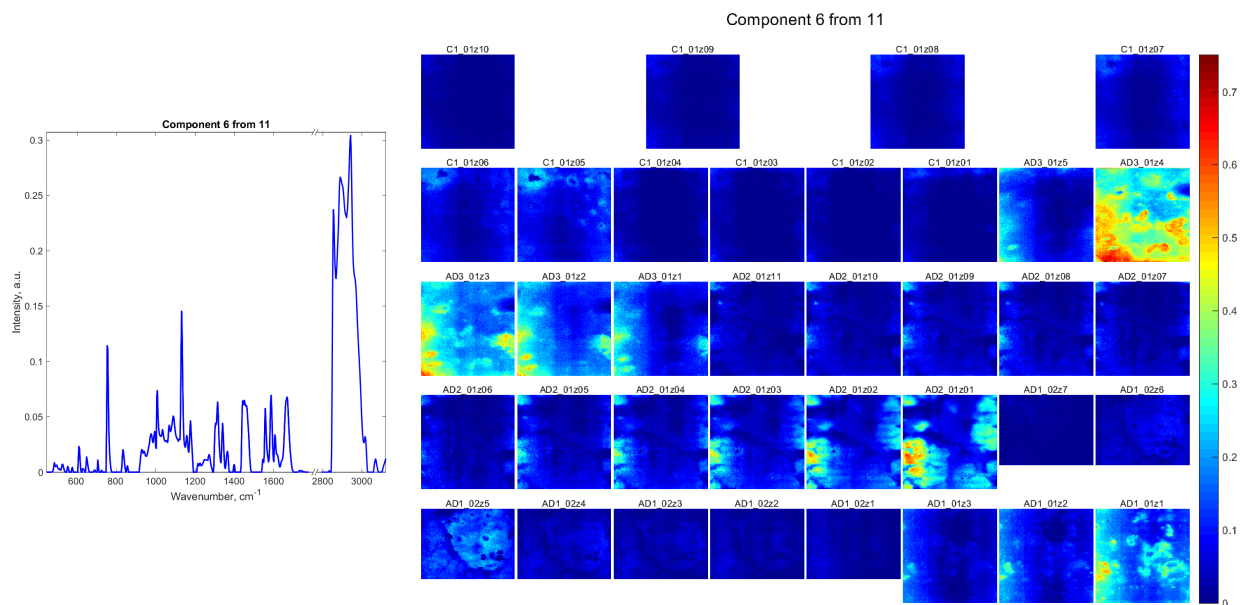


Fig. B-6: As Fig. B-1, but for C6.

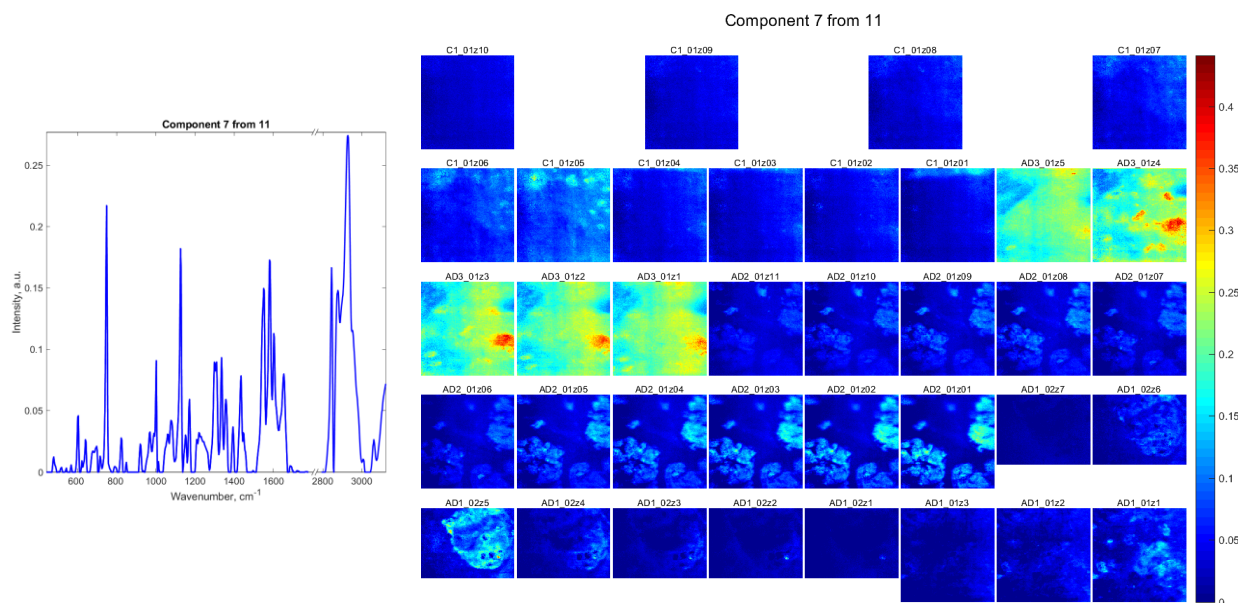


Fig. B-7: As Fig. B-1, but for C7.

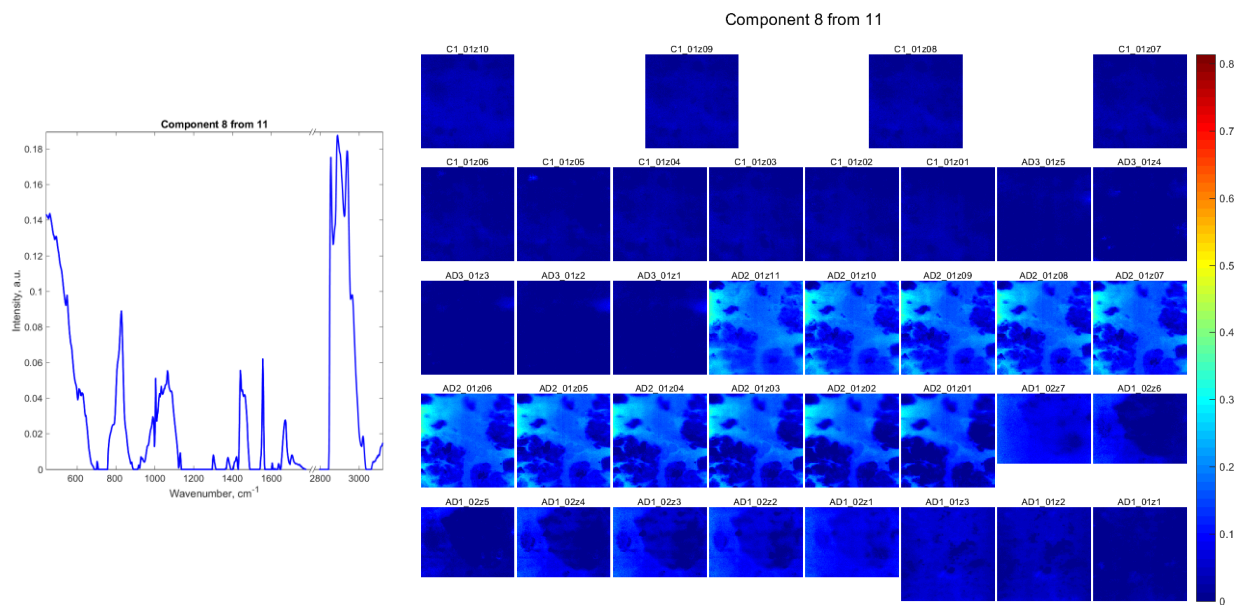


Fig. B-8: As Fig. B-1, but for C8.

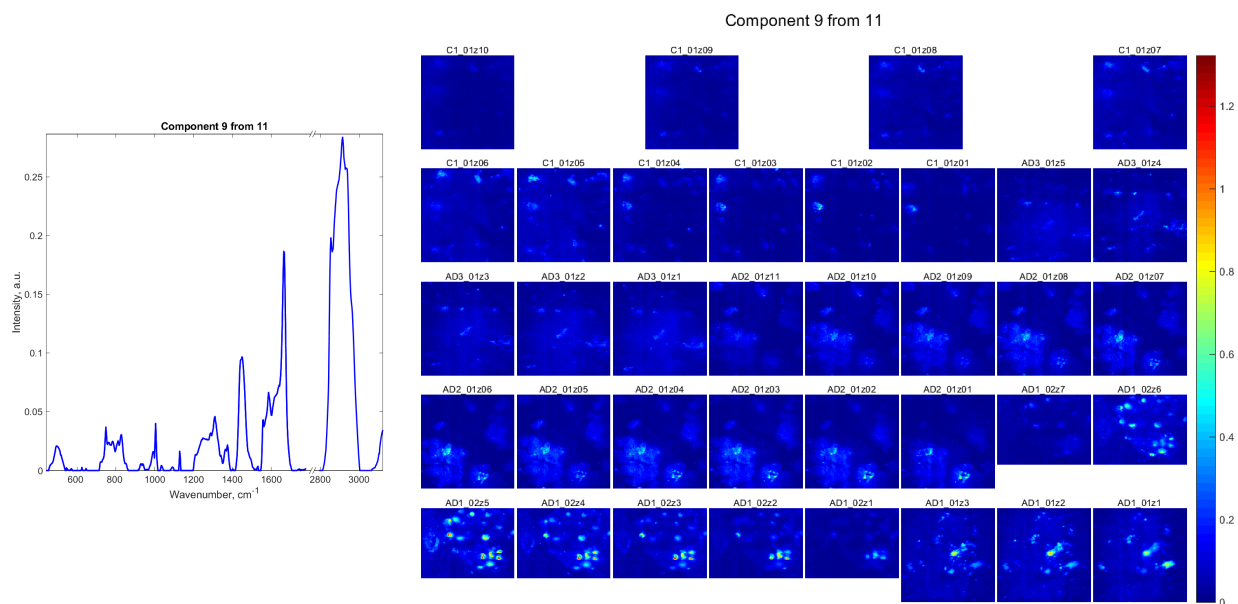


Fig. B-9: As Fig. B-1, but for C9.

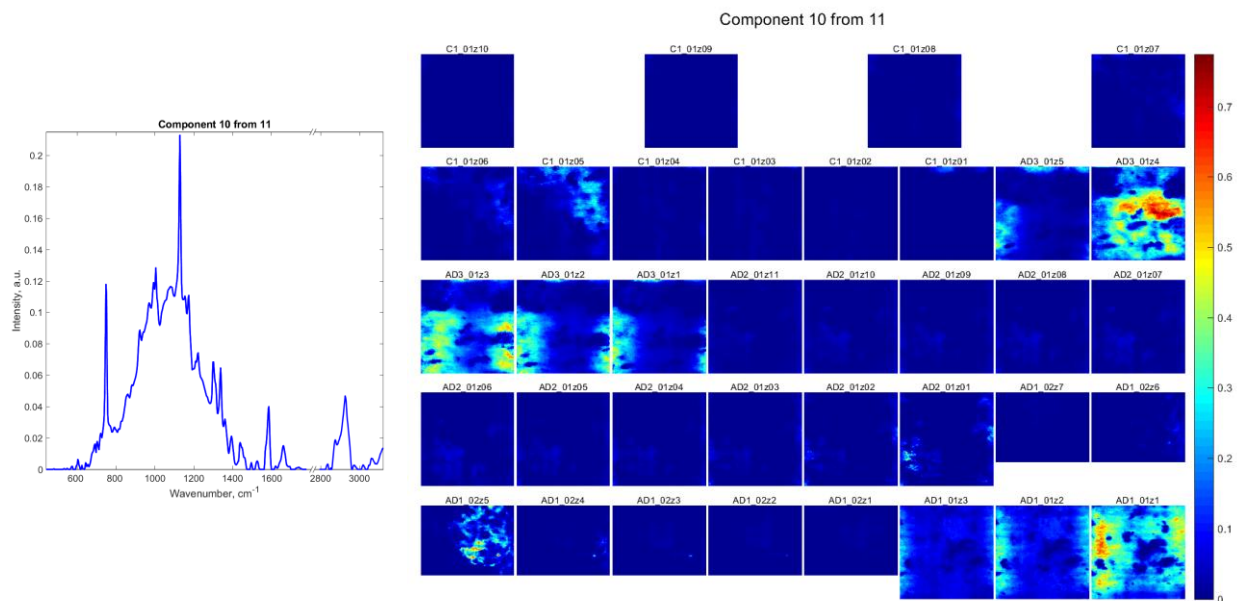


Fig. B-10: As Fig. B-1, but for C10.

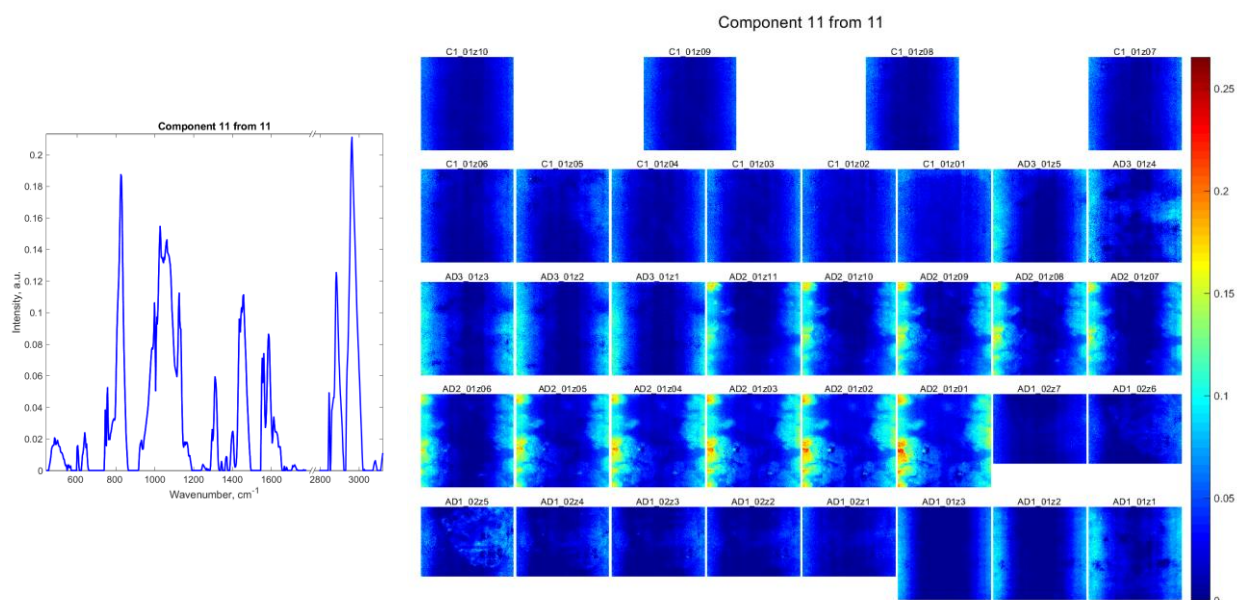


Fig. B-11: As Fig. B-1, but for C11.

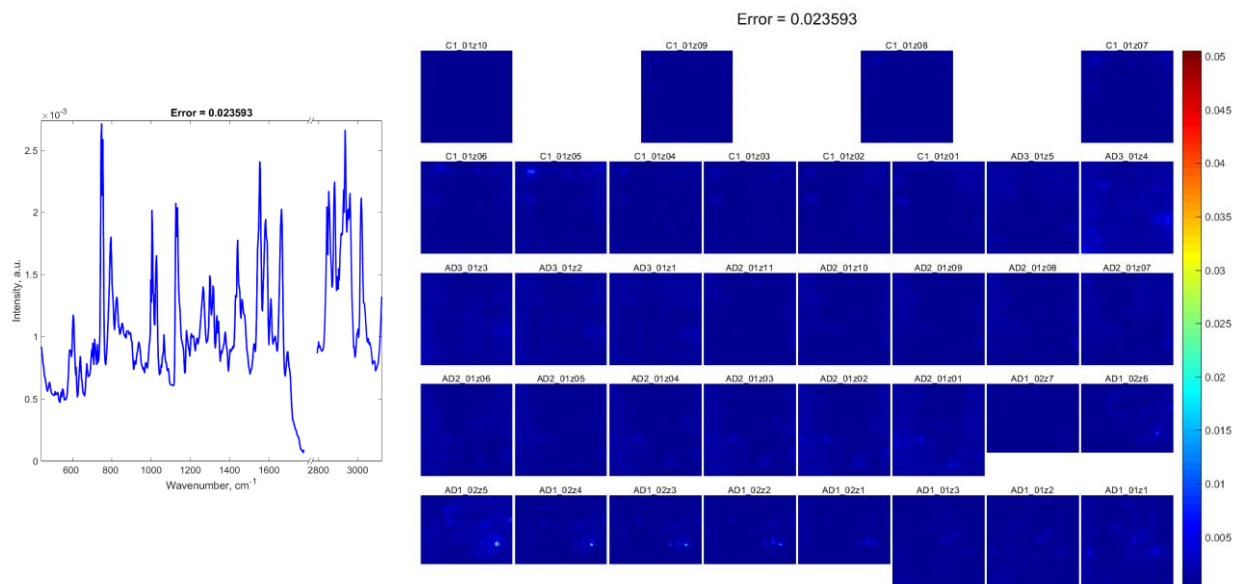


Fig. B-12: The spatial (on the right) and spectral (on the left) mean absolute factorization error resulting from the simultaneous Q-US/PS-NMF unmixing analysis of the frozen AD brain tissues together with non-demented controls shown in Fig. B-1 - Fig. B-11.

Supplementary material

The supplementary material includes a Power Point presentation showing a 3D volume view movie of merged chemical C9 (red) and C1 (blue) generated based on the AD1_02z1-z7 Raman images acquired from the frozen human brain tissue affected by AD. A 3D projection allowed to illustrate the spatial volumetric distribution of the intracellular A β aggregated with the oxidised polyunsaturated *trans* lipids (C9) within the neuronal cells that colocalize with the phosphatidylcholine-rich lipid droplets (C1).

Supplementary material (movie) can be found online at

<https://www.dropbox.com/sh/shvp56x8agof6lc/AADluH5gpWXS0BvLcjGWXx4a?dl=0>

References

- Aisen, P.S. (2002). The potential of anti-inflammatory drugs for the treatment of Alzheimer's disease. *Lancet Neurol.* **1**(5):279–284.
- Aisen, P.S., Davis, K.L., Berg, J.D., Schafer, K., Campbell, K., Thomas, R.G., ... Thal, L.J. (2000). A randomized controlled trial of prednisone in Alzheimer's disease. *Neurology* **54**(3):575–575. doi: <https://doi.org/https://doi.org/10.1212/WNL.54.3.588>.
- Aits, S. and Jaattela, M. (2013). Lysosomal cell death at a glance. *J. Cell Sci.* **126**(9):1905–1912. doi: <https://doi.org/10.1242/jcs.091181>.
- Albuquerque, C.D.L. and Poppi, R.J. (2015). Detection of malathion in food peels by surface-enhanced Raman imaging spectroscopy and multivariate curve resolution. *Anal. Chim. Acta* **879**:24–33. doi: <https://doi.org/10.1016/j.aca.2015.04.019>.
- Alzheimer's Disease International (2019). *World Alzheimer Report 2019 Attitudes to Dementia*. London: Alzheimer's Disease International (ADI).
- Andrew, J.J. and Hancewicz, T.M. (1998). Rapid analysis of Raman image data using two-way Multivariate Curve Resolution. *Appl. Spectrosc.* **52**(6):797–807. doi: <https://doi.org/10.1366/0003702981944526>.
- Baek, S.-J., Park, A., Kim, J., Shen, A. and Hu, J. (2009). A simple background elimination method for Raman spectra. *Chemom. Intell. Lab. Syst.* **98**(1):24–30. doi: <https://doi.org/10.1016/j.chemolab.2009.04.007>.
- Balce, D.R., Li, B., Allan, E.R.O., Rybicka, J.M., Krohn, R.M. and Yates, R.M. (2011). Alternative activation of macrophages by IL-4 enhances the proteolytic capacity of their phagosomes through synergistic mechanisms. *Blood* **118**(15):4199–4208. doi: <https://doi.org/10.1182/blood-2011-01-328906>.
- Bateman, R.J., Xiong, C., Benzinger, T.L.S., Fagan, A.M., Goate, A., Fox, N.C., ... Morris, J.C. (2012). Clinical and Biomarker Changes in Dominantly Inherited Alzheimer's Disease. *N. Engl. J. Med.* **367**(9):795–804. doi: <https://doi.org/10.1056/NEJMoa1202753>.
- Benseny-Cases, N., Klementieva, O., Cotte, M., Ferrer, I. and Cladera, J. (2014). Micro-FTIR reveals co-localization of lipid oxidation and amyloid plaques in human Alzheimer disease brains. *Anal. Chem.* **86**(24):12047–12054.
- Van Benthem, M.H. and Keenan, M.R. (2004). Fast algorithm for the solution of large-scale non-

negativity-constrained least squares problems. *J. Chemom.* **18**(10):441–450. doi: <https://doi.org/10.1002/cem.889>.

Bertram, L., Lill, C.M. and Tanzi, R.E. (2010). The genetics of Alzheimer disease: Back to the future. *Neuron* **68**(2):270–281. doi: <https://doi.org/10.1016/j.neuron.2010.10.013>.

Bhakdi, S. and Trantum-Jensen, J. (1991). Complement lysis: a hole is a hole. *Immunology Today* **12**(9):318–320. doi: [https://doi.org/10.1016/0167-5699\(91\)90007-G](https://doi.org/10.1016/0167-5699(91)90007-G).

Braidy, N., Poljak, A., Marjo, C., Rutledge, H., Rich, A., Jayasena, T., ... Sachdev, P. (2014). Metal and complementary molecular bioimaging in Alzheimer's disease. *Front. Aging Neurosci.* **6**:1–14. doi: <https://doi.org/10.3389/fnagi.2014.00138>.

Britschgi, M., Takeda-uchimura, Y., Rockenstein, E., Johns, H., Masliah, E. and Wyss-coray, T. (2012). Deficiency of terminal complement pathway inhibitor promotes neuronal tau pathology and degeneration in mice. *J. Neuroinflammation* **9**:220.

Broderick, L., Nardo, D. De, Franklin, B.S., Hoffman, H.M. and Latz, E. (2015). The inflammasomes and autoinflammatory syndromes. *Annu. Rev. Pathol. Mech. Dis.* **10**:395–424. doi: <https://doi.org/10.1146/annurev-pathol-012414-040431>.

Brouwers, N., Van Cauwenberghe, C., Engelborghs, S., Lambert, J.C., Bettens, K., Le Bastard, N., ... Van Broeckhoven, C. (2012). Alzheimer risk associated with a copy number variation in the complement receptor 1 increasing C3b/C4b binding sites. *Mol. Psychiatry* **17**(2):223–233. doi: <https://doi.org/10.1039/c3ee42799d>.

Brozek-Pluska, B., Musial, J., Kordek, R., Bailo, E., Dieing, T. and Abramczyk, H. (2012). Raman spectroscopy and imaging: Applications in human breast cancer diagnosis. *Analyst* **137**(16):3773–3780. doi: <https://doi.org/10.1039/c2an16179f>.

Burns, M.P., Noble, W.J., Olm, V., Gaynor, K., Casey, E., LaFrancois, J., ... Duff, K. (2003). Co-localization of cholesterol, apolipoprotein E and fibrillar Ab in amyloid plaques. *Mol. Brain Res.* **110**(1):119–125. doi: [https://doi.org/10.1016/S0169-328X\(02\)00647-2](https://doi.org/10.1016/S0169-328X(02)00647-2).

Burton, G.W. and Ingold, K.U. (1983). Beta-Carotene: An Unusual type of lipid antioxidant. *Science* **224**(4649):569–573.

Busse, P.J. and Mathur, S.K. (2012). Age-related Changes in Immune Function: Impact on Airway Inflammation. *J. Allergy Clin. Immunol.* **126**(4):690–701. doi: <https://doi.org/10.1016/j.jaci.2010.08.011>.

- Butler, H.J., Ashton, L., Bird, B., Cinque, G., Curtis, K., Dorney, J., ... Martin, F.L. (2016). Using Raman spectroscopy to characterize biological materials. *Nature Protocols* **11**(4):664–687. doi: <https://doi.org/10.1038/nprot.2016.036>.
- Butterfield, D.A., Hensley, K., Harris, M., Mattson, M. and Carney, J. (1994). β -Amyloid Peptide Free Radical Fragments Initiate Synaptosomal Lipoperoxidation in a Sequence-Specific Fashion: Implications to Alzheimer's Disease. *Biochem. Biophys. Res. Commun.* **200**(2):710–715. doi: <https://doi.org/10.1006/bbrc.1994.1508>.
- Butterfield, D.A., Lange, M.L.B. and Sultana, R. (2011). Involvements of the Lipid Peroxidation Product, HNE, in the Pathogenesis and Progression of Alzheimer's Disease. *Biochim. Biophys. Acta* **1801**(8):924–929. doi: <https://doi.org/10.1016/j.bbaliip.2010.02.005>. Involvements.
- Camp, C.H. and Cicerone, M.T. (2015). Chemically sensitive bioimaging with coherent Raman scattering. *Nat. Phot.* **9**(5):295–305. doi: <https://doi.org/10.1038/nphoton.2015.60>.
- Chan, R.B., Oliveira, T.G., Cortes, E.P., Honig, L.S., Duff, K.E., Small, S.A., ... Di Paolo, G. (2012). Comparative lipidomic analysis of mouse and human brain with Alzheimer disease. *J. Biol. Chem.* **287**(4):2678–2688. doi: <https://doi.org/10.1074/jbc.M111.274142>.
- Cheng, J.-X. and Xie, X.S. (2015). Vibrational spectroscopic imaging of living systems: an emerging platform for biology and medicine. *Science* **350**(6264):aaa8870. doi: <https://doi.org/10.1126/science.aaa8870>.
- Cherry, J.D., Olschowka, J.A. and O'Banion, M.K. (2014). Neuroinflammation and M2 microglia: The good, the bad, and the inflamed. *J. NEUROIMMUNOL.* **11**(1):1–15. doi: <https://doi.org/10.1186/1742-2094-11-98>.
- Choi, S.H., Aid, S., Caracciolo, L., Sakura Minami, S., Niikura, T., Matsuoka, Y., ... Bosetti, F. (2013). Cyclooxygenase-1 inhibition reduces amyloid pathology and improves memory deficits in a mouse model of Alzheimer's disease. *J. Neurochem.* **124**(1):59–68. doi: <https://doi.org/10.1111/jnc.12059>.
- Choo-Smith, L.-P., Garzon-Rodriguez, W., Glabe, C.G. and Surewicz, W.K. (1997). Acceleration of Amyloid Fibril Formation by Specific Binding of A β -(1–40) Peptide to Ganglioside-containing Membrane Vesicles. *J. Biol. Chem.* **272**(37):22987–22990. doi: <https://doi.org/10.1074/jbc.272.37.22987>.
- Choo-Smith, L.P., Garzon-Rodriguez, W., Glabe, C.G. and Surewicz, W.K. (1997). Acceleration of Amyloid Fibril Formation by Specific Binding of A β -(1–40) Peptide to Ganglioside-containing

Membrane Vesicles. *J. Biol. Chem.* **272**(37):22987–22990. doi: <https://doi.org/10.1074/jbc.272.37.22987>.

Choo-Smith, L.P.I. and Surewicz, W.K. (1997). The interaction between Alzheimer amyloid β (1-40) peptide and ganglioside G(M1)-containing membranes. *FEBS Letters* **402**(2–3):95–98. doi: [https://doi.org/10.1016/S0014-5793\(96\)01504-9](https://doi.org/10.1016/S0014-5793(96)01504-9).

Chun, H., Marriott, I., Lee, C.J. and Cho, H. (2018). Elucidating the Interactive Roles of Glia in Alzheimer's Disease Using Established and Newly Developed Experimental Models. *Front. Neurol.* **9**(September):1–11. doi: <https://doi.org/10.3389/fneur.2018.00797>.

Condello, C., Yuan, P., Schain, A. and Grutzendler, J. (2015). Microglia constitute a barrier that prevents neurotoxic protofibrillar A β 42 hotspots around plaques. *Nat. Commun.* **143**(5):951–959. doi: <https://doi.org/10.1017/S0950268814002131>.Tuberculosis.

Corder, E., Saunders, A., Strittmatter, W., Schmechel, D., Gaskell, P., Small, G., ... Pericak-Vance, M. (1993). Gene dose of apolipoprotein E type 4 allele and the risk of Alzheimer's disease in late onset families. *Science* **261**(5123):921–923. doi: <https://doi.org/10.1126/science.8346443>.

Cramer, P.E., Cirrito, J.R., Wesson, D.W., Lee, C.Y.D., Colleen, J., Zinn, A.E., ... Landreth, G.E. (2013). ApoE-Directed Therapeutics Rapidly Clear β -Amyloid and Reverse Deficits in AD Mouse Models. *Science* **335**(6075):1503–1506. doi: <https://doi.org/10.1126/science.1217697>.

Crawford, M.A. and Sinclair, A.J. (1971). Nutritional Influences in the Evolution of Mammalian Brain. *Lipids, Malnutrition and the Developing Brain: Ciba Foundation Symposia* **3**:267–292. doi: <https://doi.org/10.1002/9780470719862.ch16>.

Cummings, J., Lee, G., Ritter, A. and Zhong, K. (2018). Alzheimer's disease drug development pipeline: 2017. *Alzheimer's & Dementia* **4**(3):195–214. doi: <https://doi.org/10.1016/j.trci.2018.03.009>.

Czamara, K., Majzner, K., Pacia, M.Z., Kochan, K., Kaczor, A. and Baranska, M. (2015). Raman spectroscopy of lipids: A review. *J. Raman. Spectrosc.* **46**(1):4–20. doi: <https://doi.org/10.1002/jrs.4607>.

Czamara, K., Majzner, K., Selmi, A., Baranska, M., Ozaki, Y. and Kaczor, A. (2017). Unsaturated lipid bodies as a hallmark of inflammation studied by Raman 2D and 3D microscopy. *Sci. Rep.* **7**(18):40889. doi: <https://doi.org/10.1038/srep40889>.

D'Andrea, M.R., Cole, G.M. and Ard, M.D. (2004). The microglial phagocytic role with specific plaque types in the Alzheimer disease brain. *Neurobiol. Aging* **25**(5):675–683. doi:

<https://doi.org/10.1016/j.neurobiolaging.2003.12.026>.

D'Andrea, M.R. and Nagele, R.G. (2010). Morphologically distinct types of amyloid plaques point the way to a better understanding of Alzheimer's disease pathogenesis. *Biotech. Histochem.* **85**(2):133–147. doi: <https://doi.org/10.3109/10520290903389445>.

Darios, F. and Davletov, B. (2006). Omega-3 and omega-6 fatty acids stimulate cell membrane expansion by acting on syntaxin 3. *Nature* **440**(7085):813–817. doi: <https://doi.org/10.1038/nature04598>.

Deshpande, A., Mina, E., Glabe, C. and Busciglio, J. (2006). Different Conformations of Amyloid β Induce Neurotoxicity by Distinct Mechanisms in Human Cortical Neurons. *J. Neurosci.* **26**(22):6011–6018. doi: <https://doi.org/10.1523/JNEUROSCI.1189-06.2006>.

Diem, M. (2015). *Modern Vibrational Spectroscopy and Micro-Spectroscopy*. JohnWiley & Sons, Ltd.

Dong, J., Atwood, C.S., Anderson, V.E., Siedlak, S.L., Smith, M.A., Perry, G. and Carey, P.R. (2003). Metal binding and oxidation of amyloid- β within isolated senile plaque cores: Raman microscopic evidence. *Biochemistry* **42**(10):2768–2773. doi: <https://doi.org/10.1021/bi0272151>.

Eilers, P.H.C. (2003). A perfect smoother. *Anal. Chem.* **75**(14):3631–3636. doi: <https://doi.org/10.1021/ac034173t>.

Eilers, P.H.C. (2004). Parametric time warping. *Anal. Chem.* **76**(2):404–411. doi: <https://doi.org/10.1021/ac034800e>.

Emmerling, M.R., Watson, M.D., Raby, C.A. and Spiegel, K. (2000). The role of complement in Alzheimer's disease pathology. *Biochim. Biophys. Acta* **1502**:158–171.

Esterbauer, H., Schaur, R.J. and Zollner, H. (1991). Chemistry and biochemistry of 4-hydroxynonenal, malonaldehyde and related aldehydes. *Free Radic. Biol. Med.* **11**:81–128.

Felten, J., Hall, H., Jaumot, J., Tauler, R., De Juan, A. and Gorzsás, A. (2015). Vibrational spectroscopic image analysis of biological material using multivariate curve resolution-alternating least squares (MCR-ALS). *Nature Protocols* **10**(2):217–240. doi: <https://doi.org/10.1038/nprot.2015.008>.

Filik, J. and Stone, N. (2008). Analysis of human tear fluid by Raman spectroscopy. *Anal. Chim. Acta* **616**(2):177–184. doi: <https://doi.org/10.1016/j.aca.2008.04.036>.

Fleisher, A.S., Chen, K., Liu, X., Rontiva, A., Thiyyagura, P., Ayutyanont, N., ... Reiman, E.M.

- (2011). Using positron emission tomography and florbetapir F 18 to image cortical amyloid in patients with mild cognitive impairment or dementia due to Alzheimer disease. *Arch. Neurol.* **68**(11):1404–1411. doi: <https://doi.org/10.1001/archneurol.2011.150>.
- Fosbrink, M., Niculescu, F., Rus, V., Shin, M.L. and Rus, H. (2006). C5b-9-induced Endothelial Cell Proliferation and Migration Are Dependent on Akt Inactivation of Forkhead Transcription Factor FOXO1. *J. Biol. Chem.* **281**(28):19009–19018. doi: <https://doi.org/10.1074/jbc.M602055200>.
- Franklin, B.S., Bossaller, L., De Nardo, D., Ratter, J.M., Stutz, A., Engels, G., ... Latz, E. (2014). The adaptor ASC has extracellular and ‘prionoid’ activities that propagate inflammation. *Nature Immunol.* **15**(8):727–737. doi: <https://doi.org/10.1038/ni.2913>.
- Freudiger, C.W., Min, W., Saar, B.G., Lu, S., Holtom, G.R., He, C., ... Xie, X.S. (2008). Label-Free Biomedical Imaging with High Sensitivity by Stimulated Raman Scattering Microscopy. *Science* **322**(5909):1857–1861.
- Fu, D. and Xie, X.S. (2014). Reliable cell segmentation based on Spectral Phasor Analysis of hyperspectral Stimulated Raman Scattering imaging data. *Anal. Chem.* **86**:4115–4119. doi: <https://doi.org/10.1021/ac500014b>.
- Golub, G.H. and Van Loan, C.F. (2013). *Matrix Computations*. Baltimore: The Johns Hopkins University Press.
- Grasso, G. (2011). The use of mass spectrometry to study amyloid- β peptides. *Mass Spectrom. Rev.* **30**(3):347–365. doi: <https://doi.org/10.1002/mas.20281>.
- Green, A.A., Berman, M., Switzer, P. and Craig, M.D. (1988). A transformation for ordering multispectral data in terms of image quality with implications for noise removal. *IEEE Trans. Geosci. Remote Sens.* **26**(1):65–74.
- Guerreiro, R., Wojtas, A., Bras, J., Carrasquillo, M., Rogaeva, E., Majounie, E., ... Hardy, J. (2013). TREM2 Variants in Alzheimer’s Disease. *N. Engl. J. Med.* **368**(2):117–127. doi: <https://doi.org/10.1056/NEJMoa1211851>.
- Haass, C. and Selkoe, D.J. (2007). Soluble protein oligomers in neurodegeneration: Lessons from the Alzheimer’s amyloid β -peptide. *Nat. Rev. Mol. Cell Biol.* **8**(2):101–112. doi: <https://doi.org/10.1038/nrm2101>.
- Halle, A., Hornung, V., Petzold, G.C., Stewart, C.R., Monks, B.G., Reinheckel, T., ... Golenbock, D.T. (2008). The NALP3 inflammasome is involved in the innate immune response to amyloid- β .

- Nature Immunol.* **9**(8):857–865. doi: <https://doi.org/10.1038/ni.1636>.
- Harold, D., Abraham, R., Hollingworth, P., Sims, R., Gerrish, A., Hamshere, M.L., ... Williams, J. (2009). Genome-wide association study identifies variants at CLU and PICALM associated with Alzheimer's disease, and shows evidence for additional susceptibility genes. *Nat. Genet.* **41**(10):1088–1093. doi: <https://doi.org/10.1038/ng.440>. Genome-wide.
- Haskin, L.A., Wang, A., Rockow, K.M., Jolliff, B.L., Korotev, R.L. and Viskupic, K.M. (1997). Raman spectroscopy for mineral identification and quantification for in situ planetary surface analysis: A point count method. *J. Geophys. Res.* **102**(97):19293–19306. doi: <https://doi.org/10.1029/97JE01694>.
- Hayashi, H. (2004). A Seed for Alzheimer Amyloid in the Brain. *J. Neurosci.* **24**(20):4894–4902. doi: <https://doi.org/10.1523/JNEUROSCI.0861-04.2004>.
- Hedegaard, M., Matthäus, C., Hassing, S., Krafft, C., Diem, M. and Popp, J. (2011). Spectral unmixing and clustering algorithms for assessment of single cells by Raman microscopic imaging. *Theor. Chem. Acc.* **130**(4–6):1249–1260. doi: <https://doi.org/10.1007/s00214-011-0957-1>.
- Heneka, M.T., Golenbock, D.T. and Latz, E. (2015). Innate immunity in Alzheimer's disease. *Nature Immunol.* **16**(3):229–236. doi: <https://doi.org/10.1038/ni.3102>.
- Heneka, M.T., Kummer, M.P., Stutz, A., Delekate, A., Schwartz, S., Vieira-Saecker, A., ... Golenbock, D.T. (2013). NLRP3 is activated in Alzheimer's disease and contributes to pathology in APP/PS1 mice. *Nature* **493**(7434):674–678. doi: <https://doi.org/10.1038/nature11729>.
- Heneka, M.T., Nadrigny, F., Regen, T., Martinez-Hernandez, A., Dumitrescu-Ozimek, L., Terwel, D., ... Kummer, M.P. (2010). Locus ceruleus controls Alzheimer's disease pathology by modulating microglial functions through norepinephrine. *PNAS* **107**(13):6058–6063. doi: <https://doi.org/10.1073/pnas.0909586107>.
- Hickman, S.E., Allison, E.K. and El Khoury, J. (2008). Microglial Dysfunction and Defective β -Amyloid Clearance Pathways in Aging Alzheimer's Disease Mice. *J. Neurosci.* **28**(33):8354–8360. doi: <https://doi.org/10.1523/JNEUROSCI.0616-08.2008>.
- Hirokawa, K. (1980). Aids for analytical chemists. *Anal. Chem.* **52**(12):1966–1968. doi: <https://doi.org/10.1021/ac50062a046>.
- Hogasen, A.K., Hestdal, K., Hogasen, K. and Abrahamsen, T.G. (1995). Transforming growth factor beta modulates C3 and factor B biosynthesis and complement receptor 3 expression in cultured human monocytes. *J. Leukoc. Biol.* **57**(2):287–296. doi:

<https://doi.org/10.1002/jlb.57.2.287>.

Hyman, B.T., Phelps, C.H., Beach, T.G., Bigio, E.H., Cairns, N.J., Carrillo, M.C., ... Hyman, B.T. (2013). National Institute on Aging- Alzheimer's Association guidelines for the neuropathologic assessment of Alzheimer's disease. *Alzheimers Dement.* **8**(1):1–13. doi: <https://doi.org/10.1016/j.jalz.2011.10.007>. National.

Itagaki, S., Saito, H. and McGeer, P.L. (1994). Ultrastructural localization of complement membrane attack complex (MAC)-like immunoreactivity in brains of patients with Alzheimer's disease. *Brain Res.* **645**:78–84.

Iwatsubo, T., Mann, D.M.A., Odaka, A., Nohuhiro, S. and Ihara, Y. (1995). Amyloid β protein (A β) deposition: A β 42(43) precedes A β 40 in down Syndrome. *Ann. Neurol.* **42**(43):294–299.

Jack, C.R., Knopman, D.S., Jagust, W.J., Petersen, R.C., Weiner, M.W., Aisen, P.S., ... Trojanowski, J.Q. (2013). Tracking pathophysiological processes in Alzheimer's disease: An updated hypothetical model of dynamic biomarkers. *Lancet Neurol.* **12**(2):207–216. doi: [https://doi.org/10.1016/S1474-4422\(12\)70291-0](https://doi.org/10.1016/S1474-4422(12)70291-0).

Jagust, W.J., Bandy, D., Chen, K., Foster, N.L., Landau, S.M., Mathis, C.A., ... Koeppe, R.A. (2010). The Alzheimer's Disease Neuroimaging Initiative positron emission tomography core. *Alzheimer's & Dementia* **6**(3):221–229. doi: <https://doi.org/10.1016/j.jalz.2010.03.003>.

Jain, R., Calderon, D., Kierski, P.R., Schurr, M.J., Czuprynski, C.J., Murphy, C.J., ... Abbott, N.L. (2014). Raman spectroscopy enables noninvasive biochemical characterization and identification of the stage of healing of a wound. *Anal. Chem.* **86**(8):3764–3772. doi: <https://doi.org/10.1021/ac500513t>.

Jang, H., Connelly, L., Arce, F.T., Ramachandran, S., Lal, R., Kagan, B.L. and Nussinov, R. (2013). Alzheimer's disease: which type of amyloid-preventing drug agents to employ? *Phys. Chem. Chem. Phys.* **15**(23):8868. doi: <https://doi.org/10.1039/c3cp00017f>.

Jarrett, J.T., Berger, E.P. and Lansbury, P.T. (1993). The carboxy terminus of the β -amyloid protein is critical for the seeding of amyloid formation: Implications for the pathogenesis of Alzheimer's disease. *Biochemistry* **32**(18):4693–4697. doi: <https://doi.org/10.1021/bi00069a001>.

Jaumot, J., Juan, A. De and Tauler, R. (2015). MCR-ALS GUI 2.0 : New features and applications. *Chemom. Intell. Lab. Syst.* **140**:1–12. doi: <https://doi.org/10.1016/j.chemolab.2014.10.003>.

Jerome, W.G., Cash, C., Webber, R., Horton, R. and Yancey, P.G. (1998). Lysosomal lipid accumulation from oxidized low density lipoprotein is correlated with hypertrophy of the Golgi

apparatus and trans-Golgi network. *J. Lipid Res.* **39**(7):1362–1371.

Ji, M., Arbel, M., Zhang, L., Freudiger, C.W., Hou, S.S., Lin, D., ... Xie, X.S. (2018). Label-free imaging of amyloid plaques in Alzheimer's disease with stimulated Raman scattering microscopy. *Science Advances* **4**(11):eaat7715. doi: <https://doi.org/10.1126/sciadv.aat7715>.

Jimenez, S., Baglietto-Vargas, D., Caballero, C., Moreno-Gonzalez, I., Torres, M., Sanchez-Varo, R., ... Vitorica, J. (2008). Inflammatory Response in the Hippocampus of PS1M146L/APP751SL Mouse Model of Alzheimer's Disease: Age-Dependent Switch in the Microglial Phenotype from Alternative to Classic. *J. Neurosci.* **28**(45):11650–11661. doi: <https://doi.org/10.1523/JNEUROSCI.3024-08.2008>.

Jirasek, A., Schulze, G., Yu, M.M.L., Blades, M.W. and Turner, R.F.B. (2004). Accuracy and precision of manual baseline determination. *Appl. Spectrosc.* **58**(12):1488–1499. doi: <https://doi.org/10.1366/0003702042641236>.

Joshi, P., Turola, E., Ruiz, A., Bergami, A., Libera, D.D., Benussi, L., ... Verderio, C. (2014). Microglia convert aggregated amyloid- β into neurotoxic forms through the shedding of microvesicles. *Cell Death Differ.* **21**(4):582–593. doi: <https://doi.org/10.1038/cdd.2013.180>.

Kakio, A., Nishimoto, S. ichi, Yanagisawa, K., Kozutsumi, Y. and Matsuzaki, K. (2002). Interactions of amyloid β -protein with various gangliosides in raft-like membranes: Importance of GM1 ganglioside-bound form as an endogenous seed for Alzheimer amyloid. *Biochemistry* **41**(23):7385–7390. doi: <https://doi.org/10.1021/bi0255874>.

Kakio, A., Nishimoto, S.I., Yanagisawa, K., Kozutsumi, Y. and Matsuzaki, K. (2001). Cholesterol-dependent Formation of GM1 Ganglioside-bound Amyloid β -Protein, an Endogenous Seed for Alzheimer Amyloid. *J. Biol. Chem.* **276**(27):24985–24990. doi: <https://doi.org/10.1074/jbc.M100252200>.

Karch, C.M. and Goate, A.M. (2015). Alzheimer's disease risk genes and mechanisms of disease pathogenesis. *Biol. Psychiatry* **77**(1):43–51. doi: <https://doi.org/10.1016/j.biopsych.2014.05.006>.

Kawahara, M., Kuroda, Y., Arispe, N. and Rojas, E. (2000). Alzheimer's β -Amyloid, Human Islet Amylin, and Prion Protein Fragment Evoke Intracellular Free Calcium Elevations by a Common Mechanism in a Hypothalamic GnRH Neuronal Cell Line. *J. Biol. Chem.* **275**(19):14077–14083. doi: <https://doi.org/10.1074/jbc.275.19.14077>.

Kayed, R., Head, E., Thompson, J.L., McIntire, T.M., Milton, S.C., Cotman, C.W. and Glabe, C.G. (2003). Common structure of soluble amyloid oligomers implies common mechanism of

- pathogenesis. *Science* **300**(5618):486–489. doi: <https://doi.org/10.1126/science.1079469>.
- Kayed, R. and Lasagna-Reeves, C.A. (2013). Molecular mechanisms of amyloid oligomers toxicity. *J. Alzheimers Dis.* **33**:67–78. doi: <https://doi.org/10.3233/978-1-61499-154-0-67>.
- Kayed, R., Pensalfini, A., Margol, L., Sokolov, Y., Sarsoza, F., Head, E., ... Glabe, C. (2009). Annular protofibrils are structurally and functionally distinct type of amyloid oligomer. *J. Biol. Chem.* **284**(7):4230–4237. doi: <https://doi.org/10.1074/jbc.M808591200>.
- Kelenyi, G. (1967). On the histochemistry of azo group-free thiazole dyes. *J. Histochem. Cytochem.* **15**(3):172–180.
- Kim, H. and Park, H. (2007). Sparse non-negative matrix factorizations via alternating non-negativity-constrained least squares for microarray data analysis. *Bioinformatics* **23**(12):1495–1502. doi: <https://doi.org/10.1093/bioinformatics/btm134>.
- Kiskis, J., Fink, H., Nyberg, L., Thy, J., Li, J.-Y. and Enejder, A. (2015). Plaque-associated lipids in Alzheimer's diseased brain tissue visualized by nonlinear microscopy. *Sci. Rep.* **5**(1):13489. doi: <https://doi.org/10.1038/srep13489>.
- Koenigsknecht-Talboo, J. (2005). Microglial Phagocytosis Induced by Fibrillar -Amyloid and IgGs Are Differentially Regulated by Proinflammatory Cytokines. *J. Neurosci.* **25**(36):8240–8249. doi: <https://doi.org/10.1523/JNEUROSCI.1808-05.2005>.
- Krafft, C., Neudert, L., Simat, T. and Salzer, R. (2005). Near infrared Raman spectra of human brain lipids. *Spectrochim. Acta A* **61**(7):1529–1535. doi: <https://doi.org/10.1016/j.saa.2004.11.017>.
- Krafft, C., Schie, I.W., Meyer, T., Schmitt, M. and Popp, J. (2016). Developments in spontaneous and coherent Raman scattering microscopic imaging for biomedical applications. *Chem. Soc. Rev.* **45**(7):1819–1849. doi: <https://doi.org/10.1039/C5CS00564G>.
- Krafft, C., Schmitt, M., Schie, I.W., Cialla-May, D., Matthäus, C., Bocklitz, T. and Popp, J. (2017). Label-Free Molecular Imaging of Biological Cells and Tissues by Linear and Nonlinear Raman Spectroscopic Approaches. *Angew. Chem. Int. Ed.* **56**(16):4392–4430. doi: <https://doi.org/10.1002/anie.201607604>.
- Kumar, A., Singh, A. and Ekavali (2015). A review on Alzheimer's disease pathophysiology and its management: An update. *Pharmacol. Rep.* **67**(2):195–203. doi: <https://doi.org/10.1016/j.pharep.2014.09.004>.

- Kurouski, D., Van Duyne, R.P. and Lednev, I.K. (2015). Exploring the structure and formation mechanism of amyloid fibrils by Raman spectroscopy: A review. *Analyst* **140**(15):4967–4980. doi: <https://doi.org/10.1039/c5an00342c>.
- Kurouski, D., Lombardi, R.A., Dukor, R.K., Lednev, I.K. and Nafie, L.A. (2010). Direct observation and pH control of reversed supramolecular chirality in insulin fibrils by vibrational circular dichroism. *Chemical Communications* **46**(38):7154. doi: <https://doi.org/10.1039/c0cc02423f>.
- Lambert, J.C., Heath, S., Even, G., Campion, D., Sleegers, K., Hiltunen, M., ... Pilotto, A. (2009). Genome-wide association study identifies variants at CLU and CR1 associated with Alzheimer's disease. *Nat. Genet.* **41**(10):1094–1099. doi: <https://doi.org/10.1038/ng.439>.
- Lamkanfi, M. and Dixit, V.M. (2012). Inflammasomes and Their Roles in Health and Disease. *Annu. Rev. Cell Dev. Biol.* **28**(1):137–161. doi: <https://doi.org/10.1146/annurev-cellbio-101011-155745>.
- Latz, E. (2010). The inflammasomes: mechanisms of activation and function. *Curr. Opin. Immunol.* **22**(1):28–33. doi: <https://doi.org/10.1016/j.coi.2009.12.004>.
- Laudisi, F., Spreafico, R., Evrard, M., Hughes, T.R., Mandriani, B., Kandasamy, M., ... Mortellaro, A. (2013). Cutting Edge: The NLRP3 Inflammasome Links Complement-Mediated Inflammation and IL-1 Release. *J. Immunol.* **191**(3):1006–1010. doi: <https://doi.org/10.4049/jimmunol.1300489>.
- Lawson, C. and Hanson, R. (1995). *Solving Least Squares Problems*. Philadelphia: SIAM.
- Lee, D.D. and Seung, H.S. (1999). Learning the parts of objects by non-negative matrix factorization. *Nature* **401**(6755):788–91. doi: <https://doi.org/10.1038/44565>.
- Lee, D.D. and Seung, H.S. (2001). Algorithms for Non-negative Matrix Factorization. *Adv. Neural Inf. Process Syst. Vol. 13*. Massachusetts: MIT Press, pp. 556–562.
- Lee, G., Pollard, H.B. and Arispe, N. (2002). Annexin 5 and apolipoprotein E2 protect against Alzheimer's amyloid- β -peptide cytotoxicity by competitive inhibition at a common phosphatidylserine interaction site. *Peptides* **23**(7):1249–1263. doi: [https://doi.org/10.1016/S0196-9781\(02\)00060-8](https://doi.org/10.1016/S0196-9781(02)00060-8).
- Lee, J.H., Kim, D.H., Song, W.K., Oh, M.-K. and Ko, D.-K. (2015). Label-free imaging and quantitative chemical analysis of Alzheimer's disease brain samples with multimodal multiphoton nonlinear optical microspectroscopy. *J. Biomed. Opt.* **20**(5):56013. doi: <https://doi.org/10.1117/1.2544444>.

<https://doi.org/10.1117/1.JBO.20.5.056013>.

Lee, S.W., Pablo, J., Vaccari, D.R., Truettner, J.S., Dietrich, W.D. and Keane, R.W. (2019). The role of microglial inflammasome activation in pyroptotic cell death following penetrating traumatic brain injury. *J. Neuroinflamm.*:1–12. doi: <https://doi.org/10.1186/s12974-019-1423-6>.

Lemere, C.A., Blusztajn, J.K., Yamaguchi, H., Wisniewski, T., Saido, T.C. and Selkoe, D.J. (1996). Sequence of deposition of heterogeneous amyloid β -peptides and APO E in down syndrome: Implications for initial events in amyloid plaque formation. *Neurobiol. Dis.* **3**(1):16–32. doi: <https://doi.org/10.1006/nbdi.1996.0003>.

Li, S., Jin, M., Koeglsperger, T., Shepardson, N.E., Shankar, G.M. and Selkoe, D.J. (2011). Soluble A Oligomers Inhibit Long-Term Potentiation through a Mechanism Involving Excessive Activation of Extrasynaptic NR2B-Containing NMDA Receptors. *J. Neurosci.* **31**(18):6627–6638. doi: <https://doi.org/10.1523/JNEUROSCI.0203-11.2011>.

Liao, C.R., Rak, M., Lund, J., Unger, M., Platt, E., Albensi, B.C., ... Gough, K.M. (2013). Synchrotron FTIR reveals lipid around and within amyloid plaques in transgenic mice and Alzheimer's disease brain. *Analyst* **138**(14):3991. doi: <https://doi.org/10.1039/c3an00295k>.

Lim, G., Yang, F., Chu, T., Chen, P., Beech, W. and Teter B, et al. (2000). Ibuprofen suppresses plaque pathology and inflammation in a mouse model for Alzheimer's disease. *J. Neurosci.* **20**(15):5709–5714. doi: <https://doi.org/20/15/5709> [pii].

Lin, C.-Y., Suhaimi, J.L., Nien, C.L., Miljkovic, M.D., Diem, M., Jester, J. V. and Potma, E.O. (2011). Picosecond spectral coherent anti-Stokes Raman scattering imaging with principal component analysis of meibomian glands. *J. Biomed. Opt.* **16**(2):021104. doi: <https://doi.org/10.1117/1.3533716>.

Liu, L., Komatsu, H., Murray, I.V.J. and Axelsen, P.H. (2008). Promotion of Amyloid β Protein Misfolding and Fibrillogenesis by a Lipid Oxidation Product. *J. Mol. Biol.* **377**(4):1236–1250. doi: <https://doi.org/10.1016/j.jmb.2008.01.057>.

Liu, Y., Lee, Y.J. and Cicerone, M.T. (2009). Broadband CARS spectral phase retrieval using a time-domain Kramers–Kronig transform. *Optics Letters* **34**(9):1363. doi: <https://doi.org/10.1364/OL.34.001363>.

Lloret, A., Badia, M.-C., Mora, N.J., Pallardo, F. V., Alonso, M.-D. and Vina, J. (2009). Vitamin E Paradox in Alzheimer's Disease : It Does Not Prevent Loss of Cognition and May Even Be Detrimental. *J. Alzheimers Dis.* **17**:143–149. doi: <https://doi.org/10.3233/JAD-2009-1033>.

- Lobanova, E.G. and Lobanov, S.V. (2019). Efficient quantitative hyperspectral image unmixing method for large-scale Raman micro-spectroscopy data analysis. *Anal. Chim. Acta* **1050**:32–43. doi: <https://doi.org/10.1016/j.aca.2018.11.018>.
- Lucin, K.M. and Wyss-Coray, T. (2009). Immune Activation in Brain Aging and Neurodegeneration: Too Much or Too Little? *Neuron* **64**(1):110–122. doi: <https://doi.org/10.1016/j.neuron.2009.08.039>.
- Maier, M., Peng, Y., Jiang, L., Seabrook, T.J., Carroll, M.C. and Lemere, C.A. (2008). Complement C3 deficiency leads to accelerated amyloid plaque deposition and neurodegeneration and modulation of the microglia/macrophage phenotype in amyloid precursor protein transgenic mice. *J. Neurosci.* **28**(25):6333–6341. doi: <https://doi.org/10.1523/JNEUROSCI.0829-08.2008>.
- Markesbery, W.R. (1997). Oxidative stress hypothesis in Alzheimer's disease. *Free Radic. Biol. Med.* **23**(1):134–147.
- Martins, I.C., Kuperstein, I., Wilkinson, H., Maes, E., Vanbrabant, M., Jonckheere, W., ... Rousseau, F. (2008). Lipids revert inert A β amyloid fibrils to neurotoxic protofibrils that affect learning in mice. *EMBO J.* **27**(1):224–233. doi: <https://doi.org/10.1038/sj.emboj.7601953>.
- Matsuzaki, K. and Horikiri, C. (1999). Interactions of amyloid β -peptide (1-40) with ganglioside-containing membranes. *Biochemistry* **38**(13):4137–4142. doi: <https://doi.org/10.1021/bi982345o>.
- Matsuzaki, K., Kato, K. and Yanagisawa, K. (2010). A β polymerization through interaction with membrane gangliosides. *BBA – Molecular and Cell Biology of Lipids* **1801**(8):868–877. doi: <https://doi.org/10.1016/j.bbalip.2010.01.008>.
- Mawuenyega, K.G., Sigurdson, W., Ovod, V., Munsell, L., Kasten, T., Morris, J.C., ... Bateman, R.J. (2010). Decreased Clearance of CNS β -Amyloid in Alzheimer's Disease. *Science* **330**(6012):1774–1774. doi: <https://doi.org/10.1126/science.1197623>.
- McGeer, P.L., Akiyama, H., Itagaki, S. and McGeer, E.G. (1989). Activation of the classical complement pathway in brain tissue of Alzheimer patients. *Neurosci. Lett.* **107**(1–3):341–346. doi: [https://doi.org/10.1016/0304-3940\(89\)90843-4](https://doi.org/10.1016/0304-3940(89)90843-4).
- McKee, A.C., Carreras, I., Hossain, L., Ryu, H., Klein, W.L., Oddo, S., ... Dedeoglu, A. (2008). Ibuprofen reduces A β , hyperphosphorylated tau and memory deficits in Alzheimer mice. *Brain Res.* **1207**:225–236. doi: <https://doi.org/10.1016/j.brainres.2008.01.095>.
- McLaurin, J. and Chakrabartty, A. (1997). Characterization of the interactions of Alzheimer beta-amyloid peptides with phospholipid membranes. *Eur. J. Biochem.* **245**(2):355–363. doi:

<https://doi.org/10.1111/j.1432-1033.1997.t01-2-00355.x>.

McLaurin, J.A., Franklin, T., Fraser, P.E. and Chakrabarty, A. (1998). Structural transitions associated with the interaction of Alzheimer β - amyloid peptides with gangliosides. *J. Biol. Chem.* **273**(8):4506–4515. doi: <https://doi.org/10.1074/jbc.273.8.4506>.

Measey, T.J. and Schweitzer-Stenner, R. (2011). Vibrational Circular Dichroism as a Probe of Fibrillogenesis: The Origin of the Anomalous Intensity Enhancement of Amyloid-like Fibrils. *JACS* **133**(4):1066–1076. doi: <https://doi.org/10.1021/ja1089827>.

Meraz-Rios, M.A., Toral-Rios, D., Franco-Bocanegra, D., Villeda-Hernández, J. and Campos-Peña, V. (2013). Inflammatory process in Alzheimer's Disease. *Front. Integr. Neurosci.* **7**(August):1–15. doi: <https://doi.org/10.3389/fnint.2013.00059>.

Merlo, S., Spampinato, S.F., Beneventano, M. and Sortino, M.A. (2018). The contribution of microglia to early synaptic compensatory responses that precede β -amyloid-induced neuronal death. *Sci. Rep.* **8**(1):1–11. doi: <https://doi.org/10.1038/s41598-018-25453-1>.

Meyer-Luehmann, M., Spires-Jones, T.L., Prada, C., Garcia-Alloza, M., De Calignon, A., Rozkalne, A., ... Hyman, B.T. (2008). Rapid appearance and local toxicity of amyloid- β plaques in a mouse model of Alzheimer's disease. *Nature* **451**(7179):720–724. doi: <https://doi.org/10.1038/nature06616>.

Michael, R., Lenferink, A., Vrensen, G.F.J.M., Gelpi, E., Barraquer, R.I. and Otto, C. (2017). Hyperspectral Raman imaging of neuritic plaques and neurofibrillary tangles in brain tissue from Alzheimer's disease patients. *Sci. Rep.* **7**(1):15603. doi: <https://doi.org/10.1038/s41598-017-16002-3>.

Michael, R., Otto, C., Lenferink, A., Gelpi, E., Montenegro, G.A., Rosandić, J., ... Vrensen, G.F.J.M. (2014). Absence of amyloid-beta in lenses of Alzheimer patients: a confocal Raman microspectroscopic study. *Exp. Eye Res.* **119**:44–53. doi: <https://doi.org/10.1016/j.exer.2013.11.016>.

Milanesi, L., Sheynis, T., Xue, W.-F., Orlova, E. V., Hellewell, A.L., Jelinek, R. and Hewitt, E.W. (2012). Direct three-dimensional visualization of membrane disruption by amyloid fibrils. *Proc. Natl. Acad. Sci. U.S.A.* **109**(50):20455–20460. doi: <https://doi.org/10.1073/pnas.1206325109>.

Miljkovic, M., Chernenko, T., Romeo, M.J., Bird, B., Matthaus, C. and Diem, M. (2010). Label-free imaging of human cells: algorithms for image reconstruction of Raman hyperspectral datasets. *Analyst* **135**(8):2002–2013. doi: <https://doi.org/10.1039/c0an00042f>.

- Morgan, B.P., Luzio, J.P. and Campbell, A.K. (1986). Intracellular Ca²⁺ and cell injury: A paradoxical role of Ca²⁺ in complement membrane attack. *Cell Calcium* **7**(5–6):399–411. doi: [https://doi.org/10.1016/0143-4160\(86\)90042-4](https://doi.org/10.1016/0143-4160(86)90042-4).
- Mori, T., Paris, D., Town, T., Rojiani, A.M., Sparks, L., Delledonne, A., ... Mullan, M.J. (2001). Cholesterol Accumulates in Senile Plaques of Alzheimer Disease Patients and in Transgenic APP Mice. *J. Neuropathol. Exp. Neurol.* **60**(8):778–785.
- Movasaghi, Z., Rehman, S. and Rehman, I.-U. (2007). Raman Spectroscopy of Biological Tissues. *Appl. Spectrosc. Rev.* **42**(5):493–541. doi: <https://doi.org/10.1080/05704920701551530>.
- Muik, B., Lendl, B., Molina-Diaz, A. and Ayora-Canada, M.-J. (2005). Direct monitoring of lipid oxidation in edible oils by Fourier transform Raman spectroscopy. *Chem. Phys. Lipids* **134**(2):173–182. doi: <https://doi.org/10.1016/j.chemphyslip.2005.01.003>.
- Murphy, S.R., Chang, C.C., Dogbevia, G., Bryleva, E.Y., Bowen, Z., Hasan, M.T. and Chang, T.-Y. (2013). Acat1 Knockdown Gene Therapy Decreases Amyloid- β in a Mouse Model of Alzheimer's Disease. *Mol. Ther.* **21**(8):1497–1506. doi: <https://doi.org/10.1038/mt.2013.118>.
- Di Napoli, C., Pope, I., Masia, F., Langbein, W., Watson, P. and Borri, P. (2016). Quantitative spatiotemporal chemical profiling of individual lipid droplets by hyperspectral CARS microscopy in living human adipose-derived stem cells. *Anal. Chem.* **88**(7):3677–3685. doi: <https://doi.org/10.1021/acs.analchem.5b04468>.
- Nascimento, J.M.P. and Dias, J.M.B. (2005). Vertex component analysis: A fast algorithm to unmix hyperspectral data. *IEEE Transactions on Geoscience and Remote Sensing* **43**(4):898–910. doi: <https://doi.org/10.1109/TGRS.2005.844293>.
- Neumann, H., Kotter, M.R. and Franklin, R.J.M. (2009). Debris clearance by microglia: An essential link between degeneration and regeneration. *Brain* **132**(2):288–295. doi: <https://doi.org/10.1093/brain/awn109>.
- Niculescu, F. and Rus, H. (2001). Mechanisms of Signal Transduction Activated by Sublytic Assembly of Terminal Complement Complexes on Nucleated Cells. *Immunol. Res.* **24**(2):191–199.
- Oku, Y., Murakami, K., Irie, K., Hoseki, J. and Sakai, Y. (2017). Synthesized A β 42 Caused Intracellular Oxidative Damage, Leading to Cell Death, via Lysosome Rupture. *Cell Struct. Funct.* **42**(1):71–79. doi: <https://doi.org/10.1247/csf.17006>.
- Paatero, P. (1997). Least squares formulation of robust non-negative factor analysis. *Chemometr.*

- Intell. Lab. Syst.* **37**(1):23–35. doi: [https://doi.org/10.1016/S0169-7439\(96\)00044-5](https://doi.org/10.1016/S0169-7439(96)00044-5).
- Paatero, P. and Tapper, U. (1994). Positive matrix factorization: a non-negative factor model with optimal utilization of error estimates of data values. *Environmetrics* **5**(2):111–126. doi: <https://doi.org/10.1002/env.3170050203>.
- Paolo, G. Di and Kim, T.-W. (2011). Linking lipids to Alzheimer's disease: cholesterol and beyond. *Nat. Rev. Neurosci.* **12**(5):284–296.
- Di Paolo, G. and Kim, T.W. (2011). Linking lipids to Alzheimer's disease: Cholesterol and beyond. *Nature Rev. Neurosci.* **12**(5):284–296. doi: <https://doi.org/10.1038/nrn3012>.
- Parajuli, B., Sonobe, Y., Horiuchi, H., Takeuchi, H., Mizuno, T. and Suzumura, A. (2013). Oligomeric amyloid β induces IL-1 β processing via production of ROS: Implication in Alzheimer's disease. *Cell Death Dis.* **4**(12):1–8. doi: <https://doi.org/10.1038/cddis.2013.503>.
- Paul, J., Strickland, S. and Melchor, J.P. (2007). Fibrin deposition accelerates neurovascular damage and neuroinflammation in mouse models of Alzheimer's disease. *J. Exp. Med.* **204**(8):1999–2008. doi: <https://doi.org/10.1084/jem.20070304>.
- Peng, J., Peng, S., Jiang, A., Wei, J., Li, C. and Tan, J. (2010). Asymmetric least squares for multiple spectra baseline correction. *Anal. Chim. Acta* **683**(1):63–68. doi: <https://doi.org/10.1016/j.aca.2010.08.033>.
- Piqueras, S., Duponchel, L., Tauler, R. and De Juan, A. (2011). Resolution and segmentation of hyperspectral biomedical images by Multivariate Curve Resolution-Alternating Least Squares. *Anal. Chim. Acta* **705**:182–192. doi: <https://doi.org/10.1016/j.aca.2011.05.020>.
- Prasad, M.R., Lovell, M.A., Yatin, M., Dhillon, H. and Markesbery, W.R. (1998). Regional membrane phospholipid alterations in Alzheimer's Disease. *Neurochem. Res.* **23**(1):81–88.
- Puglielli, L., Konopka, G., Pack-Chung, E., Ingano, L.A., Berezovska, O., Hyman, B.T., ... Kovacs, D.M. (2001). Acyl-coenzyme A: cholesterol acyltransferase modulates the generation of the amyloid beta-peptide. *Nat. Cell Biol.* **3**(10):905–912. doi: <https://doi.org/10.1038/ncb1001-905>.
- Ramos, P., Santos, A., Pinto, N.R., Mendes, R., Magalhães, T. and Almeida, A. (2014). Iron levels in the human brain: A post-mortem study of anatomical region differences and age-related changes. *J. Trace Elem. Med. Biol.* **28**(1):13–17. doi: <https://doi.org/http://dx.doi.org/10.1016/j.jtemb.2013.08.001>.

- Rathkey, J.K., Benson, B.L., Chirieleison, S.M., Yang, J., Xiao, T.S., Dubyak, G.R., ... Abbott, D.W. (2017). Live-cell visualization of gasdermin D-driven pyroptotic cell death. *J. Biol. Chem.* **292**(35):14649–14658. doi: <https://doi.org/10.1074/jbc.M117.797217>.
- Refolo, L.M., Pappolla, M.A., Malester, B., LaFrancois, J., Bryant-Thomas, T., Wang, R., ... Duff, K. (2000). Hypercholesterolemia Accelerates the Alzheimer's Amyloid Pathology in a Transgenic Mouse Model. *Neurobiol. Dis.* **7**(4):321–331. doi: <https://doi.org/10.1006/nbdi.2000.0304>.
- Rogers, J., Cooper, N.R., Webster, S., Schultz, J., McGeer, P.L., Styren, S.D., ... Ward, P. (1992). Complement activation by beta-amyloid in Alzheimer disease. *PNAS* **89**(21):10016–10020. doi: <https://doi.org/10.1073/pnas.89.21.10016>.
- Rubio-Perez, J.M. and Morillas-Ruiz, J.M. (2012). A review: Inflammatory process in Alzheimer's disease, role of cytokines. *The Scientific World Journal* **2012**. doi: <https://doi.org/10.1100/2012/756357>.
- Rygula, A., Majzner, K., Marzec, K.M., Kaczor, A., Pilarczyk, M. and Baranska, M. (2013). Raman spectroscopy of proteins: A review. *J. Raman. Spectrosc.* **44**(8):1061–1076. doi: <https://doi.org/10.1002/jrs.4335>.
- Ryzhikova, E., Kazakov, O., Halámková, L., Celmins, D., Malone, P., Molho, E., ... Lednev, I.K. (2014). Raman spectroscopy of blood serum for Alzheimer's disease diagnostics: specificity relative to other types of dementia. *J. Biophotonics* **8**(7):1–13. doi: <https://doi.org/10.1002/jbio.201400060>.
- Sadeghi-Jorabchi, H., Wilson, R.H., Belton, P.S., Edwards-Webb, J.D. and Coxon, D.T. (1991). Quantitative analysis of oils and fats by Fourier transform Raman spectroscopy. *Spectrochimica Acta Part A: Molecular Spectroscopy* **47**(9/10):1449–1458. doi: [https://doi.org/10.1016/0584-8539\(91\)80236-C](https://doi.org/10.1016/0584-8539(91)80236-C).
- Sainati, S., Ingram, D., Talwalker, S. and Geis, G. (2000). Results of a double-blind, randomized, placebo-controlled study of celecoxib in the treatment of progression of Alzheimer's disease. *Proceedings of the Sixth International Stockholm/Springfield Symposium on Advances in Alzheimer Therapy*. Stockholm, p. 180.
- Sarlus, H. and Heneka, M.T. (2017). Microglia in Alzheimer's disease. *JCI* **127**(9):3240–3249. doi: <https://doi.org/10.1172/JCI90606>.
- Savitzky, A. and Golay, M.J.E. (1964). Smoothing and differentiation of data by simplified least squares procedures. *Anal. Chem.* **36**(8):1627–1639. doi: <https://doi.org/10.1021/ac60214a047>.

- Schafer, D.P., Lehrman, E.K., Kautzman, A.G., Koyama, R., Mardinly, A.R., Yamasaki, R., ... Stevens, B. (2012). Microglia Sculpt Postnatal Neural Circuits in an Activity and Complement-Dependent Manner. *Neuron* **74**(4):691–705. doi: <https://doi.org/10.1016/j.neuron.2012.03.026>.
- Schweitzer-Stenner, R. (2012). Conformational propensities and residual structures in unfolded peptides and proteins. *Mol. BioSyst.* **8**(1):122–133. doi: <https://doi.org/10.1039/C1MB05225J>.
- Schweitzer-Stenner, R., Measey, T., Hagarman, A., Eker, F. and Griebenow, K. (2006). Salmon Calcitonin and Amyloid β : Two Peptides with Amyloidogenic Capacity Adopt Different Conformational Manifolds in Their Unfolded States †. *Biochemistry* **45**(9):2810–2819. doi: <https://doi.org/10.1021/bi052282r>.
- Selkoe, D.J. (2001a). Presenilin, Notch, and the genesis and treatment of Alzheimer's disease. *PNAS* **98**(20):11039–11041. doi: <https://doi.org/10.1073/pnas.211352598>.
- Selkoe, D.J. (2001b). Alzheimer's Disease: Genes, Proteins, and Therapy. *Physiol. Rev.* **81**(2):741–766.
- Selkoe, D.J. and Hardy, J. (2016). The amyloid hypothesis of Alzheimer's disease at 25 years. *EMBO Mol. Med.* **8**(6):595–608. doi: <https://doi.org/10.15252/emmm.201606210>.
- Serna, M., Giles, J.L., Morgan, B.P. and Bubeck, D. (2016). Structural basis of complement membrane attack complex formation. *Nat. Commun.* **7**:10587. doi: <https://doi.org/10.1038/ncomms10587>.
- Shankar, G.M., Li, S., Mehta, T.H., Garcia-Munoz, A., Shepardson, N.E., Smith, I., ... Selkoe, D.J. (2008). Amyloid- β protein dimers isolated directly from Alzheimer's brains impair synaptic plasticity and memory. *Nat. Med.* **14**(8):837–842. doi: <https://doi.org/10.1038/nm1782>.
- Shen, Y., Li, R., Mcgeer, E.G. and Mcgeer, P.L. (1997). Neuronal expression of mRNAs for complement proteins of the classical pathway in Alzheimer brain. *Brain Res.* **769**:391–395.
- Shi, J., Zhao, Y., Wang, K., Shi, X., Wang, Y., Huang, H., ... Shao, F. (2015). Cleavage of GSDMD by inflammatory caspases determines pyroptotic cell death. *Nature* **526**(7575):660–665. doi: <https://doi.org/10.1038/nature15514>.
- Shi, Y., Kirwan, P., Smith, J., MacLean, G., Orkin, S.H. and Livesey, F.J. (2012). A Human Stem Cell Model of Early Alzheimer's Disease Pathology in Down Syndrome. *Sci. Transl. Med.* **4**(124):124ra29-124ra29. doi: <https://doi.org/10.1126/scitranslmed.3003771>.
- Simard, A.R., Soulet, D., Gowing, G., Julien, J.P. and Rivest, S. (2006). Bone marrow-derived

microglia play a critical role in restricting senile plaque formation in Alzheimer's disease. *Neuron* **49**(4):489–502. doi: <https://doi.org/10.1016/j.neuron.2006.01.022>.

Sleutel, M., Van Den Broeck, I., Van Gerven, N., Feuillie, C., Jonckheere, W., Valotteau, C., ... Remaut, H. (2017). Nucleation and growth of a bacterial functional amyloid at single-fiber resolution. *Nat. Chem. Biol.* **13**(8):902–908. doi: <https://doi.org/10.1038/nchembio.2413>.

Sojkova, J., Driscoll, I., Iacono, D., Zhou, Y., Codispoti, K.-E., Kraut, M.A., ... Resnick, S.M. (2011). In Vivo Fibrillar β -Amyloid Detected Using [11C]PiB Positron Emission Tomography and Neuropathologic Assessment in Older Adults. *Arch. Neurol.* **68**(2):612–615. doi: <https://doi.org/10.1001/archneurol.2010.357>.

Sparks, D.L., Scheff, S.W., Hunsaker III, J.C., Liu, H., Landers, T. and Gross, D.R. (1994). Induction of Alzheimer-like β -Amyloid Immunoreactivity in the Brains of Rabbits with Dietary Cholesterol. *Exp. Neurol.* **126**(1):88–94. doi: <https://doi.org/10.1006/exnr.1994.1044>.

Stefani, M. (2012). Structural features and cytotoxicity of amyloid oligomers: Implications in Alzheimer's disease and other diseases with amyloid deposits. *Prog. Neurobiol.* **99**(3):226–245. doi: <https://doi.org/10.1016/j.pneurobio.2012.03.002>.

Stocker, R. and Keaney, J.F. (2004). Role of Oxidative Modifications in Atherosclerosis. *Physiol. Rev.* **84**(4):1381–1478. doi: <https://doi.org/10.1152/physrev.00047.2003>.

Subramaniam, S.R. and Federoff, H.J. (2017). Targeting microglial activation states as a therapeutic avenue in Parkinson's disease. *Front. Aging Neurosci.* **9**(JUN):1–18. doi: <https://doi.org/10.3389/fnagi.2017.00176>.

Sung, S., Yang, H., Uryu, K., Lee, E.B., Zhao, L., Shineman, D., ... Praticò, D. (2004). Modulation of nuclear factor- κ B activity by indomethacin influences A β levels but not A β precursor protein metabolism in a model of Alzheimer's disease. *AM. J. PATHOL.* **165**(6):2197–2206. doi: [https://doi.org/10.1016/S0002-9440\(10\)63269-5](https://doi.org/10.1016/S0002-9440(10)63269-5).

Szaruga, M., Munteanu, B., Lismont, S., Veugelen, S., Horr , K., Mercken, M., ... Ch vez-Guti rrez, L. (2017). Alzheimer's-Causing Mutations Shift A β Length by Destabilizing γ -Secretase-A β n Interactions. *Cell* **170**(3):443-456.e14. doi: <https://doi.org/10.1016/j.cell.2017.07.004>.

Takami, M., Nagashima, Y., Sano, Y., Ishihara, S., Morishima-Kawashima, M., Funamoto, S. and Ihara, Y. (2009). γ -secretase: successive tripeptide and tetrapeptide release from the transmembrane domain of beta-carboxyl terminal fragment. *J. Neurosci.* **29**(41):13042–13052.

doi: <https://doi.org/10.1523/JNEUROSCI.2362-09.2009>.

Takashima, A., Noguchi, K., Sato, K., Hoshino, T. and Imahori, K. (1993). Tau protein kinase I is essential for amyloid beta-protein-induced neurotoxicity. *PNAS* **90**(16):7789–7793. doi: <https://doi.org/10.1073/pnas.90.16.7789>.

Tremi, I., Anagnostopoulos, D., Spyratou, E., Gkeka, P., Georgakilas, A.G., Chatgililoglu, C. and Cournia, Z. (2018). Effect of 5-trans Isomer of Arachidonic Acid on Model Liposomal Membranes Studied by a Combined Simulation and Experimental Approach. *J. Membr. Biol.* **251**(3):475–489. doi: <https://doi.org/10.1007/s00232-018-0029-8>.

Triantafilou, K., Hughes, T.R., Triantafilou, M. and Morgan, B.P. (2013). The complement membrane attack complex triggers intracellular Ca²⁺ fluxes leading to NLRP3 inflammasome activation. *J. Cell Sci.* **126**(13):2903–2913. doi: <https://doi.org/10.1242/jcs.124388>.

Uzunbajakava, N., Lenferink, A., Kraan, Y.M., Volokhina, E., Vrensen, G., Greve, J. and Otto, C. (2003). Nonresonant confocal Raman imaging of DNA and protein distribution in apoptotic cells. *Biophys. J.* **84**(6):3968–81. doi: [https://doi.org/10.1016/S0006-3495\(03\)75124-8](https://doi.org/10.1016/S0006-3495(03)75124-8).

Vajna, B., Farkas, A., Pataki, H., Zsigmond, Z., Igricz, T. and Marosi, G. (2012). Testing the performance of pure spectrum resolution from Raman hyperspectral images of differently manufactured pharmaceutical tablets. *Anal. Chim. Acta* **712**:45–55. doi: <https://doi.org/10.1016/j.aca.2011.10.065>.

Venegas, C., Kumar, S., Franklin, B.S., Dierkes, T., Brinkschulte, R., Tejera, D., ... Heneka, M.T. (2017). Microglia-derived ASC specks cross-seed amyloid- β in Alzheimer's disease. *Nature* **552**(7685):355–361. doi: <https://doi.org/10.1038/nature25158>.

Walport, M.J. (2001). Complement. First of two parts. *N. Engl. J. Med.* **344**(14):1058–1066. doi: <https://doi.org/10.1056/NEJM200104053441406>.

Wang, D.-S., Iwata, N., Hama, E., Saido, T.C. and Dickson, D.W. (2003). Oxidized neprilysin in aging and Alzheimer's disease brains. *Biochem. Biophys. Res. Commun.* **310**(1):236–241. doi: <https://doi.org/10.1016/j.bbrc.2003.09.003>.

Wang, Q., Wang, Y. and Lu, H.P. (2013). Revealing the secondary structural changes of amyloid β peptide by probing the spectral fingerprint characters. *J. Raman Spectrosc.* **44**(5):670–674. doi: <https://doi.org/10.1002/jrs.4253>.

Wang, W.Y., Tan, M.S., Yu, J.T. and Tan, L. (2015). Role of pro-inflammatory cytokines released from microglia in Alzheimer's disease. *Ann. Transl. Med.* **3**(10):136. doi:

<https://doi.org/10.3978/j.issn.2305-5839.2015.03.49>.

Wang, Z.J., Liang, C.L., Li, G.M., Yu, C.Y. and Yin, M. (2006). Neuroprotective effects of arachidonic acid against oxidative stress on rat hippocampal slices. *Chemico-Biological Interactions* **163**(3):207–217. doi: <https://doi.org/10.1016/j.cbi.2006.08.005>.

Warnock, D.E., Roberts, C., Lutz, M.S., Blackburn, W.A., Young, W.W. and Baenziger, J.U. (1993). Determination of plasma membrane lipid mass and composition in cultured Chinese hamster ovary cells using high gradient magnetic affinity chromatography. *J. Biol. Chem.* **268**(14):10145–10153. doi: <https://doi.org/10.1164/rccm.201203-0411OC>.

Webster, S., Lue, L.-F., Brachova, L., Tenner, A.J., McGeer, P.L., Terei, K., ... Rogers, J. (1997). Molecular and cellular characterization of the membrane attack complex, C5b-9, in Alzheimer's disease. *Neurobiol. Aging* **18**(4):415–421. doi: <https://doi.org/0197-4580/97>.

Webster, S.D., Yang, A.J., Margol, L., Garzon-Rodriguez, W., Glabe, C.G. and Tenner, A.J. (2000). Complement component C1q modulates the phagocytosis of A β by microglia. *Exp. Neurol.* **161**(1):127–138. doi: <https://doi.org/10.1006/exnr.1999.7260>.

Weiner, H.L. and Frenkel, D. (2006). Immunology and immunotherapy of Alzheimer's disease. *Nat. Rev. Immunol.* **6**(5):404–416. doi: <https://doi.org/10.1038/nri1843>.

Weiss, J.H., Pike, C.J. and Cotman, C.W. (1994). Ca²⁺ Channel Blockers Attenuate β -Amyloid Peptide Toxicity to Cortical Neurons in Culture. *J. Neurochem.* **62**(1):372–375. doi: <https://doi.org/10.1046/j.1471-4159.1994.62010372.x>.

Widenbrant, M.J.O., Rajadas, J., Sutardja, C. and Fuller, G.G. (2006). Lipid-Induced β -Amyloid Peptide Assemblage Fragmentation. *Biophys. J.* **91**(11):4071–4080. doi: <https://doi.org/10.1529/biophysj.106.085944>.

Wu, H., Volponi, J. V., Oliver, A.E., Parikh, A.N., Simmons, B.A. and Singh, S. (2011). In vivo lipidomics using single-cell Raman spectroscopy. *PNAS* **108**(9):3809–3814. doi: <https://doi.org/10.1073/pnas.1009043108>.

Wyss-Coray, T., Lin, C., Yan, F., Yu, G.-Q., Rohde, M., McConlogue, L., ... Mucke, L. (2001). TGF- β 1 promotes microglial amyloid- β clearance and reduces plaque burden in transgenic mice. *Nat. Med.* **7**(5):1–7.

Yamamoto, M., Kiyota, T., Walsh, S.M., Liu, J., Kipnis, J. and Ikezu, T. (2008). Cytokine-Mediated Inhibition of Fibrillar Amyloid- Peptide Degradation by Human Mononuclear Phagocytes. *J. Immunol.* **181**(6):3877–3886. doi: <https://doi.org/10.4049/jimmunol.181.6.3877>.

Yanagisawa, K., Odaka, A., Suzuki, N. and Ihara, Y. (1995). GM1 ganglioside-bound amyloid beta-protein (A beta): a possible form of preamyloid in Alzheimer's disease. *Nat. Med.* **1**(6):1062–1066. doi: <https://doi.org/10.1038/nm0495-365>.

Yatin, S.M., Aksenova, M., Aksenov, M., Markesbery, W.R., Aulick, T. and Allan Butterfield, D. (1998). Temporal relations among amyloid β -peptide-induced free-radical oxidative stress, neuronal toxicity, and neuronal defensive responses. *J. Mol. Neurosci.* **11**(3):183–197. doi: <https://doi.org/10.1385/JMN:11:3:183>.

Zatta, P., Drago, D., Bolognin, S. and Sensi, S.L. (2009). Alzheimer's disease , metal ions and metal homeostatic therapy. *Trends Pharmacol. Sci.* **30**(7):346–355. doi: <https://doi.org/10.1016/j.tips.2009.05.002>.

Zhang, D., Wang, P., Slipchenko, M.N., Ben-Amotz, D., Weiner, A.M. and Cheng, J.-X. (2013). Quantitative vibrational imaging by hyperspectral Stimulated Raman Scattering microscopy and Multivariate Curve Resolution analysis. *Anal. Chem.* **85**(1):98–106. doi: <https://doi.org/10.1021/ac3019119>.Quantitative.

Zhang, L., Henson, M.J. and Sekulic, S.S. (2005). Multivariate data analysis for Raman imaging of a model pharmaceutical tablet. *Anal. Chim. Acta* **545**(2):262–278. doi: <https://doi.org/10.1016/j.aca.2005.04.080>.

Publication list

Journal Papers: Refereed

- [1] Lobanova, E.G. and Lobanov, S.V. (2019). Efficient quantitative hyperspectral image unmixing method for large-scale Raman micro-spectroscopy data analysis. *Anal. Chim. Acta* **1050**:32–43. doi: <https://doi.org/10.1016/j.aca.2018.11.018>.
- [2] Lobanova, E.G., Lobanov, S.V., Khokhlova, V.A. (2014) Counterpropagation of Waves with Shock Fronts in a Nonlinear Tissue-Like Medium. *Acoustical Physics* **60**(4): 389–399. doi: <https://doi.org/10.1134/S1063771014040071>

Journal Papers: Not Refereed

- [1] Lobanova, E., Lobanov, S., Triantafilou, K., Langbein W., Borri P., Quantitative chemical imaging of amyloid- β plaques with Raman micro-spectroscopy in human Alzheimer's diseased brains, arXiv: 1803.01201 (2018).

Conference Papers:

- [1] Lobanova, E., Triantafilou, K., and Triantafilou, M. Revealing interplay between ASC specks and amyloid- β aggregation in human Alzheimer's disease brains, The Lancet Summit, Inflammation and Immunity in Disorders of the Brain and Mind, Barcelona, Spain, November 15-17, 2018.
- [2] Lobanova, E., Lobanov, S., Triantafilou, K., Langbein W., Borri P., Quantitative imaging of amyloid-lipid co-arrangements in A β plaques with label-free optical micro-spectroscopy in Alzheimer's disease: new biomarkers in diagnosis, Bio-Nano-Photonics Symposium, Cardiff, UK, September 18-19, 2017.
- [3] Lobanova, E. G., Khokhlova, V. A. Modeling nonlinear acoustic wave propagation in an inhomogeneous viscous media based on the full wave equation, Session of the Scientific Council of RAS on acoustics and XXV Session of the Russian Acoustical Society, pp. 125-128, V.1., Taganrog, September 17-20, 2012.
- [4] Lobanova, E. G., Khokhlova, V. A. Modeling of propagation nonlinear acoustic waves in a heterogeneous lossy media using the full wave equation, XIII All-Russian Workshop "Wave phenomena in heterogeneous environments", pp. 19-22, CD-ROM, Zvenigorod, May 21-26, 2012.